frontiers | Research Topics

Impact of solar activities on weather and climate

Edited by
Ziniu Xiao, Peili Wu, Limin Zhou, Irina Alexandrovna Mironova, Liang Zhao and Hiroko Miyahara

Coordinated by
Wenjuan Huo

Published in
Frontiers in Earth Science

ISSN 1664-8714
ISBN 978-2-8325-4326-9
DOI 10.3389/978-2-8325-4326-9

About Frontiers

Frontiers is more than just an open access publisher of scholarly articles: it is a pioneering approach to the world of academia, radically improving the way scholarly research is managed. The grand vision of Frontiers is a world where all people have an equal opportunity to seek, share and generate knowledge. Frontiers provides immediate and permanent online open access to all its publications, but this alone is not enough to realize our grand goals.

Frontiers journal series

The Frontiers journal series is a multi-tier and interdisciplinary set of open-access, online journals, promising a paradigm shift from the current review, selection and dissemination processes in academic publishing. All Frontiers journals are driven by researchers for researchers; therefore, they constitute a service to the scholarly community. At the same time, the *Frontiers journal series* operates on a revolutionary invention, the tiered publishing system, initially addressing specific communities of scholars, and gradually climbing up to broader public understanding, thus serving the interests of the lay society, too.

Dedication to quality

Each Frontiers article is a landmark of the highest quality, thanks to genuinely collaborative interactions between authors and review editors, who include some of the world's best academicians. Research must be certified by peers before entering a stream of knowledge that may eventually reach the public - and shape society; therefore, Frontiers only applies the most rigorous and unbiased reviews. Frontiers revolutionizes research publishing by freely delivering the most outstanding research, evaluated with no bias from both the academic and social point of view. By applying the most advanced information technologies, Frontiers is catapulting scholarly publishing into a new generation.

What are Frontiers Research Topics?

Frontiers Research Topics are very popular trademarks of the *Frontiers journals series*: they are collections of at least ten articles, all centered on a particular subject. With their unique mix of varied contributions from Original Research to Review Articles, Frontiers Research Topics unify the most influential researchers, the latest key findings and historical advances in a hot research area.

Find out more on how to host your own Frontiers Research Topic or contribute to one as an author by contacting the Frontiers editorial office: frontiersin.org/about/contact

Impact of solar activities on weather and climate

Topic editors

Ziniu Xiao — Institute of Atmospheric Physics, Chinese Academy of Sciences (CAS), China

Peili Wu — Met Office Hadley Centre (MOHC), United Kingdom

Limin Zhou — East China Normal University, China

Irina Alexandrovna Mironova — Saint Petersburg State University, Russia

Liang Zhao — State Key Laboratory of Numerical Modeling for Atmosphere Sciences and Geophysical Fluid Dynamics (LASG), Institute of Atmospheric Physics, Chinese Academy of Sciences, China

Hiroko Miyahara — Musashino Art University, Japan

Topic Coordinator

Wenjuan Huo — Centre for Marine Biotechnology, GEOMAR Helmholtz Center for Ocean Research Kiel, Helmholtz Association of German Research Centres (HZ), Germany

Citation

Xiao, Z., Wu, P., Zhou, L., Mironova, I. A., Zhao, L., Miyahara, H., Huo, W., eds. (2024). *Impact of solar activities on weather and climate*. Lausanne: Frontiers Media SA. doi: 10.3389/978-2-8325-4326-9

Table of contents

04 Editorial: Impact of solar activities on weather and climate
Ziniu Xiao, Liang Zhao, Limin Zhou, Wenjuan Huo, Irina Mironova and Hiroko Miyahara

06 The possible impact of solar activity on the summer temperature distribution over Eurasia
Wei Lu, Ziniu Xiao and Xueshang Feng

20 Decadal variability of precipitation over the Tibetan Plateau modulated by the 11-year solar cycle over the past millennium
Ying Hu, Weiyi Sun, Jian Liu, Deliang Chen, Liang Ning and Zhenghan Peng

31 Combined effect of the solar activity and ENSO on the tropical cyclone genesis frequency in the southeastern part of the western North Pacific
Shuang Li, Zhangqun Li and Sining Ling

43 Modulation of the solar activity on the connection between the NAO and the tropical pacific SST variability
Wenjuan Huo, Ziniu Xiao and Liang Zhao

57 Influence of solar forcing on multidecadal variability in the Atlantic meridional overturning circulation (AMOC)
Aihua Ye, Zhipeng Zhu, Ruyi Zhang, Ziniu Xiao and Limin Zhou

73 The triple-dip La Niña of 2020–22: updates to the correlation of ENSO with the termination of solar cycles
Robert J. Leamon

84 11-year solar cycle influences on the late-wintertime South Asian jet variability
Hedi Ma, Ruili Wang, Xing Li, Anwei Lai and Xiao Li

98 Response of high-altitude clouds to the galactic cosmic ray cycles in tropical regions
Hiroko Miyahara, Kanya Kusano, Ryuho Kataoka, Shin-ichiro Shima and Emile Touber

110 Energy transmission processes in the effectuation chain of solar forcing to the terrestrial atmosphere—a review
Jingsong Wang, Liang Zhao, Ziniu Xiao, Peng Zhang, Zhipeng Ren, Weiguo Zong, Jin Qi, Cong Huang, Ying Xu and Yixiong Lu

117 Asymmetric modulation of solar activity on tropical cyclone frequency over the western North Pacific and the possible mechanism
Delin Li, Ziniu Xiao, Jianjun Xu and Liang Zhao

frontiers | Frontiers in Earth Science

TYPE Editorial
PUBLISHED 08 January 2024
DOI 10.3389/feart.2023.1338416

OPEN ACCESS

EDITED AND REVIEWED BY
Patrick Laux,
Karlsruhe Institute of Technology (KIT), Germany

*CORRESPONDENCE
Liang Zhao,
zhaol@lasg.iap.ac.cn

RECEIVED 14 November 2023
ACCEPTED 27 December 2023
PUBLISHED 08 January 2024

CITATION
Xiao Z, Zhao L, Zhou L, Huo W, Mironova I and Miyahara H (2024), Editorial: Impact of solar activities on weather and climate.
Front. Earth Sci. 11:1338416.
doi: 10.3389/feart.2023.1338416

Editorial: Impact of solar activities on weather and climate

Ziniu Xiao[1], Liang Zhao[1]*, Limin Zhou[2], Wenjuan Huo[3], Irina Mironova[4] and Hiroko Miyahara[5]

[1]State Key Laboratory of Numerical Modeling for Atmosphere Sciences and Geophysical Fluid Dynamics (LASG), Institute of Atmospheric Physics, Chinese Academy of Sciences (CAS), Beijing, China, [2]Key Laboratory of Geographic Information Science, Ministry of Education, East China Normal University, Shanghai, China, [3]Department of Ocean Circulation and Climate Dynamics, GEOMAR Helmholtz Center for Ocean Research Kiel, Helmholtz Association of German Research Centres (HZ), Kiel, Germany, [4]Department of Earth's Physics, Saint Petersburg State University, Saint Petersburg, Russia, [5]Humanities and Sciences/Museum Careers, Musashino Art University, Tokyo, Japan

KEYWORDS

solar activity, energetic particle precipitation and cosmic ray, climate change, climate system response, monsoon and ENSO, stratosphere-troposphere coupling, atmospheric electric field

Editorial on the Research Topic
Impact of solar activities on weather and climate

The Sun drives the atmospheric dynamics of our planet and plays a role in shaping weather and climate patterns on Earth. While the exact mechanism of solar influence on weather and climate on decadal or shorter time scales is still a challenge, scientists have proposed and even observed several ways in which solar activities can affect our planet's atmospheric conditions by different energy forms and physical processes.

This Research Topic, "*Impact of Solar Activities on Weather and Climate*", includes articles that address solar effects on weather and climate and explore the physical mechanism. Papers range from the impacts of the solar activity on the temperature, precipitation, tropical cyclones (TC), North Atlantic Oscillation (NAO), Atlantic meridional overturning circulation (AMOC), the El Niño–Southern Oscillation (ENSO), South Asian jet to response of clouds to the Galactic Cosmic Ray (GCR).

Two papers in this Research Topic are focused on the relationship between solar activity and surface climate variability. Lu et al. focused on the link between solar activity and the summer temperature distribution over Eurasian land and found a significant 11-year solar periodicity in the temperature patterns, particularly in Central Asia. Solar-induced negative geopotential height anomalies in Central Asia weaken high-pressure ridges and strengthen northwesterly, leading to regional lower temperatures. Hu et al. conducted research into the decadal fluctuations in precipitation over the Tibetan Plateau, in relation to the 11-year solar cycle. In the solar maximum years, a substantial surface warming over the Asian continent enhances the Indian summer monsoon through changing land-ocean thermal contrast and increases precipitation over the central-southern Tibetan Plateau.

Two papers are focused on the relationship between solar activity and TC. The first paper by Li et al. investigated the combined effect of solar activity and ENSO on TC genesis frequency in the Western North Pacific. El Niño years during declining phases of the solar cycle show significantly strong positive anomalies in TC genesis frequency. Various atmospheric and oceanic factors, such as sea surface temperature anomalies and wind patterns, contribute to the connections between solar cycle and TC genesis frequency. The

joint effect of Sun and ENSO on the asymmetry of TC frequency found in the second paper by Li et al. The second paper by Li et al. found that intensified solar activity significantly increased the number of TCs in high-solar activity years, while no significant modulation was observed in low-solar activity years. Increased solar radiation in high-solar activity years leads to stronger surface upward latent heat flux an evaporation, thereby enhancing local upward motion and cyclonic winds over the TC source.

Three papers are focused on the relationship between solar activity and the ocean. Leamon established a correlation between the occurrence of solar cycle terminations and the transition to La Niña based on observations and understanding of the solar 22-year magnetic activity cycle. They predicted a transition to La Niña in mid-2020, which indeed occurred and persisted until 2023 as a rare "triple dip" event. However, some of the solar predictions made did not occur until late 2021. The study examined the correlations between El Niño, La Niña, and geomagnetic activity indices, providing insights into the general trends of large-scale global climate in the next decade. Huo et al. investigated the solar modulation on the connection between NAO and ENSO. They found that the boreal winter NAO-like SLP anomalies have a linear covariation with the subsequent boreal summer El Niño Modoki-like SST anomalies in the tropical Pacific in the following 1 year during the high solar activity period. The positive NAO-like SLP anomalies can enhance the influence of the North Tropical Atlantic SST on the tropical Pacific SST by triggering significant and more persistent subtropical teleconnections. Ye et al. studied the influence of solar forcing on multidecadal variability in the AMOC, a crucial component of the ocean's thermohaline circulation system. In this study, they conducted experiments using an Earth System model with different total solar irradiance (TSI) series. They found that the declining AMOC could be attributed to the decadal variation in TSI.

Besides, Ma et al. found that the 11-year solar cycle can influence the South Asian jet by two mechanisms. One mechanism involves a solar-induced tilted NAO pattern, which triggered southeastward wave activity fluxes towards the South Asian jet. Another mechanism is the decreased convective activity over the Maritime Continent area, which can be attributed to the weakening of the Pacific Walker Circulation caused by solar activity.

The study by Miyahara et al. explored how GCRs affect high-altitude clouds via deep convective activities over tropical land areas. The authors found that susceptible areas are seasonally variable, with the most notable responses observed in August. Additionally, following the activation of high-altitude cloud formation, an increase in sea surface temperature gradient was observed over the Pacific. While the influence of solar radiation on sea surface temperature has been widely studied, the authors suggested that the impact of GCRs on cloud formation and subsequent changes in atmospheric circulations could be one of the underlying mechanisms.

Wang et al. reviewed four processes of energy transmission in the effectuation chain of solar forcing to the climate system: solar energy input into the atmosphere, atmospheric absorption of the input energy, transformation of the absorbed energy into dynamic and thermodynamic responses in the atmosphere, and coupling among all the layers affected by solar forcing. The paper detailed how solar radiation varies during the solar cycle and solar eruptions, and how the terrestrial atmosphere absorbs the input solar energy.

Overall, this Research Topic highlights the Frontier discoveries and advancements in the research on sun-climate relationships. The ten works analyzed the possible mechanisms and reasons from the perspectives of solar radiation and cosmic rays. They also highlighted the challenges and questions in studying the influence of the Sun on the Earth's atmosphere and climate on decadal and shorter time scales. Finally, we would like to express our sincere gratitude to all the authors and reviewers who have contributed their valuable insights and expertise to this Research Topic.

Author contributions

ZX: Conceptualization, Writing–review and editing. LZ: Formal Analysis, Funding acquisition, Investigation, Writing–original draft, Writing–review and editing. LZ: Writing–review and editing. WH: Writing–review and editing. IM: Writing–review and editing. HM: Writing–review and editing.

Funding

The author(s) declare financial support was received for the research, authorship, and/or publication of this article. This work is supported by the National Natural Science Foundation of China (42075040 and 42274217).

Conflict of interest

The authors declare that the research was conducted in the absence of any commercial or financial relationships that could be construed as a potential conflict of interest.

Publisher's note

frontiers | Frontiers in Earth Science

TYPE Original Research
PUBLISHED 25 January 2023
DOI 10.3389/feart.2022.1087737

OPEN ACCESS

EDITED BY
Folco Giomi,
Independent Researcher, Padova, Italy

REVIEWED BY
Maxim Ogurtsov,
Ioffe Institute (RAS), Russia
Nicola Scafetta,
University of Naples Federico II, Italy

*CORRESPONDENCE
Ziniu Xiao,
xiaozn@lasg.iap.ac.cn

SPECIALTY SECTION
This article was submitted to Interdisciplinary Climate Studies, a section of the journal Frontiers in Earth Science

RECEIVED 02 November 2022
ACCEPTED 02 December 2022
PUBLISHED 25 January 2023

CITATION
Lu W, Xiao Z and Feng X (2023), The possible impact of solar activity on the summer temperature distribution over Eurasia.
Front. Earth Sci. 10:1087737.
doi: 10.3389/feart.2022.1087737

The possible impact of solar activity on the summer temperature distribution over Eurasia

Wei Lu[1,2], Ziniu Xiao[3]* and Xueshang Feng[1]

[1]SIGMA Weather Group, State Key Laboratory of Space Weather, National Space Science Center, Chinese Academy of Sciences, Beijing, China, [2]University of Chinese Academy of Sciences, Beijing, China, [3]State Key Laboratory of Numerical Modeling for Atmospheric Sciences and Geophysical Fluid Dynamics, Institute of Atmospheric Physics, Chinese Academy of Sciences, Beijing, China

The effect of solar activity on the regional temperature in winter has been widely discussed. However, whether the summer temperature of land in the northern hemisphere is sensitive to solar activity remains to be further investigated. In this study, the empirical orthogonal function (EOF) analysis, spectrum analysis, and correlation analysis are employed to reveal the possible link between the summer temperature distribution over Eurasian land (0–180°E and 20°N–80°N) and solar activity. The results show that the corresponding time series of the second pattern significantly exhibits an 11-year solar periodicity. Its tripolar temperature distribution is similar to the correlation maps between the temperature and sunspot number (SSN). Particularly, Central Asia (50°E–90°E and 30°N–60°N) is the key response region over Eurasia. The temperature of Central Asia shows a weak but significant negative correlation with SSN. Further analysis of atmospheric circulation indicates that the solar-induced cyclonic and negative geopotential height anomalies in Central Asia weaken the high-pressure ridge on the southwest side and strengthen northwesterly winds. At the same time, with the increase in the cloud cover and the decrease of shortwave radiation, the temperature is lowered. Due to the impact of solar activity, the upper atmosphere over Eurasia forms a wave train-like structure, resulting in a tripolar temperature distribution pattern. On the other hand, the 21-year sliding correlation results suggest that the connection between solar activity and the temperature in Central Asia was strong and decadal stable until 1980. Whereas the temperature and atmospheric circulations in high latitudes become more sensitive to solar activity after 1980. Anyway, solar activity still can be considered a non-negligible factor in the prediction of the summer temperature in Eurasia.

KEYWORDS

solar cycle, temperature distribution, Eurasian climate, decadal change, summer

1 Introduction

As the external forcing of the earth system, solar activity has a major impact on terrestrial climate change. Solar signals have been found in the stratosphere and troposphere. The process of the down-transmission of the solar signal to the surface is usually explained by two mechanisms, i.e., 'Top-down' and 'Bottom-up' (Gray et al., 2010; Ding, 2019). Solar radiation is a direct source of energy for the climate system, which is usually used to assess the solar influence on climate in model simulations. However, the assessment of the effects of climate on the response to solar irradiance in IPCC AR6 mainly focuses on the global scale, lacking a view of regional climate change. Then, the impact of solar activity on climate change is spatially selective. (Cao, 2021; IPCC, 2021; Xiao, 2021). In addition, Connolly et al. (2021) found that the response of the solar irradiance to solar activity in the northern hemisphere depends on the estimation methods. They claim that solar activity appears to be underestimated in modern climate change prediction. Hence, the issue of the impact of solar activity on climate change should continue to be addressed.

Temperature is one of the key parameters of climate change. Numerous statistical studies have found similar periodicities in the temperature proxy records and solar variations during the Holocene, revealing the possible linkage between temperature and solar activity on centennial-to-decadal scales (Soon, 2005; Zhao and Feng, 2014; Liu et al., 2019; Huang et al., 2020; Ogurtsov et al., 2020; Brehm et al., 2021). In the 20th century, strong correlations between solar irradiance and the temperature of the mid-upper troposphere are also found based on the proxy data (Wang et al., 2010).

Kodera et al. (2016) concluded the spatial structure of global solar signal based on the surface temperature variations from observations and model data, reflecting the differences in regional responses. The surface air temperatures over Eurasia, such as Turkey and Japan, are sensitive to solar forcing (Kilcik, 2005; Kilcik et al., 2008). Kilcik et al. (2010) proved that the response of Atlantic-Eurasian regions depends on the latitudes and solar activity affects the temperature of mid-latitudes significantly in winter. Moreover, some scientists proposed that solar forcing has a significant effect on the wintertime temperature and precipitation over Asia (Kossobokov et al., 2010; Chen et al., 2015; Ojala et al., 2015; Song et al., 2019; Chen et al., 2020; Xu et al., 2020). Recently, Xu et al. (2020) revealed that extreme cold events are highly related to the energetic particle precipitation in winter over Eurasia and the interaction of wave-mean flow in the stratosphere and troposphere is an important medium in the downward process of solar signals.

In particular, the spatial distribution of solar signals in winter is pointed to be similar to the second EOF pattern of the Eurasian temperature in the early research (Miyazaki and Yasunari, 2008; Chen et al., 2015). Maliniemi et al. (2014) found that the clearest winter temperature distribution pattern is seen in the declining phase of the solar cycle and the pattern of positive North Atlantic Oscillation is produced by the declining phase. Nevertheless, the response of summer temperature over Eurasia to solar activity has not received enough attention.

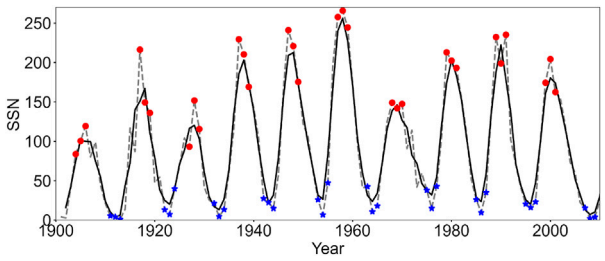

FIGURE 1
Time series of SSN. The dashed gray and solid black curves are the series of JJA SSN and 3-year running mean values of JJA SSN. The red (blue) dots mark the HS (LS) years.

Overall, we first analyze the distribution of summer temperature over Eurasian land and further do the spectrum and correlation analysis to reveal the possible linkage between solar activity and the temperature. Then we mainly analyze the mechanism of solar activity signal transmission to the surface from the perspective of atmospheric circulation. This allows us to elucidate the causes of temperature changes in regions perturbed by solar activity.

2 Datasets and methods

2.1 Datasets

In this study, 'summer' is defined as the average values of June, July, and August. The SSN is usually used to characterize solar activity in previous studies. The SSN data is obtained from Sunspot Index and Long-term Solar Observation site, which is available at https://wwwbis.sidc.be/silso/datafiles. The monthly SSN data covers the period from 1749 to the present. We mainly focus on the changes in solar activity during 1901–2010 because of the limitations of meteorological data.

Two monthly temperature datasets from ERA-20C (ERA_tmp) and CRU TS 4.05 dataset (CRU_tmp) are used. The CRU TS 4.05 dataset spans a period from 1901 to 2020, with a spatial resolution of $0.5^{\circ} \times 0.5^{\circ}$. It is a gridded monthly dataset from the Climatic Research Unit (University of East Anglia) and Met Office (Harris, 2020), which is derived by interpolating monthly anomalies from station observations. ERA-20C (1901–2020) is a twentieth-century reanalysis dataset from ECMWF, available at https://apps.ecmwf.int/datasets/data/era20c-daily/levtype=sfc/type=an/. We also use $2.5^{\circ} \times 2.5^{\circ}$ monthly mean atmospheric variations, including winds, geopotential height (HGT), cloud,

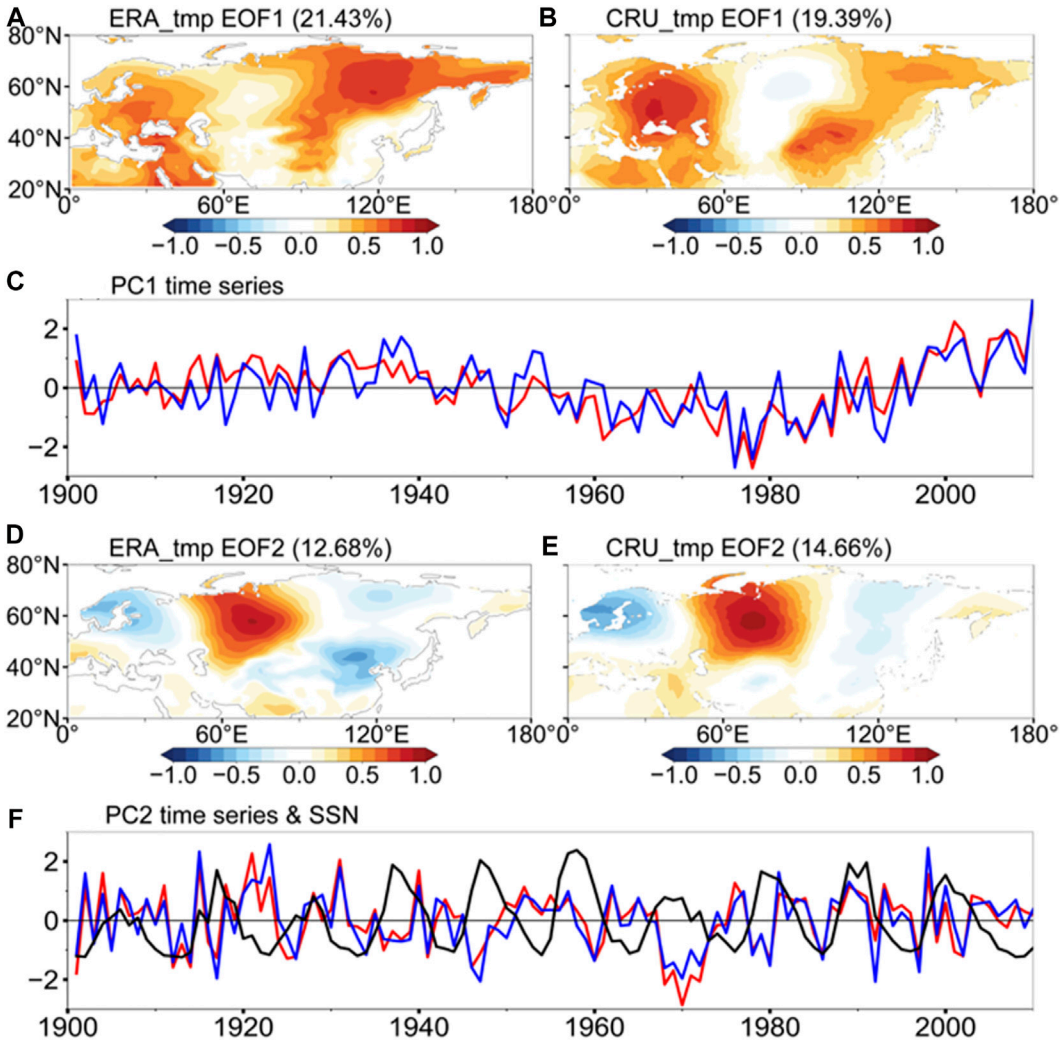

FIGURE 2
Spatial patterns and the corresponding normalized time series for the leading first **(A–C)** and second **(D–F)** EOF modes of summer land Eurasian temperature (unit: °C) anomalies over 0–180°E and 20°N –80°N during 1901–2010. The red (blue) solid lines are the corresponding time series of ERA_tmp (CRU_tmp). The black solid line is the standardized SSN.

precipitation, and radiation from the ERA-20C dataset. The boundary data of the Qinghai-Tibet Plateau comes from http://data.tpdc.ac.cn/zh-hans/data/61701a2b-31e5-41bf-b0a3-607c2a9bd3b3/(Zhang et al., 2021).

2.2 Methods

Following Thiéblemont et al. (2015) and Huo et al. (2021), we select high and low solar activity (HS and LS) years by the 3-year running mean method. Figure 1 shows the time series of JJA SSN and 3-year sliding mean JJA SSN. The HS (LS) years of each solar cycle are marked by the red (blue) dots during 1901–2020. The HS years are listed as follows: 1904, 1905, 1906, 1917, 1918, 1919, 1927, 1928, 1929, 1937, 1938, 1939, 1947, 1948, 1949, 1957, 1958, 1959, 1968, 1969, 1970, 1979, 1980, 1981, 1989, 1990, 1991, 1999, 2000, and 2001. And the LS years include 1911, 1912, 1913, 1922, 1923, 1924, 1932, 1933, 1934, 1942, 1943, 1944, 1953, 1954, 1955, 1963, 1964, 1965, 1975, 1976, 1977, 1985, 1986, 1987, 1995, 1996, 1997, 2007, 2008, and 2009. We will investigate the responses of terrestrial temperature to solar activity by composite analysis in the following part.

The EOF method is also called principal component analysis (PCA). This approach captures the dominant spatial distribution and its time-varying characteristics by deriving the orthogonal empirical eigenvectors of the covariance matrix associated with climate variables (Ionita et al., 2012; Zhang and Moore, 2015). Multi-previous studies utilized this way to extract temperature

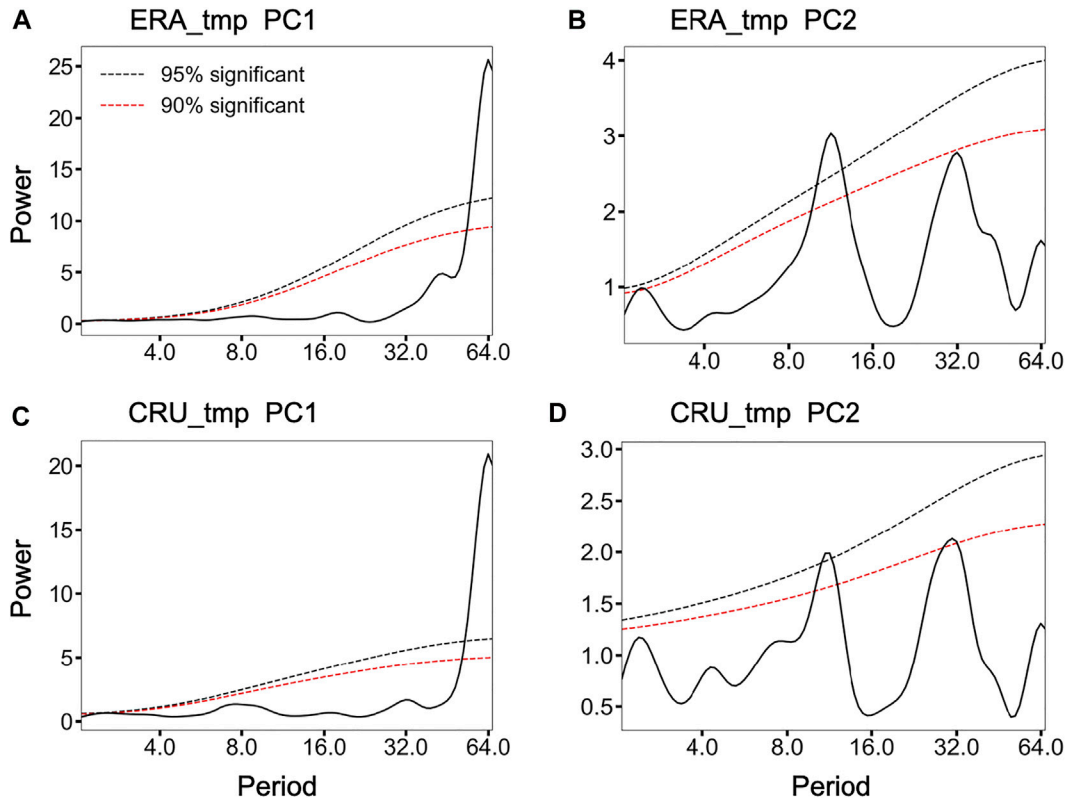

FIGURE 3
Power spectrums of the time series of the leading modes. The red (black) dashed lines indicate statistical confidence levels are 90% (95%). **(A)** ERA_tmp PC1. **(B)** ERA_tmp PC2. **(C)** CRU_tmp PC1. **(D)** CRU_tmp PC2.

patterns and analyze the causes of temperature changes (Hong et al., 2017; Ning et al., 2022; Song et al., 2022). This study takes advantage of the orthogonal characteristic between the patterns to better grasp the solar signal in the summer temperature over Eurasian. Then, correlation and composite differences analysis are combined to further explore the process of the impact of solar activity. In the last part, we conduct the sliding correlation analysis to assess the stability of the relationship between solar activity and the Eurasian summer temperature.

3 Association between solar activity and Eurasian summer temperature

3.1 The link between solar activity and the temperature spatial distribution

In this study, we first extract the first two dominant patterns and the corresponding principal component time series of summer temperature over Eurasian land (0–180° E and 20°N −80° N) through the EOF analysis method (Figure 2). The first leading mode shows positive temperature anomalies over the whole land, explaining 12.68%/14.66% of the total variance (Figures 2A,B). Previous studies pointed out the westerly jet is the main factor for the summer warming of the latitude of 40°N −65°N after 1960 (Wu and Sun, 2015). In addition, the corresponding PC1 time series have no apparent decadal periodicity (Figures 3A,C) and it shows a very weak relationship with SSN with the correlation coefficients $r = -0.02/0.01$. Hence, no more attention is paid to the first leading modes in this study.

The second EOF mode, accounting for 21.43%/19.39% of the variance, is characterized by '-+-' tripolar patterns in high latitudes, corresponding with the found by Wu and Sun (2015). They have anomalies of one positive sign centered in the region over Central Asia-Southwest of Russia and the other two negative signs over the two sides of Eurasian land, respectively (Figures 2D,E). But the 11-year solar periodicity signal is significantly present in the PC2 time series, which is above the 95% confidence level (Figures 3B,D).

To reveal the correlation between solar activity and temperature distribution, we calculate the correlation coefficients between PC2 and SSN. SSN is negatively correlated with the corresponding PC2 times series during

TABLE 1 Correlation coefficients between PC2 and the other climate indices.

	ERA_tmp-PC2	CRU_tmp-PC2
EASMi	0.10	0.11
NAO	−0.07	−0.08
PDO	0.04	0.03
SOI	0.04	0.06
Nino3.4	0.02	−0.04

1901–2010 (r = −0.12/−0.16, p<0.1), and the correlations are much weaker with PC3 (r = −0.07/0.06). The correlations are stronger than that between SSN and other climate indices listed in Table 1, such as the East Asian summer monsoon index (EASMi), North Atlantic oscillation (NAO), Pacific Decadal Oscillation (PDO), Southern Oscillation Index (SOI) and the Niño3.4 index. Namely, the second spatial distribution of summer temperature is possibly modulated by the solar cycle. Overall, we focus on the response of the Eurasian summer temperature to solar activity.

On the other hand, Figures 4A,B depict the correlation maps between detrended summer temperature and SSN during 1901–2010, revealing the significant response regions to solar activity. The impact of solar activity on Eurasian land varies regionally in summer. But in winter, strong solar activity tends to warm the temperature of most Eurasian land (Chen et al., 2015). In the middle and high latitudes of Central Asia (30°N –60°N, 50°E –90°E), the temperature is negatively correlated to the solar activity, which is opposite to that in the two sides of Eurasian land. It is also worth noting that the spatial patterns of correlation maps are alike to the second EOF modes of summer temperature over Eurasian land (Figures 2C,D).

On the other hand, Figures 4A,B depict the correlation maps between detrended summer temperature and SSN during 1901–2010, revealing the significant response regions to solar activity. The impact of solar activity on Eurasian land varies regionally in summer. But in winter, strong solar activity tends to warm the temperature of most Eurasian land (Chen et al., 2015). In the middle and high latitudes of Central Asia (30°N–60°N, 50°E–90°E), the temperature is negatively correlated to the solar activity, which is opposite to that in the two sides of Eurasian land. It is also worth noting that the spatial patterns of correlation maps are alike to the second EOF modes of summer temperature over Eurasian land (Figures 2C,D).

According to the temperature distribution pattern and the correlation maps with the solar activity, the area of Central Asia has attached attention. Huang et al. (2020) also found that the summer temperature of acid central Asia also has a common cycle with solar activity during the Holocene. We show the temperature time series of Central Asia in Figure 5. The regional temperature is positively correlated to the corresponding PC2 and the correlation coefficient between SSN and PC2 of ERA_tmp (CRU_tmp) is 0.63 (0.76), which is significantly above the 99% confidence level. Besides, the correlation coefficients between SSN and the temperature of Central Asia are −0.19/−0.24, which is significantly above the 95% confidence level. In addition, the temperature of Central Asia has an 11-year solar cycle. Hence, Central Asia is the key response area to solar activity. In the following, we mainly discuss the impact of solar activity on the summer temperature of Central Asia.

3.2 Physical process analysis

The evidence in Section 3.1 reveals the relationship between solar activity and summer temperature over Eurasia, especially in Central Asia. How does the Sun signal transmit downward? To further explore the physical process of the impact of solar activity, we pay attention to the response of the atmospheric circulation

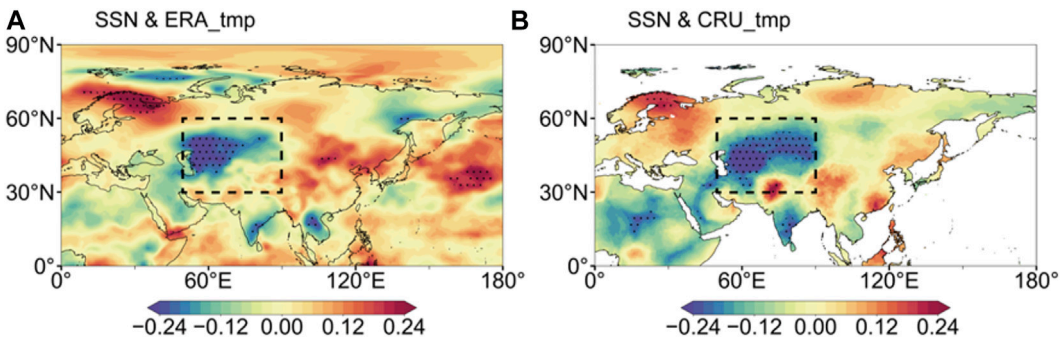

FIGURE 4
Correlation maps between detrended summer temperature and SSN over Eurasia during 1901–2010. Black dotted regions are above 95% confidence level. Central Asia (30°N–60°N and 50°E–90°E) is marked by the black dashed frame. **(A)** SSN and ERA_tmp. **(B)** SSN and CRU_tmp.

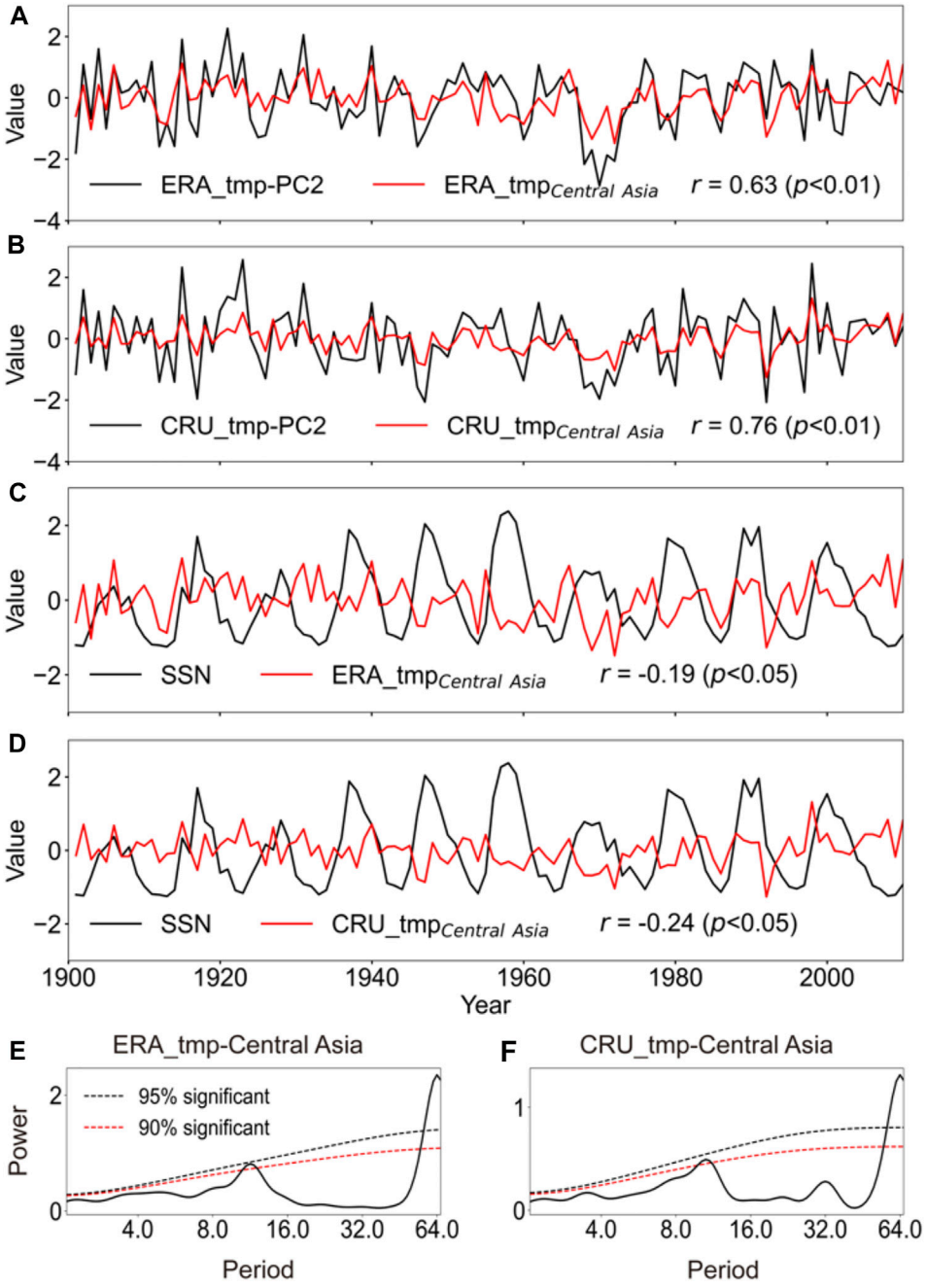

FIGURE 5
Comparison of the temperature of Central Asia (30°N–60°N and 50°E–90°E) and PC2 **(A,B)** and SSN **(C,D)**, **(E,F)** Power spectrum of the summer temperature for Central Asia. The red and black dashed lines indicate statistical confidence at the 90% and 95% confidence levels.

and cloud-radiation feedback mechanism based on the analysis of the composite differences and regression.

Figures 6A–C show composite differences between HS and LS years of geopotential height and wind at 200 hPa, 500 hPa, and 850 hPa over Central Asia. Solar activity induces positive geopotential height anomalies at 500 hPa and cyclonic anomalies at 850 hPa in most of the Eurasian land regions except Central Asia. The circulation anomalies' patterns resemble each other at 200 hPa, 500 hPa, and 850 hPa, reflecting a barotropic structure. The magnitudes of the circulation anomalies become weaker with the height from top to bottom. Meanwhile, the mean background climatology states during 1901–2010 are

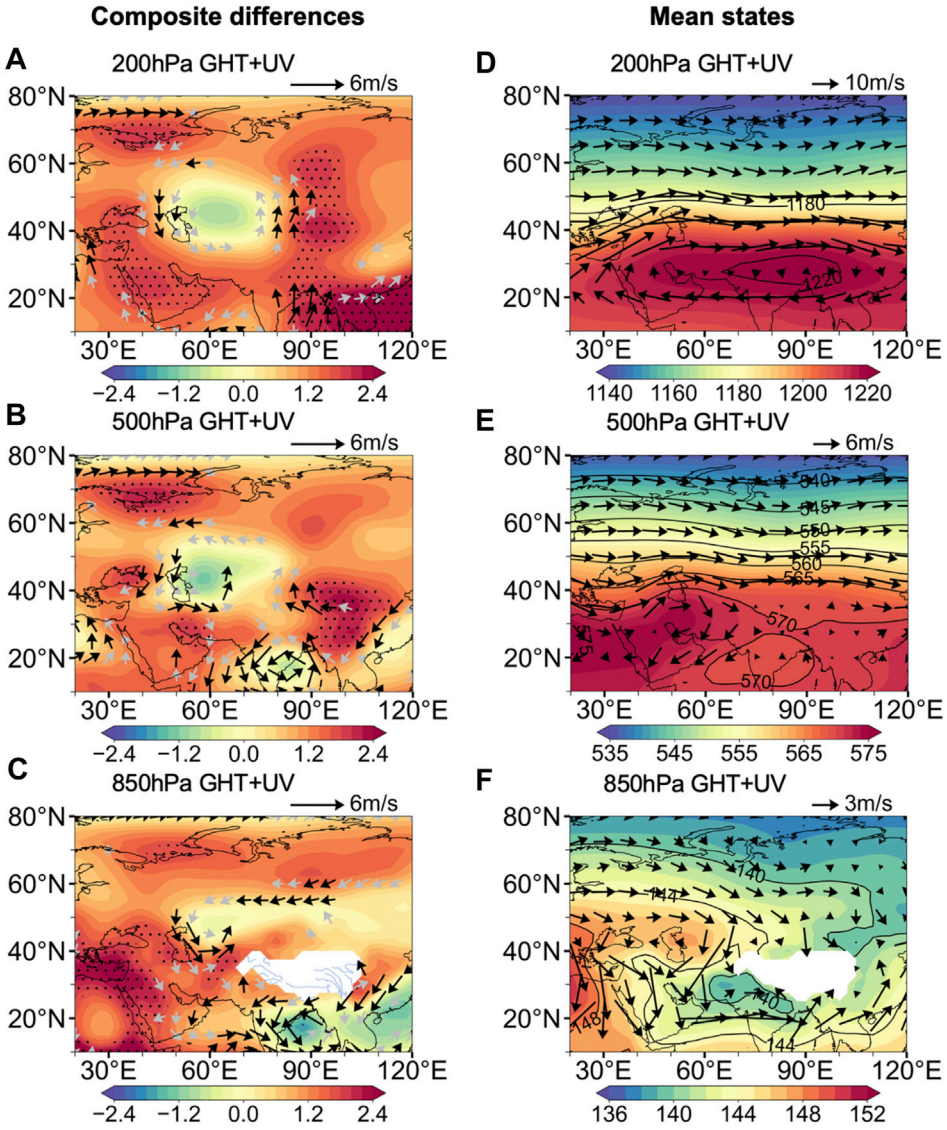

FIGURE 6
(A–C) Composite differences (HS minus LS) of wind and geopotential height (GHT, color) at 850 hPa, 500 hPa, and 200 hPa during 1901–2010. Black dots marks regions where GHT differences are above 90% confidence level. The black vectors show the wind differences are over 90% confidence level **(D–F)** Background climatology states GHT and winds at 850 hPa, 500 hPa, and 850 hPa in summer over Eurasia during 1901–2010. The wind and geopotential data at 850 hPa on the Qinghai-Tibet Plateau are ignored.

illustrated in Figures 6D–F for comparison. In the southwest of Central Asia, high pressure at 500 hPa centered at 30°N and 60°E exists. And northwesterly winds prevail at 850 hPa in summer due to the pressure gradient over Central Asia. Combining the disturbance of the atmospheric circulation field by solar activity and the climatic background field, the negative geopotential height anomalies over Central Asia, opposite to the other regions in Eurasian land, weaken the high-pressure ridge in the southwest of Central Asia. Besides, the cyclonic anomalies strengthen the northwesterly wind, causing more transport of cold advection to Central Asia.

Figure 7 presents the correlation maps between geopotential height and wind at 200 hPa, 500 hPa, and 850 hPa and SSN during 1901–2010, indicating the contribution of solar activity to circulation. A wave train-like structure of geopotential anomalies with one negative and two positive anomalies at 500 hPa shows up in the mid-high latitude, which is similar to the second pattern of the summer temperature distribution in Figure 2. The wave train-like structure is weaker in the bottom of the troposphere than that in the upper troposphere. At 850 hPa, a pair of cyclonic and anticyclonic anomalies appear in the northwest of the Eurasian land, which may affect advective transport. The

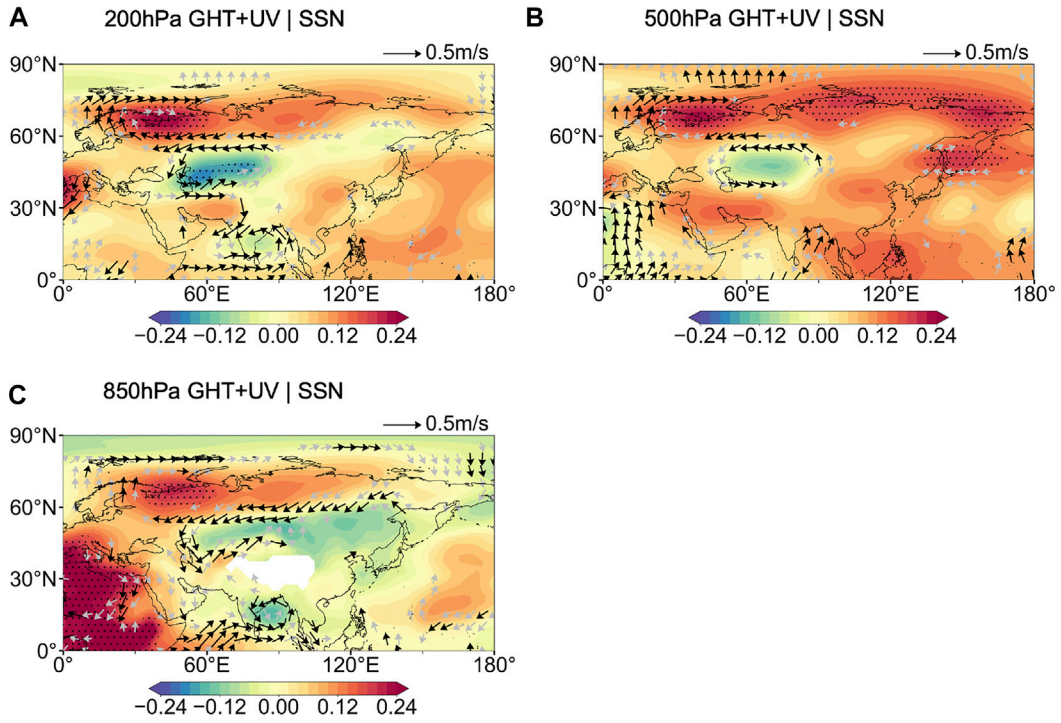

FIGURE 7
Correlation maps between **(A)** 200 hPa, **(B)** 500 hPa, and **(C)** 850 hPa geopotential height (GHT, color) and wind (vector) and SSN. Black dots marks regions where GHT differences are above 90% confidence level. The black vectors show the wind differences are over 90% confidence level. The wind and geopotential data at 850 hPa on the Qinghai-Tibet Plateau are ignored.

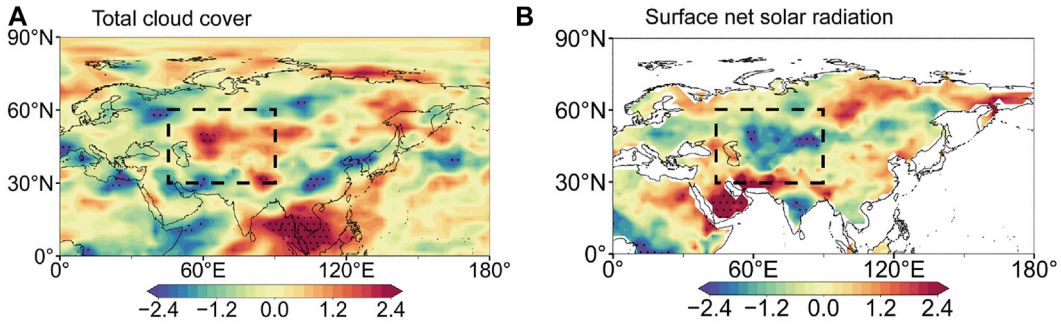

FIGURE 8
Composite differences (HS minus LS) of total cloud cover **(A)** surface net solar radiation **(B)** (units: J·m^{-2}) during 1901–2010. during 1901–2010. Central Asia (30 °N–60°N and 50°E–90°E) is marked by the black dashed frame.

results of regression analysis show no essential differences with the analysis of the composite differences, except for the size of several significant areas. Solar activity will perturb the climate background field, thereby weakening the climate system and strengthening convection.

Figure 8 illustrates the composite differences in the cloud, radiation, and precipitation between HS and LS years during 1901–2010. The composite differences patterns of total cloud cover are characterized by positive anomalies centered over Central Asia and negative anomalies in other areas of Eurasian land (Figure 8A). It is consistent with the correlation patterns between temperature and SSN in Figure 3. The pattern for surface net solar radiation is opposite to that for the total cloud cover (Figure 8B).

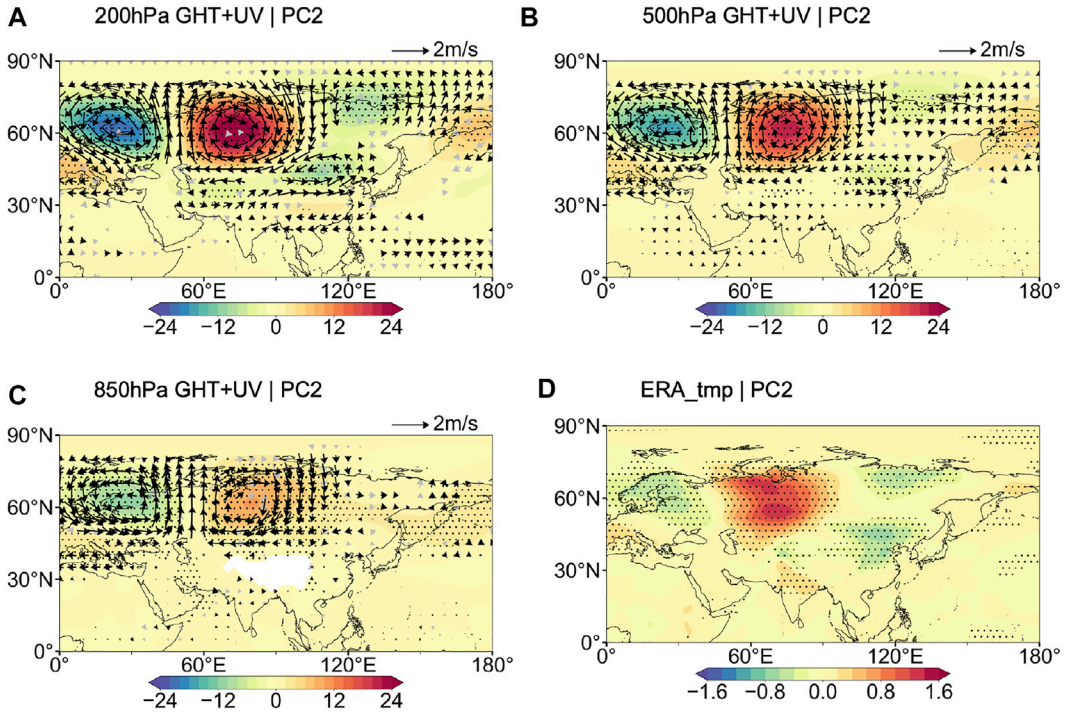

FIGURE 9
Regression maps of **(A)** 200 hPa, **(B)** 500 hPa, and **(C)** 850 hPa geopotential height (GHT, color) and wind (vector), and **(D)** ERA_tmp onto PC2. Black dots marks regions where GHT differences are above 90% confidence level. The black vectors show the wind differences are over 90% confidence level. The wind and geopotential data at 850 hPa on the Qinghai-Tibet Plateau are ignored.

Previous studies found that the temperature is sensitive to cloud-radiative feedback (Tang et al., 2012; Tang and Leng, 2012). Increased total cloud cover over Central Asia inhibits the downward transmission of solar energy, resulting in lower temperatures. The negative anomalies of the surface net solar radiation result from the increase in the total cloud cover. The synergy amplifies the effect of solar activity on the temperature.

Figure 9 depicts the atmospheric circulations and surface air temperature anomalies regressed onto the second dominant time series PC2. The GHT and wind anomalies at 200 hPa show a tripolar pattern characterized by '-+-' anomalies in mid-high latitude (Figure 9A). The significant positive anomalies centered over northern Europe, which is in contrast to other negative responses over the other regions in Eurasian. Furthermore, the similar and weaker patterns at 500 hPa and 850 hPa reflect an equivalent structure. The wave-train-like temperature anomalous pattern associated with PC2 resembles the correlation maps between solar activity and atmospheric circulation (Figure 7).

4 Discussion

In the sections above, it is revealed the response of the Eurasian summer temperature to solar activity during 1901–2010. We note that the decadal changes in the relationship between the summer temperature of the mid-upper troposphere over Eurasia have been found through proxy data and the empirical mode decomposition method (Wang et al., 2010). Based on the 449-year reconstructed temperature, Duan and Zhang (2014) found disparities between temperature in Tibet Plateau and solar activity are identified in two periods, the 1880s–1900s and the 1980s–present. It should be noted that a similar reversal of signs of solar-climatic correlation at the beginning of the 80s was also reported by Georgieva et al. (2007) and Veretenenko and Ogurtsov (2012). However, Ogurtsov and Veretenenko (2017) found responses of low atmosphere to solar activity in winter Russia changed in the 2000s approximately. Chiodo et al. (2019) suggested that the solar signal only occurs in NAO after the mid-1960s, which is not robust. The research above reveals that the decadal impacts of solar activity on regional climate are different and the persistence of the impact and the stability of the signal deserves attention.

In this study, we find the size of atmospheric response areas differs between the composite and correlation analysis results (Figure 6 and Figure 7). The correlation analysis is based on the whole data, while the composite analysis is only for the years of extreme solar activity. Therefore, we further assess the decadal

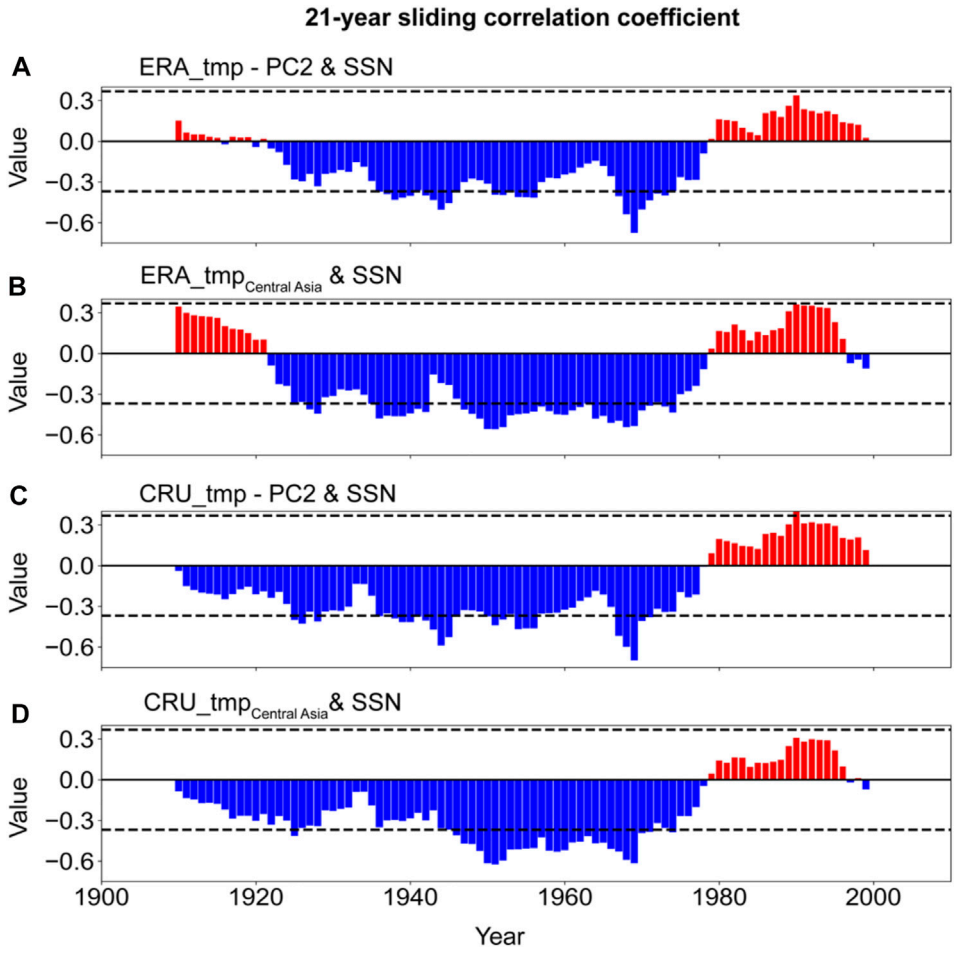

FIGURE 10
The 21-year sliding correlation coefficient between SSN and the time series of PC2 **(A–C)** and the temperature of Central Asia **(B–D)** during 1901–2010. The values of dashed lines are ± 0.369, which represents the 90% confidence level.

stability of the relationship between the Eurasian summer temperature and solar activity to expound the reasons for the differences.

Figure 10 shows the 21-year sliding correlations between SSN and PC2 and the temperature of Central Asia. The PC2 was negatively related to SSN before 1980, but the relationship became weak and positive after 1980. The relationship between the temperature of Central Asia and solar activity keeps pace with PC2. We note that the negative correlation period is about central-decadal years (Figure 10). Scafetta (2014) thought there might be another oscillation, such as a 9.1-year oscillation, beating with the 11-year solar cycle and producing a long-beat pattern. To clarify the decadal change of the impact of solar activity on the temperature and ensure consistent degrees of freedom, we chose two periods of the same length, i.e., 1951–1980 (P1) and 1981–2010 (P2) in the following part (Table 2). The correlation coefficients between PC2 and SSN during P1 are −0.31/−0.37 with above 90% significant confidence, but they are 0.23/0.29 during P2 with no statistical significance.

We also find remarkable differences are seen in the correlation maps between SSN and temperature during P1 and P2 (Figure 11). For the latitude of 30°N–60°N, strong negative connections persist during the 1951–1980 period. In contrast, the temperature is significantly positive relative to SSN in high latitudes during the 1981–2010 period. During P1, Central Asia is the significant negative response region of temperature to solar activity (r = −0.46, p<0.05/−0.52, p<0.05). However, the temperature of Central Asia becomes insensitive to solar activity after 1980 (r = 0.03/0.07). And the mid-high latitude regions, such as North Europe and East Russia, are more sensitive to solar activity. Additionally, the correlation between the temperature of Central Asia and the corresponding PC2 is weaker during P2 (r = 0.64, p<0.01/0.75, p<0.01) than that during P1 (r = 0.36, p<0.01/0.70, p<0.01). These similar changes in 1980 reveal that the link between solar activity and the second

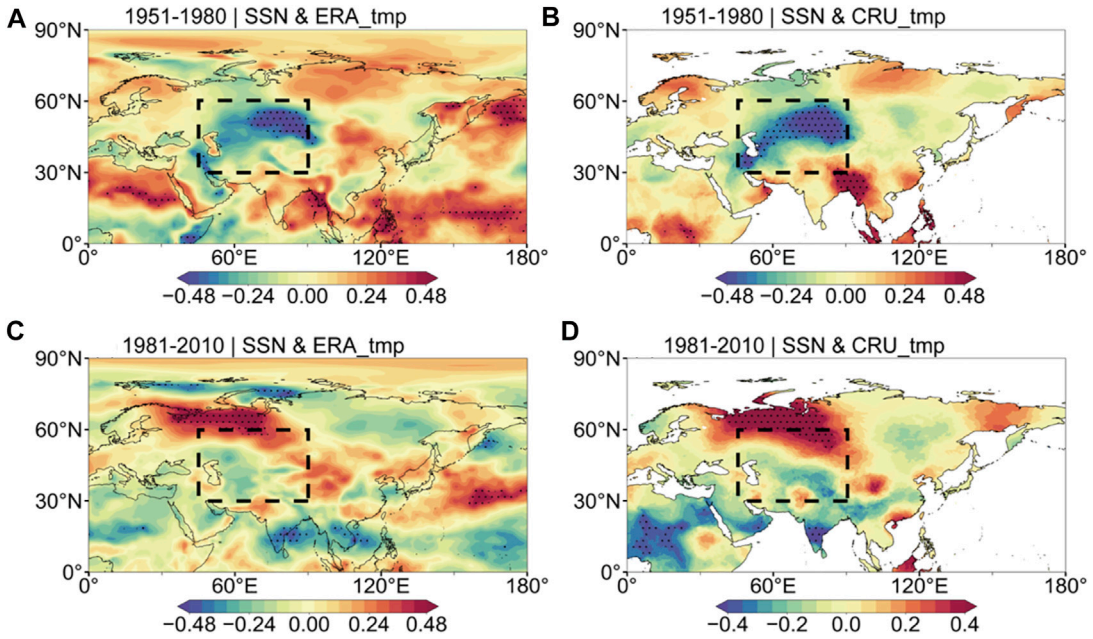

FIGURE 11
Correlation maps between SSN and temperature during 1951–1980 (P1) and 1981–2010 (P2). Dotted regions are at above 95% confidence level. Central Asia (30°N–60°N and 50°E–90°E) is marked by the black dashed frame. **(A)** 1951–1980 SSN and ERA_tmp. **(B)** 1951–1980 SSN and CRU_tmp. **(C)** 1981–2010 SSN and ERA_tmp. **(D)** 1981–2010 SSN and CRU_tmp.

TABLE 2 The correlation coefficients between the three variabilities (SSN, T_Central Asia, and PC2) during the two periods of P1 (1951–1980) and P2 (1981–2010).

SSN & $T_{Central\ Asia}$	P1	P2
ERA_tmp	−0.46 (p<0.05)	0.03
CRU_tmp	−0.52 (p<0.05)	0.07
SSN & PC2	**P1**	**P2**
ERA_tmp	−0.31 (p<0.1)	0.23
CRU_tmp	−0.37 (p<0.05)	0.29
$T_{Central\ Asia}$ & PC2	**P1**	**P2**
ERA_tmp	0.64 (p<0.01)	0.36 (p<0.01)
CRU_tmp	0.75 (p<0.01)	0.70 (p<0.01)

SSN is the series of sunspot data.
T_Central Asia is the average temperature of Central Asia.
PC2 is the corresponding time series of the temperature distribution over Eurasian land.
T_Central Asia and PC2 are calculated from the two temperature datasets, i.e., ERA_tmp and CRU_tmp.

temperature distribution may be affected by the response of the temperature in Central Asia.

The solar effect on the surface temperature depends on the atmospheric circulation condition. We compare the atmospheric background conditions between P1 and P2 below by the composite differences in geopotential height and wind to explore the reason for the decadal change in the relationship (Figure 12). The mid-high latitude differences match the change in the solar activity response areas, such as central Asia, North Europe, and East Russia. Positive potential height and cyclonic anomalies in P2, compared with that in P1, may make the solar disturbance signal insignificant. The change in the background may be caused by global warming or internal variability of the climate system. The reasons for the different responses of regional climate to solar activity and its interdecadal variation deserve further study.

5 Conclusion

In this study, we analyze the distribution of the summer temperature over Eurasian land for the past 110 years based on the EOF methods and reveal its response to solar activity. The time series corresponding to the second EOF mode has an 11-year significant power spectrum periodicity. In addition, the correlation pattern between SSN and temperature is similar to the temperature distribution pattern. Central Asia is considered to be the key region where solar activity affects the temperature distribution in Eurasia.

The physical mechanism can be explained from the perspective of atmospheric circulation. The schematic figure is shown in FIG.13. The left and the right panels compare the atmosphere response to

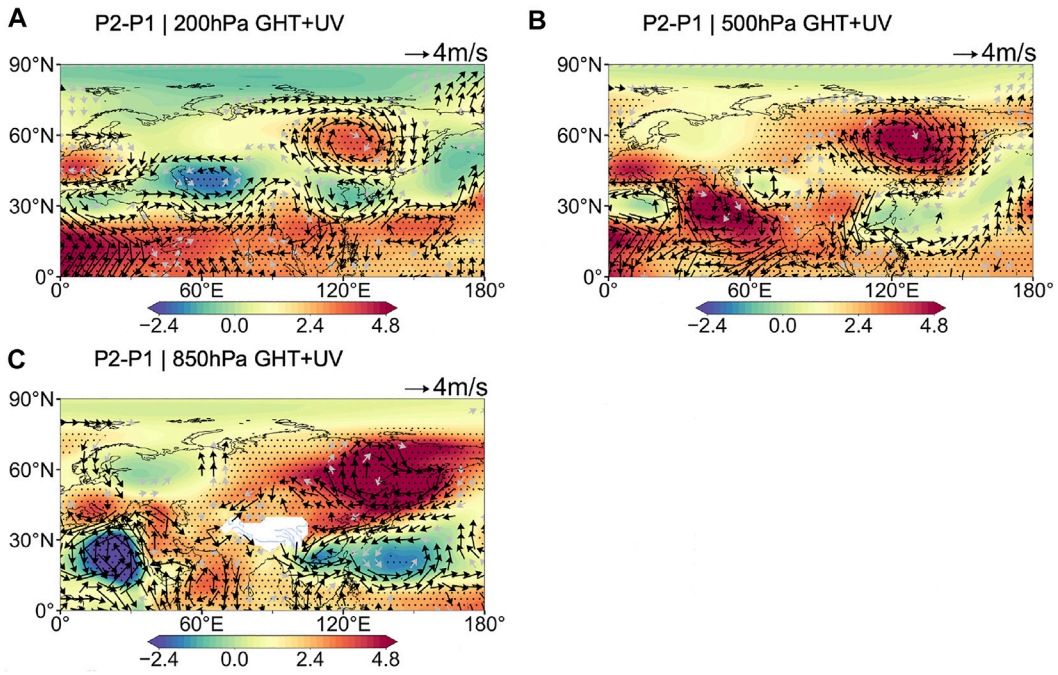

FIGURE 12
Composite differences (P2 minus P1) of atmospheric circulation between 1951 and 1980 (P1) and 1981–2010 (P2). Black dots marks regions where geopotential height (GHT) differences are above the 90% confidence level. The black vectors show the wind differences are over 90% confidence level. The wind and GHT data at 850 hPa on the Qinghai-Tibet Plateau are ignored. **(A)** P2-P1 | 200 hPa GHT+UV. **(B)** P2-P1 | 500 hPa GHT+UV. **(C)** P2-P1 | 850 hPa GHT+UV.

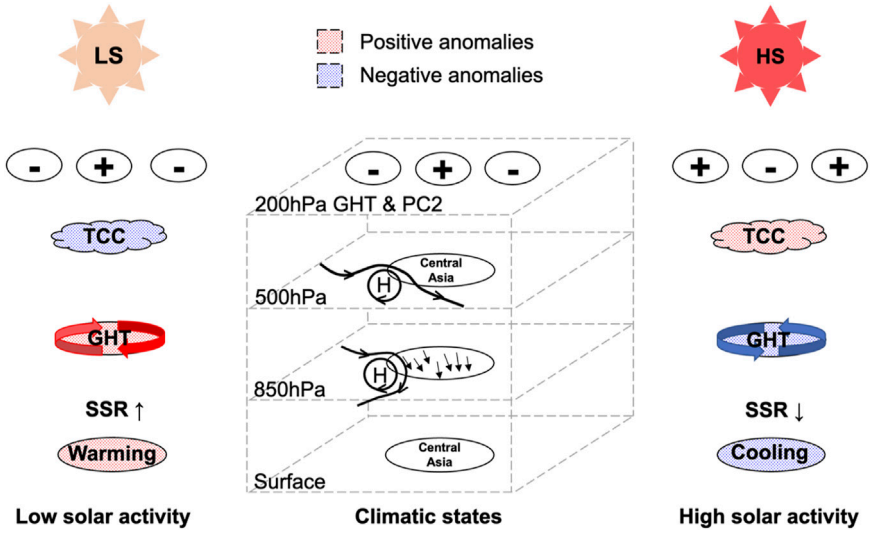

FIGURE 13
A schematic figure of the impact of solar activity on the summer temperature over Eurasia. 'TCC', 'SSR', and 'H' represent the total cloud cover, surface net solar radiation, and the high-pressure center, respectively. The black arrows in the middle panel show the north-westerly wind. Positive (Negative) anomalies are marked by red (blue) dots. The blue (red) widened vectors show the cyclonic (anti-cyclonic) anomalies.

the LS and HS and the climatic states are shown in the middle panel. The second EOF pattern of the summer temperature is alike to a wave train-like structure, with one positive and two negative anomalies across the mid-high latitudes, and causes a barotropic response of the atmospheric circulation. The two side panels of Figure 13 show the atmospheric circulation anomalies associated with HS and LS resemble the wave train-like pattern. In the key area, Central Asia, the temperature is highly related to the second temperature distribution and negatively related to solar activity. The other regions are weakly positive for solar activity. Over Central Asia, the negative potential height anomalies at 500 h Pa associated with solar activity weakened the high-pressure ridge on the southwest side. The cyclonic anomalies related to solar activity strengthen the southwesterly wind. Besides, more clouds and less radiation make the terrestrial receive less solar energy (Figure 13). Under the combined action of atmospheric circulation and cloud and radiation feedback, temperature decreases with increasing solar activity.

The connection between temperature distribution and solar activity was strong and decadal stable until 1980. The key response areas change from Central Asia in the middle latitudes to Northern Europe in the mid-high latitudes after 1980 due to the change in atmospheric conditions. As the mechanism mentioned above, the arrival of solar activity signals on the ground depends on the transport of atmospheric circulation and the reflection of the cloud-radiation process. The impact of solar activity on the temperature over Central Asia and even the whole of Eurasia would be convinced to be established again in the future if the atmospheric change stemmed from climate internal variability. Solar activity still can be considered a non-negligible factor in the prediction of the summer temperature in Eurasia.

Data availability statement

The original contributions presented in the study are included in the article/supplementary material, further inquiries can be directed to the corresponding author.

Author contributions

The authors confirm their contribution to the paper as follows: study conception and design: ZX; data collection and analysis: WL; draft manuscript preparation: WL and XF. All authors reviewed the results and approved the final version of the manuscript.

Funding

This work was supported by the Natural Science Foundation of China (U1902209, 42030204) and the Specialized Research Fund for State Key Laboratories.

Acknowledgments

We thank Liang Zhao for sharing his suggestions on this research. We are grateful for the thoughtful comments and recommendations from two reviewers.

Conflict of interest

The authors declare that the research was conducted in the absence of any commercial or financial relationships that could be construed as a potential conflict of interest.

Publisher's note

All claims expressed in this article are solely those of the authors and do not necessarily represent those of their affiliated organizations, or those of the publisher, the editors and the reviewers. Any product that may be evaluated in this article, or claim that may be made by its manufacturer, is not guaranteed or endorsed by the publisher.

References

Brehm, N., Bayliss, A., Christl, M., Synal, H.-A., Adolphi, F., Beer, J., et al. (2021). Eleven-year solar cycles over the last millennium revealed by radiocarbon in tree rings. *Nat. Geosci.* 14 (1), 10–15. doi:10.1038/s41561-020-00674-0

Cao, L. (2021). Climate system response to solar radiation modification. *Clim. Change Res.* 17 (6), 671–684. doi:10.12006/j.issn.1673-1719.2021.170

Chen, H., Ma, H., Li, X., and Sun, S. (2015). Solar influences on spatial patterns of Eurasian winter temperature and atmospheric general circulation anomalies. *J. Geophys. Res. Atmos.* 120 (17), 8642–8657. doi:10.1002/2015jd023415

Chen, S., Wu, R., Chen, W., Yao, S., and Yu, B. (2020). Coherent interannual variations of springtime surface temperature and temperature extremes between central-northern Europe and northeast Asia. *J. Geophys. Res. Atmos.* 125 (11). doi:10.1029/2019jd032226

Chiodo, G., Oehrlein, J., Polvani, L. M., Fyfe, J. C., and Smith, A. K. (2019). Insignificant influence of the 11-year solar cycle on the north Atlantic oscillation. *Nat. Geosci.* 12 (2), 94–99. doi:10.1038/s41561-018-0293-3

Connolly, R., Soon, W., Connolly, M., Baliunas, S., Berglund, J., Butler, C. J., et al. (2021). How much has the sun influenced northern hemisphere temperature trends? An ongoing debate. *Res. Astron. Astrophys.* 21 (6), 131. doi:10.1088/1674-4527/21/6/131

Ding, Y. (2019). Effect of solar activity on Earth's climate and weather. *Meteorol. Mon. (in Chin.* 45 (03), 297–304. doi:10.7519/j.issn.1000-0526.2019.03.001

Duan, J., and Zhang, Q.-B. (2014). A 449 year warm season temperature reconstruction in the southeastern Tibetan Plateau and its relation to solar activity. *J. Geophys. Res. Atmos.* 119 (2011), 11,578–11,592. doi:10.1002/2014jd022422

Georgieva, K., Kirov, B., Tonev, P., Guineva, V., and Atanasov, D. (2007). Long-term variations in the correlation between NAO and solar activity: The importance of north–south solar activity asymmetry for atmospheric circulation. *Adv. Space Res.* 40 (7), 1152–1166. doi:10.1016/j.asr.2007.02.091

Gray, L. J., Beer, J., Geller, M., Haigh, J. D., Lockwood, M., Matthes, K., et al. (2010). Solar influences on climate. *Rev. Geophys.* 48 (4), RG4001. doi:10.1029/2009rg000282

Hong, X., Lu, R., and Li, S. (2017). Amplified summer warming in europe–west Asia and northeast Asia after the mid-1990s. *Environ. Res. Lett.* 12 (9), 094007. doi:10.1088/1748-9326/aa7909

Huang, C., Rao, Z., Li, Y., Yang, W., Liu, L., Zhang, X., et al. (2020). Holocene summer temperature in arid central Asia linked to millennial-scale North Atlantic climate events and driven by centennial-scale solar activity. *Palaeogeogr. Palaeoclimatol. Palaeoecol.* 556, 109880. doi:10.1016/j.palaeo.2020.109880

Huo, W., Xiao, Z., Wang, X., and Zhao, L. (2021). Lagged responses of the tropical pacific to the 11-yr solar cycle forcing and possible mechanisms. *J. Meteorol. Res.* 35 (3), 444–459. doi:10.1007/s13351-021-0137-8

Ionita, M., Lohmann, G., Rimbu, N., and Scholz, P. (2012). Dominant modes of Diurnal Temperature Range variability over Europe and their relationships with large-scale atmospheric circulation and sea surface temperature anomaly patterns. *J. Geophys. Res.* 117 (D15), n/a. doi:10.1029/2011jd016669

IPCC (2021). *Climate change 2021: The physical science basis*. Switzerland, Geneva: C.C.U. Press.

Kilcik, A., Ozguc, A., and Rozelot, J. P. (2010). Latitude dependency of solar flare index-temperature relation occuring over middle and high latitudes of Atlantic-Eurasian region. *J. Atmos. SOLAR-TERRESTRIAL Phys.* 72 (18), 1379–1386. doi:10.1016/j.jastp.2010.10.002

Kilcik, A., Özgüç, A., Rozelot, J. P., and Yeşilyurt, S. (2008). Possible traces of solar activity effect on the surface air temperature of Turkey. *J. Atmos. Solar-Terrestrial Phys.* 70 (13), 1669–1677. doi:10.1016/j.jastp.2008.07.002

Kilcik, A. (2005). Regional sun–climate interaction. *J. Atmos. Solar-Terrestrial Phys.* 67 (16), 1573–1579. doi:10.1016/j.jastp.2005.09.003

Kodera, K., Thiéblemont, R., Yukimoto, S., and Matthes, K. (2016). How can we understand the global distribution of the solar cycle signal on the Earth's surface? *Atmos. Chem. Phys.* 16 (20), 12925–12944. doi:10.5194/acp-16-12925-2016

Kossobokov, V., Le Mouël, J.-L., and Courtillot, V. (2010). A statistically significant signature of multi-decadal solar activity changes in atmospheric temperatures at three European stations. *J. Atmos. Solar-Terrestrial Phys.* 72 (7-8), 595–606. doi:10.1016/j.jastp.2010.02.016

Liu, X., Rao, Z., Shen, C. C., Liu, J., Chen, J., Chen, S., et al. (2019). Holocene solar activity imprint on centennial- to multidecadal-scale hydroclimatic oscillations in arid central Asia. *J. Geophys. Res. Atmos.* 124 (5), 2562–2573. doi:10.1029/2018jd029699

Maliniemi, V., Asikainen, T., and Mursula, K. (2014). Spatial distribution of Northern Hemisphere winter temperatures during different phases of the solar cycle. *J. Geophys. Res. Atmos.* 119 (16), 9752–9764. doi:10.1002/2013jd021343

Miyazaki, C., and Yasunari, T. (2008). Dominant interannual and decadal variability of winter surface air temperature over Asia and the surrounding oceans. *J. Clim.* 21 (6), 1371–1386. doi:10.1175/2007jcli1845.1

Ning, G., Luo, M., Wang, S., Liu, Z., Wang, P., and Yang, Y. (2022). Dominant modes of summer wet bulb temperature in China. *Clim. Dyn.* 59 (5-6), 1473–1488. doi:10.1007/s00382-021-06051-w

Ogurtsov, M. G., and Veretenenko, S. V. (2017). Possible contribution of variations in the galactic cosmic ray flux to the global temperature rise in recent decades. *Geomagn. Aeron.* 57 (7), 886–890. doi:10.1134/s0016793217070143

Ogurtsov, M., Veretenenko, S. V., Helama, S., Jalkanen, R., and Lindholm, M. (2020). Assessing the signals of the Hale solar cycle in temperature proxy records from Northern Fennoscandia. *Adv. Space Res.* 66 (9), 2113–2121. doi:10.1016/j.asr.2020.07.038

Ojala, A. E. K., Launonen, I., Holmström, L., and Tiljander, M. (2015). Effects of solar forcing and North Atlantic oscillation on the climate of continental Scandinavia during the Holocene. *Quat. Sci. Rev.* 112, 153–171. doi:10.1016/j.quascirev.2015.01.021

Scafetta, N. (2014). Discussion on the spectral coherence between planetary, solar and climate oscillations: A reply to some critiques. *Astrophys. Space Sci.* 354 (2), 275–299. doi:10.1007/s10509-014-2111-8

Song, Y., Chen, H., and Yang, J. (2022). The dominant modes of spring land surface temperature over western Eurasia and their possible linkages with large-scale atmospheric teleconnection patterns. *JGR. Atmos.* 127 (4). doi:10.1029/2021jd035720

Song, Y., Li, Z., Gu, Y., Liou, K.-N., Zhang, X., and Xiao, Z. (2019). The effect of solar cycle on climate of northeast Asia. *J. Meteorol. Res.* 33 (5), 885–894. doi:10.1007/s13351-019-8132-z

Soon, W. W. H. (2005). Variable solar irradiance as a plausible agent for multidecadal variations in the Arctic-wide surface air temperature record of the past 130 years. *Geophys. Res. Lett.* 32 (16), L16712. doi:10.1029/2005gl023429

Tang, Q., and Leng, G. (2012). Damped summer warming accompanied with cloud cover increase over Eurasia from 1982 to 2009. *Environ. Res. Lett.* 7 (1), 014004. doi:10.1088/1748-9326/7/1/014004

Tang, Q., Leng, G., and Groisman, P. Y. (2012). European hot summers associated with a reduction of cloudiness. *J. Clim.* 25 (10), 3637–3644. doi:10.1175/jcli-d-12-00040.1

Thiéblemont, R., Matthes, K., Omrani, N.-E., Kodera, K., and Hansen, F. (2015). Solar forcing synchronizes decadal North Atlantic climate variability. *Nat. Commun.* 6 (1), 8268. doi:10.1038/ncomms9268

Veretenenko, S., and Ogurtsov, M. (2012). Regional and temporal variability of solar activity and galactic cosmic ray effects on the lower atmosphere circulation. *Adv. Space Res.* 49 (4), 770–783. doi:10.1016/j.asr.2011.11.020

Wang, Y., Miao, Q.-L., E, C.-Y., Han, J.-K., and Ding, Y.-Y. (2010). Relation between temperature changes of the mid-upper troposphere over Eurasian mid-high latitudes and solar irradiance in the twentieth century. *Environ. Earth Sci.* 60 (6), 1257–1266. doi:10.1007/s12665-009-0266-3

Wu, X., and Sun, Z. (2015). Climatic features of summer land surface temperature in Eurasian continent and its relationship with atmospheric circulation. *Trans. Atmos. Sci. (in Chin.* 38 (02), 195–204.

Xiao, Z., Liu, J., Liu, S. H., Petridis, L., Cai, C., Cao, L., et al. (2021). Novel small molecule fibroblast growth factor 23 inhibitors increase serum phosphate and improve skeletal abnormalities in *hyp* mice. *Mol. Pharmacol.* 43 (06), 408–421. doi:10.1124/molpharm.121.000471

Xu, X., He, S., and Wang, H. (2020). Relationship between solar wind—magnetosphere energy and eurasian winter cold events. *Adv. Atmos. Sci.* 37 (6), 652–661. doi:10.1007/s00376-020-9153-3

Zhang, Y., Liu, L., Li, B., and Zheng, D. (2021). Comparison of Qinghai-Tibet Plateau extent dataset 2021 edition with 2014 edition. *J. Glob. Change Data & Discov.* 5 (3).

Zhang, Z., and Moore, J. C. (2015). "Chapter 6 - empirical orthogonal functions," in *Mathematical and physical fundamentals of climate change*. Editors Z. Zhang and J. C. Moore (Boston: Elsevier), 161–197.

Zhao, X., and Feng, X. (2014). Periodicities of solar activity and the surface temperature variation of the Earth and their correlations. *Chin. Sci. Bull.* 59 (14), 1284–1292. doi:10.1360/972013-1089

frontiers | Frontiers in Earth Science

TYPE Original Research
PUBLISHED 16 February 2023
DOI 10.3389/feart.2023.1137205

OPEN ACCESS

EDITED BY
Ziniu Xiao,
Institute of Atmospheric Physics (CAS), China

REVIEWED BY
Huopo Chen,
Institute of Atmospheric Physics (CAS), China
Ke Fan,
School of Atmospheric Sciences, Sun Yat-sen University, China

*CORRESPONDENCE
Weiyi Sun,
weiyisun@njnu.edu.cn

SPECIALTY SECTION
This article was submitted to Interdisciplinary Climate Studies, a section of the journal Frontiers in Earth Science

RECEIVED 04 January 2023
ACCEPTED 06 February 2023
PUBLISHED 16 February 2023

CITATION
Hu Y, Sun W, Liu J, Chen D, Ning L and Peng Z (2023), Decadal variability of precipitation over the Tibetan Plateau modulated by the 11-year solar cycle over the past millennium.
Front. Earth Sci. 11:1137205.
doi: 10.3389/feart.2023.1137205

Decadal variability of precipitation over the Tibetan Plateau modulated by the 11-year solar cycle over the past millennium

Ying Hu[1,2,3,4], Weiyi Sun[1,2,3,4]*, Jian Liu[1,2,3,4,5,6], Deliang Chen[7], Liang Ning[1,2,3,4] and Zhenghan Peng[1,2,3,4]

[1]Key Laboratory for Virtual Geographic Environment, Ministry of Education, Nanjing, China, [2]State Key Laboratory Cultivation Base of Geographical Environment Evolution of Jiangsu Province, Nanjing, China, [3]Jiangsu Center for Collaborative Innovation in Geographical Information Resource Development and Application, Nanjing, China, [4]School of Geography Science, Nanjing Normal University, Nanjing, China, [5]Jiangsu Provincial Key Laboratory for Numerical Simulation of Large Scale Complex Systems, School of Mathematical Science, Nanjing Normal University, Nanjing, China, [6]Open Studio for the Simulation of Ocean-Climate-Isotope, Qingdao National Laboratory for Marine Science and Technology, Qingdao, China, [7]Regional Climate Group, Department of Earth Sciences, University of Gothenburg, Gothenburg, Sweden

Introduction: Knowledge of precipitation over the Tibetan Plateau, often referred to as the "Asian water tower", is crucial for water resource management, infrastructure planning, and disaster mitigation. However, the decadal variability of Tibetan Plateau precipitation in response to the 11-year solar cycle remains unknown.

Methods: Here, we used observational data obtained between 1901 and 2013, together with proxy-based reconstructions of the past five centuries, and discovered a notable summer wet condition over the central–southern Tibetan Plateau, accompanied by a dry condition over the southeastern Tibetan Plateau, during peaks in the 11-year solar cycle. Using an ensemble mean of four solar-only sensitivity experiments from the Community Earth System Model Last Millennium Ensemble (CESM–LME), we further demonstrated that the 11-year solar cycle can induce this anomalous pattern of a wet central–southern and dry southeastern Tibetan Plateau.

Results and discussion: The modeling results indicated that, under a solar maximum, a substantial surface warming occurs over the Asian continent, especially the Tibetan Plateau region; this causes an anomalous Tibetan Plateau–Indian Ocean thermal contrast, which enhances the Indian summer monsoon. The additional Tibetan Plateau heating also enhances and causes a northward shift of the South Asian High, which further intensifies the Indian summer monsoon. The enhanced Indian summer monsoon transports water vapor to the northern Indian continent, which rises upon reaching the central–southern Tibetan Plateau, substantially increasing precipitation. Meanwhile, a negative Pacific Decadal Oscillation-like sea surface temperature pattern occurs under a solar maximum, leading to a large-scale anticyclonic anomaly over the Yangtze River basin, southeastern Tibetan Plateau, and southern Japan, substantially decreasing precipitation in these regions.

KEYWORDS

Tibetan Plateau, decadal variability of precipitation, 11-year solar cycle, Tibetan Plateau-Indian Ocean thermal contrast, South Asian High, Pacific Decadal Oscillation

1 Introduction

The Tibetan Plateau (TP) climate is one of Earth's most active regional climate systems, having considerable land–air interaction and playing an important role in Asian hydrological cycles (Yao et al., 2015; Wu, 2020). The TP is often referred to as the "Asian water tower" as it directly affects the hydrology of the surrounding regions, in particular the flow of major Asian rivers (Yao et al., 2022), such as the Yangtze, Yellow, Nu, Lancang, Yarlung Zangbo, Ganges, and Indus. Changing TP precipitation is also one of the driving mechanisms of the retreat and advance of glaciers (Yao et al., 2012). Understanding the variability of TP precipitation is crucial for the ecosystem, agriculture, water resource management, and social development of the Asian region.

Instrumental data has demonstrated the decadal variability of TP precipitation. For example, Liu et al. (2021) analyzed summer precipitation over the TP based on 151 meteorological stations during the period 1976–2015 and found an interdecadal variation in southern TP precipitation, with an increase from 1976 to 1998 and a decrease from 1999 to 2015. Using station rainfall data from 1979 to 2018, Yue et al. (2021) found a decadal variation in precipitation over the southern TP, with a periodicity peaking at 10 years. The wet phase of decadal precipitation variation has been shown to be associated with cold sea surface temperature (SST) anomalies over the equatorial central Pacific and warm SST anomalies over the Indo–Pacific warm pool (Yue et al., 2021). This SST pattern resembles the pattern of Pacific quasi-decadal oscillation (QDO), with an 11-year signal, which might originate from internal variabilities, such as the low-frequency mega-El Niño/Southern Oscillation (ENSO) variability (e.g., Wang et al., 2014). Besides this internal variability, some studies have also suggested that the decadal solar cycle can also contribute to the formation of QDO (White and Liu, 2008; Jin et al., 2020) and decadal variation of the East Asian summer monsoon (Zhao et al., 2012). However, owing to the limited temporal length of observational data, it is difficult to understand how the decadal variability of TP precipitation responds to external forcing (i.e., solar activity).

The period of the last millennium provides opportunities to study the decadal variability of TP precipitation, benefiting from a large number of high-resolution proxy datasets. These studies provide new insights into the causes and processes behind the decadal variability. Xu et al. (2014) reconstructed the temperature on the eastern edge of the TP over the past four centuries, and found that the decadal variation in temperature was synchronized with precipitation, which was likely affected by solar activity. Shi et al. (2018a) reconstructed the relative humidity variation on the southeastern TP during the period 1751–2005 and suggested that the relative humidity could be modulated by the ENSO and Pacific Decadal Oscillation (PDO). In addition, stalagmite $\delta^{18}O$ records from the southeastern TP have indicated marked 11-, 12-, and 22-year periodicities on the decadal time scale, suggesting the importance of solar forcing (Tan et al., 2018). Specifically, precipitation was shown to increase over the southeastern TP at solar minima. The stalagmite $\delta^{18}O$ record from Tianmen Cave, central–southern TP, showed a close agreement with the Indian summer monsoon (ISM) and a marked 11-year periodicity, implying that solar activity may have influenced the ISM and further affected the $\delta^{18}O$ record (Cai et al., 2012). On the centennial timescale, precipitation records over the Asian monsoon region show centennial–multi-centennial variability, which lags the 200-year (DeVries cycle) or 300–500-year solar activity cycles by approximately several decades (Breitenmoser et al., 2012; Sun et al., 2022b). The above research has demonstrated the similar periodicities of TP precipitation and solar activity, and imply that TP precipitation may be affected by solar activity. However, some scholars have questioned the impact of solar activity on climate, citing the variation range of total solar irradiance being too small (Vieira et al., 2011; Chiodo et al., 2019). Moreover, reconstructions have failed to reveal the physical mechanisms behind the decadal variability of TP precipitation.

Previous studies have suggested that the 11-year solar activity cycle significantly impacts climate on a decadal time scale. The multi-model mean result from the Coupled Model Inter-Comparison Project (CMIP5) showed a significant increase in global mean surface air temperature 1–2 years after the peaks of 11-year solar cycles (Misios et al., 2015). Using the ensemble of four solar-only sensitivity experiments from the Community Earth System Model Last Millennium Ensemble (CESM–LME), Jin et al. (2019) found that the decadal variation of the East Asian summer monsoon was significantly correlated with strong 11-year solar cycles over the last millennium; this was associated with a negative PDO-like SST pattern at each solar maximum, but this relationship disappeared during weak 11-year solar cycle epochs. Using observations and climate models, La Niña-like events have been identified over the equatorial eastern Pacific at the peaks of 11-year solar cycles, followed by El Niño-like events several years later (van Loon et al., 2007; Meehl et al., 2008; Meehl and Arblaster, 2009; Meehl et al., 2009). In contrast, Misios et al. (2019) used multiple regression analysis to suggest a weakened Pacific Walker circulation at solar cycle maxima, caused by a thermodynamics-induced muted hydrology mechanism. Both the ENSO-like and PDO-like SST patterns under solar forcing can further influence precipitation over eastern China (Ma et al., 2021; Liu et al., 2022; Xue et al., 2022). However, the effect of the 11-year solar activity cycle on TP precipitation remains unknown.

This study aims to address the following questions: 1) Has the decadal variability of TP precipitation been modulated by the 11-year solar cycle over the last millennium? 2) If so, how does solar activity affect TP precipitation? Here, we used instrumental data, reconstructions, and simulations from the CESM–LME to investigate the impact of the 11-year solar activity cycle on TP precipitation over the last millennium. The remainder of the paper is organized as follows: Section 2 describes the data we used; Section 3 shows the characteristics and possible physical mechanisms causing changes in the precipitation over the TP under the influence of the 11-year solar cycle; and our discussion and conclusions are summarized in Section 4.

2 Data

2.1 Observational data

Observational data were used to validate reconstructed data and model simulations. The precipitation observations were derived from the Global Precipitation Climatology Centre (GPCC) full data monthly product version 2018 (Schneider et al., 2018), which is calculated from approximately 80,000 global station data points. The horizontal resolution of the data is 1 × 1 and the period covered is 1891–2016. We also used two sets of SST observations: one was the Extended Reconstructed Sea Surface Temperature version 5 (ERSST v5) global SST monthly data (Huang et al., 2017) covering the period 1854–2020, whose horizontal resolution is approximately 2 × 2; the other was the Hadley Center Sea Ice and SST dataset version 1.1 (HadiSST 1.1) (Rayner et al., 2003) covering the period 1871–2020, whose horizontal resolution is approximately 1 × 1.

2.2 Simulation data

We used simulation data to explore the spatiotemporal pattern and physical mechanism of the TP precipitation response to the 11-year solar cycle. The simulation data were derived from the CESM–LME (Otto-Bliesner et al., 2015), which was conducted using CESM version 1.1 (Hurrell et al., 2013). The resolution of the atmosphere and land components is ~2, while that of the ocean and sea ice components is ~1.

The simulations used here contained a control experiment (CTRL) run from the year 850 onwards, an ensemble of 13 all-forcing (AF) experiments, and an ensemble of four total solar irradiance (TSI) forcing experiments. The time range of the AF and TSI simulations was 850–2005. The AF experiments were forced by solar activity, volcanic eruptions, land use/land cover changes, greenhouse gases, ozone, aerosols, and orbital changes (Otto-Bliesner et al., 2015). For the TSI experiments, only the reconstructed solar irradiance forcing (Vieira et al., 2011) was used to drive the simulations; the other external forcings were kept the same as in the CTRL. Differences among the ensemble members comprised the small random round-off differences in the air temperature field at the start of each run. On this basis, the ensemble-mean results from the AF and TSI experiments represented the net effect of all external forcings and solar activity forcing, respectively. Simulations imposed an estimated 11-year solar cycle and used linear regression of TSI at each spectral interval to derive spectral solar irradiance (Schmidt et al., 2011).

2.3 Proxy-based reconstructions

We used reconstructed data to reflect climate change over the last millennium. A proxy-based gridded reconstruction dataset, namely, the Asian summer precipitation (RAP) dataset during the period 1470–2013 (Shi et al., 2018b), was merged with 453 tree-ring-width chronologies and 71 historical documentary records. The RAP dataset comprises gridded data with a spatial range spanning 8.8°S–55.3°N, 61.3°–143.3°E, and a spatial resolution of approximately 2; it reconstructs the June–August (JJA) mean precipitation with an annual temporal resolution. Some previous studies have confirmed the inter annual–decadal variability of monsoon precipitation using the RAP and its relationship with the ENSO and Atlantic multi-decadal oscillation, and comparisons with instrumental data, other climatic reconstructions, and climate model simulations (Shi et al., 2019; Shi and Wang, 2019; Shen et al., 2022). In addition to the gridded reconstructions, we also collated some other high-resolution tree-ring and stalagmite reconstructions from different regions of the TP (Table 1).

3 Results

3.1 Validation of reconstructions and simulations

Precipitation over the TP is dominated by the summer mean precipitation (e.g., Feng and Zhou, 2012); hence, we focused on the JJA precipitation. To verify the reliability of the reconstructions and simulations, we compared the climatological precipitation derived from the GPCC, RAP, and CESM–LME, respectively (Figure 1). The GPCC data (Figure 1A) showed that the JJA mean precipitation decreases from southeast to northwest over the TP; a similar pattern was seen in both the RAP and CESM–LME data (Figures 1B, C). The results of the CESM–LME were computed by the ensemble mean of 13 AF experiments, and the results of each experiment were generally similar to the ensemble mean result (Supplementary Figure S1). The spatial correlation coefficient between RAP and GPCC was 0.77 with a root mean square error (RMSE) of 1.9 mm day^{-1}, while the correlation coefficient between CESM–LME and GPCC was 0.74 with an RMSE of 3.7 mm day^{-1}. However, both the RAP and CESM–LME exhibited some wet bias over the southern TP, which is a common error in global climate models (GCMs) (Zhu et al., 2020; Chen et al., 2022). In addition, to detect the decadal variability of precipitation, we conducted the empirical orthogonal function (EOF) analysis during the period 1901–2000 for GPCC, RAP, and CESM–LME. The EOF first modes of all the three show an east–west zonal dipole pattern (Figure omitted). Overall, the RAP and CESM–LME reasonably captured the spatial pattern of climatological JJA mean precipitation and the decadal variability of precipitation over the TP.

3.2 Response of TP precipitation to the 11-year solar activity cycle

According to the wavelet analysis of the TSI during the period 850–2000 (Supplementary Figure S2A), we selected three periods with substantial 11-year solar cycle signals as the active epochs: 850–1400, 1550–1650, and 1730–2000. Then based on the solar activity sequence (Supplementary Figure S2B), we manually selected the solar maximum (Smax) and minimum (Smin) phases for each 11-year solar cycle epoch in the selected three periods. To test the net effect of solar activity on TP precipitation, we performed a composite analysis of JJA mean precipitation between the Smax

TABLE 1 Reconstructions from different regions of the TP.

No.	Location	Elevation (m)	Period	References
1	(27°–33°N, 90°–102°E)	3,040–4,440	1,135–2,010	Wang et al. (2020)
2	(30.4°N, 95.1°E)	3,100	1,352–2,012	Wernicke et al. (2016)
3	(29.5°N, 96.4°E)	3,950	1,592–2,011	Wernicke et al. (2016)
4	(36.6°N, 75.0°E)	3,900	1,000–1,998	Treydte et al. (2006)
5	(32.2°N, 77.2°E)	2,700	1,767–2,008	Sano et al. (2017)
6	(29.6°N, 79.9°E)	3,849	1,621–2,008	Xu et al. (2017)
7	(29.9°N, 81.93°E)	3,848	1,778–2,000	Sano et al. (2012)
8	(37°–38.7°N, 97°–100°E)	2,863–4,175	850–2,011	Yang et al. (2014)
9	(37.5°N, 97.7°E)	3,570–4,085	0–2,012	Yang et al. (2021)
10	(32.2°–33°N, 76.5°–77.5°E)	2,640–3,016	1,460–2,008	Yadav and Bhutiyani (2013)
11	(28°6′N, 103°1′E)	1,407	−315 to 2,000	Tan et al. (2018)

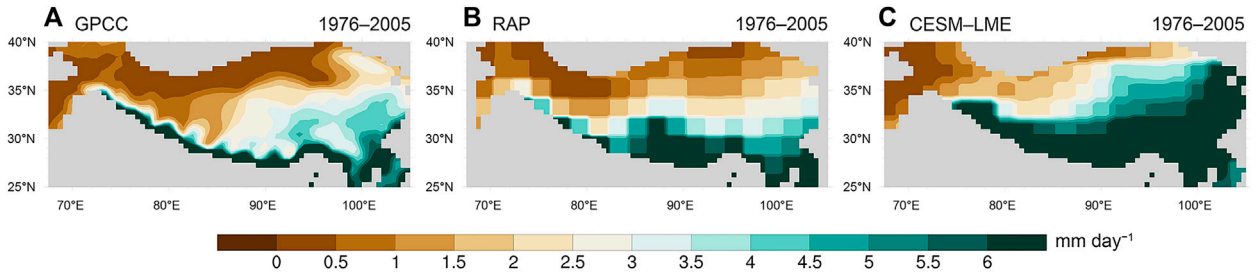

FIGURE 1
Climatological Jun–Aug (JJA) mean precipitation (mm day^{-1}) during the period 1976–2005 derived from **(A)** GPCC, **(B)** RAP, and **(C)** CESM–LME.

and Smin (Figure 2). During the instrumental period of 1901–2013, there were 10 cases for the differences between Smax and Smin. The GPCC data showed that the precipitation significantly increased by approximately 0.6 mm day^{-1} over the area of 28°–36°N, 85°–95°E, accounting for 36% of the mean climatological value during the period 1901–2013 (Figure 2A). The precipitation decreased over the southeastern and southwestern TP. The results from the RAP also indicated a similar pattern of precipitation anomalies over the TP, but the amplitude of wet conditions over the central–southern TP was slightly weaker (Figure 2B) than that indicated by the GPCC data. Meanwhile, we also tested the composite results from two other well-known gridded precipitation reconstructions, those of Cook et al. (2010) and Shi et al. (2017). However, the patterns of precipitation shown by these datasets were different from the observations, with an overall drying over the TP region under solar peaks, especially over the central–southern TP, and a wet condition over the southeastern TP (Supplementary Figure S3). Therefore, our further analysis used only the RAP gridded reconstruction because it compared favorably with the instrumental data when reproducing precipitation changes over the TP under the 11-year solar cycle.

The above analysis may contain the influence of internal variability because the sample size of the 11-year solar cycle is small during the instrumental period. Hence, we extended the sampling period to the past millennium using the reconstructions and CESM–LME simulations. The composite results with 39 cases for the differences between Smax and Smin from the RAP during the period 1470–2013 were very similar to the result from the instrumental period (Figure 2C), which suggests that enhanced solar irradiance causes an increase in precipitation over the central–southern TP and a decrease in precipitation over the southeastern and southwestern TP. We further performed a correlation analysis between TSI sequence and RAP during 1470–2010, and the result was similar to that using the composite analysis (Figure omitted). These results indicate that the effect of the 11-year solar activity cycle on TP precipitation was stable over the entire sampling period. Moreover, this solar-forced pattern of TP precipitation can be confirmed by other reconstruction studies. For example, Cai et al. (2012) found that the stalagmite $\delta^{18}O$ record from the central–southern TP was correlated with the ISM on the decadal timescale, which bears a significant 11-year periodicity. The stalagmite $\delta^{18}O$ record from the southeastern TP indicated a significant 11-year periodicity,

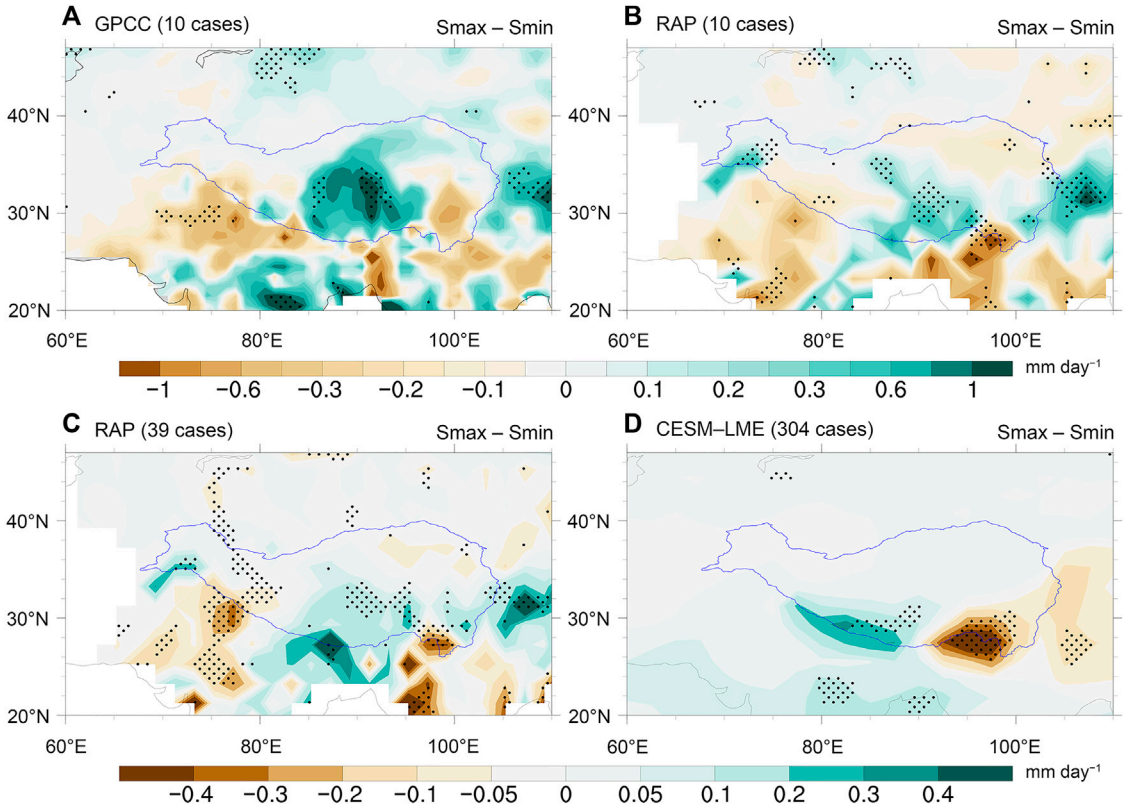

FIGURE 2
Composite differences in JJA mean precipitation (mm day^{-1}) between the 11-year solar maximum (Smax) and minimum (Smin) phases. **(A)** Results from the GPCC during 1901–2013 (10 cases). **(B)** Results from the RAP reconstruction during 1901–2013 (10 cases). **(C)** Results from the RAP during 1470–2013 (39 cases). **(D)** Ensemble-mean result of four TSI experiments (304 cases). The black dots denote significance at the 90% confidence level (two-tailed Student's *t*-test). The solid blue lines denote the elevation contour of 2,000 m.

with a wet condition during solar minima (Tan et al., 2018). We further analyzed the TP precipitation response to solar forcing based on the TSI sensitivity experiments in the CESM–LME. The ensemble mean result of 304 cases from the TSI experiments showed a dipole precipitation pattern, with a notable wet condition over the central–southern TP and a notable dry condition over the southeastern TP (Figure 2D), consistent with the reconstructions. However, there was no drying over the southwestern TP in the TSI simulations, suggesting a degree of uncertainty in the model.

We then conducted a power spectrum analysis of the TP precipitation derived from the RAP and other high-resolution proxy data (Figure 3). Since the response of RAP to 11-year solar activity cycle is out-of-phase over central–southern and southeastern TP, we performed the power spectrum analysis to the RAP over the two sub-regions, respectively. The result from the RAP showed a marked quasi-11-year cycle (Figures 3A–B), suggesting the notable effect of the 11-year solar cycle. Ten of the eleven tree-ring-based and stalagmite $\delta^{18}O$-based proxy records across the TP (Table 1) also indicated substantial 10–12-year periodicities (Figures 3C–M), similar to the RAP data. To further detect the effect of the 11-year solar cycle in controlling the periodicities of precipitation, we conducted a power spectrum analysis of simulated TP precipitation from the TSI experiments (Figures 3N–O). The four-member ensemble-mean result of TSI experiments further showed a statistically significant 11-year periodicity. Thus, this timescale analysis confirms that the 11-year solar cycle significantly influences precipitation over the TP.

3.3 Physical mechanism underlying the precipitation response

To understand the physical mechanism of TP precipitation under the influence of the 11-year solar activity cycles, we analyzed the results from the TSI experiments of CESM–LME. We first examined the composite differences from the surface to 300-hPa vertically integrated water vapor transport between the 11-year Smax and Smin phases (Figure 4A). We identified an enhanced westerly anomaly over the tropical Indian Ocean and an anomalous cyclonic circulation over the Bay of Bengal, which produces an anomalous moisture transport from the Indian Ocean to the central–southern TP. This may contribute to the increased precipitation over the northern Indian subcontinent. Meanwhile, a significant anomalous anticyclonic anomaly occurs over Japan and northern China, enhancing the transport of water vapor from the Pacific Ocean and southern China to northern and northeastern China; this induces a dry band-like zone over the Yangtze River basin, southeastern TP, and southern Japan.

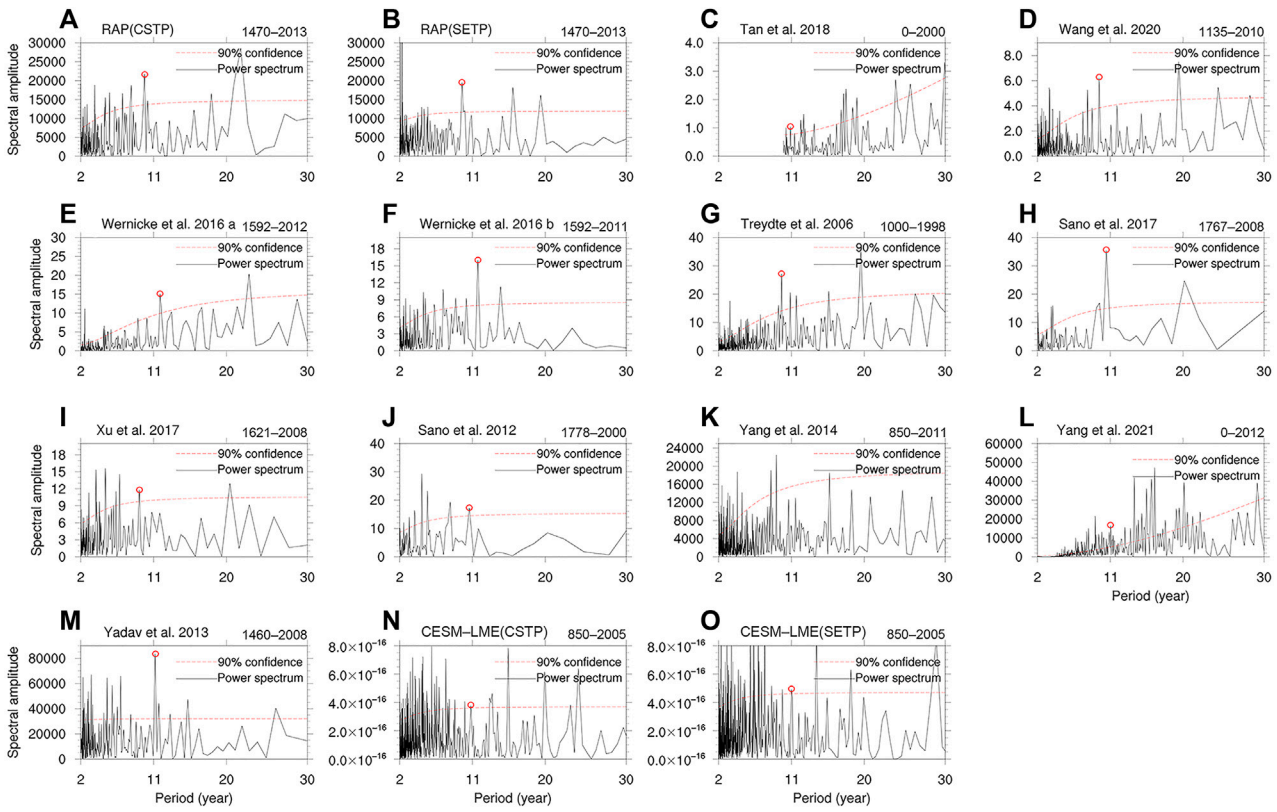

FIGURE 3
Power spectrum analysis of reconstructions **(A–M)** and simulations **(N–O)**. **(A)** Result of RAP over central–southern TP. **(B)** same as **(A)**, but over southeastern TP **(C–M)** Results from different proxy records across the TP listed in Table 1. **(N)** Results from the ensemble mean of four TSI experiments over central–southern TP. **(O)** same as **(N)**, but over southeastern TP. Red dashed lines represent the 90% significance level; red circles mark the significant 11-year cycle.

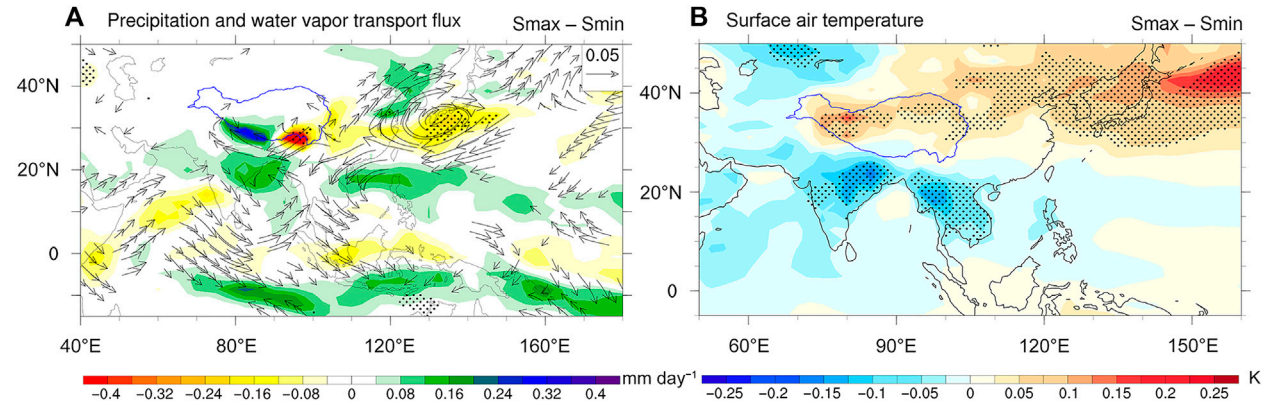

FIGURE 4
Composite differences in JJA mean precipitation (shading, mm day^{-1}) overlain on the **(A)** water vapor transport flux (kg·m^{-1} s^{-1}) and **(B)** surface air temperature (K) between the 11-year Smax and Smin phases from the ensemble-mean result of four TSI experiments in the CESM–LME. The black dots denote significance at the 90% confidence level (two-tailed Student's *t*-test).

A previous study found that precipitation over the central–southern TP can be affected by the TP–Indian Ocean thermal contrast, which causes northward water vapor transport over the Indian Ocean (Li and Xiao, 2022). We investigated the composite differences in surface air temperature between the 11-year Smax and Smin phases (Figure 4B). The result showed that, when

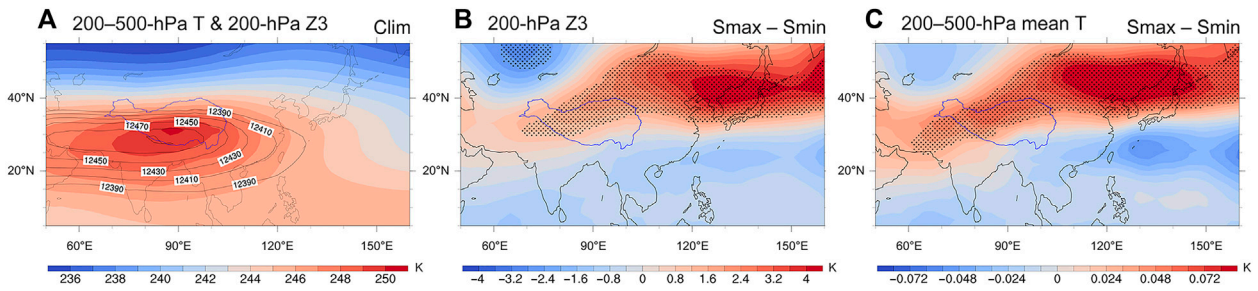

FIGURE 5
(A) Climatological JJA mean 200-hPa geopotential height (contours, gpm) and 200–500-hPa mean upper-tropospheric temperature (shading, K) during the period 1976–2005. **(B)** Composite differences in JJA mean geopotential height between the 11-year Smax and Smin phases from the ensemble-mean result of four TSI experiments in the CESM–LME. **(C)** Same as **(B)**, but for 200–500-hPa mean upper-tropospheric temperature (K). The black dots denote significance at the 90% confidence level (two-tailed Student's *t*-test).

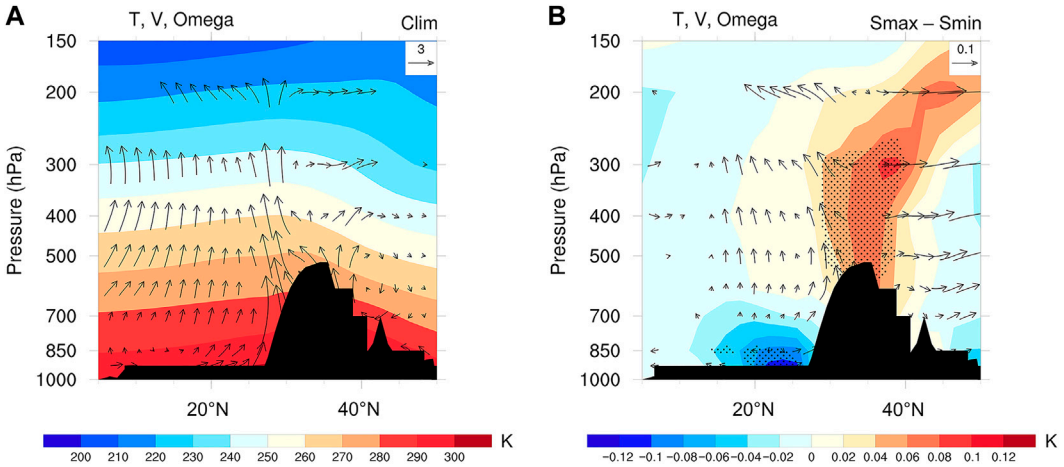

FIGURE 6
(A) Zonally averaged (77.5°–87.5°E) climatological JJA mean pressure–latitude cross section of temperature (shading, K), vertical velocity (vectors, 0.02 Pa s^{-1}), and meridional winds (m s^{-1}) during the period 1976–2005. **(B)** Same as **(A)**, but for the composite differences between the 11-year Smax and Smin phases from the ensemble-mean result of four TSI experiments in the CESM–LME. The black dots in **(B)** denote significance at the 90% confidence level (two-tailed Student's *t*-test).

solar irradiance increases, there is a significant warming over mid-latitude regions of the TP, northern China, Mongolia, and Pacific Ocean, accompanied by a cooling anomaly over low-latitude regions, such as the Indian Ocean, India, and Southeast Asia. This causes an enhanced land–sea thermal contrast between the TP and Indian Ocean, with a difference of approximately 0.1 K, which enhances the ISM and transports more moisture to the central–southern TP.

Surface warming over the TP region can further heat the mid–upper troposphere through diabatic heating (Figure 5C), which increases the geopotential height at the upper troposphere (Figure 5B). The climatological South Asian High (SAH) is located over southern Asia (Figure 5A) and is an important indicator for the Asian monsoon (Wei et al., 2015). The anomaly pattern of 200-hPa geopotential height showed an enhancement and northward shift of the SAH, compared with the normal climatological position of the SAH (Figures 5A, B). Some previous studies have suggested that the onset of the Asian summer monsoon is closely related to the northward shift of the SAH, which triggers a monsoon vortex over the Bay of Bengal through the upper-level divergence pumping effect (Liu et al., 2013; Wu et al., 2015). Hence, the strengthening and northward shift of the SAH under solar maxima may contribute to the enhancement of the ISM.

Surface warming over the TP region also decreases sea level pressure (SLP), which induces an ascending motion over the central–southern TP and northern Indian subcontinent regions (Supplementary Figure S4). We further investigated the pressure–latitude cross section of zonally averaged temperature, vertical velocity, and meridional winds over the region 77.5–87.5°E (Figure 6). We found a uniform climatological upward motion over the central–southern TP and northern India

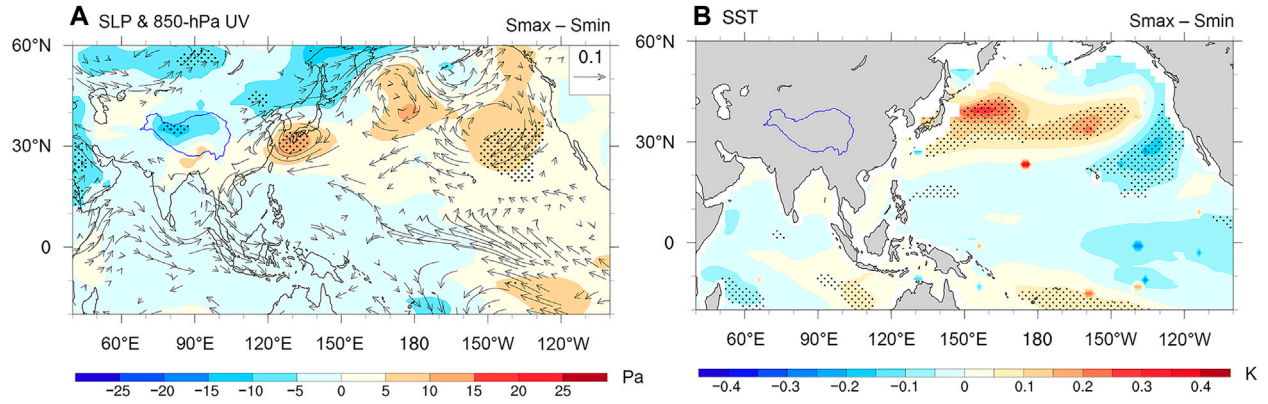

FIGURE 7
Composite differences in **(A)** JJA mean 850-hPa wind (vectors, m s^{-1}) and precipitation (shading, mm day^{-1}) and **(B)** sea surface temperature (SST, K) between the 11-year Smax and Smin phases from the ensemble-mean result of four TSI experiments in the CESM–LME. The black dots denote significance at the 90% confidence level (two-tailed Student's *t*-test).

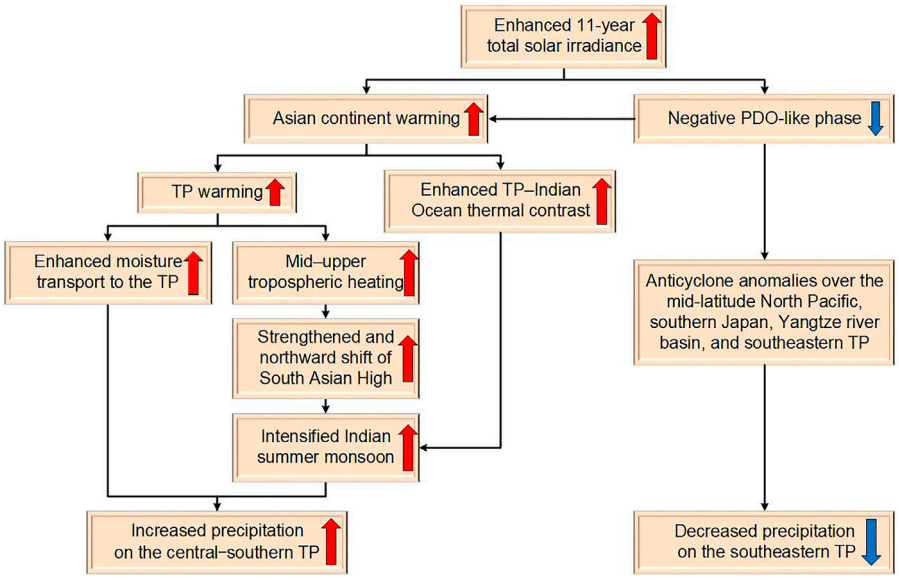

FIGURE 8
Schematic diagram of the mechanism responsible for the change in TP precipitation under the 11-year solar cycle.

during the boreal summer (Figure 6A). When solar irradiance increases, the ascending motion is enhanced over the central–southern TP and the meridional circulation is also strengthened (Figure 6B). The enhanced water vapor carried by the ISM flow rises upon reaching the central–southern TP, causing an anomalous upward motion, and substantially increasing precipitation in this region.

We also examined the changes in SST and winds at 850 hPa under the 11-year solar cycle (Figure 7). The result showed that a warm SST anomaly occurs over the Kuroshio–Oyashio Extension and North Pacific, while a cold SST anomaly occurs along the North American coastline, resembling the negative PDO phase (Figure 7B). A previous study indicated that a cool PDO-like SST pattern can be induced by solar forcing during strong 11-year solar cycle epochs (Jin et al., 2019). On the basis of observational data, our composite analysis also showed a negative PDO-like pattern between the 11-year Smax and Smin phases (Supplementary Figure S5); this is similar to the TSI modeling result from the CESM–LME (Figure 7B). The negative PDO may induce a rise in SLP over the mid-latitude central and western North Pacific, causing a large-scale anomalous anticyclone over the extratropical North Pacific (Figure 7A) (Sun et al., 2022c). Asian continental warming induces a low SLP anomaly. Then, the large SLP gradient between the western North Pacific high and northern and northeastern China low anomalies generates strong southwesterlies over eastern China (Figure 7A); this causes wet conditions over northern and

northeastern China, and dry conditions over the Yangtze River basin, southeastern TP, and southern Japan (Figure 4A).

To explore whether the negative PDO-like SST pattern could induce this anomalous atmospheric circulation and precipitation over East Asia, we examined the PDO mode and its net effect in the CTRL experiment (Supplementary Figure S6). The EOF first mode of North Pacific SST anomalies showed a negative PDO pattern and its explained variance was approximately 40.6% (Supplementary Figure S6), similar to that in the observations (Sun et al., 2022a). We then analyzed the climatic impact of the negative PDO using the regression map of surface air temperature, 850-hPa winds, and precipitation on the associated principal component 1 (PC1). We found a remarkable warm anomaly over the mid-latitude central and western North Pacific, and a cold anomaly along the west coast of North America (Supplementary Figure S6B), inducing a large-scale North Pacific anticyclonic anomaly (Supplementary Figure S6C). Meanwhile, mid-latitude Asian continental warming causes a drop in SLP, which leads to an SLP gradient between the mid-latitude Asian continent and western North Pacific. This enhances the southwesterly flow over eastern China, which induces dry conditions over southern Japan, southern China, and the southeastern TP. The anomalous precipitation, low-level circulation and surface air temperature over East Asia caused by the negative PDO in the CTRL experiment (Supplementary Figure S6) are similar to the result under the 11-year solar cycle from the TSI experiments (Figures 4, 7). This means that when solar irradiance induces a negative PDO-like SST pattern, this SST pattern can further contribute to the drying over the Yangtze River basin and southeastern TP, and can also further enhance the land–sea thermal contrast leading to the strengthening of the Indian monsoon. A schematic diagram of the mechanism of TP precipitation variation under the 11-year solar cycle is shown in Figure 8.

4 Discussion and conclusion

This study investigated the response of precipitation over the TP to the 11-year solar cycle during the past millennium. On the basis of observations during the period 1901–2013, proxy-based reconstructions over the past five centuries, and other high-resolution reconstructions, we found a significant quasi-11-year cycle of TP precipitation. The TSI sensitivity experiments from the CESM–LME showed that this quasi-11-year cycle is modulated by the 11-year solar activity cycle. Meanwhile, observations and reconstructions demonstrated a significant summer wet condition over the central–southern TP, accompanied by a dry condition over the southeastern TP, during peaks in the 11-year solar cycle; this was also captured by the TSI sensitivity experiments. Modeling results showed that, under solar maxima, a significant surface warming occurs over the Asian continent, especially for the TP region, causing a strengthened TP–Indian Ocean thermal contrast, which enhances the ISM. The TP heating induces mid–upper tropospheric warming, which causes a strengthening and northward shift of the SAH; this further intensifies the ISM. The enhanced ISM transports more water vapor from the Indian Ocean to the northern Indian subcontinent, which rises upon reaching the central–southern TP, substantially increasing precipitation in this region. A negative PDO-like SST pattern occurs under solar maxima, leading to a significant SLP gradient between the anomalous mid-latitude Asian continental low and North Pacific high; this induces a large-scale anticyclonic anomaly over the mid-latitude North Pacific, southern Japan, Yangtze River basin, and southeastern TP, substantially decreasing precipitation over the southeastern TP.

Many early studies have demonstrated a dipole pattern of precipitation anomalies over the northern and southern TP on the inter annual time scale (Li et al., 2021). However, the EOF mode (Figure omitted) shows that on the decadal time scale, the main precipitation mode exhibits an east–west dipole pattern. Meanwhile, the climatological mean precipitation suggests that, precipitation over the northern TP is basically below 1.5 mm day^{-1}, while precipitation over the southern TP is even more than 6 mm day^{-1} (Figure 1). The large precipitation magnitude might lead to a stronger decadal variability of precipitation over the southern TP. However, under the influence of the 11-year solar activity cycle, the GPCC and RAP data show a "dry–wet–dry" zonal tripolar pattern over the southern TP (Figures 2A–C), while the TSI experiments show a "wet–dry" zonal dipole pattern over the central–southern and southeastern TP (Figure 2D). We postulate that the bias in precipitation over the southwestern TP may be associated with the model's uncertainty in simulating the precipitation over the western TP, which is a common problem in GCMs (e.g., Zhu et al., 2020). This type of model deficiency limits our understanding of the mechanisms responsible for TP precipitation variability. Meanwhile, there are two potential mechanisms that can explain the influence of solar activity on the climate system, namely, the "top-down" stratospheric ozone mechanism (Haigh, 1996) and "bottom-up" coupled air–sea mechanism (Meehl et al., 2008). In this paper, only the latter mechanism is considered; however, the former mechanism might also contribute to the decadal precipitation variability over the TP under the 11-year solar cycle. Thus, further development of high-resolution models and improvement of the model physics and parameters will be critical to understanding the response of the TP climate to external forcing (i.e., solar activity).

Data availability statement

Publicly available datasets were analyzed in this study. This data can be found here: https://www.cesm.ucar.edu/community-projects/lme/data-sets https://psl.noaa.gov/data/gridded/data.gpcc.html https://psl.noaa.gov/data/gridded/data.noaa.ersst.v5.html https://www.metoffice.gov.uk/hadobs/hadisst/https://www.ncei.noaa.gov/access/paleo-search/.

Author contributions

YH: data curation, formal analysis, investigation, visualization, writing—original draft; WS (corresponding author): conceptualization, methodology, validation, supervision, writing—review and editing; JL: conceptualization, funding acquisition, project administration, resources, supervision; DC: conceptualization, writing—review and editing, funding acquisition; LN: methodology, supervision; ZP: visualization.

Funding

Our study was supported by the National Natural Science Foundation of China (Grant Numbers 42130604, 42105044,

41971108, and 42111530182) and Swedish STINT (Grant Number CH 2019-8377).

Acknowledgments

We thank the CESM–LME, GPCC, ERSST, HadISST, RAP, and other reconstruction teams (Table 1) for providing simulation, observation, and reconstruction data.

Conflict of interest

The authors declare that the research was conducted in the absence of any commercial or financial relationships that could be construed as a potential conflict of interest.

Publisher's note

Supplementary material

The Supplementary Material for this article can be found online at: https://www.frontiersin.org/articles/10.3389/feart.2023.1137205/full#supplementary-material

References

Breitenmoser, P., Beer, J., Brönnimann, S., Frank, D., Steinhilber, F., and Wanner, H. (2012). Solar and volcanic fingerprints in tree-ring chronologies over the past 2000years. *Palaeogeogr. Palaeoclimatol. Palaeoecol.* 313–314, 127–139. doi:10.1016/j.palaeo.2011.10.014

Cai, Y., Zhang, H., Cheng, H., An, Z., Lawrence Edwards, R., Wang, X., et al. (2012). The Holocene Indian monsoon variability over the southern Tibetan Plateau and its teleconnections. *Earth Planet. Sci. Lett.* 335–336, 135–144. doi:10.1016/j.epsl.2012.04.035

Chen, Q., Ge, F., Jin, Z., and Lin, Z. (2022). How well do the CMIP6 HighResMIP models simulate precipitation over the Tibetan Plateau? *Atmos. Res.* 279, 106393. doi:10.1016/j.atmosres.2022.106393

Chiodo, G., Oehrlein, J., Polvani, L. M., Fyfe, J. C., and Smith, A. K. (2019). Insignificant influence of the 11-year solar cycle on the North atlantic oscillation. *Nat. Geosci.* 12, 94–99. doi:10.1038/s41561-018-0293-3

Cook, E. R., Anchukaitis, K. J., Buckley, B. M., D'arrigo, R. D., Jacoby, G. C., and Wright, W. E. (2010). Asian monsoon failure and megadrought during the last millennium. *Science* 328, 486–489. doi:10.1126/science.1185188

Feng, L., and Zhou, T. (2012). Water vapor transport for summer precipitation over the Tibetan Plateau: Multidata set analysis. *J. Geophys. Res.-Atmos.* 117, D20114. doi:10.1029/2011jd017012

Haigh, J. D. (1996). The impact of solar variability on climate. *Science* 272, 981–984. doi:10.1126/science.272.5264.981

Huang, B., Thorne, P., Banzon, V., Boyer, T., Chepurin, G., Lawrimore, J., et al. (2017). Extended reconstructed Sea Surface temperature, version 5 (ERSSTv5): Upgrades, validations, and intercomparisons. *J. Clim.* 30, 8179–8205. doi:10.1175/JCLI-D-16-0836.1

Hurrell, J. W., Holland, M., Gent, P., Ghan, S., Kay, J., Kushner, P., et al. (2013). The community earth system model: A framework for collaborative research. *Bull. Am. Meteorol. Soc.* 94, 1339–1360. doi:10.1175/BAMS-D-12-00121.1

Jin, C., Liu, J., Wang, B., Yan, M., and Ning, L. (2019). Decadal variations of the East Asian summer monsoon forced by the 11-year insolation cycle. *J. Clim.* 32, 2735–2745. doi:10.1175/JCLI-D-18-0288.1

Jin, C., Wang, B., and Liu, J. (2020). Emerging pacific quasi-decadal oscillation over the past 70 years. *Geophys. Res. Lett.* 48, 1–11. doi:10.1029/2020GL090851

Li, L., Zhang, R., Wen, M., and Lv, J. (2021). Regionally different precipitation trends over the Tibetan plateau in the warming context: A perspective of the Tibetan plateau vortices. *Geophys. Res. Lett.* 48 (11), e2020GL091680. doi:10.1029/2020GL091680

Li, Z., and Xiao, Z. (2022). The role of Tibetan plateau–Indian Ocean thermal contrast in the significant increasing precipitation over the southern Tibetan plateau in may after the mid-1990s. *J. Clim.* 35, 4061–4075. doi:10.1175/jcli-d-21-0619.1

Liu, B., Wu, G., Mao, J., and He, J. (2013). Genesis of the South Asian high and its impact on the asian summer monsoon onset. *J. Clim.* 26, 2976–2991. doi:10.1175/JCLI-D-12-00286.1

Liu, Y., Chen, H., Li, H., Zhang, G., and Wang, H. (2021). What induces the interdecadal shift of the dipole patterns of summer precipitation trends over the Tibetan Plateau? *Int. J. Climatol.* 41, 5159–5177. doi:10.1002/joc.7122

Liu, F., Gao, C., Chai, J., Robock, A., Wang, B., Li, J., et al. (2022). Tropical volcanism enhanced the East Asian summer monsoon during the last millennium. *Nat. Commun.* 13, 3429. doi:10.1038/s41467-022-31108-7

Ma, H., Wang, R., Lai, A., Li, X., Wang, F., Zhou, Z., et al. (2021). Solar activity modulates the El Niño-Southern Oscillation-induced precipitation anomalies over southern China in early spring. *Int. J. Climatol.* 41, 6589–6601. doi:10.1002/joc.7214

Meehl, G., and Arblaster, J. (2009). A lagged warm event–like response to peaks in solar forcing in the pacific region. *J. Clim.* 22, 3647–3660. doi:10.1175/2009JCLI2619.1

Meehl, G., Arblaster, J., Branstator, G., and Van Loon, H. (2008). A coupled air sea response mechanism to solar forcing in the pacific region. *J. Clim.* 21, 2883–2897. doi:10.1175/2007JCLI1776.1

Meehl, G., Arblaster, J., Matthes, K., Sassi, F., and Van Loon, H. (2009). Amplifying the pacific climate system response to a small 11-year solar cycle forcing. *Science* 325, 1114–1118. doi:10.1126/science.1172872

Misios, S., Mitchell, D., Gray, L., Tourpali, K., Matthes, K., Hood, L., et al. (2015). Solar signals in CMIP-5 simulations: Effects of atmosphere-ocean coupling. *Q. J. R. Meteorol. Soc.* 142, 928–941. doi:10.1002/qj.2695

Misios, S., Gray, L., Knudsen, M., Karoff, C., Schmidt, H., and Haigh, J. (2019). Slowdown of the Walker circulation at solar cycle maximum. *Proc. Natl. Acad. Sci.* 116, 7186–7191. doi:10.1073/pnas.1815060116

Otto-Bliesner, B., Brady, E., Fasullo, J., Jahn, A., Landrum, L., Stevenson, S., et al. (2015). Climate variability and change since 850 CE: An ensemble approach with the community earth system model. *Bull. Am. Meteorol. Soc.* 97, 735–754. doi:10.1175/BAMS-D-14-00233.1

Rayner, N. A., Parker, D., Horton, E. B., Folland, C., Alexander, L., Rowell, D., et al. (2003). Global analyses of sea surface temperature, sea ice, and night marine air temperature since the late Nineteenth Century. *J. Geophys. Res.* 108, 4407. doi:10.1029/2002JD002670

Sano, M., Ramesh, R., and Sukumar, R. (2012). Increasing aridity over the past 223 Years in the Nepal himalaya inferred from a tree-ring δ18O chronology. *Holocene* 22, 809–817. doi:10.1177/0959683611430338

Sano, M., Dimri, A. P., Ramesh, R., Xu, C., Li, Z., and Nakatsuka, T. (2017). Moisture source signals preserved in a 242-year tree-ring δ 18 O chronology in the Western Himalaya. *Glob. Planet. Change* 157, 73–82. doi:10.1016/j.gloplacha.2017.08.009

Schmidt, G., Jungclaus, J., Ammann, C., Bard, E., P, B., Crowley, T., et al. (2011). Climate forcing reconstructions for use in PMIP simulations of the Last Millennium (v1.0). *Geosci. Model. Dev.* 4, 33–45. doi:10.5194/gmd-4-33-2011

Schneider, U., Becker, A., Finger, P., Meyer-Christoffer, A., and Ziese, M. (2018). *GPCC full data monthly product version 2018 at 1.0°: Monthly land-surface precipitation from rain-gauges built on GTS-based and historical data*. doi:10.5676/DWD_GPCC/FD_M_V2018_100

Shen, T., Sun, W., Liu, J., Wang, B., Chen, D., Ning, L., et al. (2022). Secular changes of the decadal relationship between the northern hemisphere land monsoon rainfall and Sea Surface temperature over the past millennium in climate model simulations. *J. Geophys. Res.-Atmos.* 127, e2022JD037065. doi:10.1029/2022JD037065

Shi, H., and Wang, B. (2019). How does the Asian summer precipitation-ENSO relationship change over the past 544 years? *Clim. Dyn.* 52, 4583–4598. doi:10.1007/s00382-018-4392-z

Shi, F., Zhao, S., Guo, Z., Goosse, H., and Yin, Q. (2017). Multi-proxy reconstructions of May–September precipitation field in China over the past 500 years. *Clim. Past.* 13, 1919–1938. doi:10.5194/cp-13-1919-2017

Shi, C., Daux, V., Li, Z., Wu, X., Fan, T., Ma, Q., et al. (2018a). The response of relative humidity to centennial-scale warming over the southeastern Tibetan Plateau inferred from tree-ring width chronologies. *Clim. Dyn.* 51, 3735–3746. doi:10.1007/s00382-018-4107-5

Shi, H., Wang, B., Cook, E., Liu, J., and Liu, F. (2018b). Asian summer precipitation over the past 544 Years reconstructed by merging tree rings and historical documentary records. *J. Clim.* 31, 7845–7861. doi:10.1175/JCLI-D-18-0003.1

Shi, H., Wang, B., Liu, J., and Liu, F. (2019). Decadal–Multidecadal variations of asian summer rainfall from the little ice age to the present. *J. Clim.* 32, 7663–7674. doi:10.1175/JCLI-D-18-0743.1

Sun, W., Liu, J., Wang, B., Chen, D., and Gao, C. (2022a). Pacific multidecadal (50–70 year) variability instigated by volcanic forcing during the Little Ice Age (1250–1850). *Clim. Dyn.* 59, 231–244. doi:10.1007/s00382-021-06127-7

Sun, W., Liu, J., Wang, B., Chen, D., Wan, L., and Wang, J. (2022b). Holocene multi-centennial variations of the asian summer monsoon triggered by solar activity. *Geophys. Res. Lett.* 49, e2022GL098625. doi:10.1029/2022GL098625

Sun, W., Wang, B., Liu, J., and Dai, Y. (2022c). Recent changes of pacific decadal variability shaped by greenhouse forcing and internal variability. *J. Geophys. Res.-Atmos.* 127, e2021JD035812. doi:10.1029/2021JD035812

Tan, L., Cai, Y., Cheng, H., Edwards, L. R., Lan, J., Zhang, H., et al. (2018). High resolution monsoon precipitation changes on southeastern Tibetan Plateau over the past 2300 years. *Quat. Sci. Rev.* 195, 122–132. doi:10.1016/j.quascirev.2018.07.021

Treydte, K., Schleser, G., Helle, G., Frank, D., Winiger, M., Haug, G., et al. (2006). The twentieth century was the wettest period in northern Pakistan over the past Millennium. *Nature* 440, 1179–1182. doi:10.1038/nature04743

Van Loon, H., Meehl, G., and Shea, D. (2007). Coupled air-sea response to solar forcing in the Pacific region during northern winter. *J. Geophys. Res.* 112, D02108. doi:10.1029/2006JD007378

Vieira, L., Solanki, S., Krivova, N., and Usoskin, I. (2011). Evolution of the solar irradiance during the Holocene. *Astron. Astrophys.* 531, A6. doi:10.1051/0004-6361/201015843

Wang, S.-Y., Hakala Assendelft, K., Gillies, R., and Capehart, W. (2014). The Pacific Quasi-Decadal Oscillation (QDO) - an important precursor toward anticipating major flood events in the Missouri River Basin? *Geophys. Res. Lett.* 41, 991–997. doi:10.1002/2013GL059042

Wang, J., Yang, B., and Ljungqvist, F. (2020). Moisture and temperature covariability over the southeastern Tibetan plateau during the past nine centuries. *J. Clim.* 33, 6583–6598. doi:10.1175/JCLI-D-19-0363.1

Wei, W., Zhang, R., Wen, M., Kim, B.-J., and Nam, J.-C. (2015). Interannual variation of the South Asian high and its relation with Indian and east Asian summer monsoon rainfall. *J. Clim.* 28, 2623–2634. doi:10.1175/JCLI-D-14-00454.1

Wernicke, J., Hochreuther, P., Grießinger, J., Zhu, H., Wang, L., and Brauning, A. (2016). Multi-century humidity reconstructions from the southeastern Tibetan Plateau inferred from tree-ring δ18O. *Glob. Planet. Change* 149, 26–35. doi:10.1016/j.gloplacha.2016.12.013

White, W., and Liu, Z. (2008). Resonant excitation of the quasi-decadal oscillation by the 11-year signal in the Sun's irradiance. *J. Geophys. Res.* 113, C01002. doi:10.1029/2006JC004057

Wu, G., Duan, A., Liu, Y., Mao, J., Ren, R., Bao, Q., et al. (2015). Tibetan Plateau climate dynamics: Recent research progress and outlook. *Natl. Sci. Rev.* 2, 100–116. doi:10.1093/nsr/nwu045

Wu, G. (2020). Land–air coupling over the Tibetan Plateau and its climate impacts. *Natl. Sci. Rev.* 7, 485. doi:10.1093/nsr/nwaa012

Xu, H., Sheng, E., Lan, J., Yu, K., and Che, S. (2014). Decadal/multi-decadal temperature discrepancies along the eastern margin of the Tibetan Plateau. *Quat. Sci. Rev.* 89, 85–93. doi:10.1016/j.quascirev.2014.02.011

Xu, C., Sano, M., Dimri, A. P., Ramesh, R., Nakatsuka, T., Shi, F., et al. (2017). Decreasing Indian summer monsoon in northern Indian sub-continent during the last 180 years: Evidence from five tree cellulose oxygen isotope chronologies. *Clim. Past. Discuss.* 14, 653–664. doi:10.5194/cp-2016-132

Xue, J., Ning, L., Liu, Z., Qin, Y., Chen, K., Yan, M., et al. (2022). The combined influences of Solar Radiation and PDO on Precipitation over Eastern China during the last millennium. *Clim. Dyn.* 60, 1137–1150 doi:10.1007/s00382-022-06372-4

Yadav, R., and Bhutiyani, M. (2013). Tree-ring-based snowfall record for cold arid Western Himalaya, India since A.D. 1460. *J. Geophys. Res. Atmos.* 118, 7516–7522. doi:10.1002/jgrd.50583

Yang, B., Qin, C., Wang, J., He, M., Melvin, T., Osborn, T., et al. (2014). A 3,500-year tree-ring record of annual precipitation on the northeastern Tibetan Plateau. *Proc. Natl. Acad. Sci. U. S. A.* 111, 2903–2908. doi:10.1073/pnas.1319238111

Yang, B., Qin, C., Osborn, T., Trouet, V., Ljungqvist, F., Esper, J., et al. (2021). Long-term decrease in Asian monsoon rainfall and abrupt climate change events over the past 6,700 years. *Proc. Natl. Acad. Sci.* 118, e2102007118. doi:10.1073/pnas.2102007118

Yao, T., Thompson, L., Yang, W., Yu, W., Gao, Y., Guo, X., et al. (2012). Different Glacier status with atmospheric circulations in Tibetan plateau and surroundings. *Nat. Clim. Change* 2, 663–667. doi:10.1038/nclimate1580

Yao, T., Wu, F., Ding, L., Sun, J., Zhu, L., Piao, S., et al. (2015). Multispherical interactions and their effects on the Tibetan plateau's Earth system: A review of the recent researches. *Natl. Sci. Rev.* 2, 468–488. doi:10.1093/nsr/nwv070

Yao, T., Bolch, T., Chen, D., Gao, J., Immerzeel, W. W., Piao, S., et al. (2022). The imbalance of the Asian water tower. *Nat. Rev. Earth Environ.* 3, 618–632. doi:10.1038/s43017-022-00299-4

Yue, S., Wang, B., Yang, K., Xie, Z., Lu, H., and He, J. (2021). Mechanisms of the decadal variability of monsoon rainfall in the southern Tibetan Plateau. *Environ. Res. Lett.* 16, 014011. doi:10.1088/1748-9326/abcb36

Zhao, L., Wang, J., and Zhao, H. (2012). Solar cycle signature in decadal variability of monsoon precipitation in China. *J. Meteorol. Soc. Jpn.* 90, 1–9. doi:10.2151/jmsj.2012-101

Zhu, H., Jiang, Z., Li, J., Li, W., Sun, C., and Li, L. (2020). Does CMIP6 inspire more confidence in simulating climate extremes over China? *Adv. Atmos. Sci.* 37, 1119–1132. doi:10.1007/s00376-020-9289-1

frontiers | Frontiers in Earth Science

TYPE Original Research
PUBLISHED 14 March 2023
DOI 10.3389/feart.2023.1139699

OPEN ACCESS

EDITED BY
Hiroko Miyahara,
Musashino Art University, Japan

REVIEWED BY
Limin Zhou,
East China Normal University, China
Xin Wang,
South China Sea Institute of Oceanology (CAS), China

*CORRESPONDENCE
Zhangqun Li,
lizhangqun@lasg.iap.ac.cn

SPECIALTY SECTION
This article was submitted to Interdisciplinary Climate Studies, a section of the journal Frontiers in Earth Science

RECEIVED 07 January 2023
ACCEPTED 24 February 2023
PUBLISHED 14 March 2023

CITATION
Li S, Li Z and Ling S (2023), Combined effect of the solar activity and ENSO on the tropical cyclone genesis frequency in the southeastern part of the western North Pacific.
Front. Earth Sci. 11:1139699.
doi: 10.3389/feart.2023.1139699

Combined effect of the solar activity and ENSO on the tropical cyclone genesis frequency in the southeastern part of the western North Pacific

Shuang Li[1,2,3], Zhangqun Li[3]* and Sining Ling[3]

[1]Tianjin Key Laboratory for Oceanic Meteorology, Tianjin, China, [2]Tianjin Institute of Meteorological Science, Tianjin, China, [3]State Key Laboratory of Numerical Modeling for Atmospheric Sciences and Geophysical Fluid Dynamics, Institute of Atmospheric Physics, Chinese Academy of Sciences, Beijing, China

This study analyzes the frequency characteristics of tropical cyclone (TC) genesis in the southeastern part of the western North Pacific (SEWNP) during June–November from 1965 to 2019 and investigates the possible combined effect of the solar activity and El Niño-Southern Oscillation (ENSO). Results suggest that TCs generated in the SEWNP have the longest lifetime and greatest strength, and its frequency has apparent interannual and decadal variations, which is jointly affected by the solar activity and ENSO. In El Niño years during declining phases of solar cycle (1–3 years following the solar maximum), positive TC genesis frequency anomalies in the SEWNP are significantly strong and tend to occur in extremes. While the opposite is true for La Niña during ascending phases of solar cycle (1–3 years following the solar minimum). However, there exists no significant feature in the combined effect of La Niña (El Niño) and declining (ascending) phases of solar cycle. When declining (ascending) phases of solar cycle and El Niño (La Niña) are combined, the overlapping effect leads to apparently warmer (colder) sea surface temperature (SST) anomalies in the central equatorial Pacific and colder (warmer) SST anomalies in the western Pacific, so the SST anomalies gradient are stronger. It enhances low-level westerly (easterly) wind anomalies and upper-level easterly (westerly) wind anomalies, which is favorable for the further decrease (increase) of the vertical wind shear in the eastern (most) part of SEWNP. Moreover, the stronger and more westward low-level convergence (divergence) center appears in the Pacific, causing stronger low-level convergent (divergent) flow and upper-level divergent (convergent) flow anomalies, and strengthened (suppressed) ascending movement anomalies in the SEWNP. As a result, the TC genesis frequency in the SEWNP is much higher (lower). Further diagnoses show that absolute vorticity plays a leading role in El Niño years during declining phases of solar cycle, and its contribution is obviously much greater than other environmental factors. It is not perfectly symmetrical in La Niña years during ascending phases of solar cycle when the contribution of absolute vorticity is the greatest, but vertical wind shear is also important.

KEYWORDS

tropical cyclone genesis, solar cycle phases, El Niño-southern Oscillation, combined effect, environmental factors

1 Introduction

Tropical cyclones (TCs) could not only bring severe weather with significant casualties and economic losses, but also make an impact on the atmospheric circulation (Zhong, 2006; Ren et al., 2007; Zhong and Hu, 2007; Chen et al., 2017; Wang et al., 2019; Ling and Lu, 2022), so understanding the TC activity is of great importance. TC genesis has attracted considerable attention, but its prediction has been a difficult topic for the past few decades (Cao et al., 2022). The western North Pacific (WNP) is known to be the most prolific tropical cyclone basin, accounting for about 1/3 of all the global TCs (Chan, 2005; Huang and Chen, 2007; Woodruff et al., 2013), and the southeastern part of the WNP (SEWNP) is an important key region for the TC genesis (Wang and Chan, 2002; Camargo and Sobel, 2005; Zhang et al., 2017; Liu et al., 2019; Shan and Yu, 2021; Cao et al., 2022; Song et al., 2022). Zhang et al. (2017) found that the Atlantic meridional mode affects TC activity in the WNP mainly through changes in the TC genesis in the SEWNP. What is more, the TC genesis frequency in the SEWNP is associated with that in the eastern North Pacific and tropical North Atlantic Ocean. When more TCs generate in the SEWNP, more TCs generate in the eastern North Pacific, but less in the tropical North Atlantic Ocean (Cao et al., 2022). The sudden decrease in TC genesis frequency in the SEWNP also leads to the abrupt reduction of the frequency of TC landfall in southern China in the post-peak season, owing to the abrupt decline in westward-moving tracks (Shan and Yu, 2021). In addition, the increased TC activity in the SEWNP contributes significantly to the intensity of El Niño after 3 months by weakening the Walker circulation and strengthening the eastward propagating oceanic Kelvin waves in the tropical Pacific (Wang et al., 2019). Consequently, the TC genesis in the SEWNP is noteworthy.

As the most significant signal of interannual variability in the coupled atmosphere-ocean system, El Niño-Southern Oscillation (ENSO) plays a crucial role in TC genesis in the WNP (Pan, 1982; Chan, 1985; Li, 1987; Lander, 1994; Chen et al., 1998; Chan, 2000; Wang and Chan, 2002; Elsner and Liu, 2003; Chu, 2004; Camargo et al., 2007; Kim et al., 2011, 2016; Zhan et al., 2011; Wang et al., 2014; Zhao and Wang, 2019; Song et al., 2022). A general consensus is that the relationship between ENSO and TC genesis frequency is weak in the entire WNP, but ENSO remarkably affects the shift of TC genesis location. The TC genesis frequency increases in the SEWNP and decreases in the northwestern part of the WNP (NWWNP) during El Niño years. Wang and Chan (2002) attributed the more TCs in the SEWNP to the increase of the low-level vorticity, and fewer TCs in the NWWNP to the upper-level convergence induced by the strengthening of the East Asian trough and WNP subtropical high, which are all forced by El Niño. Camargo and Sobel (2005) suggested that more TCs generated in the SEWNP take relatively longer time to make landfall or encounter colder mid-latitude water during El Niño years, which results in more opportunities to obtain energy and enhance TC intensity.

Besides the interannual variation, the frequency of TC genesis in the WNP has the decadal feature, which is modulated by several decadal influencing factors. The solar activity has a remarkable quasi-11-year cycle and plays an important role in driving climate (Herschel, 1801; Meehl et al., 2008; Gray et al., 2010). As previous studies have shown, the solar activity exerts an influence on sea surface temperature (SST) in the central tropical Pacific (Kodera et al., 2016; Huo et al., 2021; Lin et al., 2021), and El Niño Modoki events are found within 1–3 years following the solar maximum (Huo and Xiao, 2016, 2017). Huo and Xiao (2017) proposed two mechanisms to explain it. One is the direct effect that the lagging warming response of the central tropical Pacific to the solar radiation is amplified by the coupled atmosphere-ocean processes. The other is the indirect effect that the anomalous atmospheric circulation at mid-high latitudes is modulated by the heating effect propagating from the upper atmosphere, which may trigger an El Niño Modoki event in the 1–3 years following the solar maximum through wind-evaporation-SST feedback and the seasonal footprint mechanism. Enfield and Cid (1991) found that the persistence of ENSO is shorter (longer) in low (high) solar activity years. In addition, the solar activity could also modulate the impact of ENSO on the Pacific North American teleconnection, South Asia high, East Asian winter monsoon, and precipitation in southern China (Huth et al., 2006; Zhou et al., 2013; Liu et al., 2014; Li and Xiao, 2018; Xue et al., 2020; Ma et al., 2021; Wang et al., 2021).

Although Li et al. (2019) have pointed out that the solar activity is closely related to all the global TC genesis frequency, the relationship between the solar activity and TC genesis frequency in the WNP is less studied. It is still unclear whether the influence of ENSO on the TC genesis frequency in the WNP depends on the solar activity. Considering the significance of the SEWNP, this study focuses mainly on the modulation of the effect of ENSO on the TC genesis frequency in the SEWNP by different solar activities to provide evidence for the forecast of TC genesis frequency in the SEWNP and improve the forecast accuracy.

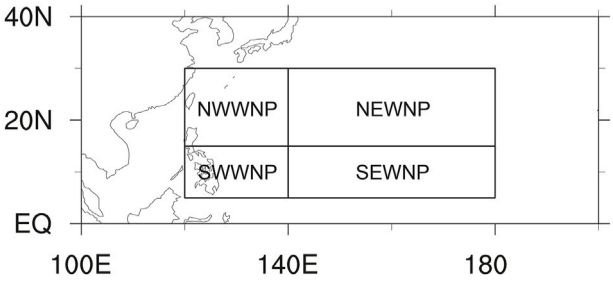

FIGURE 1
Four subregions of the WNP (black box).

2 Data and methods

In this study, the TC best-track data are derived from the Shanghai Typhoon Institute of the China Meteorological Administration (CMA), including the information on TC location (latitude and longitude) and intensity at 6-h intervals during 1965–2019 (Ying et al., 2014; Lu et al., 2021). Owing to the uncertainty of tropical depression, a TC here refers to reaching tropical storm intensity (17.2 m s^{-2}) and generating in the west of 180°C in the WNP. The TC genesis location is defined as the position where the TC reaches tropical storm intensity at the first time. As suggested by Cao et al. (2022), the WNP is divided into southeastern

TABLE 1 Characteristics of TCs generated in the four subregions of the WNP in JJASON during 1965–2019.

	SEWNP	NWWNP	NEWNP	SWWNP
Average annual TC genesis frequency	3.8	5.9	4.9	3.1
Lifetime of each TC (h)	202.7	129.6	151.4	154.4
Average annual accumulated cyclone energy (10^5 m^2 s^{-2})	2.0	1.1	1.3	0.8
TC genesis frequency and proportion reaching typhoon intensity	196 (93%)	180 (55%)	171 (63%)	132 (79%)
TC genesis frequency and proportion reaching super typhoon intensity	131 (62%)	42 (13%)	47 (17%)	32 (19%)

(5°N–15°N, 140°E–180°), northeastern (15°N–30°N, 140°E–180°), northwestern (15°N–30°N, 120°E–140°E) and southwestern (5°N–15°N, 120°E–140°E) regions (Figure 1). This analysis focuses on the active TC season in the WNP, which is from June to November (JJASON).

The monthly atmospheric fields including wind, temperature, relative humidity, specific humidity, sea level pressure, total cloud cover, and surface heat flux are obtained from the National Centers for Environmental Prediction and National Center for Atmospheric Research (NCEP/NCAR) reanalysis dataset on 2.5°C × 2.5°C grids (Kalnay et al., 1996). The monthly SST data are taken from the National Oceanic and Atmospheric Administration (NOAA)'s Extended Reconstructed SST version 5 (ERSST.v5) with a horizontal resolution of 2°C × 2°C (Huang et al., 2017). The data cover the period 1965–2019, and the linear trend is removed before the analysis. The power spectrum, Pearson correlation, linear regression, and composite analysis are used in this work, and the statistical significance is evaluated based on the Student *t*-test. According to Yan et al. (2004) and Yu et al. (2019), the effective degree of freedom of low-pass filtering is calculated.

The Niño3.4 index (5°S–5°N, 170°W–120°W) is from the NOAA's Climate Prediction Center. We identify ENSO based on the ±0.5 standard deviations of the June–November-averaged Niño3.4 index. An El Niño (La Niña) event is identified when the Niño3.4 index is greater (less) than + (−) 0.5 standard deviations. The sunspot numbers (SSN) index from the World Data Center at the Royal Observatory of Belgium is used to quantify the solar activity. An 11-year fast Fourier low-pass filtering is applied to the June–November-averaged SSN index to obtain the solar maximum (minimum), which are greater (less) than 0 standard deviations. The declining (ascending) phase of solar cycle is then defined as the 1–3 years following the solar maximum (minimum).

To quantitatively diagnose the contributions of different environmental factors to TC genesis, the genesis potential index (GPI) from Emanuel and Nolan (2004) is employed, which is calculated as follows:

$$GPI = T1 \times T2 \times T3 \times T4$$

Where $T1 = |10^5\eta|^{\frac{3}{2}}$, $T2 = (1 + 0.1V_{shear})^{-2}$, $T3 = (\frac{H}{50})^3$, $T4 = (\frac{V_{pot}}{70})^3$, η is the absolute vorticity at 850 hPa (s^{-1}), V_{shear} is calculated as the magnitude of the vertical wind shear between 200 and 850 hPa (m s^{-1}), H is the relative humidity at 600 hPa (%), and V_{pot} is the potential intensity (PI; m s^{-1}), which is estimated in detail following the study of Bister and Emanuel (2002). According to the method of Li et al. (2013), the deviation of *GPI* is evaluated as follows:

$$GPI' = T1' \times \overline{T2} \times \overline{T3} \times \overline{T4} + \overline{T1} \times T2' \times \overline{T3} \times \overline{T4} + \overline{T1} \times \overline{T2} \times T3' \times \overline{T4} + \overline{T1} \times \overline{T2} \times \overline{T3} \times T4'$$

where the bar represents the climatological mean, and the prime indicates the deviation from the climatological mean. The four terms in the right-hand side of the above equation denote the contributions of lower-level absolute vorticity, vertical wind shear between 200 hPa and 850 hPa, mid-level relative humidity, and PI, respectively.

3 Results

3.1 Frequency characteristics of TC genesis in the SEWNP and NWWNP

Characteristics of TCs generated in the four subregions of the WNP are shown in Table 1. In the NWWNP, the average TC genesis frequency in JJASON during 1965–2019 is 5.9 per year, with the highest in the four subregions of the WNP, and there is an insignificant linear decreasing trend with a value of −0.01 per year. The NWWNP is so close to East Asia that more TCs generated here tend to have a serious impact on East Asia. Compared to that in the NWWNP and northeastern part of the WNP (NEWNP), TC genesis frequency in the SEWNP of 3.8 is lower, with a linear trend of −0.04 at the 90% confidence level. However, TCs generated in the SEWNP have the longest average lifetime of 202.7 h, which far exceeds the second value of 154.4 h in the southwestern part of the WNP (SWWNP). The shortest average TC lifetime appears in the NWWNP with a value of 129.6 h. Additionally, the strongest TCs generate in the SEWNP with the average annual accumulated cyclone energy (ACE) of 2×10^5 m^2 s^{-2}, while the smallest ACE is in the SWWNP. To further confirm the feature, TC genesis frequency reaching typhoon intensity (32.7 m s^{-1}) and super typhoon intensity (51 m s^{-1}) are checked. It is found that in the SEWNP, there are 196 TCs reaching typhoon grade, accounting for 93% of the total number, while 131 TCs reaching super typhoon grade, accounting for 62% of the total number. It outdistances that in the other three subregions, which also verifies TCs generated in the SEWNP are the strongest in general. To sum up, TCs generated in the SEWNP have the longest lifetime and the greatest strength, while the TC genesis frequency in the NWWNP is the highest. Furthermore, ENSO has a great influence on the TC genesis in the SEWNP and NWWNP (Lander, 1994; Chen et al., 1998; Wang and Chan, 2002; Elsner and Liu, 2003; Chu, 2004;

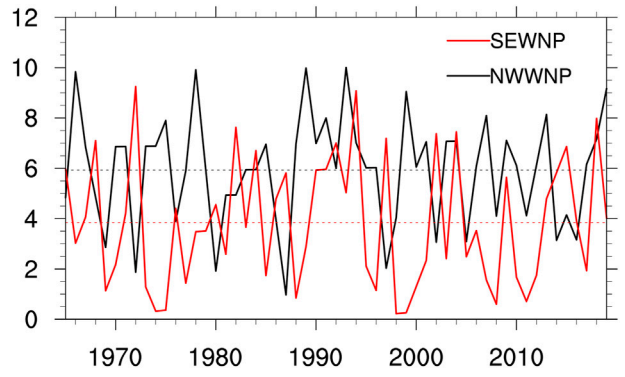

FIGURE 2
Time series of TC genesis frequency in the SEWNP (red line) and NWWNP (black line) in JJASON during 1965–2019. The dotted line denotes the average.

Camargo et al., 2007; Kim et al., 2011; Zhan et al., 2011; Song et al., 2022). Therefore, it is of great significance to study the TC genesis in the SEWNP and NWWNP, which is the focus of our analysis below.

As can be seen in Figure 2, there are apparent interannual and decadal variations in the TC genesis frequency in the SEWNP, with the highest TC genesis frequency occurring in 1972 and 1994, which is approximately 9 TCs. The corresponding power spectrum of TC genesis frequency in the SEWNP shows obvious peaks at cycles of 2–4 years and 11 years, in which the 11-year cycle is the most significant (Figure 3A). By means of filtering, the decadal variance contribution is proved to be significant, explaining 26% of the total variance. Therefore, in addition to the interannual influence, the TC genesis frequency in the SEWNP may be modulated by decadal factors. It is well known that solar activity has a remarkable quasi-11-year cycle and ENSO is the strongest signal of interannual variation in the coupled atmosphere-ocean system. Thus, a hypothesis naturally comes out that the TC genesis frequency in the SEWNP may be jointly affected by solar activity and ENSO. With regards to the TC genesis frequency in the NWWNP, the interannual variation is dominant and the highest TC genesis frequency occurred in 1966, 1978, 1989, and 1993, with about 10 TCs (Figure 2). The power spectrum also confirms that it has a significant peak at cycles of 3–4 years (Figure 3B). The TC genesis frequency in the NWWNP is primarily influenced by interannual factors.

3.2 Association between ENSO and TC genesis frequency in the SEWNP and NWWNP during different solar cycle phases

Previous studies have verified that ENSO plays an important role in TC genesis frequency in the SEWNP and NWWNP (Lander, 1994; Chen et al., 1998; Wang and Chan, 2002; Elsner and Liu, 2003; Chu, 2004; Camargo et al., 2007; Kim et al., 2011; Zhan et al., 2011; Song et al., 2022). The researchers suggested that El Niño contributes to the increase of TC genesis frequency in the SEWNP and the decrease in the NWWNP, while the effect of La Niña is roughly opposite. We calculated the correlation coefficient again and found a highly strong correlation between TC genesis frequency in the SEWNP and Niño3.4 index in JJASON during 1965–2019, with a value of 0.74 at the 99% confidence level. The TC genesis frequency in the NWWNP has a significant negative correlation with Niño3.4 index, with a value of −0.41 at the 99% confidence level. These results are consistent with the previous findings. Then what are the relationships between the SSN index and TC genesis frequency in the SEWNP and NWWNP on the decadal time scale? As demonstrated in the lead-lag correlation on the decadal time scale, TC genesis frequency in the SEWNP has a significant positive correlation with the SSN index in the leading 1–3 years (Table 2). When the SSN index leads 2–3 years, the correlation coefficients of 0.77 and 0.75 are the largest, both at the 99% confidence level. In addition, no obvious correlations are found between the TC genesis frequency in the NWWNP and the SSN index in the leading 1–3 years. In consequence, the relationship between the SSN index and TC genesis frequency in the SEWNP is different from that in the NWWNP, meaning that the declining phase of solar cycle only favors increasing TC genesis frequency in the SEWNP. It is unlike El Niño, which also has an impact on the TC genesis frequency in the NWWNP.

According to the above analysis, the TC genesis frequency in the SEWNP has a significant positive correlation with the SSN index on the decadal time scale. Furthermore, the decadal variance contribution of the TC genesis frequency in the SEWNP is large, so can the influence of ENSO on TC genesis frequency in the SEWNP be modulated by the solar activity? The previous studies

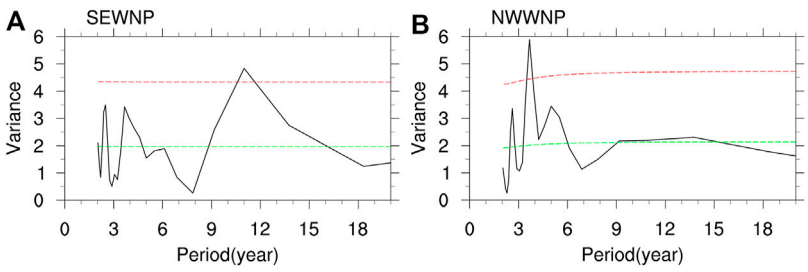

FIGURE 3
Power spectrum analysis of TC genesis frequency in the **(A)** SEWNP and **(B)** NWWNP. The green line indicates the red noise spectrum and the red line denotes statistical significance at the 95% confidence level.

TABLE 2 Correlation coefficients of TC genesis frequency in the SEWNP with the SSN index in the leading 0–3 years on the decadal time scale in JJASON during 1965–2019. * (***) denotes the 90% (99%) confidence level.

Leading 0 year	Leading 1 year	Leading 2 years	Leading 3 years
0.2	0.57*	0.77***	0.75***

TABLE 3 Mean standardized TC genesis frequency in the SEWNP in El Niño and La Niña years during different solar cycle phases from 1965 to 2019. ** (***) denotes the 95% (99%) confidence level.

	1 year following the solar maximum or minimum	2 years following the solar maximum or minimum	3 years following the solar maximum or minimum
El Niño during declining phases of solar cycle	+1.1***	+1.0**	+1.3***
El Niño during ascending phases of solar cycle	+0.6	+0.5	+0.3
La Niña during declining phases of solar cycle	−0.4	0	−0.3
La Niña during ascending phases of solar cycle	−0.9***	−1.2***	−1.2***

TABLE 4 Standardized TC genesis frequency in the SEWNP during ENSO in the 3 years following the solar maximum and solar minimum from 1965 to 2019.

	3 years following the solar maximum (1967–1970, 1978–1982, 1988–1992, 1998–2003, 2011–2015)	3 years following the solar minimum (1965–1966, 1971–1977, 1983–1987, 1993–1997, 2004–2010, 2016–2019)
El Niño (16 years)	1972(+2.2), 1982(+1.5), 1991(+0.8), 1994(+2.1), 2002(+1.4), 2004(+1.4), 2006(−0.1), 2015(+1.2)	1968(+1.3), 1969(−1.1), 1976(+0.2), 1977(−1.0), 1986(+0.4), 1987(+0.8), 1997(+1.3), 2009(+0.7)
La Niña (16 years)	1970(−0.7), 1971(+0.2), 1973(−1.0), 1984(+1.1), 1985(−0.8), 1995(−0.7), 2007(−0.9), 2016(0)	1974(−1.4), 1975(−1.4), 1988(−1.2), 1998(−1.4), 1999(−1.4), 2000(−1.0), 2010(−0.9), 2011(−1.2)

indicated that the influence of solar activity on the tropical Pacific SST lags for more than 1 year (Huo and Xiao, 2016, 2017), and TC genesis frequency in the SEWNP is significantly related to the SSN index in the leading 1–3 years. Thus, the following study focuses mainly on the situation of the SSN index in the leading 1–3 years in detail. As described in Part 2 of this study, the declining (ascending) phase of solar cycle is defined as the 1–3 years following the solar maximum (minimum). During declining phases of solar cycle, El Niño events are associated with significantly strong positive TC genesis frequency anomalies in the SEWNP. It tends to occur in extreme value, and the standardized anomalies exceed +1.0 in the overwhelming majority of El Niño years. TCs in the SEWNP are more numerous, with the mean of +1.1, +1.0, and +1.3 in the 1–3 years following the solar maximum, passing the 95% or 99% confidence level, respectively (Table 3). During ascending phases of solar cycle, there are negative or relatively weak positive TC genesis frequency anomalies in the SEWNP in El Niño years, and the mean of +0.6, +0.5, and +0.3 are all not significant. On the contrary, in La Niña years, there are generally obviously fewer TCs and the average anomalies are −0.9, −1.2, and −1.2 at the 99% confidence level in the 1–3 years following the solar minimum. However, in La Niña years during declining phases of solar cycle, there are nearly half more-TC years and the average negative anomalies of −0.4, 0, and −0.3 are all weak.

For the combined impact of ENSO and solar cycle phases, it is the most obvious in the 3 years following the solar maximum and minimum, so take this as an example to show the detailed anomalous TC genesis frequency in the SEWNP (Table 4). As can be seen, during El Niño in the 3 years following the solar maximum, TC genesis frequency anomalies are greater than or equal to +0.8 in all years, except 2006 when it is only −0.1. As a result, the positive anomalies are quite high. However, during El Niño in the 3 years following the solar minimum, TC genesis frequency anomalies are smaller than −1.0 for 2 years, and weak positive anomalies also appear for 2 years in all 8 years. Similarly, La Niña events are associated with all the negative TC genesis frequency anomalies smaller than or equal to −0.9 in the 3 years following the solar minimum, while this feature is weak in the 3 years following the solar maximum. To sum up, with regards to the TC genesis frequency in the SEWNP influenced by ENSO, solar activity is an important modulation in the decadal background. In El Niño (La Niña) years during declining (ascending) phases of solar cycle, there are significantly strong positive (negative) TC genesis frequency anomalies in the SEWNP, which may be synergistic. Resulting from the opposite effect of El Niño (La Niña) and ascending (declining) phases of solar cycle, TC genesis frequency anomalies in the SEWNP have no significant feature.

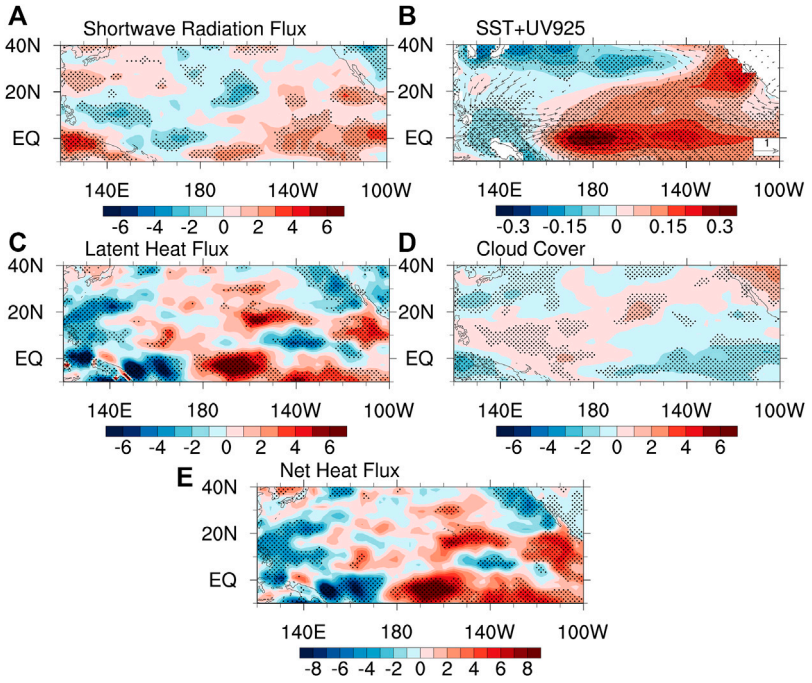

FIGURE 4
Regression of **(A)** shortwave radiation flux anomalies (units: W m^{-2}), **(B)** SST anomalies (shaded; units: °C) and wind anomalies at 925 hPa (vector; units: m s^{-1}; vectors denote statistical significance at the 95% confidence level), **(C)** latent heat flux anomalies (units: W m^{-2}), **(D)** cloud cover anomalies (units: %), and **(E)** net heat flux anomalies (units: W m^{-2}) in the lagging 2 years onto the SSN index on the decadal time scale. Dots indicate statistical significance at the 95% confidence level.

Although there is no significant lead-lag relationship between TC genesis frequency in the NWWNP and the SSN index on the decadal time scale, it is hard to judge whether solar activity modulates the effect of ENSO on the TC genesis frequency in the NWWNP or not. It is essential to carry out statistical analysis in detail. In El Niño years during ascending phases of solar cycle, the TCs in the NWWNP are significantly reduced. However, the effects of El Niño and ascending phases of solar cycle are out of phase, so TC genesis frequency in the NWWNP is dominated by El Niño, which is less modulated by ascending phases of solar cycle. In addition, the TC genesis frequency anomalies in the NWWNP are all not significant in the combined effects of La Niña and ascending or declining phases of solar cycle. Consequently, the modulation of ENSO's influence on the TC genesis frequency in the NWWNP by solar activity is little.

3.3 Physical mechanism for the solar activity to modulate the effect of ENSO on TC genesis frequency in the SEWNP

According to the previous studies, the solar activity has an effect on the anomalous SST in the central equatorial Pacific (Huo and Xiao, 2016, 2017; Kodera et al., 2016; Huo et al., 2021; Lin et al., 2021), so the SST in the central equatorial Pacific may be the key modulated by solar activity in the influencing process of ENSO on TC genesis frequency in the SEWNP. To explain it, the anomalous SST, cloud cover, and surface heat fluxes in the 1–3 years following the solar activity are regressed onto the SSN index on the decadal time scale (Figure 4), which are primarily alike from the lagging 1 year to the lagging 3 years. The downward (upward) surface heat flux is defined as the positive (negative). During the declining phases of solar cycle, the negative shortwave radiation flux anomalies appear in the western equatorial Pacific and positive anomalies in the central-eastern equatorial Pacific (Figure 4A), which contributes to the negative and positive SST anomalies in the western and central-eastern equatorial Pacific, respectively (Figure 4B). It is well known that the shortwave radiation flux is dominantly controlled by the cloud cover. The distribution of the cloud cover anomalies is also essentially in agreement with that of the shortwave radiation flux anomalies in the equatorial Pacific (Figure 4D). Meanwhile, the westerly wind anomalies over the central equatorial Pacific on account of the zonal SST anomalies gradient reduce the climatological trade winds, which reduces the surface evaporation and upward latent heat flux (Figure 4C). Besides, the longwave radiation flux anomalies are negative and sensible heat flux anomalies are positive in the central equatorial Pacific (Figure omitted). Thus, the positive net heat flux anomalies (Figure 4E) contribute to the warm SST anomalies in the central equatorial Pacific. In consequence, by means of the direct radiative effect of solar activity and wind-evaporation-SST feedback, the declining phases of the solar cycle cause warm SST anomalies in the central equatorial Pacific, which verifies the findings of Huo and Xiao (2017) and Huo et al. (2021).

Then how does the solar activity modulate the effect of ENSO on TC genesis frequency in the SEWNP through anomalous

10.3389/feart.2023.1139699

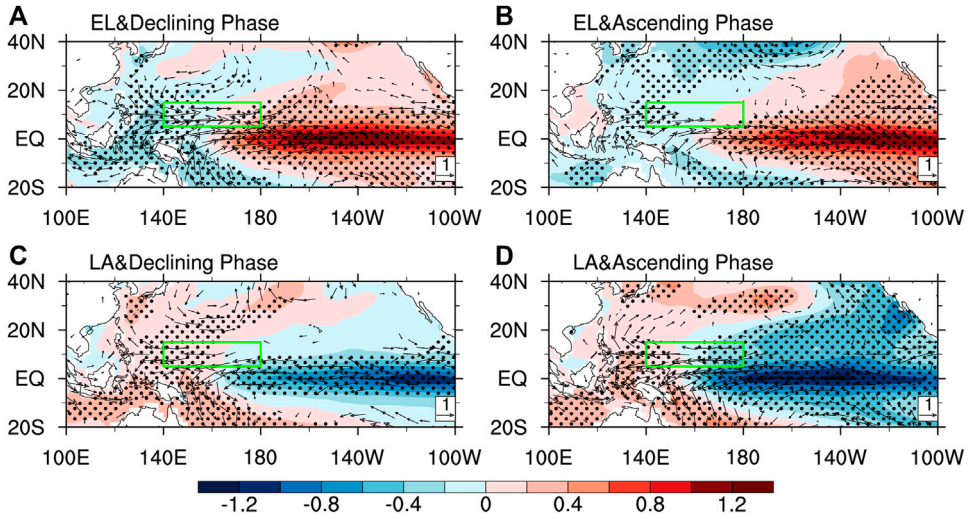

FIGURE 5
Composite SST anomalies (shaded; units: °C) and wind anomalies at 925 hPa (vector; units: m s^{-1}) in JJASON in **(A)**, **(B)** El Niño and **(C)**, **(D)** La Niña years during different solar cycle phases. Dots (vectors) indicate SST (wind) anomalies are significant at the 99% confidence level.

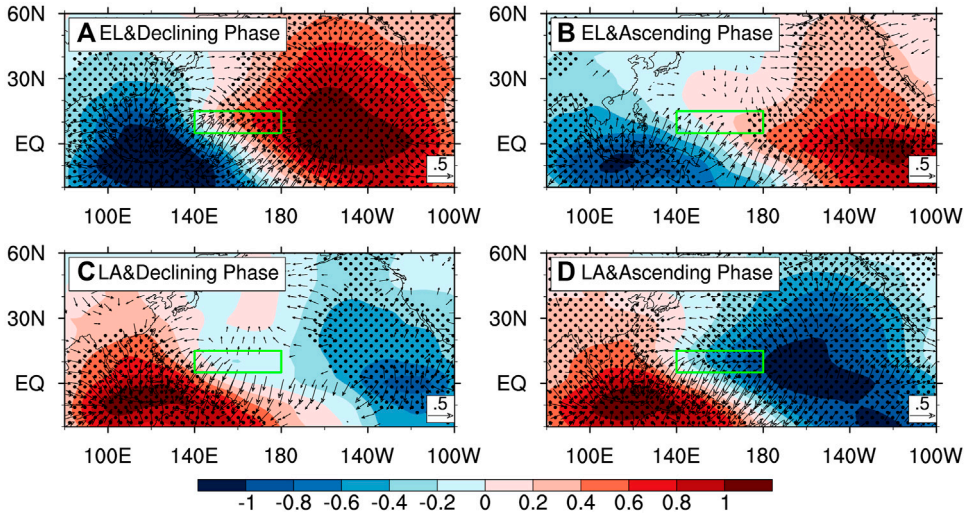

FIGURE 6
Composite velocity potential anomalies (shaded; units: 10^6 m^2 s^{-1}) and divergent wind anomalies at 925 hPa (vector; units: m s^{-1}) in JJASON in **(A)**, **(B)** El Niño and **(C)**, **(D)** La Niña years during different solar cycle phases. Dots (vectors) indicate velocity potential (divergent wind) anomalies are significant at the 99% confidence level.

atmospheric circulation? Because the distributions of anomalous SST and atmospheric variables during ENSO in the 1–3 years following the solar maximum or solar minimum are basically similar, the physical fields from the following 1 year to the following 3 years are averagely composited. As shown in the composited SST and wind anomalies at 925 hPa (Figures 5A, B), owing to the effect of solar cycle phases, compared to El Niño during ascending phases of solar cycle, there are apparently warmer SST anomalies in the central equatorial Pacific and colder SST anomalies in the western Pacific in El Niño years during declining phases of solar cycle, along with the stronger SST gradient anomalies between the central equatorial Pacific and western Pacific. Therefore, the overlapping of declining phases of solar cycle and El Niño possibly enhances the low-level westerly wind anomalies in the SEWNP, where the upper-level easterly wind anomalies are also stronger. In the climatological mean, the SEWNP is dominated by the easterly wind at low levels, while dominated by the westerly wind at eastern high levels and the easterly wind at western high levels. As a result, the vertical wind shear between 200 hPa and 850 hPa in the eastern SEWNP is further reduced, which is more favorable for TC genesis

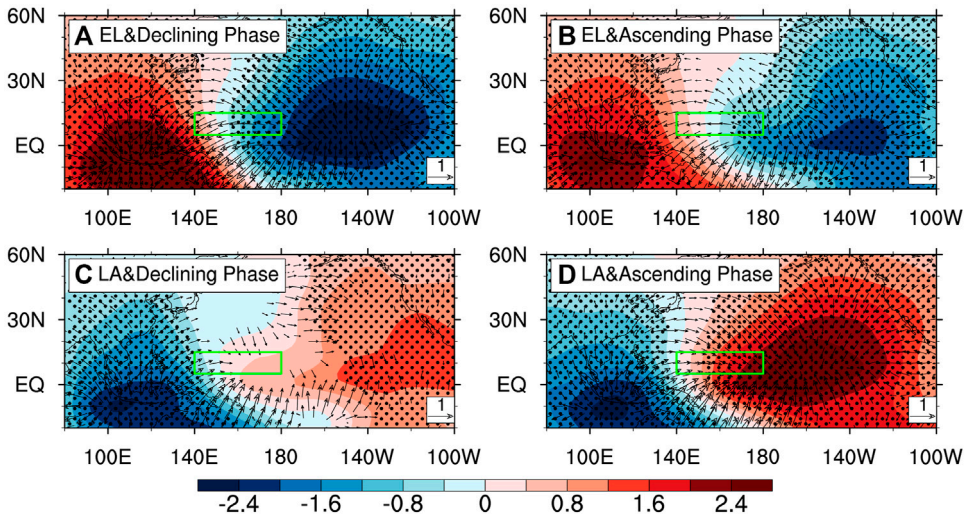

FIGURE 7
Composite velocity potential anomalies (shaded; units: 10^6 m^2 s^{-1}) and divergent wind anomalies at 200 hPa (vector; units: m s^{-1}) in JJASON in **(A)**, **(B)** El Niño and **(C)**, **(D)** La Niña years during different solar cycle phases. Dots (vectors) indicate velocity potential (divergent wind) anomalies are significant at the 99% confidence level.

in the eastern SEWNP. Additionally, it can be seen in the low-level velocity potential and divergent wind anomalies (Figures 6A, B) that a stronger and more westward convergence center exists in the Pacific in the combined effect of El Niño and declining phases of solar cycle, which is conducive to the stronger low-level convergent flow and high-level divergent flow anomalies in the SEWNP (Figures 7A, B). Correspondingly, the ascending movement and convection anomalies are strengthened, leading to more TCs in the SEWNP.

Compared to the declining phases of solar cycle, La Niña brings the obviously colder SST anomalies in the central equatorial Pacific and warmer SST anomalies in the western Pacific during ascending phases of solar cycle (Figures 5C, D). As a result, the SST anomalies gradient are stronger and low-level easterly wind and upper-level westerly anomalies are also stronger in the SEWNP. It further increases the vertical wind shear between 200 hPa and 850 hPa in most parts of the SEWNP, resulting in the further suppression of TC genesis. In La Niña years during ascending phases of solar cycle, the low-level divergent and high-level convergent flow anomalies in the SEWNP become more pronounced (Figures 6C, 6D, 7C, 7D) and the descending movement anomalies become more enhanced, accompanied with weaker humidity and convection, which suppress TC genesis in the SEWNP in further.

The vertical wind shear, low-level vorticity, and middle-level relative humidity are three important environment factors for TC genesis (Gao et al., 2018; Liu and Chan, 2018). In El Niño years during declining phases of solar cycle, the warmer SST anomalies in the central equatorial Pacific induce a stronger Rossby wave response in the northwest compared to the ascending phases of solar cycle, causing the stronger cyclonic circulation anomalies. As a result, the positive low-level relative vorticity anomalies are further intensified in the SEWNP (Figures 8A, B), which is beneficial to more TCs. It exhibits different characteristics of the vertical wind shear anomalies in the eastern and western SEWNP, that is the stronger positive anomalies are in the western SEWNP, while the stronger negative anomalies are in the eastern SEWNP (Figures 8E, F). Thus, the vertical wind shear favors TC genesis in the eastern SEWNP and suppresses TC genesis in the western SEWNP. In terms of middle-level relative humidity, during declining phases of solar cycle, El Niño events are associated with stronger positive relative humidity anomalies in most parts of the SEWNP compared to the ascending phases of solar cycle (Figures 8I, J). It is more favorable for TC genesis and leads to higher TC genesis frequency in the SEWNP. In La Niña years during ascending phases of solar cycle, the negative relative vorticity anomalies are stronger in the SEWNP (Figures 6C, D), and the positive vertical wind shear anomalies (Figures 8G, H) and the negative relative humidity anomalies (Figures 8K, L) are also stronger in most parts of the SEWNP compared to the declining phases of solar cycle. These environment conditions further inhibit TC genesis, resulting in the lower TC genesis frequency in the SEWNP.

To ascertain which environmental factor plays a dominant role in TC genesis, the GPI is employed to quantitatively diagnose the relative contributions of environmental factors to TC genesis in the SEWNP. The detailed calculation method of the anomalous GPI is described in Part 2 of this study, which consists of the low-level absolute vorticity, vertical wind shear between 200 hPa and 850 hPa, mid-level relative humidity, and PI terms. Cao et al. (2022) pointed out that absolute vorticity contributes the most to the GPI anomalies in the SEWNP, along with the secondary contribution of relative humidity and vertical wind shear terms. How is it in our study? On account of the overlapping effect of the declining (ascending) phases of solar cycle and El Niño (La Niña), the regional averages of the four terms in the SEWNP are composited in El Niño (La Niña) years during declining (ascending) phases of solar cycle (Figure 9). As shown in Figure 9A, the positive GPI anomalies appear in the SEWNP, corresponding to the increase of TC genesis frequency in El Niño years during declining phases of solar cycle. The absolute vorticity term makes the largest contribution to the GPI anomalies, and it is obviously much larger than the other terms. The

10.3389/feart.2023.1139699

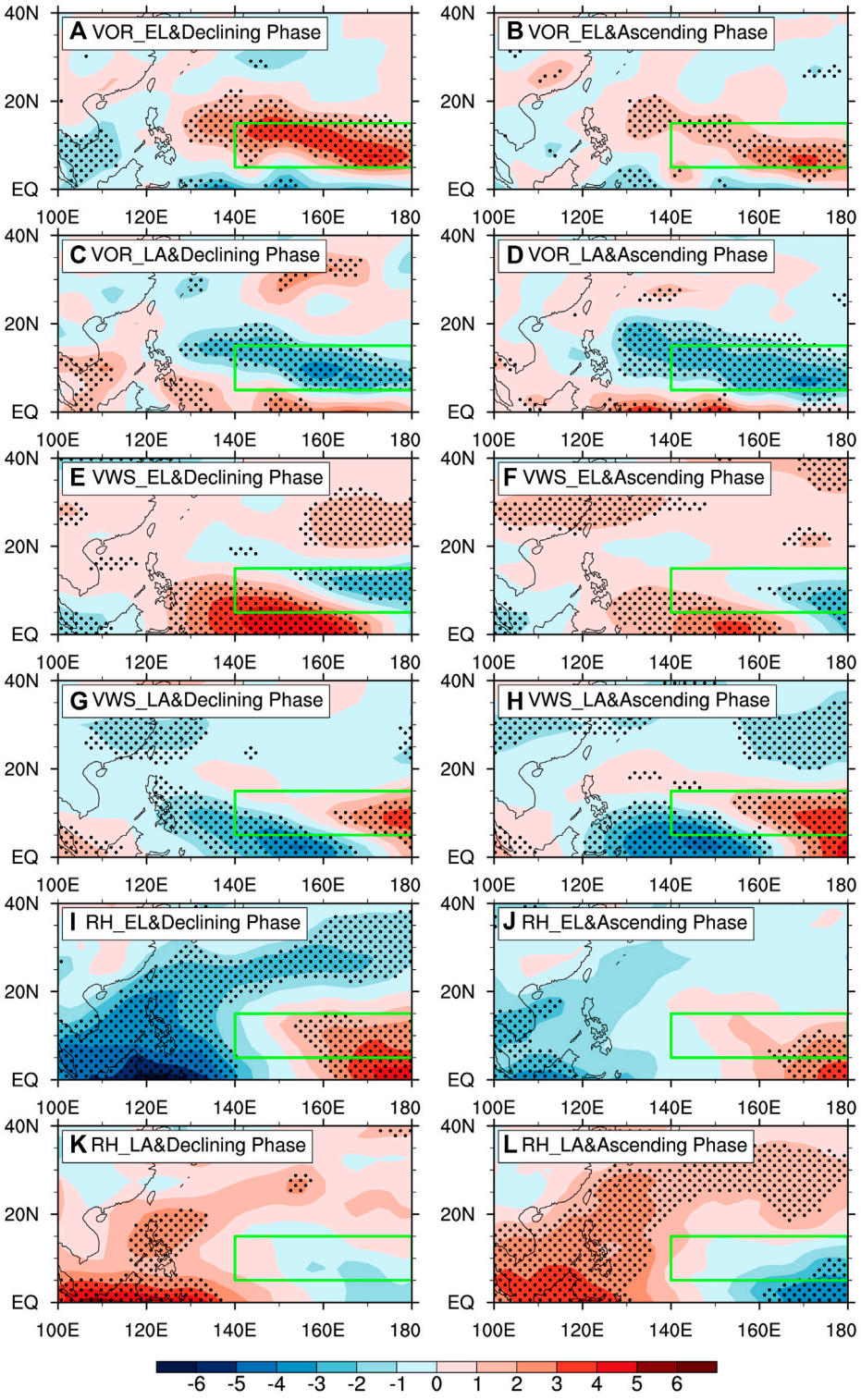

FIGURE 8
Composite **(A–D)** relative vorticity anomalies (units: 10^{-6} s^{-1}), **(E–H)** vertical wind shear anomalies between 200 hPa and 850 hPa (units: m s^{-1}), and **(I–L)** relative humidity anomalies at 600 hPa (units: %) in JJASON during ENSO in different solar cycle phases. Dots indicate statistical significance at the 99% confidence level.

contributions of the other terms are different in El Niño years during declining phases of solar cycle. The second largest contribution is the vertical wind shear term in the 1 year following the solar maximum, and the relative humidity term in the 2–3 years following the solar maximum. In conclusion, the absolute vorticity term plays a leading role in the GPI anomalies, whose contribution is obviously much

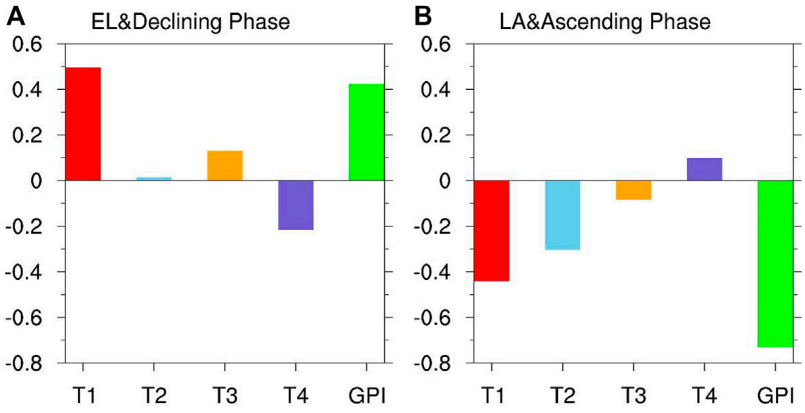

FIGURE 9
Composite regional mean absolute vorticity term (T1), vertical wind shear term (T2), relative humidity term (T3), potential intensity term (T4), and GPI anomalies in the SEWNP in **(A)** El Niño years during declining phases of solar cycle and **(B)** La Niña years during ascending phases of solar cycle.

larger than the other terms. In the meanwhile, it is not perfectly symmetrical with the combined effect of La Niña and ascending phases of solar cycle. During this period, the negative GPI anomalies are accordant to the decrease in TC genesis frequency (Figure 9B). The absolute vorticity term makes the largest contribution to the GPI anomalies and the second largestt contribution is the vertical wind shear term. It is different from that in El Niño during declining phases of solar cycle because the vertical wind shear term is also important. The above conclusions are basically consistent with the analysis in Figure 8.

4 Summary and discussion

Previous studies have suggested that ENSO has an important impact on the TC genesis frequency in the SEWNP and NWWNP (Lander, 1994; Chen et al., 1998; Wang and Chan, 2002; Elsner and Liu, 2003; Chu, 2004; Camargo et al., 2007; Kim et al., 2011; Zhan et al., 2011; Song et al., 2022). However, few studies have focused on the influence of solar activity on TC genesis frequency in the WNP. In this study, the combined effect of solar activity and ENSO on the TC genesis frequency in the SEWNP during JJASON from 1965 to 2019 has been primarily investigated. The results indicate that as for the four subregions in the WNP, TCs generated in the SEWNP have the longest lifetime and greatest strength, with an average lifetime of 202.7 h and an average annual ACE of 2×10^5 m^2 s^{-2}, far larger than that in the other subregions in the WNP. The overwhelming majority of TCs generated in the SEWNP reach typhoon intensity and super typhoons accounting for 62% of the total number. Additionally, The TC genesis frequency in the SEWNP has apparent interannual and decadal variations, reflecting both the interannual influencing factors and decadal background factors.

The lead-lag correlation shows that TC genesis frequency in the SEWNP has a significant positive correlation with the SSN index in the leading 1–3 years on the decadal time scale, and it is the largest when the SSN index leads 2–3 years. However, no significant correlations are found between the TC genesis frequency in the NWWNP and the SSN index in the leading 1–3 years. Further analysis indicates that the effect of ENSO on TC genesis frequency in the SEWNP is modulated by the decadal background of the solar activity. In El Niño (La Niña) years during declining (ascending) phases of solar cycle, there are significantly strong positive (negative) TC genesis frequency anomalies in the SEWNP, which tends to occur in extreme value. Resulting from the opposite effect of El Niño (La Niña) and ascending (declining) phases of solar cycle, TC genesis frequency anomalies in the SEWNP have no significant feature.

For El Niño (La Niña) modulated by declining (ascending) phases of solar cycle, the overlapping effect leads to apparently warmer (colder) SST anomalies in the central equatorial Pacific and colder (warmer) SST anomalies in the western Pacific, along with the stronger SST anomalies gradient between the central (western) equatorial Pacific and western (central) equatorial Pacific. It enhances low-level westerly (easterly) wind anomalies and upper-level easterly (westerly) wind anomalies, which is favorable for the further decrease (increase) of vertical wind shear between 200 hPa and 850 hPa in the eastern (most) parts of SEWNP. Moreover, there exists a stronger and more westerly low-level convergence (divergence) center in the Pacific, resulting in stronger low-level convergent (divergent) flow and high-level divergent (convergent) flow anomalies in the SEWNP. Correspondingly, the ascending movement and convection anomalies are strengthened (suppressed). As a result, more (fewer) TCs generate in the SEWNP.

The TC genesis factors including vertical wind shear, low-level vorticity, and middle-level relative humidity are examined. In El Niño years during declining phases of solar cycle, the stronger cyclonic circulation anomalies bring about the stronger positive low-level vorticity anomalies in the SEWNP, which is beneficial to more TCs. The stronger positive vertical wind shear anomalies appear in the western SEWNP, while the stronger negative anomalies are in the eastern SEWNP. El Niño events are associated with stronger positive middle-level relative humidity anomalies in most parts of the SEWNP. In La Niña years during ascending phases of solar cycle, the negative vorticity anomalies, positive vertical wind shear anomalies, and negative relative humidity anomalies are stronger in most parts of the SEWNP, resulting in the lower TC genesis frequency in the SEWNP.

The relative contributions of environmental factors to TC genesis in the SEWNP are further quantitatively diagnosed by the GPI. The major characteristic in the combined effect of El Niño and declining phases of solar cycle is different from that in the combined effect of La Niña and ascending phases of solar cycle. During El Niño years in declining phases of solar cycle, the absolute vorticity plays a leading role in the GPI anomalies, whose contribution is obviously much greater than other terms. In La Niña during ascending phases of solar cycle, the absolute vorticity term has the greatest contribution to GPI anomalies, but the vertical wind shear is also important, which is secondary.

In this study, the combined effect of solar activity and ENSO on the TC genesis frequency in the SEWNP is primarily investigated. It helps us to make better forecasts for the TC genesis frequency in the SEWNP. However, the influence of solar activity on the TC genesis frequency in the other subregions of WNP is unknown. Especially, the feature of TC genesis in the South China Sea is different from that in the WNP, how is the combined effect of solar activity and ENSO? The questions deserve to be carried out in the following work.

Data availability statement

The TC best-track data from the CMA can be found from http://tcdata.typhoon.org.cn/dlrdqx_sm.html. The NCEP/NCAR reanalysis data and ERSST.v5 sea surface temperature data are available at https://www.psl.noaa.gov/data/gridded/. The SSN index can be accessed via http://www.sidc.be/silso/datafiles. The Niño3.4 index can be downloaded from https://www.cpc.ncep.noaa.gov/data/indices/ersst5.nino.mth.81-10.ascii.

Author contributions

ShL and ZL contributed to conception and design of the study. SiL calculated the GPI index. ShL wrote the first draft of the manuscript. All authors contributed to the revision of the manuscript.

Funding

This work was supported by the National Key Basic Research and Development Program of China (2012CB957800) and the National Natural Science Foundation of China (U1902209).

Conflict of interest

The authors declare that the research was conducted in the absence of any commercial or financial relationships that could be construed as a potential conflict of interest.

Publisher's note

All claims expressed in this article are solely those of the authors and do not necessarily represent those of their affiliated organizations, or those of the publisher, the editors and the reviewers. Any product that may be evaluated in this article, or claim that may be made by its manufacturer, is not guaranteed or endorsed by the publisher.

References

Bister, M., and Emanuel, K. A. (2002). Low frequency variability of tropical cyclone potential intensity 1. Interannual to interdecadal variability. *J. Geophys. Res. Atmos.* 107, D24. doi:10.1029/2001JD000776

Camargo, S. J., Emanuel, K. A., and Sobel, A. H. (2007). Use of a Genesis potential index to diagnose ENSO effects on tropical cyclone Genesis. *J. Clim.* 20, 4819–4834. doi:10.1175/JCLI4282.1

Camargo, S. J., and Sobel, A. H. (2005). Western North Pacific tropical cyclone intensity and ENSO. *J. Clim.* 18, 2996–3006. doi:10.1175/JCLI3457.1

Cao, X., Wu, R., Xu, J., Sun, Y., Bi, M., Dai, Y., et al. (2022). Coherent variations of tropical cyclogenesis over the North Pacific and North Atlantic. *Clim. Dyn.* doi:10.1007/s00382-022-06381-3

Chan, J. C. L. (1985). Tropical cyclone activity in the northwest pacific in relation to the El niño/southern oscillation phenomenon. *Mon. Weather Rev.* 113, 599–606. doi:10.1175/1520-0493(1985)113<0599:TCAITN>2.0.CO;2

Chan, J. C. L. (2000). Tropical cyclone activity over the Western North Pacific associated with El nino and La nina events. *J. Clim.* 13, 2960–2972. doi:10.1175/1520-0442(2000)013<2960:TCAOTW>2.0.CO;2

Chan, J. C. L. (2005). Interannual and interdecadal variations of tropical cyclone activity over the Western North Pacific. *Meteorol. Atmos. Phys.* 89, 143–152. doi:10.1007/s00703-005-0126-y

Chen, T. C., Weng, S. P., Yamazaki, N., and Kiehne, S. (1998). Interannual variation in the tropical cyclone formation over the Western North Pacific. *Mon. Weather Rev.* 126, 1080–1090. doi:10.1175/1520-0493(1998)126<1080:IVITTC>2.0.CO;2

Chen, X., Zhong, Z., and Lu, W. (2017). Association of the poleward shift of East Asian subtropical upper-level jet with frequent tropical cyclone activities over the Western North Pacific in summer. *J. Clim.* 30, 5597–5603. doi:10.1175/JCLI-D-16-0334.1

Chu, P. S. (2004). "ENSO and tropical cyclone activity," in *Hurricanes and typhoons, past, Present and future*. Editors R. J. Murnane and K. B. Liu (Columbia University Press), 297–332.

Elsner, J. B., and Liu, K. B. (2003). Examining the ENSO-typhoon hypothesis. *Clim. Res.* 25, 43–54. doi:10.3354/cr025043

Emanuel, K. A., and Nolan, D. S. (2004). "Tropical cyclone activity and the global climate system," in *Preprints, 26th conf. On hurricanes and tropical meteorology* (Miami, FL: Amer. Meteor. Soc.), 10A.2.

Enfield, D. B., and Cid, L. S. (1991). Low-frequency changes in El nino-southern oscillation. *J. Clim.* 4, 1137–1146. doi:10.1175/1520-0442(1991)004<1137:LFCIEN>2.0.CO;2

Gao, S., Chen, Z., and Zhang, W. (2018). Impacts of tropical North Atlantic SST on western North Pacific landfalling tropical cyclones. *J. Clim.* 31, 853–862. doi:10.1175/JCLI-D-17-0325.1

Gray, L. J., Beer, J., Geller, M., Haigh, J. D., Lockwood, M., Matthes, K., et al. (2010). Solar influences on climate. *Rev. Geophys.* 48. doi:10.1029/2009RG000282

Herschel, W. (1801). Observations tending to investigate the nature of the sun, in order to find the causes or symptoms of its variable emission of light and heat: With remarks on the use that may possibly be drawn from solar observations. *Phil. Trans. Roy. Soc. Lond.* 91, 265–318. doi:10.1098/rstl.1801.0015

Huang, B., Thorne, P. W., Banzon, V. F., Boyer, T., Chepurin, G., Lawrimore, J. H., et al. (2017). Extended reconstructed Sea surface temperature, Version 5 (ERSSTv5): Upgrades, validations, and intercomparisons. *J. Clim.* 30, 8179–8205. doi:10.1175/JCLI-D-16-0836.1

Huang, R., and Chen, G. (2007). Research on interannual variations of tracks of tropical cyclones over Northwest Pacific and their physical mechanism (in Chinese). *Acta Meteor. Sin.* 65, 683–694.

Huo, W., and Xiao, Z. (2016). The impact of solar activity on the 2015/16 El Niño event. *Atmos. Ocean. Sci. Lett.* 9, 428–435. doi:10.1080/16742834.2016.1231567

Huo, W., and Xiao, Z. (2017). Modulations of solar activity on El Niño Modoki and possible mechanisms. *J. Atmos. Solar-Terrestrial Phys.* 160, 34–47. doi:10.1016/j.jastp.2017.05.008

Huo, W., Xiao, Z., Wang, X., and Zhao, L. (2021). Lagged responses of the tropical pacific to the 11-yr solar cycle forcing and possible mechanisms. *J. Meteorol. Res.* 35, 444–459. doi:10.1007/s13351-021-0137-8

Huth, R., Pokorná, L., Bochníček, J., and Hejda, P. (2006). Solar cycle effects on modes of low-frequency circulation variability. *J. Geophys. Res. Atmos.* 111, D22107. doi:10.1029/2005JD006813

Kalnay, E., Kanamitsu, M., Kistler, R., Collins, W., Deaven, D., Gandin, L., et al. (1996). The NCEP/NCAR 40-year reanalysis project. *Bull. Amer. Meteor. Soc.* 77, 437–472. doi:10.1175/1520-0477(1996)077,0437:TNYRP.2.0.CO;2

Kim, H. M., Webster, P. J., and Curry, J. A. (2011). Modulation of North Pacific tropical cyclone activity by three phases of ENSO. *J. Clim.* 24, 1839–1849. doi:10.1175/2010JCLI3939.1

Kim, J. S., Kim, S. T., Wang, L., Wang, X., and Il Moon, Y. (2016). Tropical cyclone activity in the northwestern pacific associated with decaying central pacific El niños. *Stoch. Environ. Res. Risk Assess.* 30, 1335–1345. doi:10.1007/s00477-016-1256-0

Kodera, K., Thiéblemont, R., Yukimoto, S., and Matthes, K. (2016). How can we understand the global distribution of the solar cycle signal on the Earth's surface? *Atmos. Chem. Phys.* 16, 12925–12944. doi:10.5194/acp-16-12925-2016

Lander, M. A. (1994). An exploratory analysis of the relationship between tropical storm formation in the Western North Pacific and ENSO. *Mon. Weather Rev.* 122, 636–651. doi:10.1175/1520-0493(1994)122<0636:AEAOTR>2.0.CO;2

Li, C. (1987). A study on the influence of El Nino upon typhoon action over Western Pacific. *Acta Meteor. Sin.* 45, 229–236. (in Chinese).

Li, D., and Xiao, Z. (2018). Can solar cycle modulate the ENSO effect on the Pacific/North American pattern? *J. Atmos. Solar-Terrestrial Phys.* 167, 30–38. doi:10.1016/j.jastp.2017.10.007

Li, Z., Yu, W., Li, T., Murty, V. S. N., and Tangang, F. (2013). Bimodal character of cyclone climatology in the bay of bengal modulated by monsoon seasonal cycle. *J. Clim.* 26, 1033–1046. doi:10.1175/JCLI-D-11-00627.1

Li, H., Wang, C., He, S., Wang, H., Tu, C., Xu, J., et al. (2019). Plausible modulation of solar wind energy flux input on global tropical cyclone activity. *J. Atmos. Solar-Terrestrial Phys.* 192, 104775. doi:10.1016/j.jastp.2018.01.018

Lin, Y. F., Yu, J. Y., Wu, C. R., and Zheng, F. (2021). The footprint of the 11-year solar cycle in northeastern pacific SSTs and its influence on the central pacific El Niño. *Geophys. Res. Lett.* 48, e2020GL091369. doi:10.1029/2020GL091369

Ling, S., and Lu, R. (2022). Tropical cyclones over the western North Pacific strengthen the East asia—pacific pattern during summer. *Adv. Atmos. Sci.* 39, 249–259. doi:10.1007/s00376-021-1171-2

Liu, Z., Yoshimura, K., Buenning, N. H., and He, X. (2014). Solar cycle modulation of the Pacific-North American teleconnection influence on North American winter climate. *Environ. Res. Lett.* 9, 024004. doi:10.1088/1748-9326/9/2/024004

Liu, C., Zhang, W., Stuecker, M. F., and Jin, F. F. (2019). Pacific meridional mode-western North Pacific tropical cyclone linkage explained by tropical pacific quasi-decadal variability. *Geophys. Res. Lett.* 46, 13346–13354. doi:10.1029/2019GL085340

Liu, K. S., and Chan, J. C. L. (2018). Changing relationship between La Niña and tropical cyclone landfalling activity in South China (La Niña and TC landfalling activity in South China). *Int. J. Climatol.* 38, 1270–1284. doi:10.1002/joc.5242

Lu, X., Yu, H., Ying, M., Zhao, B., Zhang, S., Lin, L., et al. (2021). Western North pacific tropical cyclone database created by the China meteorological administration. *Adv. Atmos. Sci.* 38, 690–699. doi:10.1007/s00376-020-0211-7

Ma, H., Wang, R., Lai, A., Li, X., Wang, F., Zhou, Z., et al. (2021). Solar activity modulates the El Niño-Southern Oscillation-induced precipitation anomalies over southern China in early spring. *Int. J. Climatol.* 41, 6589–6601. doi:10.1002/joc.7214

Meehl, G. A., Arblaster, J. M., Branstator, G., and van Loon, H. (2008). A coupled air-sea response mechanism to solar forcing in the Pacific region. *J. Clim.* 21, 2883–2897. doi:10.1175/2007JCLI1776.1

Pan, Y. (1982). The effect of the thermal state of equatorial eastern Pacific on the frequency of typhoons over Western Pacific (in Chinese). *Acta Meteor. Sin.* 40, 24–34.

Ren, S., Liu, Y., and Wu, G. (2007). Interactions between typhoon and subtropical anticyclone over Western Pacific revealed by numerical experiments (in Chinese). *Acta Meteor. Sin.* 65, 329–340. doi:10.11676/qxxb2007.032

Shan, K., and Yu, X. (2021). Variability of tropical cyclone landfalls in China. *J. Clim.* 34, 9235–9247. doi:10.1175/JCLI-D-21-0031.1

Song, J., Klotzbach, P. J., Wang, Y. F., and Duan, Y. (2022). Influence of different La Niña decay types on tropical cyclone Genesis over the Western North Pacific. *Atmos. Res.* 280, 106419. doi:10.1016/j.atmosres.2022.106419

Wang, B., and Chan, J. C. L. (2002). How strong ENSO events affect tropical storm activity over the Western North Pacific. *J. Clim.* 15, 1643–1658. doi:10.1175/1520-0442(2002)015<1643:HSEEAT>2.0.CO;2

Wang, X., Zhou, W., Li, C., and Wang, D. (2014). Comparison of the impact of two types of El Niño on tropical cyclone Genesis over the South China Sea. *Int. J. Climatol.* 34, 2651–2660. doi:10.1002/joc.3865

Wang, Q., Li, J., Jin, F. F., Chan, J. C. L., Wang, C., Ding, R., et al. (2019). Tropical cyclones act to intensify El Niño. *Nat. Commun.* 10, 3793. doi:10.1038/s41467-019-11720-w

Wang, R., Ma, H., Xiao, Z., Li, X., Gao, C., Gao, Y., et al. (2021). The combined effects of ENSO and solar activity on mid-winter precipitation anomalies over southern China. *Front. Earth Sci.* 9, 1–15. doi:10.3389/feart.2021.771234

Woodruff, J. D., Irish, J. L., and Camargo, S. J. (2013). Coastal flooding by tropical cyclones and sea-level rise. *Nature* 504, 44–52. doi:10.1038/nature12855

Xue, X., Chen, W., and Zhou, Q. (2020). Solar cycle modulation of the connection between boreal winter ENSO and following summer South Asia high. *J. Atmos. Solar-Terrestrial Phys.* 211, 105466. doi:10.1016/j.jastp.2020.105466

Yan, H., Zhong, M., and Zhu, Y. (2004). Determination of the degree of freedom of digital filtered time series with an application to the correlation analysis between the length of day and the Southern Oscillation index. *Chin. Astron. Astrophys.* 28, 120–126. doi:10.1016/S0275-1062(04)90014-8

Ying, M., Zhang, W., Yu, H., Lu, X., Feng, J., Fan, Y. X., et al. (2014). An overview of the China meteorological administration tropical cyclone database. *J. Atmos. Ocean. Technol.* 31, 287–301. doi:10.1175/JTECH-D-12-00119.1

Yu, M., Zhu, C., and Jiang, N. (2019). Subseasonal mode of cold and wet climate in South China during the cold season: A climatological view. *Atmos. Ocean. Sci. Lett.* 12, 73–79. doi:10.1080/16742834.2019.1568164

Zhan, R., Wang, Y., and Lei, X. (2011). Contributions of ENSO and East Indian ocean SSTA to the interannual variability of northwest pacific tropical cyclone frequency. *J. Clim.* 24, 509–521. doi:10.1175/2010JCLI3808.1

Zhang, W., Vecchi, G. A., Villarini, G., Murakami, H., Rosati, A., Yang, X., et al. (2017). Modulation of Western North Pacific tropical cyclone activity by the atlantic meridional mode. *Clim. Dyn.* 48, 631–647. doi:10.1007/s00382-016-3099-2

Zhao, H., and Wang, C. (2019). On the relationship between ENSO and tropical cyclones in the Western North Pacific during the boreal summer. *Clim. Dyn.* 52, 275–288. doi:10.1007/s00382-018-4136-0

Zhong, Z. (2006). A possible cause of a regional climate model's failure in simulating the east Asian summer monsoon. *Geophys. Res. Lett.* 33, L24707. doi:10.1029/2006GL027654

Zhong, Z., and Hu, Y. (2007). Impacts of tropical cyclones on the regional climate: An East Asian summer monsoon case. *Atmos. Sci. Lett.* 8, 93–99. doi:10.1002/asl.158

Zhou, Q., Chen, W., and Zhou, W. (2013). Solar cycle modulation of the ENSO impact on the winter climate of East Asia. *J. Geophys. Res. Atmos.* 118, 5111–5119. doi:10.1002/jgrd.50453

frontiers | Frontiers in Earth Science

TYPE Original Research
PUBLISHED 15 March 2023
DOI 10.3389/feart.2023.1147582

OPEN ACCESS

EDITED BY
Shangfeng Chen,
Institute of Atmospheric Physics (CAS), China

REVIEWED BY
Gang Zeng,
Nanjing University of Information Science and Technology, China
Cai Qingyu,
Yunnan University, China
Tianjiao Ma,
Institute of Atmospheric Physics (CAS), China
Xue Xu,
Guizhou University, China

*CORRESPONDENCE
Wenjuan Huo,
whuo@geomar.de

SPECIALTY SECTION
This article was submitted to Interdisciplinary Climate Studies, a section of the journal Frontiers in Earth Science

RECEIVED 18 January 2023
ACCEPTED 07 March 2023
PUBLISHED 15 March 2023

CITATION
Huo W, Xiao Z and Zhao L (2023), Modulation of the solar activity on the connection between the NAO and the tropical pacific SST variability.
Front. Earth Sci. 11:1147582.
doi: 10.3389/feart.2023.1147582

Modulation of the solar activity on the connection between the NAO and the tropical pacific SST variability

Wenjuan Huo[1,2]*, Ziniu Xiao[1] and Liang Zhao[1]

[1]State Key Laboratory of Numerical Modeling for Atmospheric Sciences and Geophysical Fluid Dynamics, Institute of Atmospheric Physics, Chinese Academy of Sciences, Beijing, China, [2]GEOMAR Helmholtz Centre for Ocean Research Kiel, Kiel, Germany

Previous studies indicated that the North Tropical Atlantic (NTA) SST can serve as a precursor for the El Niño–Southern Oscillation (ENSO) predictability and the connection of NTA-ENSO is modulated by the mid-high latitude atmospheric variability. Despite significant solar footprints being found in the North Atlantic and tropical Pacific separately, their role in the two basins' connection is still missing. In this study, we systematically examined this point by using observational/reanalysis datasets and outputs of a pair of sensitivity experiments with and without solar forcings (SOL and NOSOL). In observations, DJF-mean NAO-like SLP anomalies have a linear covariation with the subsequent JJA-mean El Niño Modoki-like SST anomalies in the tropical Pacific in the following 1 year. This observed SLP-SST covariation shows up in the high solar activity (HS) subset and disappears in the low solar activity (LS) subset. In the HS years, positive NAO-like SLP anomalies are produced by the stronger solar-UV radiation through a "top-down" mechanism. These atmospheric anomalies can enhance the influence of the NTA on the tropical Pacific SST by triggering significant and more persistent subtropical teleconnections. Here we proposed an indirect possible mechanism that the solar-UV forcing can modulate the tropical Pacific SST variability *via* its impacts on the atmospheric anomalies over the North Atlantic region. However, based on the same analysis method, we found a different coupled mode of the SLP and SST anomalies in the modeling outputs. The SLP anomalies in the North Atlantic, with a triple pattern (negative SLP anomalies in the Pole and the NTA, positive SLP anomalies in the mid-latitude), have "lead-lag" covariations with the Eastern Pacific El Niño-like SST anomalies in both the SOL and NOSOL. Although the impact of the solar activity is found in the North Atlantic and the tropical Pacific respectively in the SOL, no solar effect is involved in the simulated SLP-SST coupled mode.

KEYWORDS

solar activity, North Atlantic Oscillation, tropical Pacific, El Niño Modoki, decadal variability

1 Introduction

The tropical Pacific sea surface temperature (SST) anomaly has a dramatic impact on the global weather and climate, its interannual variability as well as global teleconnections are dominated by an El Niño–Southern Oscillation (ENSO). An ENSO-like SST pattern is also found on the decadal timescale (Chen and Wallace, 2015). Although the interannual and

decadal variability of the tropical Pacific SST can be internally generated without any change to external forcings (Kirtman et al., 2013), its response to external forcings may modulate the internal variability (Huo and Xiao, 2017; Hua et al., 2018; Liguori and Di Lorenzo, 2018; Li et al., 2020). The solar radiative forcings, as the major energy source out of the climate system, has a significant quasi-decadal variability (e.g., 11-year solar cycle). Changes in solar radiation have significant footprints in the tropical Pacific climate system, showing a lagged warming in the tropical Pacific (Meehl and Arblaster, 2009; Misios et al., 2016; Huo and Xiao, 2017; Huo et al., 2021) and a slowdown Pacific Walker circulation (Xiao et al., 2016; Misios et al., 2019). The warm response first appears in the central equatorial Pacific (Kodera et al., 2016; Huo and Xiao, 2017) and then extends into the eastern Pacific through air-sea interactions (Misios et al., 2019; Huo et al., 2021). This warm response is suggested to confine in the ocean layers above the main thermocline (White et al., 1997; Wang et al., 2018; Huo et al., 2021) and can impact the Pacific Walker circulation through a bottom thermal control effect (Xiao et al., 2016; Misios et al., 2019; Huo et al., 2023).

Besides, the north tropical Atlantic (NTA) SST anomaly is suggested can drive the tropical Pacific SST interannual variability and modulate the ENSO variability through anomalous Walker circulation (McGregor et al., 2014; Meehl et al., 2021; Ren et al., 2021), crossing continent wind (Xie et al., 2008; Wang et al., 2009; Karnauskas, 2014), and subtropical teleconnections (Wang et al., 2009; Ham et al., 2013a; Li et al., 2016). The spring NTA cooling (warming) could trigger an El Niño (La Niña) event the following winter (Ham et al., 2013a; b; Ham and Kug, 2015; He and Ma, 2021; Jiang and Li, 2021) and therefore could serve as a potential precursor for ENSO (Martín-Rey et al., 2015). This observed NTA-ENSO connection shows a multidecadal variation, which has been attributed to the Atlantic multidecadal oscillation (Wang et al., 2017), Atlantic warming trends (Chen and Wu, 2017; Park et al., 2019), and the multidecadal variations of the North Atlantic Oscillation (NAO) (Ding et al., 2023). However, the simulated NTA-ENSO connection shows a large diversity among either ensemble members of a single climate model (Chen et al., 2022) or among multiple models (Zheng et al., 2021). This could be due to the internal variability in the North Pacific (Chen et al., 2022) and the model's ability in reproducing spring Arctic Oscillation (AO)-associated atmospheric anomalies over the subtropical North Pacific (Zheng et al., 2021). So, these previous studies imply that the atmospheric variations over the mid-high latitude (AO/NAO-like) appear to modulate the NTA-ENSO connection (Chen et al., 2017; Chen et al., 2018; Ding et al., 2023). In particular, the NAO-like atmospheric anomalies tend to depict an atmosphere-to-ocean forcing to the central tropical Pacific SST anomalies through the NTA SST anomalies (Wu, 2010; Karnauskas, 2014; Ding et al., 2017; Ding et al., 2023). As NAO-like footprints of the 11-year solar cycle are found in previous studies (Thiéblemont et al., 2015; Drews et al., 2022; Kuroda et al., 2022), we assume that the basin connection between NTA and tropical Pacific may provide a possible indirect route for the 11-year solar cycle impact on the tropical Pacific SST.

For the possible mechanisms of the 11-year solar cycle impacts on the tropical Pacific SST, one is the so-called "bottom-up" route, first proposed by Van Loon et al. (2007) and Meehl et al. (2009), is related to the changes in the total solar irradiance (TSI). More solar radiation in solar-maximum years coming in the subtropical "cloud-free" regions, can increase the local latent heat flux and evaporation. As a result, more moisture is carried to the convergence zones by the anomalous trade winds and enhances the precipitation in the climatology maximum regimes. This intensified precipitation could trigger a set of coupled feedbacks including strengthened trade winds, large-scale circulations (both the north-south Hadley circulation and east-west Walker cell), and an intensified subsidence in the subtropics to further reduce the cloud cover there and let more solar radiation incoming. These coupled processes can amplify the initial solar signal and lead to a La Niña-like SST anomaly in the boreal winter (DJF mean) of the solar-maximum years (Van Loon et al., 2007; Meehl et al., 2009). Further, the La Niña-like SST anomaly in the solar-maximum years produces wind-forced ocean Rossby waves in the equator, which reflect off the western boundary and produce equatorial Kelvin waves to lead to a lagged warm response in the years after the solar-maximum (Meehl and Arblaster, 2009). Please notice, the La Niña-like SST anomalies in the winter seasons of the solar-maximum years are aliased by La Niña events in the observation, which only can be ruled out when the analyzed database is large enough (Haam and Tung, 2012; Roy and Haigh, 2012). But the lagged warm response does not depend on the "cold response" in the solar-maximum years and sustains for 3 years after the solar maximum (White and Liu, 2008; Huo et al., 2021). This lagged warm response shows a phase-locked covariation with the 11-year solar cycle and can be explained by the accumulative solar radiation (Huo et al., 2023) or a delayed oscillator in the tropical Pacific (White and Liu, 2008).

In addition to the "bottom-up" mechanism, a "top-down" mechanism related to variations of the solar UV radiation was widely used to explain the observed NAO-like response in the boreal winter. The enhanced solar-UV radiation in the solar-maximum years increases the air temperature in the tropical upper stratosphere by directly radiative heating and increasing ozone production (Gray et al., 2009; Gray et al., 2010). This can increase the meridional temperature gradient and change the mean flow. The solar signal could propagate downward through interactions between the mean flow and upward planetary waves (Kodera and Kuroda, 2002; Matthes et al., 2006). Once the solar signal propagates down to the surface, the AO is more active and stronger (Huth et al., 2007). Meanwhile, the spatial structure of the NAO shows a hemispherical structure extending into the stratosphere in the solar-maximum years, whereas it is confined in the Atlantic sector during the solar-minimum years (Kodera, 2002; Kodera, 2003; Kodera and Kuroda, 2005; Tourpali, et al., 2005). The response of the NAO to the 11-year solar cycle can be amplified by the positive feedback from the ocean with a few years lagged (Gray et al., 2013; Scaife et al., 2013; Gray et al., 2016; Yukimoto et al., 2017). But the lagged NAO response is absent in some climate simulations, which may be due to insufficient ocean feedback in the climate models (Andrews et al., 2015; Drews et al., 2022). This solar UV-forced "top-down" mechanism may exert an indirect effect on the tropical Pacific SST and modulate the NTA-ENSO connection. Therefore, in this study, we will explore this

possibility based on observation/reanalysis datasets and a pair of sensitivity experiments. Details of the data and methods used in this study are described in Section 2. Section 3 presents the results and Section 4 includes conclusions and discussions.

2 Data and methods

2.1 Observational/reanalysis data

The solar radio flux at a wavelength of 10.7 cm (F10.7) is used as an index of the solar activity, which can be obtained from the SOLARIS-HEPPA CMIP6 solar forcing dataset (Matthes et al., 2017) on their website (https://solarisheppa.geomar.de/cmip6). The NOAA Extended Reconstructed SST dataset version 5 (ERSST v5, Huang et al., 2017) is used to investigate the SST response to solar activity, which is provided by the NOAA/OAR/ESRL PSL, Boulder, Colorado, United States from their website at https://psl.noaa.gov/data/gridded/data.noaa.ersst.v5.html. The HadSLP2r (Allan and Ansell, 2006) provided by Met Office Hadley Center (https://www.metoffice.gov.uk/hadobs/hadslp2/data/download.html) is used to investigate the solar signals in SLP anomalies. In addition, surface winds and precipitation rates from the National Centers for Atmospheric Prediction (NCEP) and the National Center for Atmospheric Research (NCAR) Reanalysis 1 dataset are used in this paper, covering the period 1948–present (https://www.esrl.noaa.gov/psd/data/gridded/data.ncep.reanalysis.html). The NAO index from 1950 to the present is provided by the NOAA Climate Prediction Center (CPC) on their website: https://www.cpc.ncep.noaa.gov/products/precip/CWlink/pna/nao.shtml. The CPC NAO index is derived by applying the Rotated Principal Component Analysis to monthly standardized 500-mb height anomalies in a region of 20°N–90°N. More details about the methodology used by CPC to calculate the NAO index can be found on their website: https://www.cpc.ncep.noaa.gov/products/precip/CWlink/daily_ao_index/history/method.shtml. Besides, monthly 3-D zonal wind and air temperature covering 1979–2016 from ERA-Interim reanalysis dataset (Dee et al., 2011) are used to investigate the "top-down" solar signals. This dataset is available on the European Centre for Medium-Range Weather Forecasts (ECWMF) website: https://apps.ecmwf.int/datasets/data/interim-full-daily/levtype=sfc/.

TABLE 1 All the years included in the high solar activity (HS) and low solar activity (LS) subsets for both the observation and simulation.

Observations	HS	1956–1959, 1967–1970, 1978–1981, 1988–1991, 1999–2002, 2013–2014
	LS	1953–1956,1963–1966, 1975–1978, 1985–1988, 1995–1998, 2007–2008
Simulations (SOL and NOSOL)	HS	1956–1959, 1967–1970, 1978–1981, 1988–1991, 1999–2002, 2013–2016, 2024–2027, 2033–2036, 2043–2046, 2056–2059, 2067–2070, 2077–2080, 2088
	LS	1963–1966, 1975–1978, 1985–1988, 1995–1998, 2007–2010, 2019–2022, 2029–2032, 2039–2042, 2052–2055, 2063–2066, 2073–2076, 2083–2086, 2095

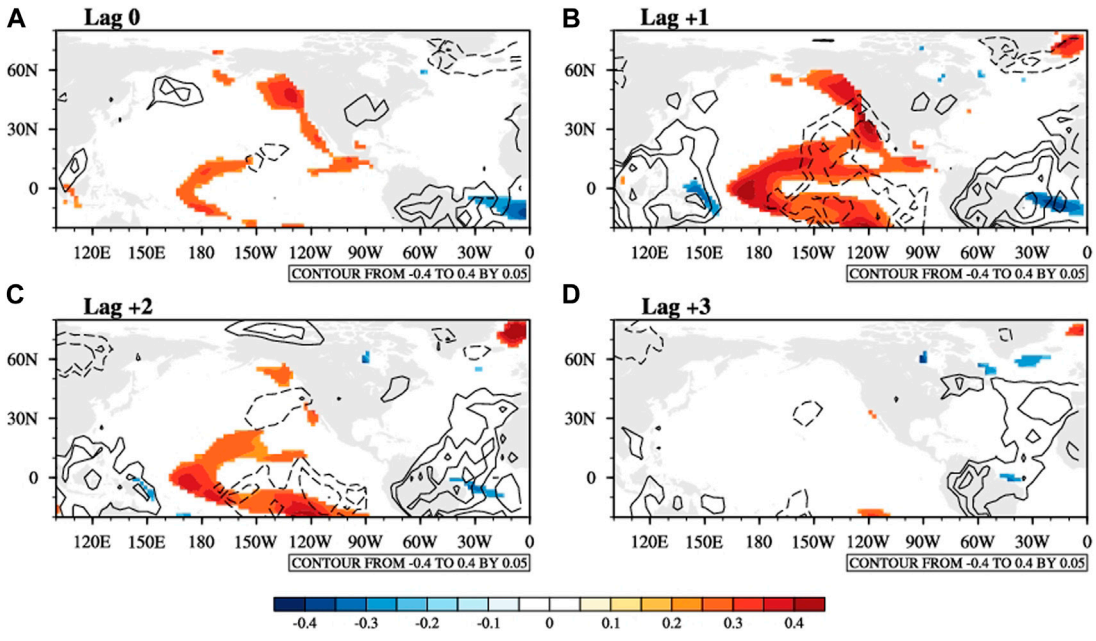

FIGURE 1
(A–D) Lagged correlation maps of observed DJF-mean F10.7 index with the observed DJF-mean SLP (contours) and JJA-mean SST (color shading contours) anomalies (1950–2018) at a lag of 0–3 years. The contour interval is 0.05 and only the values above the 90% confidence level are shown.

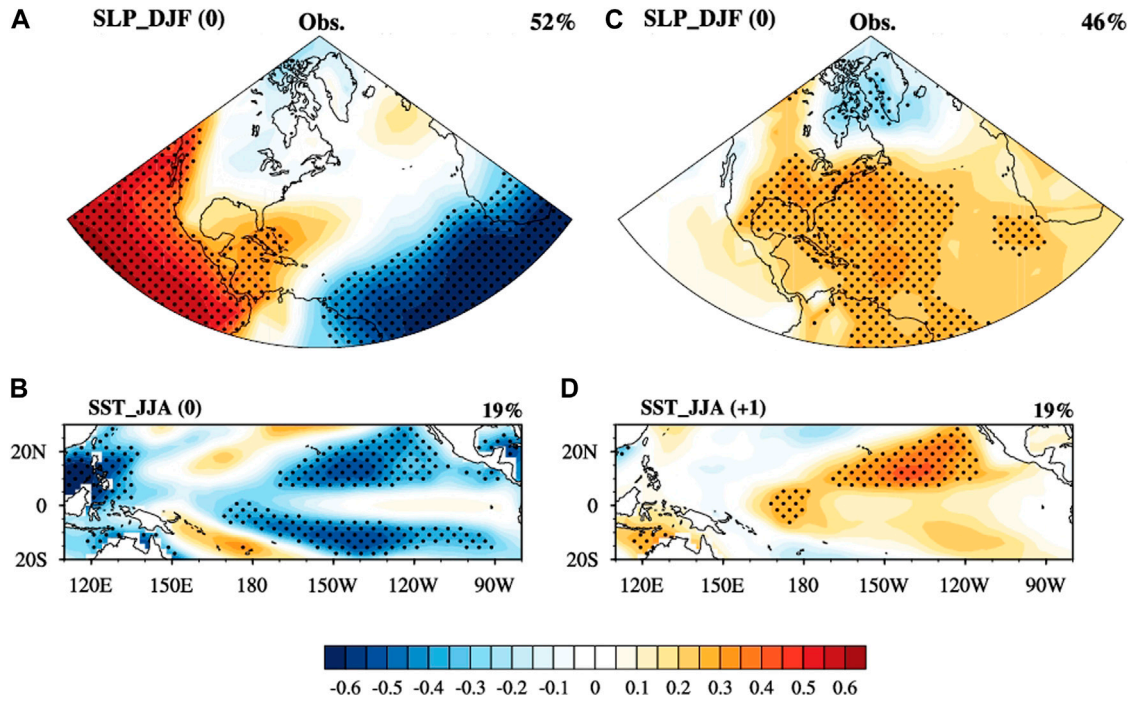

FIGURE 2
Heterogeneous correlation maps of the leading SVD mode of the DJF-mean SLP anomalies in North America and the North Atlantic [110°W–0, 20°N–90°N] and the following JJA-mean SST anomalies in the tropical Pacific [170°E–60°W, 10°S–30°N] in the same year **(A,B)** and lagged 1 year **(C,D)**. Stippled regions indicate above the 90% significance level based on the Student's t-test.

2.2 Model description and sensitivity experiments

The Community Earth System Model (CESM 1.0) developed by NCAR is a fully coupled chemistry-climate model, which includes an interactive ocean (POP), land (CLM), sea ice (CICE), and an atmospheric component with interactive chemistry (WACCM 3.5) (Marsh et al., 2013). The POP ocean component has 60 depth levels and a tripolar horizontal grid of $1^{\circ} \times 1^{\circ}$. The WACCM 3.5 has 66 vertical levels and a "high-top" (from the Earth's surface up to approx. 145 km). Its horizontal resolution is $1.9^{\circ} \times 2.5^{\circ}$ (latitude ×longitude). Spectrally daily resolved solar variability from the NRLSSI1 data set (Wang et al., 2005) is included in WACCM 3.5. The modeled tropical zonal winds from 86 to 4-mb (22°S–22°N) are relaxed to observations to present the time-varying Quasi-Biennial Oscillation (QBO) (more details can be found in Matthes et al. (2010)).

Two sensitivity experiments based on the CESM-WACCM, covering 145 years from 1955 to 2099, were used in this study. One includes the complete solar variability, which was forced by observed daily solar irradiance from 1955 to 2009 and by twice repeating the four solar cycles of 1965–2008 from 2010 to 2099 (SOL). The other one was forced by a fixed solar forcing of averaged value between 1965 and 2008 (NOSOL). To exclude the anthropogenic impact, both experiments fixed greenhouse gases and ozone-depleting substances at 1960s levels. The same observed volcanic forcing over 1955–2000 was applied to the two experiments, including three large volcanic eruptions—namely, Mt Agung (1963), El Chichón (1982), and Pinatubo (1991).

All the observational/reanalysis variables and indexes from 1950 to 2018 are used in this study. For both the observations and modeling outputs, the seasonal mean is calculated from monthly data and the SST is detrended by the least-squares quadratic at every grid point. The seasonal anomaly is calculated by removing the climatological seasonal means of the whole analyzed period. All the indexes were standardized before being used in regression analysis.

2.3 Methods

Singular value decomposition (SVD) (Bretherton et al., 1992) is used to analyze the covariance structure of a temporal covariance matrix between two geophysical fields. The linear combinations of variables extracted by SVD tend to have the maximum covariance. In this study, we applied the SVD analysis on the winter (DJF-mean) SLP anomalies over the North America and Atlantic region [110°W–0, 20°N–80°N] and the following summer (JJA-mean) SST anomalies in the tropical Pacific [110°E–80°W, 20°S–30°N] to isolate the most coherent pairs of spatial patterns and their associated time series. Please notice, we took December of the last year as the first month of the winter season of the current year in this study, i.e., DJF-mean indicates the average value of December of the last year and January and February of the current year. To investigate the modulation of the solar activity on the

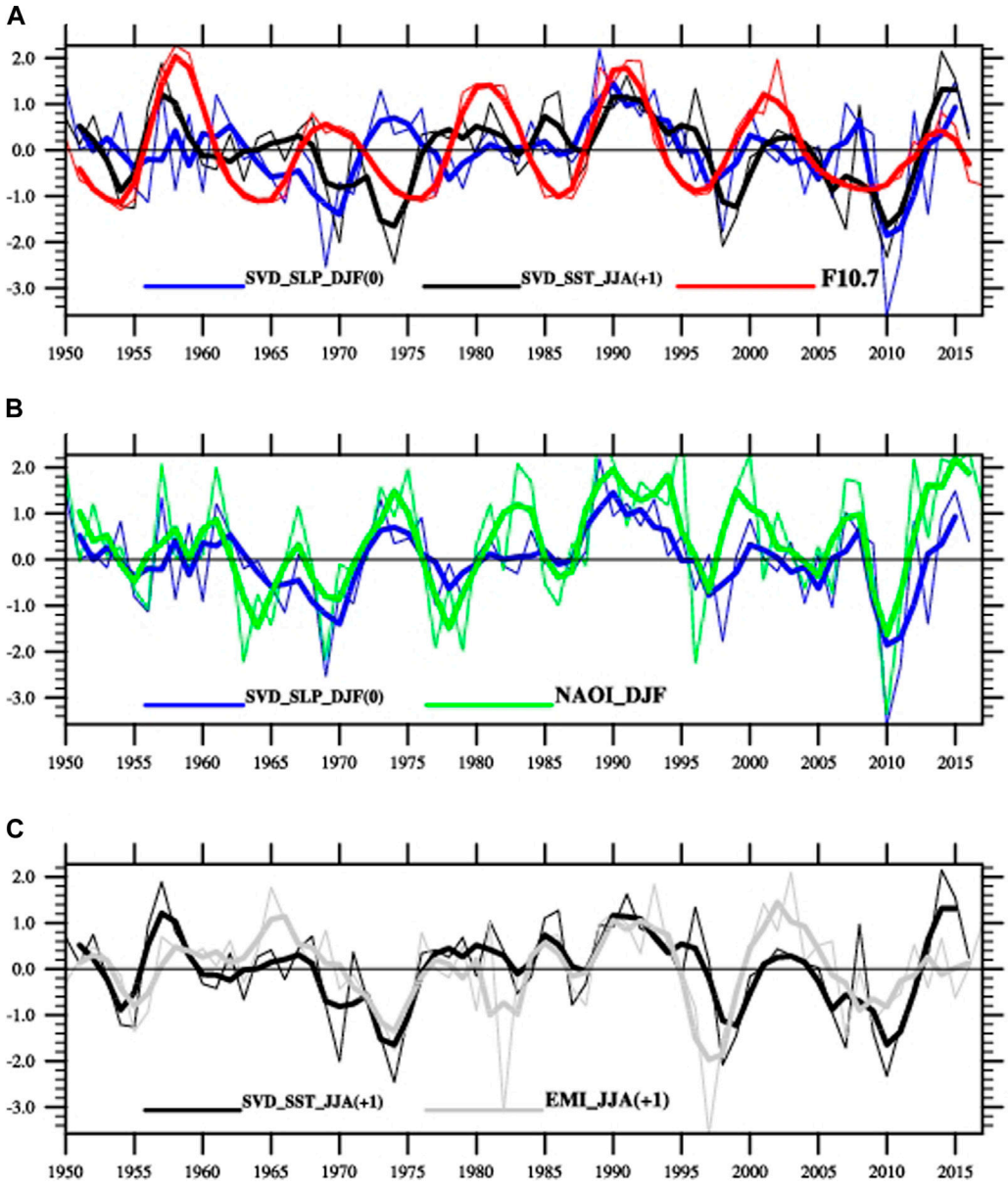

FIGURE 3
(A) Standardized expansion coefficients of the leading SVD mode of the observed DJF-mean SLP anomalies (thin blue line) and the 1-year lagged JJA-mean SST anomalies (thin black line) (Their corresponding heterogeneous correlation maps are shown in Figures 2C,D). The thin red line in **(A)** is the observed standardized DJF-mean F10.7 index. All the bold lines are smoothed by a 3-year running mean. **(B)** The blue lines are the same as in **(A)**. The thin (bold) green line is the DJF-mean NAO index (smoothed with the 3-year running mean). The black lines in **(C)** are the same as in **(A)**. The thin grey line in **(C)** is the El Niño Modoki index, defined following the method of Ashok et al. (2007) and its 3-year running mean (bold grey line).

connection between the North Atlantic SLP and the tropical Pacific SST anomalies, we separate the observational/reanalysis data as well as the modeling outputs into two subsets according to the strength of the solar activity, i.e., high solar activity (HS) and low solar activity (LS). Considering the lagged response in the tropical Pacific SST anomalies, we defined the HS as four years around the maximum of DJF-mean F10.7 for each solar cycle (e.g., 1 year ahead of the maximum and 2 years following the maximum). The LS is the same as the HS but includes four years around the DJF-mean F10.7 minima. The years included in each subset are listed in Table 1. Significance levels of the correlation coefficients and regression coefficients are assessed by the two-tailed Student's t-test. The effective degrees of freedom of the time series in the correlation and regression analysis are calculated following the method used by Huo et al. (2023). A composite mean difference method based on the solar cycle (Camp and Tung, 2007; Zhou and Tung, 2012) is used to assess the responses in the simulation and observation. The 90% statistical significance of the composite results was estimated by a 1000-fold bootstrapping test with replacement (Diaconis and Efron, 1983).

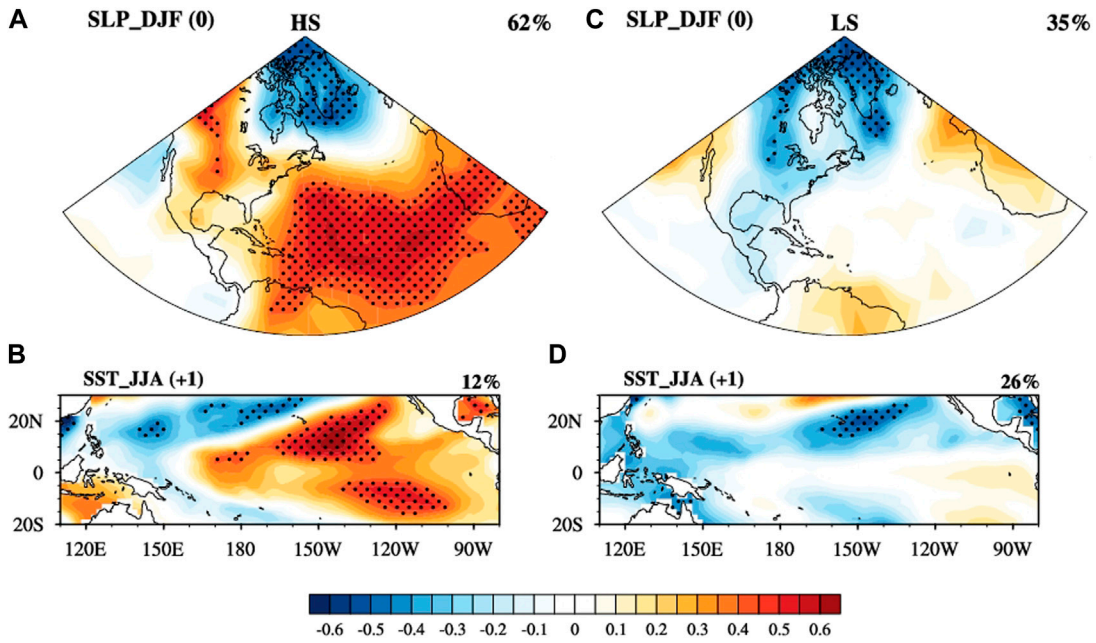

FIGURE 4
(A–D) Are the same as Figures 2C,D, but for the observed DJF-mean SLP and 1-year lagged JJA-mean SST anomalies in subsets of the high solar activity (HS, left column) and the low solar activity (LS, right column).

3 Results

Figure 1 presents the lagged correlation maps of the DJF-mean F10.7 index with the DJF-mean SLP and SST anomalies for the period 1950–2018. At a lag of 0 years, statistically significant positive correlation coefficients between the F10.7 and SST anomalies only appear in some small regions of the northeastern subtropical Pacific and the central tropical Pacific (color shading contours in Figure 1A). For the relationship of F10.7 with the SLP anomalies, negative correlation coefficients are found in the north of 60°N in the North Atlantic and positive correlation in the tropical Atlantic at a lag of 0 years (contours in Figure 1A). Both the SLP and SST anomalies have high correlation coefficients with the F10.7 at the lag of 1–2 years (Figures 1B, C). The SST pattern resembles the central Pacific El Niño (or refer as El Niño Modoki) and the SLP pattern resembles the surface fingerprints of the Walker cell, these results are consistent with previous works (Huo and Xiao, 2017; Misios et al., 2019; Huo et al., 2021). These lagged responses of SLP and SST anomalies to the solar cycle forcing may modulate the connections between the tropical Pacific and the NTA. To explore this point, we first extracted the possible "coupled" mode of DJF-mean SLP anomalies over the North Atlantic and the following JJA-mean SST anomalies in the tropical Pacific by the SVD analysis. The heterogeneous correlation maps of the leading SVD mode are shown in Figure 2.

The SLP anomalies with a zonal dipole pattern in the tropics have linear covariations with the tropical Pacific cooling in the following summer (Figures 2A, B). A meridional dipole pattern of the DJF-mean SLP anomalies over the North Atlantic and North America (Figure 2C), resembling the positive NAO, has maximum covariations with the positive JJA-mean SST anomalies at a lag of 1 year (Figure 2D). The spatial pattern of the 1-year lagged SST anomalies resembles the decadal component of the El Niño Modoki events (Sullivan et al., 2016).

The time series of the expansion coefficients for the SLP (blue lines) and SST anomalies (black lines) from the leading SVD mode are shown in Figure 3A. Please notice, we named the time series achieved by SVD analysis as SLP-svd time series and SST-svd time series hereafter. Both the SLP-svd and the SST-svd time series show a clear decadal variability after smoothed by a 3-year running mean (thick blue and black lines). Except for the period of 1964–1978 (covering solar cycle 20), the decadal variation of the SLP-svd and SST-svd time series are in-phase with the solar cycle (indicated by F10.7, red line in Figure 3A). The correlation coefficient between the SLP-svd time series (thick blue line) and the F10.7 is 0.43, above the 95% significance level. The correlation coefficient between the DJF-mean NAO index and the SLP-svd time series is 0.73 (Figure 3B), which suggests the variation of the winter SLP anomalies achieved by the SVD in this study (Figure 2C) is dominated by the NAO. The SST-svd time series has a significant positive correlation with the El Niño Modoki index (Figure 3C), the latter is defined following the method of Ashok et al. (2007). These statistical results suggest that the DJF-mean SLP anomalies over North America and the North Atlantic are strongly coupled with the tropical Pacific SST anomaly 1 year later. Both of them have a significant positive correlation with the local climate variability modes (e.g., NAO and El Niño Modoki) and show an in-phase decadal covariation with the 11-year solar cycle.

To further investigate the possible modulation of the solar activity on the relationship between tropical Pacific SST and the atmosphere anomalies at mid-high latitude, we performed the same SVD analysis on two subsets, which were grouped according to the

10.3389/feart.2023.1147582

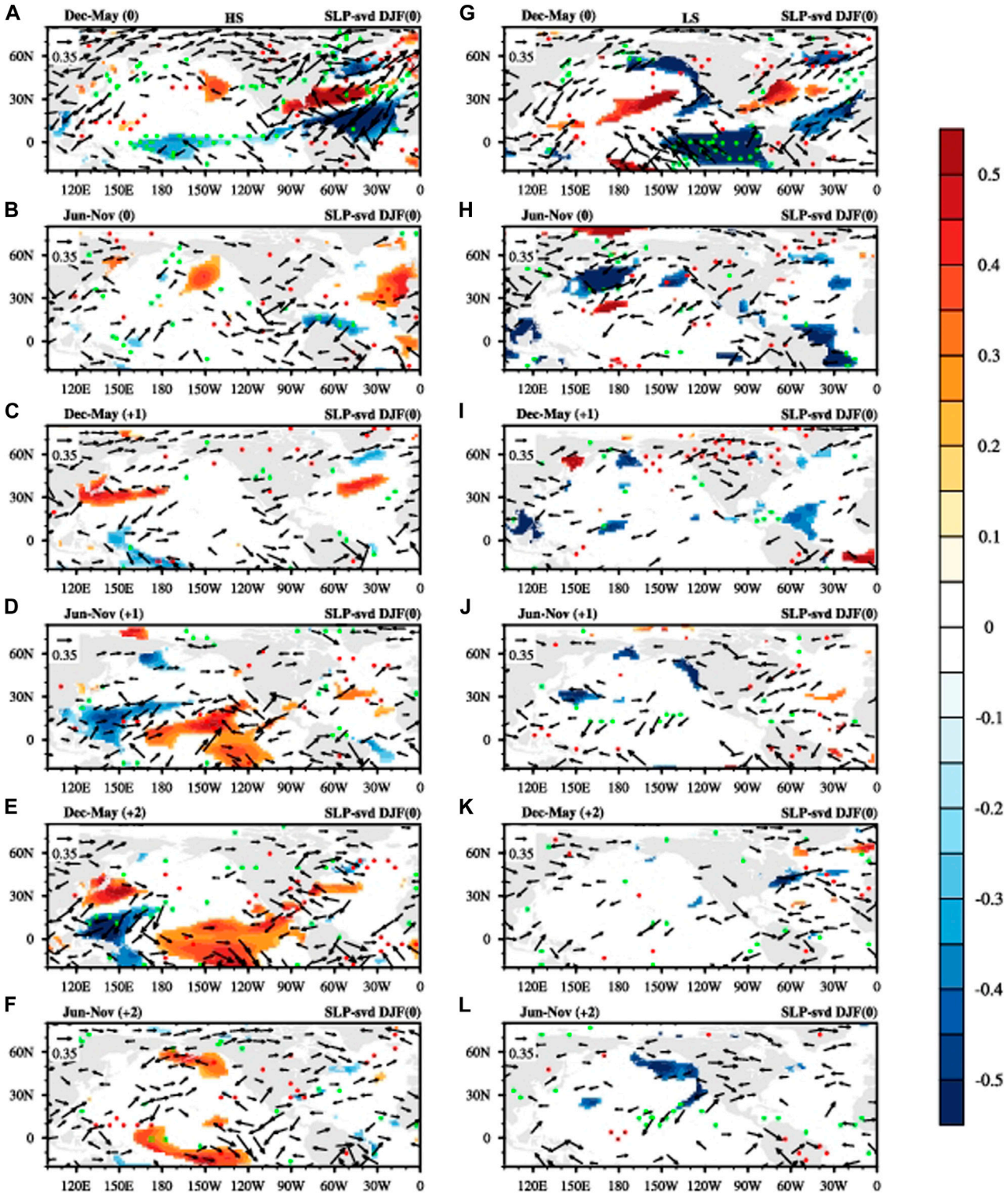

FIGURE 5
Left column: Lagged regression of the standardized SLP-svd time series onto the observed 6-month mean (December–May mean and June–November mean) SST anomalies (shading), surface wind anomalies (vectors), and precipitation rate anomalies (stippled red (positive) and green (negative)) in the same year **(A,B)**, lagged 1 year **(C,D)** and lagged 2 years **(E,F)** in the HS subset. Right column: **(G–L)** is the same as **(A–F)**, but for the LS subset. For all the variables, only the values above the 90% significance level are shown. Please notice, here we took December of last year as the beginning of the winter season of the current year.

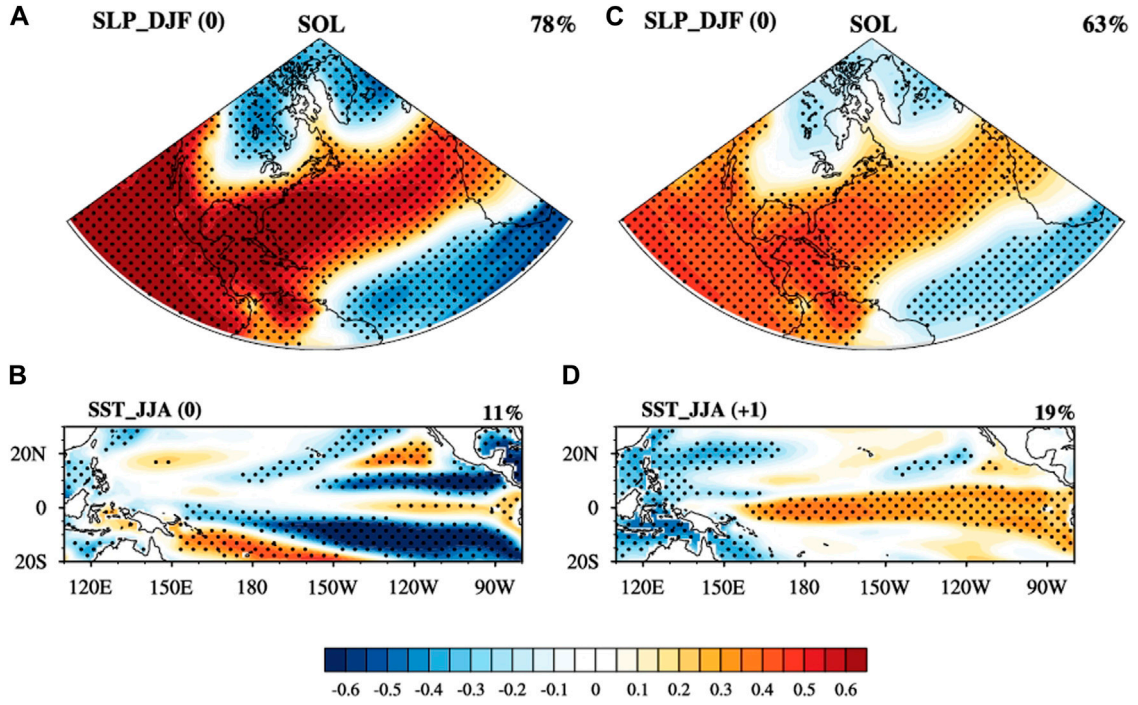

FIGURE 6
(A–D) are same as Figures 2A–D, but produced by using the simulated DJF-mean SLP and JJA-mean SST anomalies in the SOL experiment.

strength of the solar activity (i.e., the HS and LS, details can be found in the method section). Figure 4 shows the leading SVD mode of the DJF-mean SLP and the 1-year lagged JJA-mean SST anomalies in the HS and LS subsets. The heterogeneous patterns of the SLP and SST anomalies in the HS subset (Figures 4A, B) are similar to the patterns when all years are included (Figures 2C, D). The DJF-mean SLP anomalies in HS (Figure 4A) also present a meridional dipole pattern over North America and the North Atlantic, but with higher correlation coefficients and larger regions above the 95% significance level than the whole dataset. The JJA-mean SST anomalies in the following 1 year show an El Niño Modoki-like pattern (Figure 4B). The leading SVD mode of SLP anomaly in the HS subset with an NAO-like pattern explains a larger fraction of the total squared covariance than the whole dataset (approximately 62% vs. 46%) and the LS subset (approximately 62% vs. 35%). This implies a stronger positive NAO in the high solar activity years, which is consistent with the previous work (Kodera, 2002; Kodera, 2003; Huth et al., 2007; Drews et al., 2022; Kuroda et al., 2022). No such anomalous SLP-SST coupled mode was found in the LS subset (Figures 4C, D). Negative SLP anomalies in the Pole and North America may have a connection with the 1-year lagged tropical Pacific cooling in the LS years, but very few grids passed the significance test (Figures 4C, D). Our results suggest that the high solar activity favors a NAO-like SLP anomaly in the winter season, which may lead to an El Niño Modoki-like SST anomaly in the following 1 year.

To investigate the possible physical processes responsible for this NAO- El Niño Modoki connection in the HS years, we performed a lagged regression of the DJF-mean SLP-svd time series on the SST, surface wind and precipitation rate anomalies in the subsequent seasons of the same year and the following 2 years. The NAO-associated circulation anomalies and SST anomalies in the HS subset sustain in both winter and spring. In addition, the lagged subtropical teleconnections exist in both the summer and the autumn (figures are not shown here). So, here we calculated 6-month averaged surface variables to better show the results. As shown in Figure 5A (color shading contours), in Dec–May (0) of the HS, a triple pattern of SST anomalies appears in the North Atlantic with negative SST anomalies in the north tropical Atlantic and the Labrador See, and a warm anomaly in the middle West Atlantic. This cold-warm-cold tripolar SST pattern is tightly related to the NAO-like SLP anomalies (Visbeck et al., 2001). Previous studies have revealed that solar signals can propagate down to the troposphere through a "polar route" (i.e., "top-down" mechanism) and lead to an AO/NAO-positive phase with westerly (easterly) wind anomalies centered at 60°N (30°N) in the solar-maximum years (Kuroda and Kodera, 1999; Kuroda and Kodera, 2004; Drews et al., 2022). These surface wind responses are confirmed in Figure 5A (vectors). An anomalous cyclone over the North Atlantic (north of 30°N) and an anticyclone anomaly over the northern tropical Atlantic (south of 30°N) can maintain the cold-warm-cold tripolar pattern of SST anomalies in winter and spring through a positive wind-evaporation-SST (WES) feedback (stippled regions in Figure 5A) (Xie and Philander, 1994). Negative SST anomalies in the NTA, together with the negative precipitation anomalies (stippled green in Figures 5A, B), induce suppressed convection *in situ* and a low-level anticyclonic flow to its west as a Gill-type Rossby wave response (around subtropical eastern Pacific and the west coast of North America and Mexico (70°W–120°W, 0–30°N)) in the subsequent seasons (vectors in Figures 5A–C).

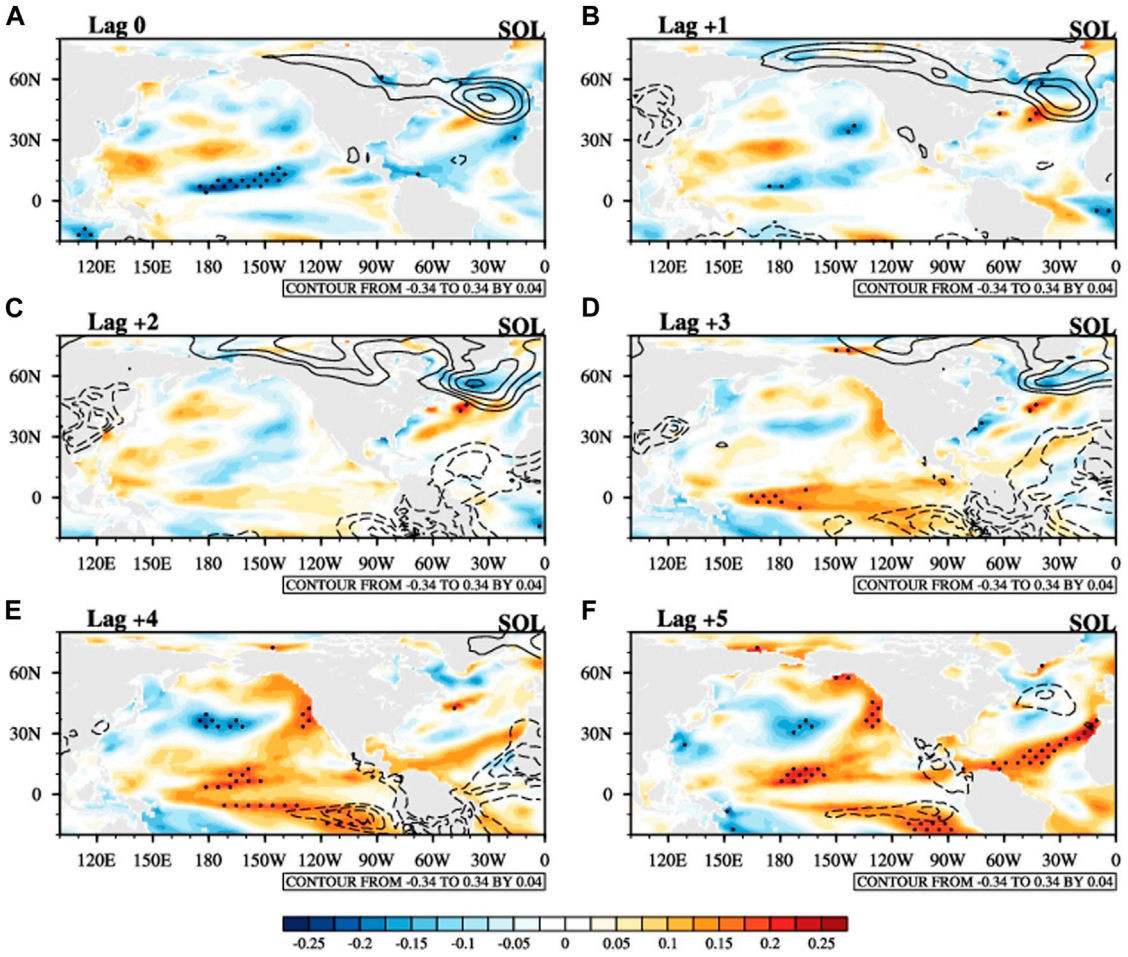

FIGURE 7
(A–F) Lagged correlation maps between the DJF-mean F10.7 index and the simulated DJF-mean SLP (contours) and JJA-mean SST (color shading contours) anomalies in the SOL experiment at the lag of 0–5 years. The black dotted regions of the color shading contours indicate above the 90% significance level. The contour interval for the SLP anomaly is 0.04 and only the values above the 90% confidence level are shown.

These anomalous flows maintain in the following 1 year (Figures 5C, D) and trigger an anomalous cyclone over the western tropical Pacific (west of the dateline; Figures 5C, D). In Jun–Nov (+1), the anomalous westerly winds over the western equatorial pacific (vectors in Figure 5D) reduce the local wind speed and surface-wind-induced evaporation, leading to positive SST anomalies in the central and eastern tropical Pacific (color shading contours in Figure 5D). The positive SST anomalies are maintained in the following year due to the WES feedback (Dec–May (+2) and Jun–Nov (+2) in Figures 5E, F).

For comparison, we performed the same regression analysis with the LS subset. In the Dec–May (0) of the solar-minimum years, the cyclone over the high latitude and the anticyclone over the subtropics are confined in the North Atlantic, these atmospheric anomalies are accompanied by relatively weaker SST anomalies in the North Atlantic (color shading contours in Figure 5G). Negative SST anomalies appear in the eastern equatorial Pacific, and the anomalous southeasterly winds across the equator provide positive feedback to the negative SST anomalies by more cold water upwelling and less local precipitation (Figure 5G). This eastern equatorial Pacific cooling disappears in the following 2 years and no El Niño Modoki-like warming shows up (Figures 5H–L). The above analysis suggests that the stronger wintertime NAO-like SLP anomalies over North America and the North Atlantic can trigger an El Niño Modoki-like warming in the tropical Pacific in the subsequent seasons under the HS condition. As the SLP-svd time series has a high positive correlation coefficient with the NAO index (r=0.73), it is not surprising that similar SST evolution maps can be achieved by regressions with the DJF-mean NAO index (as shown in Supplementary Figure S1). Therefore, the El Niño Modoki-like warming in the tropical Pacific response to the solar cycle forcing (Figure 1) could be partly due to the "atmosphere-to-ocean" forcing processes of the North Atlantic.

To further examine the role of the solar forcings in the above SLP-SST SVD mode, we performed the same SVD analysis on the DJF-mean SLP and the following JJA-mean SST anomalies for both the SOL and NOSOL experiments. As shown in Figure 6 (SOL) and Supplementary Figure S2 (NOSOL), the spatial patterns of the leading SVD modes of the SLP and SST anomalies in the SOL and NOSOL are quite similar, suggesting the simulated SLP-SST

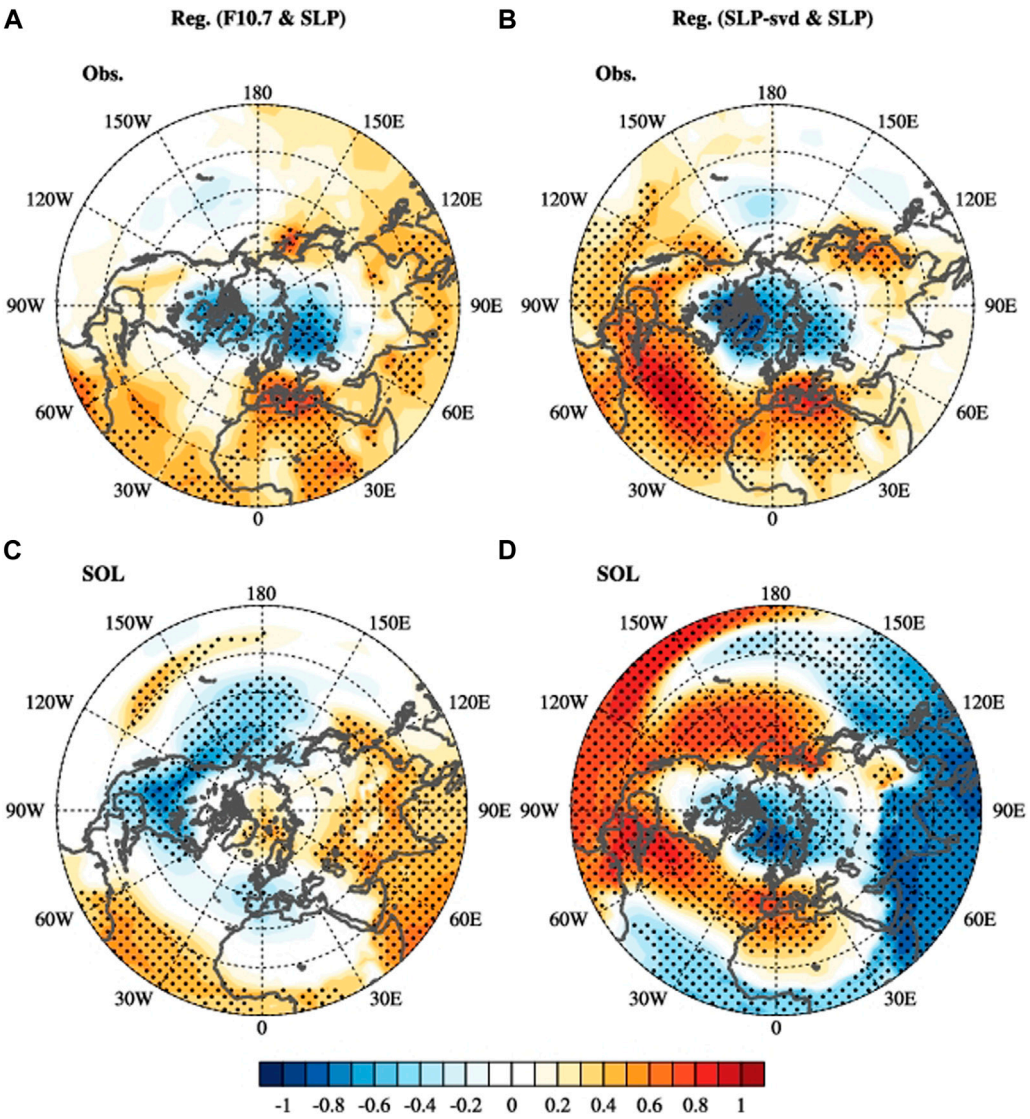

FIGURE 8
(A) Regression map of the DJF-mean F10.7 index onto the observed DJF-mean SLP anomalies in the HS subset. **(B)** Same as **(A)**, but regressed by the standardized SLP-svd time series. **(C,D)** Are the same as the **(A,B)**, but produced by using the DJF-mean F10.7 index and the simulated DJF-mean SLP anomalies in the SOL experiment. Stippled regions indicate statistical significance above the 90% level.

SVD mode is independent of the solar forcings. The simulated high-pressure zones of the SLP SVD modes locate further north in the North Atlantic (Figure 6C) than the observation (Figure 2C). The SST SVD modes resemble the EP El Niño for both the SOL and NOSOL experiments (Figure 6D; Supplementary Figure S2D). We separated the outputs of the SOL experiment into HS and LS two groups (as listed in Table 1) and performed the same SVD analysis as we did with the observation. Supplementary Figure S3A–D show the DJF-mean NAO-like SLP anomalies have a coupled covariance with the JJA-mean EP El Niño-like SST anomalies in the lagged 1 year for both the HS and LS. Therefore, the solar activity does not provide any superiority to the simulated SLP-SST SVD mode in the SOL experiment.

However, previous studies revealed a synchronization of the solar cycle and the quasi-decadal NAO variability (Thiéblemont et al., 2015) and a lagged warming response in the tropical Pacific by using the same experiments (Huo et al., 2023). As shown in Figure 7, the lagged correlation maps between the DJF-mean F10.7 index and the DJF-mean SLP anomalies of the SOL show an NAO-like pattern at the lag of 1 and 2 years (contours in Figure 7), which is absent in the NOSOL (contours in Supplementary Figure S4). A lagged warming response appears in the central equatorial Pacific at the lag of 3 and 4 years (color shading contours in Figure 7) and disappears in the NOSOL experiment (Supplementary Figure S4). Different from the observations, the above analysis based on the SOL experiment suggests that solar forcings have footprints in the North Atlantic and the tropical Pacific basins separately. Although the solar cycle can modulate the NAO temporal variability at quasi-decadal timescales *via* the solar-UV forced "top-down" mechanism in the SOL experiment (Thiéblemont et al., 2015), it cannot enhance

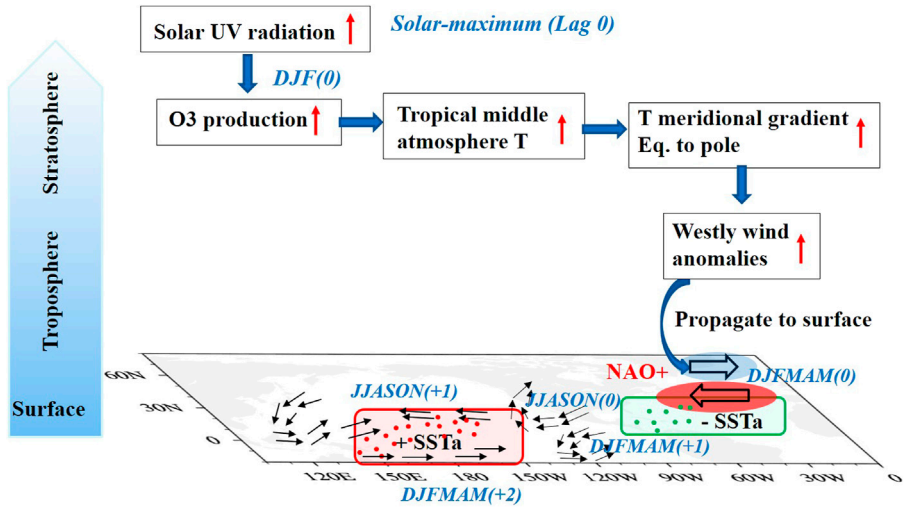

FIGURE 9
Schematic diagram representing the possible mechanism of the solar cycle modulation on the connection between DJF-mean NAO-like SLP anomalies and the followed El Niño Modoki-like SST anomalies.

the observed NAO-forced "atmosphere-to-ocean" processes to the tropical Pacific SST variability.

To discuss the possible reasons for this inconsistency between the observation and the SOL experiment, we regressed the F10.7 index and the SLP-svd time series to the SLP anomalies for the HS subset, as shown in Figure 8. For the observation (Figures 8A, B), the solar-forced footprints of SLP anomalies show a similar spatial pattern as the SVD leading mode in the HS years, which resemble the positive phase of AO. However, the positive SLP anomalies in the NTA only can be found in the F10.7 regression map in the SOL (Figure 8C), which does not show up in the leading SVD mode (Figure 8D). Besides, the regression maps based on the observational data suggest the enhanced solar forcings (high solar activity) can increase the negative SLP anomaly at the North Pole (Figures 8A, B), which shifts to the high latitude in the SOL experiment (Figure 8C). Therefore, the absence of solar effects on the simulated SLP-SST SVD mode might be due to the different locations of the active centers of the solar-related NAO-like pattern in the SOL. To further check this difference, we calculated the composite mean difference between solar maximum and minimum for the zonal mean air temperature and zonal mean zonal wind, as shown in Supplementary Figures S5, S6. Consistent with previous studies (Kodera and Kuroda, 2002; Matthes et al., 2006; Gray et al., 2009; Gray et al., 2010; Thiéblemont et al., 2015; Drews et al., 2022; Kuroda et al., 2022), both the SOL experiment and the ERA-Interim reanalysis (1979-2016) show significant warm responses in the upper stratosphere (above 7 hPa) and the lower tropical stratosphere (Supplementary Figures S5A, S6A). The warming responses in the tropical region could increase the meridional temperature gradient and lead to an anomalous westerly wind (Supplementary Figures S5B, S6B). Although the westerly wind anomalies in the stratosphere are much weaker in the experiment (Supplementary Figure S6B) than in the EAR-Interim (Supplementary Figure S5B), the westerly wind anomalies in the troposphere of the experiment are quite comparable to the ERA-Interim. However, compared to the observation, the anomalous easterly (westerly) winds in the north subtropics (mid-high latitude) shift a bit equatorward in the experiment (Supplementary Figures S5B, S6B). This difference in the solar-forced zonal wind anomalies is responsible for the different locations of the active centers of the solar-forced SLP anomalies (Figures 8A, C).

4 Conclusion and discussion

In this study, using the observational/reanalysis datasets and outputs of a pair of sensitivity experiments with and without solar cycle forcings, we investigate a possible linear co-variability between the NH wintertime SLP anomalies over North Atlantic and the following summer SST anomalies in the tropical Pacific by an SVD analysis. We found the DJF-mean NAO-like SLP anomalies have a "lead-lag" covariation with the El Niño Modoki-like SST anomalies in the tropical Pacific in the following 1 year in the observations. This NAO- El Niño Modoki connection only shows up in the HS years when the NAO and the related teleconnections are stronger and more persistent due to the stronger solar radiation. The high solar activity could enhance the "atmosphere-to-ocean" forcing processes from the North Atlantic atmosphere anomalies to the SST anomalies in the NTA and the tropical Pacific. Here we propose a possible indirect mechanism that the solar-UV forcing can modulate the tropical Pacific SST variability *via* its impacts on the mid-high latitude atmosphere anomalies. As summarized in Figure 9, the enhanced solar UV radiation in the solar-maximum years (Lag 0 years) increases the ozone production and tropical stratosphere temperature in boreal winter. This increases the poleward temperature gradient and leads to an anomalous westerly wind in the polar vortex region. These solar signals propagate down to the surface and lead to positive NAO-like SLP anomalies. This NAO-like SLP pattern sustaining in the winter

and spring [DJFMAM (0)], is companied by an anomalous "cold-warm-cold" triple SST pattern. The negative SST anomalies and the less precipitation in the NTA lead to an anomalous anticyclone over the northeastern tropical Pacific in the subsequent seasons [JJASON (0)]. Anomalous cyclones appear over the eastern equatorial Pacific and the western tropical Pacific in the following 1 year as a Gill-type Rossby wave response (i.e., DJFMAM (+1) and JJASON (+1)). These anomalous flows reduce the trade winds in their south flanks and lead to positive SST anomalies in the tropical central Pacific [JJASON (+1)]. The positive SST anomalies sustain in the following year [i.e., DJFMAM (+2) and JJASON (+2)] due to the WES feedback.

However, when we performed the same SVD analysis on the CESM-WACCM modeling outputs of two sensitivity experiments with and without solar forcings (SOL and NOSOL), a similar SVD mode of the DJF-mean SLP and JJA-mean SST anomalies is found in these two experiments, but are different from the observations. The SLP SVD modes show a triple pattern in the North Atlantic with negative SLP anomalies in the Pole and the NTA, and positive SLP anomalies in the mid-latitude in both the SOL and NOSOL. They could have "lead-lag" covariations with the EP El Niño-like SST anomalies no matter whether the solar forcings are included or not. Although the impacts of the 11-year solar cycle are found in the North Atlantic and the tropical Pacific in the SOL, the responses seem to happen separately in these two basins. No solar effect can be found in the simulated SLP-SST SVD mode in the HS subset of the SOL experiment. This may be due to the relative equatorward shifting of the solar-forced SLP anomalies in the SOL experiment compared to the observation. The locations of the active centers of the SLP anomalies response to the solar cycle highly relate to the "top-down" solar signals propagation. Therefore, although all the solar forcings are included in the SOL, compared to observations, the CESM-WACCM still underestimated the impact of the solar forcings on the tropical Pacific climate variability due to the absence of the possible "atmosphere-to-ocean" forcings and less ocean feedback in the North Atlantic (Thiéblemont et al., 2015; Drews et al., 2022). Here, we have to notice that the observation, as well as the SOL experiment, includes only 1-member, possible aliasing of the internal variability and the solar signals cannot totally rule out. Further analysis based on large ensemble simulations will be done in near future.

Data availability statement

The raw data supporting the conclusion of this article will be made available by the authors, without undue reservation.

Author contributions

WH did the analysis, produced all the figures, and wrote the manuscript. ZX and LZ assisted with the interpretation of the results and review of the manuscript.

Funding

This study is supported by a project from the Natural Science Foundation of China (42075040).

Acknowledgments

We would like to thank Katja Matthes and Rémi Thiéblemon who performed the two model simulations based on CESM-WACCM and thank all the contributors to the development of the CESM and WACCM. We thank Katja Matthes and the reviewers for the very helpful suggestions.

Conflict of interest

The authors declare that the research was conducted in the absence of any commercial or financial relationships that could be construed as a potential conflict of interest.

Publisher's note

Supplementary material

The Supplementary Material for this article can be found online at: https://www.frontiersin.org/articles/10.3389/feart.2023.1147582/full#supplementary-material

SUPPLEMENTARY FIGURE S1
Same as Figure 5, but regressed by the standardized time series of the DJF-mean NAO index.

SUPPLEMENTARY FIGURE S2
Same as Figure 6, but for the NOSOL experiment.

SUPPLEMENTARY FIGURE S3
Same as Figure 4, but using the data from the SOL experiment.

SUPPLEMENTARY FIGURE S4
Same as Figure 7, but for the NOSOL experiment.

SUPPLEMENTARY FIGURE S5
Solar cycle response in zonal mean temperatures (left) and zonal mean zonal wind (right) in Dec-Jan-Feb mean based on ERA-Interim (1979-2016). Latitude-height cross sections from 30°S to 90°N and 1000 hPa to 1 hPa of solar-cycle-based composite differences (in K) at lag 0. Significance levels are indicated by black dots (90%) based on a 1000-fold bootstrapping test.

SUPPLEMENTARY FIGURE S6
Same as Supplementary Figure S5, but for the composite difference between the SOL and NOSOL experiments.

References

Allan, R., and Ansell, T. (2006). A new globally complete monthly historical gridded mean sea level pressure dataset (HadSLP2): 1850–2004. *J. Clim.* 19, 5816–5842. doi:10.1175/JCLI3937.1

Andrews, M. B., Knight, J. R., and Gray, L. J. (2015). A simulated lagged response of the North Atlantic Oscillation to the solar cycle over the period 1960–2009. *Environ. Res. Lett.* 10, 054022. doi:10.1088/1748-9326/10/5/054022

Ashok, K., Behera, S. K., Bao, S. A., Weng, H., and Yamagata, T. (2007). El Niño Modoki and its possible teleconnection. *J. Geophys. Res. Oceans.* 112, C11007. doi:10.1029/2006JC003798

Bretherton, C. S., Smith, C., and Wallace, J. M. (1992). An intercomparison of methods for finding coupled patterns in climate data. *J. Clim.* 5, 541–560. doi:10.1175/1520-0442(1992)005<0541:AIOMFF>2.0.CO;2

Camp, C. D., and Tung, K.-K. (2007). Surface warming by the solar cycle as revealed by the composite mean difference projection. *Geophys. Res. Lett.* 34, L14703. doi:10.1029/2007GL030207

Chen, S., Chen, W., Yu, B., and Li, Z. (2022). Impact of internal climate variability on the relationship between spring northern tropical atlantic SST anomalies and succedent winter ENSO: The role of the North pacific oscillation. *J. Clim.* 35, 537–559. doi:10.1175/JCLI-D-21-0505.1

Chen, S., Chen, W., and Yu, B. (2018). Modulation of the relationship between spring AO and the subsequent winter ENSO by the preceding November AO. *Sci. Rep.* 8, 6943. doi:10.1038/s41598-018-25303-0

Chen, S., Chen, W., and Yu, B. (2017). The influence of boreal spring Arctic Oscillation on the subsequent winter ENSO in CMIP5 models. *Clim. Dyn.* 48, 2949–2965. doi:10.1007/s00382-016-3243-z

Chen, S. F., and Wu, R. G. (2017). An enhanced influence of sea surface temperature in the tropical northern Atlantic on the following winter ENSO since the early 1980s. *Atmos. Ocean. Sci. Lett.* 10, 175–182. doi:10.1080/16742834.2016.1259542

Chen, X., and Wallace, J. M. (2015). ENSO-like variability: 1900–2013. *J. Clim.* 28, 9623–9641. doi:10.1175/JCLI-D-15-0322.1

Dee, D. P., Uppala, S. M., Simmons, A. J., Berrisford, P., Poli, P., Kobayashi, S., et al. (2011). The ERA-interim reanalysis: Configuration and performance of the data assimilation system. *Q.J.R. Meteorol. Soc.* 137, 553–597. doi:10.1002/qj.828

Diaconis, P., and Efron, B. (1983). Computer intensive methods in statistics. *Sci. Amer.* 248, 116–130. doi:10.1038/scientificamerican0583-116

Ding, R., Li, J., Tseng, Y., Sun, C., and Zheng, F. (2017). Linking a sea level pressure anomaly dipole over North America to the central Pacific El Niño. *Clim. Dyn.* 49, 1321–1339. doi:10.1007/s00382-016-3389-8

Ding, R., Nnamchi, H. C., Yu, J. Y., Li, T., Sun, C., Li, J., et al. (2023). North Atlantic oscillation controls multidecadal changes in the North Tropical Atlantic–Pacific connection. *Nat. Commun.* 14, 862. doi:10.1038/s41467-023-36564-3

Drews, A., Huo, W., Matthes, K., Kodera, K., and Kruschke, T. (2022). The Sun's role in decadal climate predictability in the North Atlantic. *Atmos. Chem. Phys.* 22, 7893–7904. doi:10.5194/acp-22-7893-2022

Gray, L. J., Beer, J., Geller, M., Haigh, J. D., Lockwood, M., Matthes, K., et al. (2010). Solar influences on climate. *Rev. Geophys.* 48, RG4001. doi:10.1029/2009RG000282

Gray, L. J., Rumbold, S. T., and Shine, K. P. (2009). Stratospheric temperature and radiative forcing response to 11-year solar cycle changes in irradiance and ozone. *J. Atmos. Sci.* 66, 2402–2417. doi:10.1175/2009JAS2866.1

Gray, L. J., Scaife, A. A., Mitchell, D. M., Osprey, S., Ineson, S., Hardiman, S., et al. (2013). A lagged response to the 11-year solar cycle in observed winter Atlantic/European weather patterns. *J. Geophys. Res.* 118 (13), 13405–13420. doi:10.1002/2013JD020062

Gray, L. J., Wollings, T. J., Andrews, M., and Knight, J. (2016). Eleven-year solar cycle signal in the NAO and Atlantic/European blocking. *Quart. J. Roy. Meteor. Soc.* 142, 1890–1903. doi:10.1002/qj.2782

Haam, E., and Tung, K. K. (2012). Statistics of solar cycle–La Niña connection: Correlation of two autocorrelated time series. *J. Atmos. Sci.* 69 (10), 2934–2939. doi:10.1175/jas-d-12-0101.1

Ham, Y. G., Kug, J. S., Park, J. Y., and Jin, F. F. (2013b). Sea surface temperature in the north tropical Atlantic as a trigger for El Niño/Southern Oscillation events. *Nat. Geosci.* 6, 112–116. doi:10.1038/ngeo1686

Ham, Y. G., Kug, J. S., and Park, J. Y. (2013a). Two distinct roles of atlantic SSTs in ENSO variability: North tropical atlantic SST and atlantic Niño. *Geophys. Res. Lett.* 40, 4012–4017. doi:10.1002/grl.50729

Ham, Y. G., and Kug, J. S. (2015). Role of north tropical atlantic SST on the ENSO simulated using CMIP3 and CMIP5 models. *Clim. Dyn.* 45, 3103–3117. doi:10.1007/s00382-015-2527-z

He, W.-B., and Ma, J. (2021). Interaction between the tropical atlantic and pacific oceans on an interannual time scale. *Atmos.-Ocean.* 59 (4–5), 285–298. doi:10.1080/07055900.2021.2014300

Hua, W., Dai, A., and Qin, M. (2018). Contributions of internal variability and external forcing to the recent pacific decadal variations. *Geophys. Res. Lett.* 45, 7084–7092. doi:10.1029/2018GL079033

Huang, B., Thorne, P. W., Banzon, V. F., Boyer, T., Chepurin, G., Lawrimore, J. H., et al. (2017). Extended reconstructed sea surface temperature, version 5 (ERSSTv5): Upgrades, validations, and intercomparisons. *J. Clim.* 30, 8179–8205. doi:10.1175/JCLI-D-16-0836.1

Huo, W. J., and Xiao, Z. N. (2017). Modulations of solar activity on El Niño Modoki and possible mechanisms. *J. Atmos. Sol.-Terr. Phys.* 160, 34–47. doi:10.1016/j.jastp.2017.05.008

Huo, W. J., Xiao, Z. N., and Zhao, L. (2021). Lagged responses of the tropical pacific to the 11-yr solar cycle forcing and possible mechanisms. *J. Meteor. Res.* 35 (3), 444–459. doi:10.1007/s13351-021-0137-8

Huo, W. J., Xiao, Z. N., and Zhao, L. (2023). Phase-locked impact of the 11-year solar cycle on tropical pacific decadal variability. *J. Clim.* 36 (2), 421–439. doi:10.1175/JCLI-D-21-0595.1

Huth, R., Bochníček, J., and Hejda, P. (2007). The 11-year solar cycle affects the intensity and annularity of the Arctic Oscillation. *J. Atmos. Sol.-Terr. Phys.* 69, 1095–1109. doi:10.1016/j.jastp.2007.03.006

Jiang, L., and Li, T. (2021). Impacts of tropical North Atlantic and equatorial atlantic SST anomalies on ENSO. *J. Clim.* 34, 1–58. doi:10.1175/JCLI-D-20-0835.1

Karnauskas, K. B. (2014). Arctic forcing of decadal variability in the tropical Pacific Ocean in a high-resolution global coupled GCM. *Clim. Dyn.* 42, 3375–3388. doi:10.1007/s00382-013-1836-3

Kirtman, B., Power, S. B., Adedoyin, J. A., Boer, G. J., Bojariu, R., Camilloni, I., et al. (2013). "Near-term climate change: Projections and predictability," in *Climate change 2013: The physical science basis. Contribution of working group I to the fifth assessment report of the intergovernmental panel on climate change*. Editors T. F. Stocker, D. Qin, G.-K. Plattner, M. Tignor, S. K. Allen, J. Boschung, et al. (Cambridge, United Kingdom and New York, NY, USA: Cambridge University Press), 953–1028.

Kodera, K., and Kuroda, Y. (2005). A possible mechanism of solar modulation of the spatial structure of the North Atlantic Oscillation. *J. Geophys. Res.* 110, D02111. doi:10.1029/2004JD005258

Kodera, K., and Kuroda, Y. (2002). Dynamical response to the solar cycle: Winter stratopause and lower stratosphere. *J. Geophys. Res.* 107 (24), 4749. doi:10.1029/2002JD002224

Kodera, K. (2002). Solar cycle modulation of the North atlantic oscillation: Implication in the spatial structure of the NAO. *Geophys. Res. Lett.* 29 (8), 59. doi:10.1029/2001GL014557

Kodera, K. (2003). Solar influence on the spatial structure of the NAO during the winter 1900-1999. *Geophys. Res. Lett.* 30 (4), 2002GL016584. doi:10.1029/2002GL016584

Kodera, K., Thieblemont, R., Yukimoto, S., and Matthes, K. (2016). How can we understand the global distribution of the solar cycle signal on the Earth's surface? *Atmos. Chem. Phys.* 16, 12925–12944. doi:10.5194/acp-16-12925-2016

Kuroda, Y., and Kodera, K. (1999). Role of planetary waves in the stratosphere-troposphere coupled variability in the northern hemisphere winter. *Geophys. Res. Lett.* 26, 2375–2378. doi:10.1029/1999GL900507

Kuroda, Y., and Kodera, K. (2004). Role of the polar-night jet oscillation on the formation of the arctic oscillation in the northern hemisphere winter. *J. Geophys. Res.* 109, D11112. doi:10.1029/2003JD004123

Kuroda, Y., Kodera, K., Yoshida, K., Yukimoto, S., and Gray, L. (2022). Influence of the solar cycle on the North atlantic oscillation. *J. Geophys. Res. Atmos.* 127, e2021JD035519. doi:10.1029/2021JD035519

Li, S., Wu, L., Yang, Y., Geng, T., CaiGan, W. B., et al. (2020). The Pacific Decadal Oscillation less predictable under greenhouse warming. *Nat. Clim. Chang.* 10, 30–34. doi:10.1038/s41558-019-0663-x

Li, X., Xie, S. P., Gille, S. T., and Yoo, C. (2016). Atlantic-induced pan-tropical climate change over the past three decades. *Nat. Clim. Change* 6, 275–279. doi:10.1038/nclimate2840

Liguori, G., and Di Lorenzo, E. (2018). Meridional modes and increasing pacific decadal variability under anthropogenic forcing. *Geophys. Res. Lett.* 45, 983–991. doi:10.1002/2017GL076548

Marsh, D. R., Mills, M. J., Kinnison, D. E., Lamarque, J., Calvo, N., and Polvani, L. M. (2013). Climate change from 1850 to 2005 simulated in CESM1 (WACCM). *J. Clim.* 26, 7372–7391. doi:10.1175/JCLI-D-12-00558.1

Martín-Rey, M., Rodríguez-Fonseca, B., and Polo, I. (2015). Atlantic opportunities for ENSO prediction. *Geophys. Res. Lett.* 42, 6802–6810. doi:10.1002/2015GL065062

Matthes, K., Funke, B., Andersson, M. E., Barnard, L., Beer, J., Charbonneau, P., et al. (2017). Solar forcing for CMIP6 (v3.2). *Geosci. Model Dev.* 10, 2247–2302. doi:10.5194/gmd-10-2247-2017

Matthes, K., Kuroda, Y., Kodera, K., and Langematz, U. (2006). Transfer of the solar signal from the stratosphere to the troposphere: Northern winter. *J. Geophys. Res.* 111, D06108. doi:10.1029/2005JD006283

Matthes, K., Marsh, D. R., Garcia, R. R., Kinnison, D. E., Sassi, F., and Walters, S. (2010). Role of the QBO in modulating the influence of the 11-year solar cycle on the atmosphere using constant forcings. *J. Geophys. Res.* 115, D18110. doi:10.1029/2009JD013020

McGregor, S., Timmermann, A., Stuecker, M., England, M., MerrifieldJin, M. F.-F., et al. (2014). Recent Walker circulation strengthening and Pacific cooling amplified by Atlantic warming. *Nat. Clim. Change* 4, 888–892. doi:10.1038/nclimate2330

Meehl, G. A., and Arblaster, J. M. (2009). A lagged warm event-like response to peaks in solar forcing in the Pacific region. *J. Clim.* 22 (13), 3647–3660. doi:10.1175/2009JCLI2619.1

Meehl, G. A., Arblaster, J. M., Matthes, K., Sassi, F., and van Loon, H. (2009). Amplifying the Pacific climate system response to a small 11-year solar cycle forcing. *Sci* 325, 1114–1118. doi:10.1126/science.1172872

Meehl, G. A., Hu, A., Castruccio, F., England, M., Bates, S., Danabasoglu, G., et al. (2021). Atlantic and Pacific tropics connected by mutually interactive decadal-timescale processes. *Nat. Geosci.* 14, 36–42. doi:10.1038/s41561-020-00669-x

Misios, S., Gray, L. J., Knudsen, M. F., Karoff, C., Schmidt, H., and Haigh, J. D. (2019). Slowdown of the Walker circulation at solar cycle maximum. *Proc. Natl. Acad. Sci.* 116, 7186–7191. doi:10.1073/pnas.1815060116

Misios, S., Mitchell, D. M., Gray, L. J., Tourpali, K., Matthes, K., Hood, L., et al. (2016). Solar signals in CMIP-5 simulations: Effects of atmosphere-ocean coupling. *Q. J. R. Meteorol. Soc.* 142, 928–941. doi:10.1002/qj.2695

Park, J. H., Li, T., Yeh, S. W., and Kim, H. (2019). Effect of recent Atlantic warming in strengthening Atlantic–Pacific teleconnection on interannual timescale via enhanced connection with the Pacific meridional mode. *Clim. Dyn.* 53, 371–387. doi:10.1007/s00382-018-4591-7

Ren, S.-M., Zhang, S.-Q., Lu, L., Jiang, Y-J., and Ma, Y.-W. (2021). Impact of tropical Atlantic warming on the Pacific Walker circulation with numerical experiments of CGCM. *Adv. Clim. Chang. Res.* 12 (6), 757–771. doi:10.1016/j.accre.2021.09.012

Roy, I., and Haigh, J. D. (2012). Solar cycle signals in the pacific and the issue of timings. *J. Atmos. Sci.* 69 (4), 1446–1451. doi:10.1175/jas-d-11-0277.1

Scaife, A. A., Ineson, S., Knight, J. R., Gray, L., Kodera, K., and Smith, D. M. (2013). A mechanism for lagged North Atlantic climate response to solar variability. *Geophys. Res. Lett.* 40 (2), 434–439. doi:10.1002/grl.50099

Sullivan, A., Luo, J., Hirst, A. C., Bi, D., Cai, W., and He, J. (2016). Robust contribution of decadal anomalies to the frequency of central-Pacific El Niño. *Sci. Rep.* 6, 38540. doi:10.1038/srep38540

Thiéblemont, R., Matthes, K., Omrani, N.-E., Kodera, K., and Hansen, F. (2015). Solar forcing synchronizes decadal North Atlantic climate variability. *Nat. Commun.* 6, 8268. doi:10.1038/ncomms9268

Tourpali, K., Schuurmans, C. J. E., van Dorland, R., Steil, B., Brühl, C., and Manzini, E. (2005). Solar cycle modulation of the Arctic Oscillation in a chemistry-climate model. *Geophys. Res. Lett.* 32, L17803. doi:10.1029/2005GL023509

Van Loon, H., Meehl, G. A., and Shea, D. J. (2007). Coupled air-sea response to solar forcing in the Pacific region during northern winter. *J. Geophys. Res.* 112, D02108. doi:10.1029/2006JD007378

Visbeck, M. H., Hurrell, J. W., Polvani, L., and Cullen, H. M. (2001). The North atlantic oscillation: Past, present, and future. *Proc. Natl. Acad. Sci.* 98 (23), 12876–12877. doi:10.1073/pnas.231391598

Wang, C., Kucharski, F., Barimalala, R., and Bracco, A. (2009). Teleconnections of the tropical atlantic to the tropical Indian and pacific oceans: A review of recent findings. *Meteorol. Z.* 18 (4), 445–454. doi:10.1127/0941-2948/2009/0394

Wang, L., Yu, J. Y., and Paek, H. (2017). Enhanced biennial variability in the Pacific due to Atlantic capacitor effect. *Nat. Commun.* 8, 14887. doi:10.1038/ncomms14887

Wang, W., Matthes, K., Tian, W., Park, W., Shang, M., and Ding, A. (2018). Solar impacts on decadal variability of tropopause temperature and lower stratospheric (LS) water vapour: A mechanism through ocean-atmosphere coupling. *Clim. Dyn.* 52 (9), 5585–5604. doi:10.1007/s00382-018-4464-0

Wang, Y.-M., Lean, J. L., and Sheeley, N. R., Jr (2005). Modeling the Sun's magnetic field and irradiance since 1713. *Astrophys. J.* 625, 522–538. doi:10.1086/429689

White, W. B., and Liu, Z. Y. (2008). Resonant excitation of the quasi-decadal oscillation by the 11-year signal in the Sun's irradiance. *J. Geophys. Res.* 113, C01002. doi:10.1029/2006JC004057

White, W., Lean, J., Cayan, D., and Dettinger, M. (1997). Response of global upper ocean temperature to changing solar irradiance. *J. Geophys. Res.* 102, 3255–3266. doi:10.1029/96JC03549

Wu, Q. (2010). Forcing of tropical SST anomalies by wintertime AO-like variability. *J. Clim.* 23 (10), 2465–2472. doi:10.1175/2009JCLI2749.1

Xiao, Z., Liao, Y., and Li, C. (2016). Possible impact of solar activity on the convection dipole over the tropical Pacific Ocean. *J. Atmos. Sol.-Terr. Phys.* 140, 94–107. doi:10.1016/j.jastp.2016.02.008

Xie, S., Okumura, Y., Miyama, T., and Timmermann, A. (2008). Influences of Atlantic climate change on the tropical Pacific via the central American isthmus. *J. Clim.* 21 (15), 3914–3928. doi:10.1175/2008JCLI2231.1

Xie, S. P., and Philander, S. G. H. (1994). A coupled ocean-atmosphere model of relevance to the ITCZ in the eastern Pacific. *Tellus, Ser. A* 46, 340–350. doi:10.1034/j.1600-0870.1994.t01-1-00001.x

Yukimoto, S., Kodera, K., and Thiéblemont, R. (2017). Delayed North Atlantic response to solar forcing of the stratospheric polar vortex. *SOLA* 13, 53–58. doi:10.2151/sola.2017-010

Zheng, Y., Chen, S., Chen, W., and Yu, B. (2021). Diverse influences of spring arctic oscillation on the following winter El niño–southern oscillation in CMIP5 models. *Clim. Dyn.* 56, 275–297. doi:10.1007/s00382-020-05483-0

Zhou, J.-S., and Tung, K.-K. (2012). On the CMD projection method and the associated statistical tests in climate data analysis. *Adv. Data Sci. Adapt. Anal.* 4, 1250001–1250002. doi:10.1142/S179353691250001X

frontiers | Frontiers in Earth Science

TYPE Original Research
PUBLISHED 19 May 2023
DOI 10.3389/feart.2023.1165386

OPEN ACCESS

EDITED BY
Nicola Scafetta,
University of Naples Federico II, Italy

REVIEWED BY
Anthony Lupo,
University of Missouri, United States
Ana G. Elias,
Universidad Nacional de Tucumán, Argentina

*CORRESPONDENCE
Limin Zhou,
lmzhou@geo.ecnu.edu.cn

RECEIVED 14 February 2023
ACCEPTED 02 May 2023
PUBLISHED 19 May 2023

CITATION
Ye A, Zhu Z, Zhang R, Xiao Z and Zhou L (2023), Influence of solar forcing on multidecadal variability in the Atlantic meridional overturning circulation (AMOC).
Front. Earth Sci. 11:1165386.
doi: 10.3389/feart.2023.1165386

Influence of solar forcing on multidecadal variability in the Atlantic meridional overturning circulation (AMOC)

Aihua Ye[1], Zhipeng Zhu[1], Ruyi Zhang[1], Ziniu Xiao[2] and Limin Zhou[1,3]*

[1]Key Laboratory of Geographic Information Science, Ministry of Education, East China Normal University, Shanghai, China, [2]State Key Laboratory of Numerical Modelling for Atmospheric Sciences and Geophysical Fluid Dynamics, Institute of Atmospheric Physics, Beijing, China, [3]Institute of Eco-Chongming, Shanghai, China

There is a growing debate regarding the influence of solar activity on climate change as the solar forcing signal on decadal/multidecadal timescales is not robust in long-term reconstructed climate data or numerical simulations. However, solar forcing could be amplified by ocean–atmosphere coupling in sensitive regions, including the North Atlantic Ocean (N.A.). This study assessed the influence of varied total solar irradiance (TSI) due to the effects of solar activity on Atlantic Meridional Overturning Circulation (AMOC) based on an Earth System model with intermediate complexity (PLASIM-GENIE). Three groups of experiments with different TSI series; i.e., constant (NS), decadal varied (DS), and reconstructed whole (AS) for 1610–2000, were conducted and the AMOC response was investigated. The results showed that the internal forcing of the climate system led to quasi-35-year and quasi-65-year AMOC cycles and a significant and stable negative correlation between TSI and AMOC on a multidecadal timescale. The period was significantly extended due to solar forcing. The declining AMOC trend occurred in simulations after 1800. Thus, solar forcing contributed to a weakening AMOC at a rate of 0.41 Sv per century. The decadal variation in TSI was the main contributor to this decline due to solar forcing.

KEYWORDS

solar forcing, AMOC, multidecadal variability, sensitivity test, period

Abbreviations: AMOC, Atlantic meridional overturning circulation; AMOCI, AMOC index; AS, reconstructed whole total solar irradiance forcing test; BRS, Barents Sea; BSW, Barents sea water; DS, decadal varied total solar irradiance forcing test; EGC, East Greenland Current; EMD, empirical mode decomposition; GNS, Greenland–Norway Sea; GrIS, Greenland ice sheet; HadGEM2-ES, Hadley Centre Global Environment Model 2, with Earth System components; IPCC-AR6, the Sixth Assessment Report of the Intergovernmental Panel on Climate Change; LAS, Labrador Sea; LAS-wSPG, Labrador Sea and west subpolar gyre; MLD, mixed layer depth; N.A., North Atlantic; NS, constant total solar irradiance (1,364.5 W/m^2) forcing test; PLASIM-GENIE, Earth System model with intermediate complexity used in this research; RAPID, Rapid Climate Change program; SIC, sea–ice cover; SPG, subpolar gyre; SSS, sea surface salinity; SST, sea surface temperature; Sv, Sverdrup, the unit of AMOC. 1 Sv = 1x10^6 $m^3/s^{(-1)}$; TSI, total solar irradiance.

1 Introduction

Evidence from observations and geologic proxies indicates that solar forcing is among the key natural driving forces affecting decadal/multidecadal climate variation (Eddy, 1976; Haigh, 1996; Wang et al., 2005; Liu et al., 2013; Gray et al., 2018; Xu et al., 2019; Kuroda et al., 2022). Although various linking mechanisms have been proposed, such as the "top-down" regime (stratospheric ozone ultraviolet radiation effect) or "bottom-up" regime (total radiation irradiance effect) (Haigh, 1994; Gray et al., 2009; Mann et al., 2009), recent studies based on climate models or reconstructed long-term reanalysis data have challenged the certainty of this linkage. A robust solar signal on decadal climate change was lacking in the long-term reanalysis or modeling data. Previous studies occasionally observed this linkage (Sjolte et al., 2018). Instead of solar forcing, volcanic eruptions or internal driving forces could also induce decadal climate variations (Mann et al., 2021). Consequently, the Sixth Assessment Report of the Intergovernmental Panel on Climate Change (IPCC-AR6) suggested that there exists great uncertainty regarding the influence of solar activity on decadal/multidecadal climate changes (Masson-Delmotte, 2021). The key to addressing this contradiction is to establish robust linking mechanisms between solar activity and climate systems.

Although the total solar irradiance (TSI) only fluctuates by approximately 0.1%–0.2% in the solar cycle of the 11-year Schwabe cycle (Foukal et al., 2006), the changes could accumulate and be amplified in sensitive ocean regions and lead to significant impacts on regional or even global climate. The North Atlantic Ocean region (N.A.) is considered a sensitive region (Gray et al., 2013; Scaife et al., 2013; Andrews et al., 2015; Cheng et al., 2016). Andrews et al. (2015) and Gray et al. (2016) declared that the accumulated solar energy in the mixed layer of the N.A. could generate a response lag of 3–4 years of surface pressure to the decadal solar cycle. In the N.A., the local ocean response could cause a global climate effect due to thermohaline circulation. Many studies have suggested that the Atlantic Meridional Overturning Circulation (AMOC) plays an important role in Atlantic multidecadal variability. Atlantic hurricane activity, frequency of drought events in the United States, and changes in rainfall in Europe and the East Asian summer monsoon are all reportedly related to the AMOC (Delworth et al., 1993; Timmermann et al., 1998; Sutton and Hodson, 2005; Zhang and Delworth, 2006; Yu Lei, 2009; Ting et al., 2011). Thus, the connection between solar forcing and the AMOC seems to be an important part of transmitting solar signals in climate systems (Shindell et al., 2001; Scaife et al., 2013).

Moreover, the AMOC fluctuates on variable timescales; i.e., from decadal to centennial to millennial (Zhang, 2008; Chylek et al., 2012; Park and Latif, 2012). Geological proxy records (Ran Lihua, 2008; Liu Jing, 2014; Zhao Yun, 2015; Li Dongling, 2016) and model simulations (Jiang et al., 2014) reveal the significant relationship between the AMOC and variations in sea surface temperature (SST) and ice sheets in the N.A. on a millennial scale. Lin et al. (2019) claimed that the AMOC shows two groups of decadal/multidecadal oscillations of 10–30 years and 50–80 years and that the formation of these two oscillations accounted for internal oscillation and trans-basin processes in the N.A. Bagatinsky and Diansky (2021) revealed that the Atlantic multidecadal oscillation was associated with the AMOC sinking branch at 60°N latitude and the rising branch at 25°N latitude and was part of a quasi-60-year cycle. Additionally, the multidecadal variation in AMOC would shift with global climate background changes (Cheng et al., 2016).

Various mechanisms of AMOC multidecadal fluctuation due to internal or external forcings have been proposed (Gregory et al., 2005; Yu et al., 2010; Lynch-Stieglitz, 2017). The meridional density gradient (Lee and Wang, 2010; Huang et al., 2014), fresh water flux, and deep convective variation (Sutton and Hodson, 2005) control the variation in AMOC by changing the N.A. SST and salinity. Solar activity could contribute to these factors by impacting the heat capacity, planetary waves (Huck et al., 2001), and melted sea–ice freshwater injections (Yu et al., 2010; Lynch-Stieglitz, 2017).

The relationship between AMOC and TSI, controlled by orbital factors or solar activity, has been studied through observations and model simulations. Paleoclimatic evidence from deep-sea cores indicated that the AMOC decreases with weakened solar radiation on a millennium timescale (Negre et al., 2010). Based on reconstructed N.A. climate data over the past 200 years, Gary et al. (2010) proposed that TSI can affect the AMOC on a decadal time scale through the storage of solar energy in the mixed layer in the N.A. region (Gray et al., 2010; Ineson et al., 2011; Scaife et al., 2013; Andrews et al., 2015). Numerical simulations by Scaife et al. (2013) also concluded that the AMOC could amplify the solar signal and shape the regional response patterns in the N.A. region. Menary and Scaife (2014) operated 150-year experiments with the HadGEM2-ES (Hadley Centre Global Environment Model 2, with Earth System components) model and found that increased TSI could affect atmospheric circulation by changing SST on the multidecadal timescale. Consequently, the impact on seawater evaporation and ocean stratification in the N.A. leads to AMOC enhancement. However, simulations by Muthers et al. (2016) based on the SOCOL-MPIOM model demonstrated that weakened TSI was followed by colder SST and enhanced sea–ice cover, which would increase the N.A. upper water density and speed the AMOC on a multidecadal time scale. However, a weakened TSI could also induce a negative AO phase, which could decrease the AMOC intensity. Other modeling results also revealed that TSI variation could cause either positive or negative effects on the strength of AMOC on different time scales (Zorita et al., 2004; Goosse and Renssen, 2006; Sedlacek and Mysak, 2009; Swingedouw et al., 2011).

The weakening trend of the AMOC has been detected by observations (Holliday et al., 2020) and paleoclimate proxies (Caesar et al., 2021). Although there is an argument for the origin of the weakening of the AMOC, the fluctuation in eddies (Lozier et al., 2019), internal tides (de Lavergne et al., 2017), and wind forcing (Swingedouw et al., 2022), in other words, internal or external forcing, are the main contributors to this weakening trend. Solar forcing with TSI variability on multiple timescales could affect the weakening trend of the AMOC; however, its contribution has not been fully investigated.

Regarding simulation of the AMOC, although the climate model with a high-resolution ocean part, in which eddies are permitted, could simulate key processes of the AMOC, such as the transformation of water masses, strong biases remain due to the possible serious underestimation of some uncertainties (Jackson et al., 2020). The coarse-resolution model could capture the first order of driving the AMOC (Swingedouw et al., 2022), the results of

which may be more consistent with the present observations. Therefore, the solar forcing effect on AMOC is still useful for initial testing with the coarse-resolution model.

In this article, we use a coupled intermediate complexity earth system model, PLASIM-GENIE, to explore the influence of varied TSIs with multi-timescale (decadal to centennial) cycles on the AMOC. The model can operate the first order of the driving process and provide the main characteristics of the climate system, in which the ocean and sea–ice modules can well simulate AMOC variability. It is suitable for long-term large-scale ensemble studies.

Concretely, we designed 390-year single-factor forcing simulation experiments with different time scale variations in TSI based on the reconstructed series and investigated the responses of the AMOC. The structure of this article is as follows: the second section describes the climate model and experimental design; the third section provides experimental results and discussion; and the fourth section provides the conclusion.

2 Model and experimental setup

2.1 Model

This study used an Earth system model with intermediate complexity (PLASIM-Genie version 1.0), which coupled the planetary simulator (PLASIM) and ocean (GOLDSTEIN), sea ice (GOLDSTEINSEAICE), and land surface components (GENIE Earth System model), and can reproduce the main feature of the climate system (Marsh et al., 2004; Zorita et al., 2004).

The primitive equation of the atmosphere includes chaotic, three-dimensional (3-D) motion and interactive radiation and cloud cover, and dominates the computational load compared to the relatively simpler frictional geostrophic ocean, which neglects momentum advection. This model is suitable for long-term or global-scale comprehensive simulations. Based on the original slab ocean and sea–ice module with flux correction, the model tuned each module, which allowed the model to improve the prediction of the characteristics of ocean circulation and the climate system. The GOLDSTEIN sub-model can adopt surface wind speed, net energy, and net humidity fluxes provided by PLASIM-GENIE, perform relevant sea–ice correction, and output responses such as SST, salinity, and sea–ice thickness. GOLDSTEIN also improves the vapor transport process, which can not only represent the variability in ocean currents, such as AMOC caused by changes in the ocean interior, but also simulate the variability in AMOC driven by wind.

The PLASIM-GENIE model has a horizontal resolution of T21 (5.6°x5.6°, 32x64) (Lenton et al., 2007). Marsh et al. (2004) successfully investigated the operating pattern of thermohalines on decadal to millennial time scales with the GENIE model. PLASIM has a vertical resolution of 10 layers for the top at the tropopause. GOLDSTEIN has a vertical resolution of 32 layers, from the ocean surface down to the bottom. Compared to other EMICs, such as OSUVic, PLASIM-GENIE performs moisture flux adjustment, and a weak (9Sv) AMOC can be simulated. Holden et al. (2016)provided a more detailed description and model evaluation.

2.2 Experimental design

This study performed three experimental tests with different series of TSI. Figure 1 shows the five series of decomposed TSI reconstructed by Lean (2010) using the empirical mode decomposition (EMD) method. Figure 2 lists the three reconstructed TSI series in the simulations. The gray line represents the constant solar irradiance of 1364.6 W/m^2 (NS). The blue line represents the original reconstructed TSI (AS). The red line represents the solar irradiance without 100-year and 22-year fluctuations, which is combined with the decomposed series of EMD1, EMD2, and EMD5 and calibrated with the mean of 1364.6 W/m^2 (DS).

Figure 3 shows the results of wavelet analysis of DS (panel a) and AS (panel b) with a significant 11-year period fluctuation in the DS series and significant quasi-11-year and centennial period variations in the AS series.

To exclude the influence of human activity, other initial atmospheric parameters of simulations were kept at a constant value in 1850, i.e., the CO_2 concentration was maintained at 280 ppm, which was the atmospheric CO_2 concentration during the Holocene interglaciation (Lourantou et al., 2010). This value is often used as the equilibrium concentration of CO_2 in idealized experiments (Eby et al., 2013).

Each test used three ensembles. The initial 200 years running with a constant solar irradiance of 1364.6 W/m^2 are carried out in each group of simulations to make the model run stably. The annual averaged results of the simulation are output.

3 Results

3.1 Comparison with reanalysis data

The EN4 surface/subsurface temperatures and salinity dataset of the global oceans from the Hadley Center was used to evaluate the simulation results. Since the reanalysis data only cover the period from 1900 to 2022, the 1900–2000 temperature and salinity from the AS test were used for comparison.

Figure 4 shows the comparison of annual mean temperature and salinity at the surface and subsurface layers between the EN4 and AS tests, with SST shown in panels (a) and (c), subsurface sea temperature (300-meter-depth) shown in panels (b) and (d), sea surface salinity shown in panels (e) and (g), and subsurface sea salinity (300-meter-depth) shown in panels (f) and (h). The main spatial patterns of the whole-period averaged sea temperature and salinity were consistent between the reanalysis data and the simulation results. The surface salinity results of the simulation at the middle and low latitudes in the South Atlantic Ocean were lower. Based on previous model assessments (Liu et al., 2013; Holden et al., 2016), the PLASIM-GENIE model used in our work was able to reproduce the main features of the climate system in the Atlantic Ocean.

The temperature and salinity changes in the North Atlantic region from 1900 to 2000 were analyzed, as shown in Figure 5. The regional average temperature and salinity were standardized, which showed that the changes in the SST in the AS test were basically consistent with those observed during the whole period

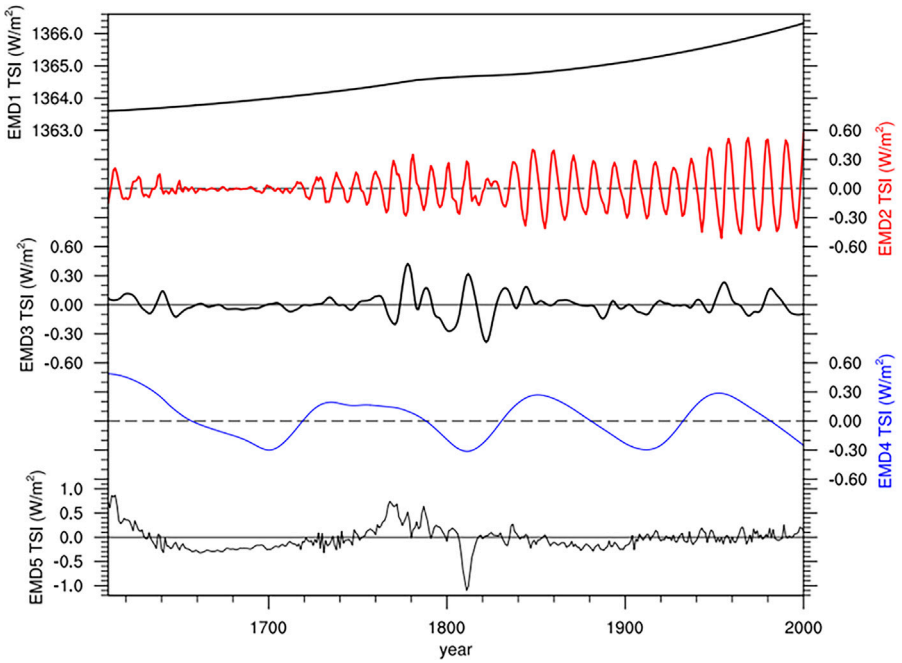

FIGURE 1
Five TSI EMD sequences used for reconstruction. EMD2 has a significant 11-year cycle. EMD4 has a significant 100-year cycle. EMD5 is the random item.

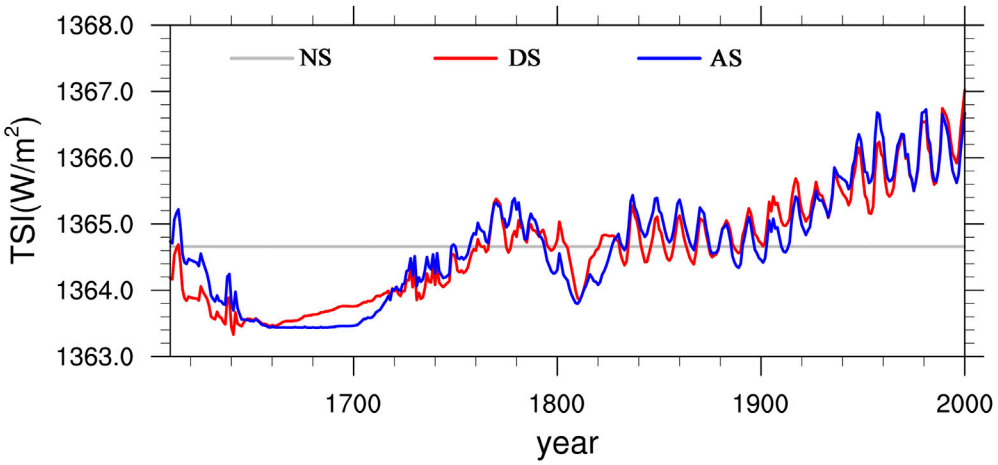

FIGURE 2
Three TSI sequences used for model forcing. NS: constant 1364.66 W/m² (gray); DS: combination of EMD1, EMD2, and EMD5 (red); AS: combination of the entire sequence, which is the TSI reconstructed by Lean (2010).

(Figure 5A). However, because the design of the model is not completely consistent with the actual climate change, certain differences in the trend changes of SST were observed in the last 10 years. After correlation analysis, the two sequences had a positive correlation of 0.272 by the 99% significance test for an EN4 SST lag of 3 years. SSS changes over the entire North Atlantic region were simulated poorly compared to temperature, with no significant correlation (Figure omitted). However, we further considered the changes over the small range of the sub-polar North Atlantic region (60°N–90°N, 80°W–30°E) where sea ice influence is significant in the AS test and EN4 datasets, and found a good correlation between the two. As shown in Figure 5B, the SSS changes of the two groups of data are very similar, with a positive correlation of 0.375 that passes the 99% significance test. Therefore, from the perspective of time change, the model well simulated the temperature and salinity changes in the North

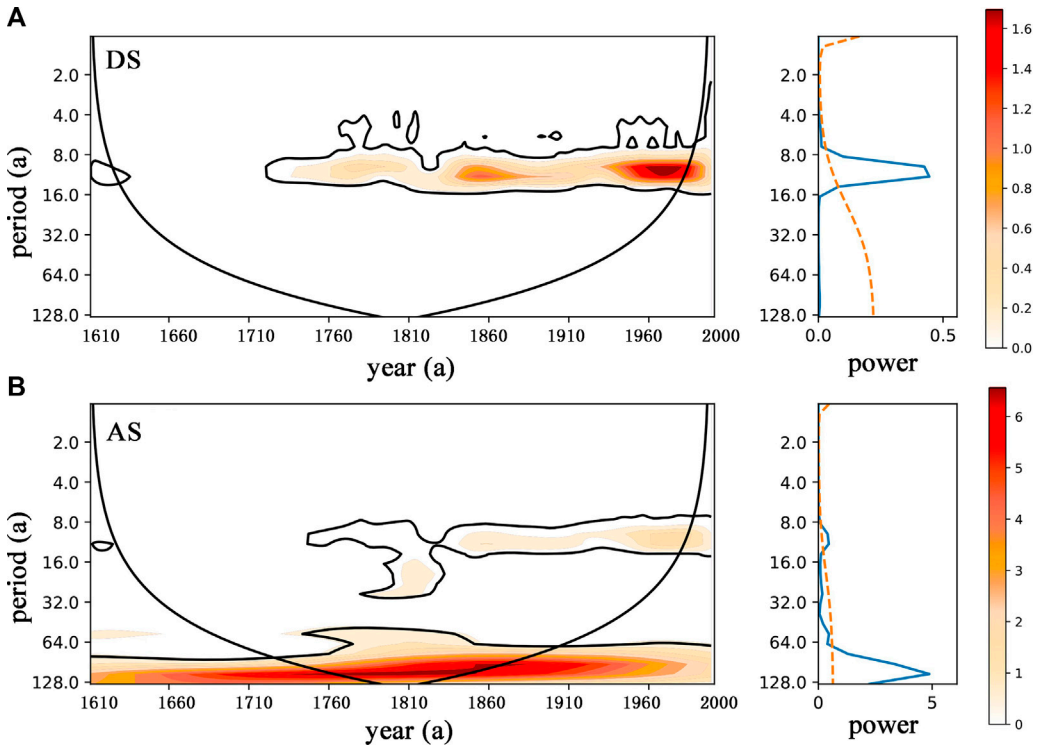

FIGURE 3
Wavelet analysis of TSI for the DS **(A)** and AS **(B)** tests. (Data are detrended. The dotted orange line is the 95% significance test).

Atlantic region, which provides a basis for further analysis of AMOC changes.

3.2 Long-term response of the AMOC

Lozier et al. (2019) defined the AMOC index (AMOCI) as the maximum value of the overturning stream function in the density space. Other studies also selected the maximum value of the overturning stream function at a certain latitude as the AMOC index (Huang et al., 2014; Menary and Scaife, 2014; Cheng et al., 2016). In our work, the maximum value of the overturning stream function in the depth profile at 48°N was set as the AMOCI. Figure 6 shows the mean AMOCI of the three tests with 11 years of smoothing, with a fitting curve from 1800 to 2000. The gray line is the NS test, the red line is the DS, and the blue line is the AS. The AMOCI of the NS varied between 12.16 Sv and 18.83 Sv (Sv: 1 Sverdrup = 1×10^6 $m^3/s^{(-1)}$), with a mean of 15.3 ± 1.27 Sv. The results of the DS and AS tests showed mean AMOC strengths of 15.21 ± 0.63 Sv and 15.23 ± 0.57 Sv, respectively.

The AMOCI of the NS test was consistent with the control run results by the Kiel Climate Model, in which the variation range of the AMOCI was 11–18 Sv (Park and Latif, 2012). The preindustrial control simulation in the HadGEM2-ES climate model had a mean AMOC strength of 13.6 ± 1.0 Sv (Menary et al., 2013). Menary and Scaife (2014) studied the influence of external forcings, such as volcanic eruptions and solar radiation, on the multidecadal AMOC change and found that the AMOC with multidecadal oscillation fluctuated between 12 Sv and 15 Sv during their 140-year experimental period. Compared with the recent observation dataset of the Rapid Climate Change (RAPID) program (AMOC intensity =18 ± 2.1 Sv) (Kanzow et al., 2010), the value of the NS experiment was slightly smaller. This result may be caused by the setting of other experimental conditions; for example, the fixed CO_2 concentration, to preindustrial values.

The fitting curve in Figure 6 shows an obviously declining centennial trend after 1800. In the DS test, the largest weakening trend was observed, with a decline rate of 0.51 Sv per hundred years (Sv/100a), while the values were 0.41 Sv/(100a) in the AS test and 0.18 Sv/(100a) in the NS test. That is, the AMOCI in the DS test decreased the most, followed by the AS test, while the NS test decreased the least.

A variable negative correlation between TSI and AMOC was observed during 1610–2000. In the DS test, the AMOCI had a maximum negative correlation of −0.292 with TSI with no lag at the 99% significance level. In the AS test, the correlation coefficient was −0.279 with no lag at the 99% significance level.

Figure 7 shows the results of wavelet analysis on the AMOCI series from the NS, AS, and DS tests. Panel (a) shows the results of the NS test, panel (b) shows the results of the DS test, and panel (c) shows the results of the AS test. In Figure 7A, significant quasi-35-year and quasi-65-year periodic cycles of the AMOCI are observed in the NS test, which should be attributed to the internal fluctuation of the climate system. In Figure 7B, two significant multidecadal

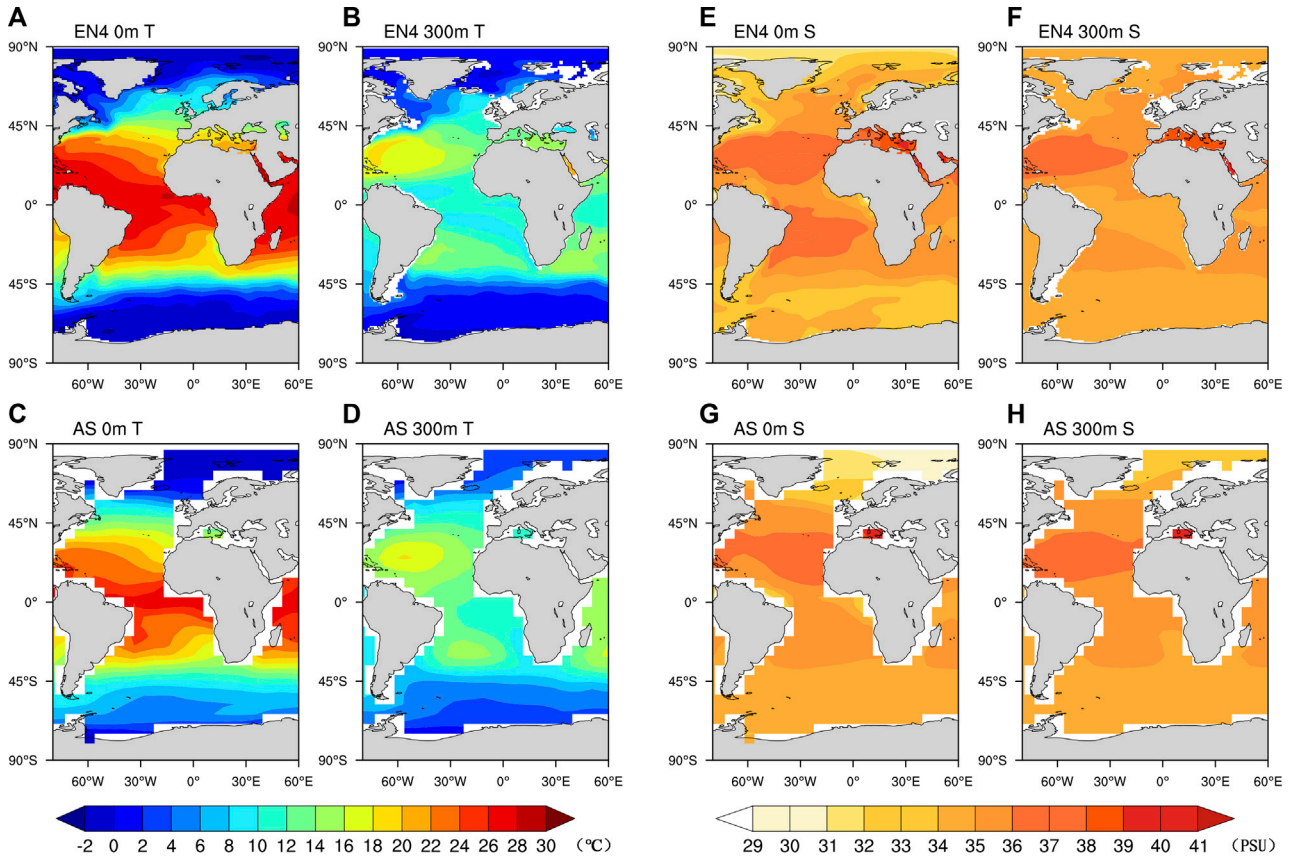

FIGURE 4
Results of the EN4 (top) and AS tests (bottom) from 1900 to 2000. Annual mean sea temperature at the surface (panels **(A,C)**) and 300 m depth (panels **(B,D)**). Annual mean sea salinity at the surface (panel **(E,G)**) and 300 m depth (panel **(F,H)**).

periodic cycles of quasi-40 years and quasi-70 years are observed, which are consistent with the two multidecadal variabilities in the AMOC suggested by other works (Delworth et al., 1993; Ortega et al., 2015). Compared with the result in NS, the two periodic cycles in the DS test show a 5-year extension. Figure 7C shows the two significant multidecadal cycles of quasi-40 years and quasi-100 years, in which the 100-year cycle has a larger spectrum power. Compared with the NS test (Figure 7A), in the AS test, the quasi-100 years cycle dominates the variability in AMOCI, which shows an entrainment effect (Park and Latif, 2012).

3.3 Effect of solar forcing

In Section 3.2, on one hand, AMOCI decreased in the three groups during the period from 1800 to 2000 and the decline rate in DS was the largest, followed by the AS test. On the other hand, the AMOCI showed obvious characteristics of two groups of multidecadal cycles, in which the cycle of AMOCI in the AS test was the longest, followed by the DS and NS tests. The AMOC showed an obvious significant response in strength and extended time scale variability to decadal and centennial TSI variations. Since ocean temperature and salinity are key factors influencing the AMOC, we investigated the responses of ocean temperature and salinity.

Figure 8 shows the difference in the ocean temperatures between the DS and NS tests (a–c) and between the AS and NS tests (b–f) at three ocean depths. Panels (a) and (d) show the results at the surface (SST). Panels (b) and (e) show the results at a depth of 300 m. Panels (c) and (f) show the results at a depth of 1,000 m.

The typical tripolar pattern of the SST in the N.A. region is shown in Figure 8A. The warming SST appears from the polar region to the Greenland–Norway Sea (GNS) with 95% confidence. A significant cooling at a depth of 300 m located on the east side of the Atlantic subtropical gyre was detected, as shown in Figure 8B, which is consistent with Canary cold current flows. Panel (c) shows significant cooling in the whole circulation field in the N.A. at a depth of 1,000 m. In the results showing the difference between AS and NS in Figure 8D, more area with a significant positive response of SST was observed in the GNS.

Figure 9 is similar to Figure 8, but it shows the differences in salinity. Figures 9A, D show a significant negative anomaly in the surface salinity in the Barents Sea (BRS) in the DS and AS tests. The significant westward extension of this negative anomaly was revealed in the DS test.

Figure 10 shows the differences in sea–ice cover (SIC) between the DS and AS tests and the control run (NS). Comparing panels (a) and (b), in the AS test, the full variability in TSI leads to more significant ice melting in the Arctic region.

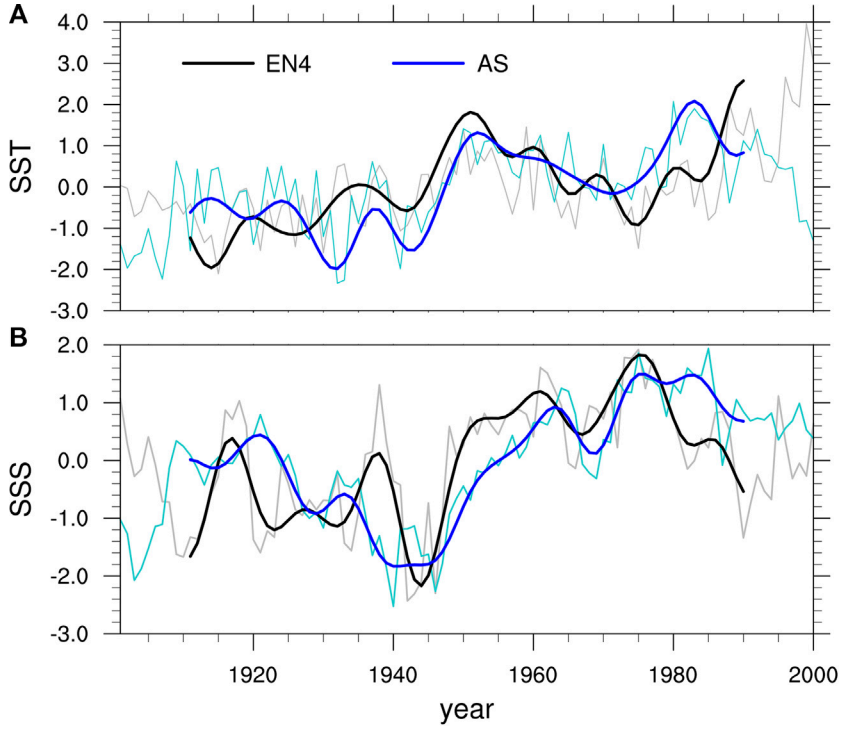

FIGURE 5
SST and SSS time sequences in the North Atlantic region of the AS test and EN4 dataset. **(A)** SST variation in the North Atlantic region (0°N–90°N, 80°W–30°E). **(B)** SSS variation in the subpolar North Atlantic region (60°N–90°N, 80°W–30°E). The data were all standardized.

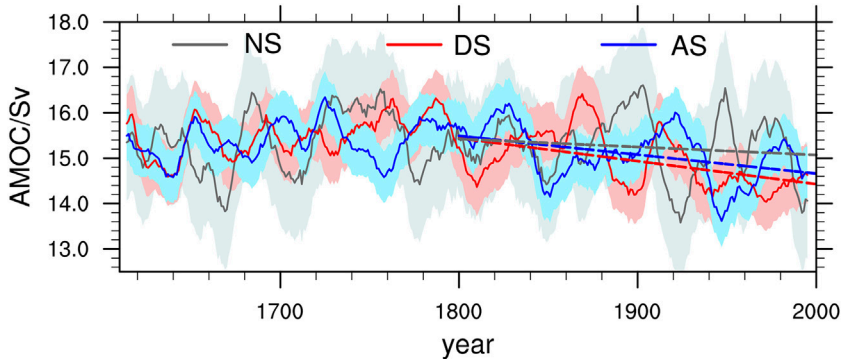

FIGURE 6
Eleven-year smoothed AMOCI for the composite mean of the three groups. NS is represented in gray; DS, in red; and AS, in blue. The shadow is the standard deviation of the AMOCI. The dashed line is the fitting curve of the AMOCI from 1800 to 2000.

Figure 11 shows the wind stress discrepancy among DS (panel (a)), AS (panel (b)), and NS. With the solar forcing, the wind stress in the Greenland Sea is significantly strengthened. In the DS test, there is a clear southward enhancement of wind stress, which would increase the East Greenland Current (EGC) and transport more melted fresh water from the Arctic to the west subpolar gyre (wSPG). Consequently, the salinity and temperature in the SPG would decline.

Figure 12 shows the mixed layer depth (MLD) discrepancy among DS (panel (a)), AS (panel (b)), and NS. With solar forcing, the MLD in the wSPG is shallower than that in the NS test. The DS test shows a significant negative response, which is consistent with the intensified EGC shown in Figure 11. This finding could lead to a decline in the AMOC.

To understand the accelerated weakening trend of the AMOC since 1800 due to solar forcing, the correlation of SST/sea surface

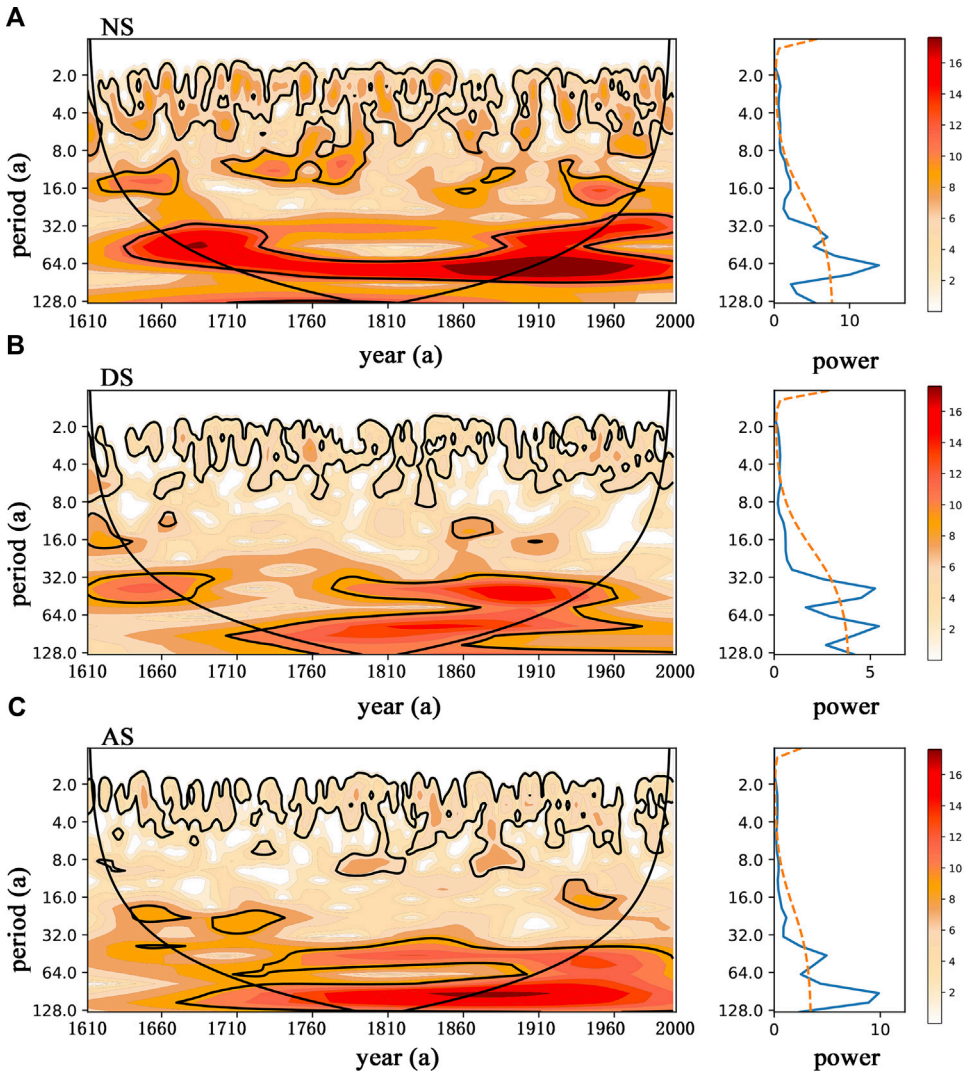

FIGURE 7
Wavelet power spectrum analysis of the composite mean AMOCI in the NS test **(A)**, DS test **(B),** and AS test **(C)**. The conical lines are wavelet cones, which denote the confidence region. The areas surrounded by the black lines in the wavelet cones are the areas that pass the 95% significance test. The power spectrum is shown on the right, with the dashed line indicating the 95% significance test line.

salinity (SSS) with the AMOCI was determined, as shown in Figure 13, in which panels (a–c) show the correlations between the SST and AMOCI, and panels (d–f) show the correlations between the SSS and AMOCI.

As shown in Figures 13A, D, with a constant TSI, SST and SSS in the SPG and the Labrador Sea (LAS) have a significant positive correlation with the AMOCI. In the DS and AS tests, the significant negative contribution of SSS in the BRS would be induced by varied TSI, which is shown in panels (e) and (f). The DS test showed more positive contributions to SST and SSS than in the AS test.

Figure 14 reveals the correlation between the TSI of the DS and AS tests and the SST/SSS results. In the DS test, TSI is negatively correlated with SST in the SPG and LAS. TSI was also positively correlated with SSS in the BRS. However, in the AS test, only a positive correlation between TSI and SSS could be found in the BRS, and a weak positive correlation between TSI and SST was detected in SPG and LAS.

By combining the results in Figure 8 with those in Figure 14, the SST in the SPG and the SSS in the BRS may account for the weakening of the AMOC in the DS test. The TSI was negatively correlated with SST in the SPG and positively correlated with SSS in the BRS, which would cause a negative contribution to the AMOC. In the AS test, the negative contribution of the SSS in the BRS to the AMOC could be partly balanced by the positive contribution of the SST in SPG. The Atlantic water heat transport through the BRS Opening and solar heat flux has been proposed to contribute equally to the climate variability in the BRS (Sando et al., 2010). A coupled ice–ocean model simulation by Long and Perrie (2017) revealed that increased lateral heat transport and solar radiation account for the increasing SST in the southern BRS, which is consistent with our simulation.

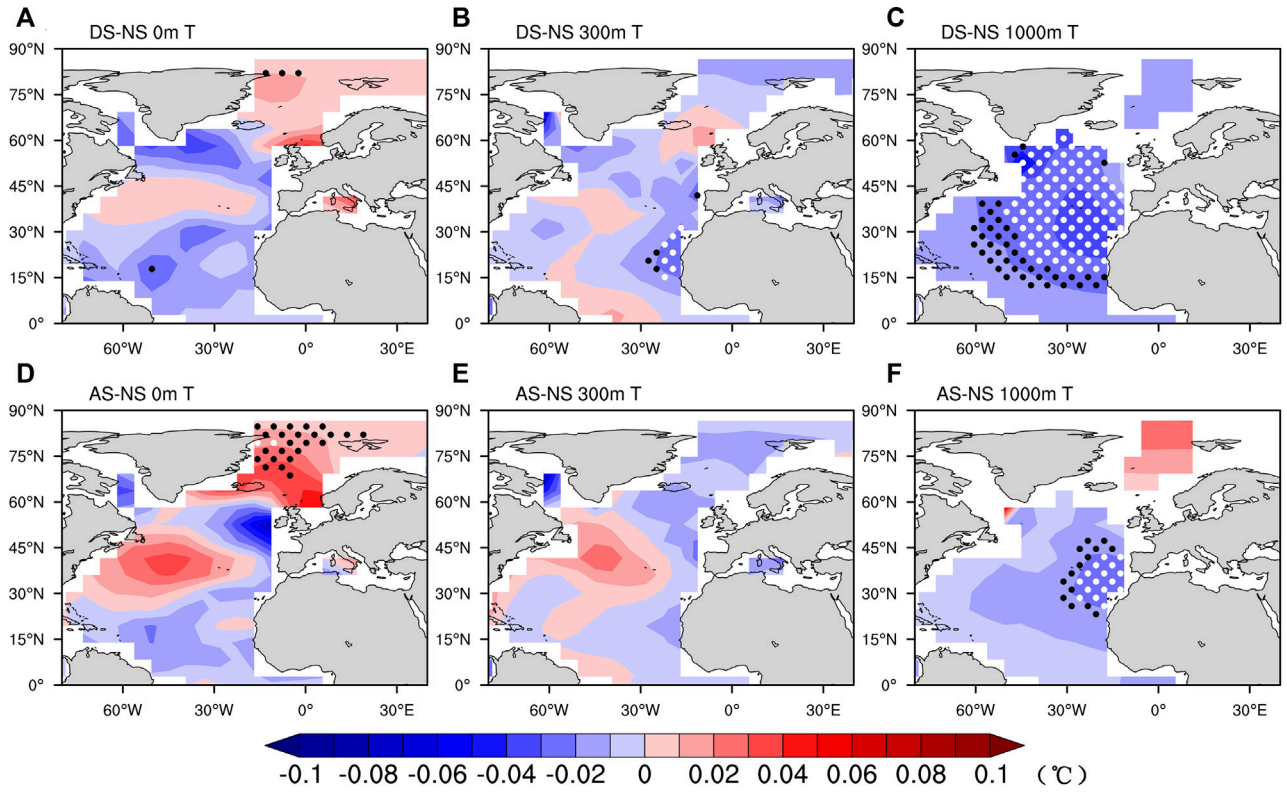

FIGURE 8
Sea temperature differences in the surface layer **(A)**, 300 m depth **(B),** and 1,000 m depth **(C)** in DS and NS between 1610 and 2000. **(D–F)** shows the differences temperature at surface, 300 m, 1000 m depth between AS and NS. The black dotted area is significant at the 95% level for a two-tailed T-test, and the white area is the 99% significance test.

The branch of Atlantic water transits the BRS, forming BRS Water (BSW) (Harris et al., 1998; Schauer et al., 2002). BSW is entrained in Arctic Intermediate Water (Schauer et al., 1997; Maslowski et al., 2004), which is ultimately exported to the N.A. and in turn contributes to the deeper branch of the AMOC (Aagaard and Woodgate, 2001; Barton et al., 2018). Therefore, SST and SSS in the BRS and SPG were treated as the key factors affecting the AMOC. Figures 15A, B show the regional mean SST and SSS in the BRS, 75°N–90°N, 20–60°E) and Figures 15C, D show those in the Labrador Sea and west SPG (LAS-wSPG, 50°N–70°N, 45°W–65°W) based on the NS (gray line), DS (red line), and AS (blue line) tests. The dashed line is the fitting curve of the results after 1800.

In the BRS, according to all three tests, the long-term trend of SST maintained a very small change and showed continuous increasing trends in SSS. Without the varied TSI forcing, the quantitative values of SST and SSS in the NS test were larger than those in the DS and AS tests. The increasing trend of SSS in the BRS may have contributed to the weakening trend of the AMOC after 1800.

In the LAS-wSPG region, the NS and DS tests showed a decreasing trend in SST. In the DS test, the trend showed a larger decreasing rate than that in the NS test. In the AS test, in the long term, the trend remained nearly constant; even after 1940, the SST showed a continuous increase. For the SSS in LAS-wSPG, the NS and AS tests showed a slight long-term increasing trend. The DS test showed a significant long-term decreasing trend. Thus, in the DS test, the decreased SSS is attributed to the intensified EGC and Greenland ice sheet (GrIS) melting.

Multilinear regression analysis was performed to evaluate the potential effects of the SST and SSS in the BRS and LAS-wSPG. The results are shown in Table 1, in which the SSS in LAS-wSPG accounted for most of the AMOC in all three tests. Compared with the results in Figures 13–15, in both the DS and AS tests with variable TSI, the increased SSS in the BRS led to a weakening of the AMOC. In the DS test, the decreased SSS in LAS-wSPG could strengthen this weakening trend. However, in the AS test, the increased SSS had a positive effect on the AMOC, which partly balanced the negative contribution of the SSS to the BRS.

4 Discussion and conclusion

Many previous simulations have addressed two kinds of multidecadal variations in AMOC and have reported two main variabilities at 20–30 and 50–70 years, which accounted for the internal interaction of ocean currents or ice–ocean–atmosphere in the N.A. region (Delworth et al., 1993; Timmermann et al., 1998; Ortega et al., 2015). In our simulation, the control simulation of NS reproduced both variabilities. The whole solar forcing in the AS test showed a

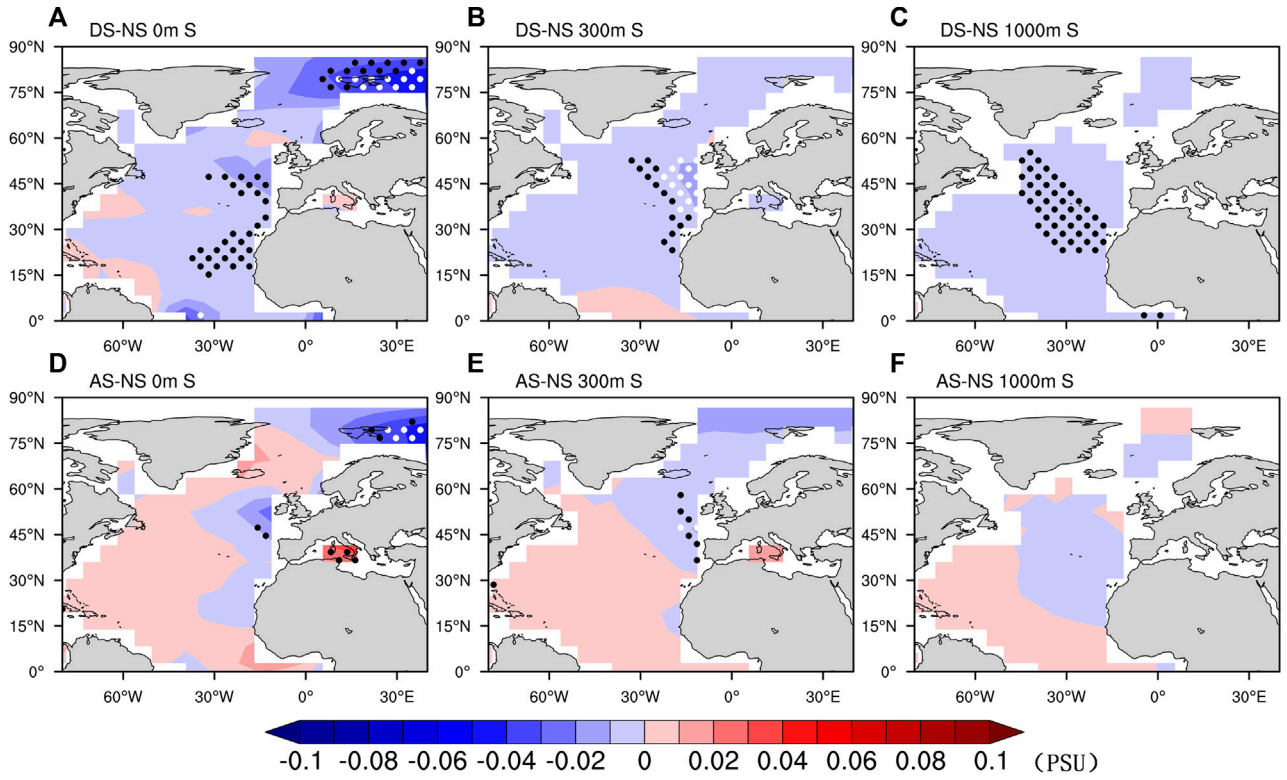

FIGURE 9
Same as Figure 8 but for the difference in salinity.

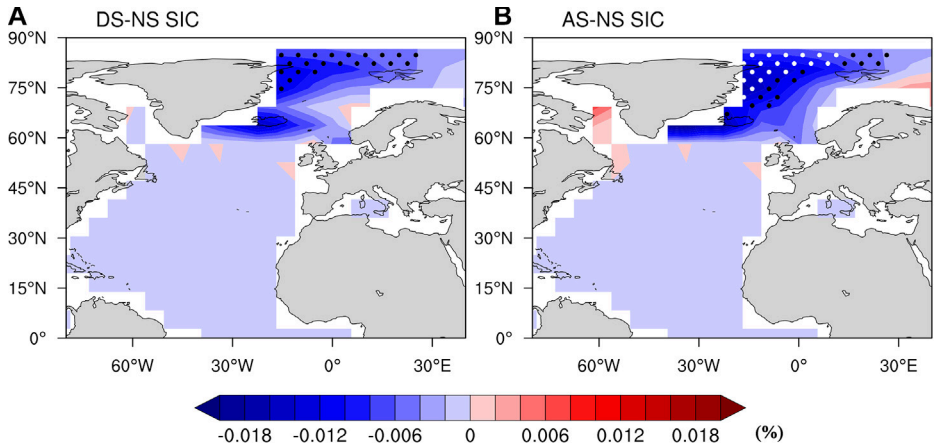

FIGURE 10
ea–ice cover (SIC) difference among DS **(A)**, AS **(B)**, and NS. The black dotted area is significant at the 95% level for a two-tailed T-test, while the white area is significant at the 99% level.

significantly extended period cycle. The high-frequency part of 30–40 years remained, and a low frequency of 100-year variation appeared due to the centennial variation in TSI, which could contribute to the low frequency (60–100 years) of variability in the AMOC based on the tree ring proxy (Gray et al., 2004).

The DS and AS tests showed that the SPG and BRS are crucial regions and that the SSS in these two regions is the main factor affecting the solar forcing that links to the AMOC. In the DS test, the SSS in SPG dominated the AMOC variability. Although we expected that the variation in GrIS melting due to the solar

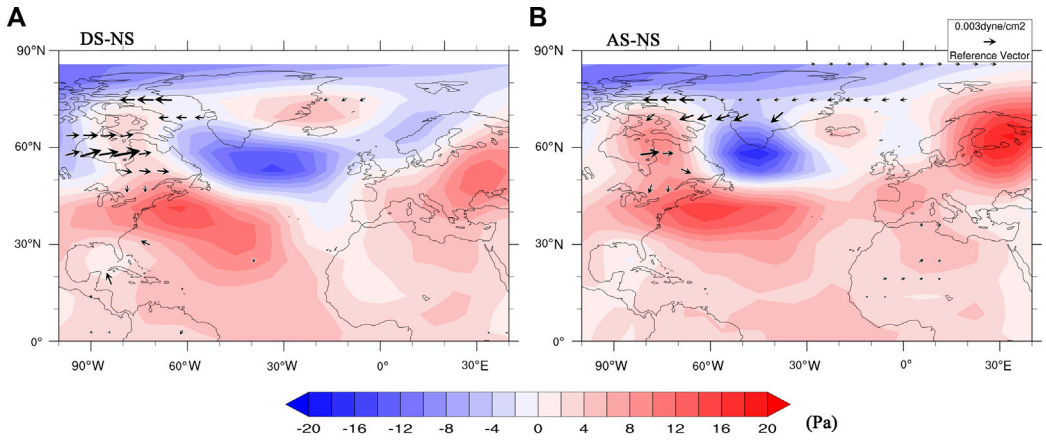

FIGURE 11
Wind stress discrepancy among DS **(A)**, AS **(B)**, and NS. The arrow represents the result with statistical significance at 99%. The contour indicates the difference in surface pressure.

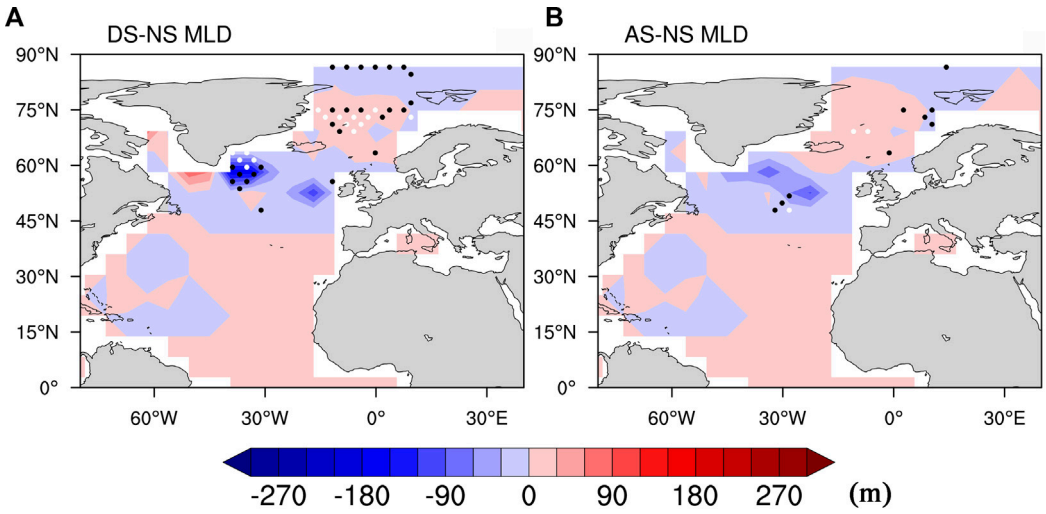

FIGURE 12
Same as Figure 10 but for the difference in MLD.

forcing would dominate the SSS variability in wSPG, the meridional wind was the key factor, which is consistent with other studies, including the study by Li et al. (2021). In the DS and AS tests, the solar forcing led to a significant positive effect on the strength of the southward meridional wind along East Greenland, which controls the EGC intensity. EGC intensity was negatively related to the SSS in SPG and was even considered to account for the phase reversal of a bidecadal ocean mode in the N.A (Escudier et al., 2013). Then, linked by EGC intensity, the decadal variation in TSI was negatively connected to the SSS in SPG. In the BRS, seawater is considered a water source that feeds the AMOC through the Nordic Sea (Lozier et al., 2019). The SIC has been proposed to be negatively related to the AMOC due to "the Barents Sea cooling machine" (øystein Skagseth, 2020), which suggested that the low SIC in the BRS increased the heat loss and weakened the deep thermal convection. The solar forcing in the DS or AS test positively affected the SIC in the BRS, which led to a negative effect on the AMOC due to the Barents Sea cooling machine.

The weakening of the AMOC in recent decades or even in the past few centuries has been reported (Caesar et al., 2018; Collins, 2019); however, this declining trend is controversial (Moat et al., 2020). The origin of the weakening has been attributed to anthropogenic effects (Swingedouw et al., 2022) or natural forcing (Latif et al., 2022). Our work assessed the contribution of solar forcing-modified TSI. With the real TSI in the AS test, the weakening AMOC with a decline rate of −0.41 Sv per century was investigated, which is approximately 24% of the whole AMOC weakening trend assessed by Caesar et al. (2018). Based on the sensitivity tests, the main effect of the TSI on AMOC weakening

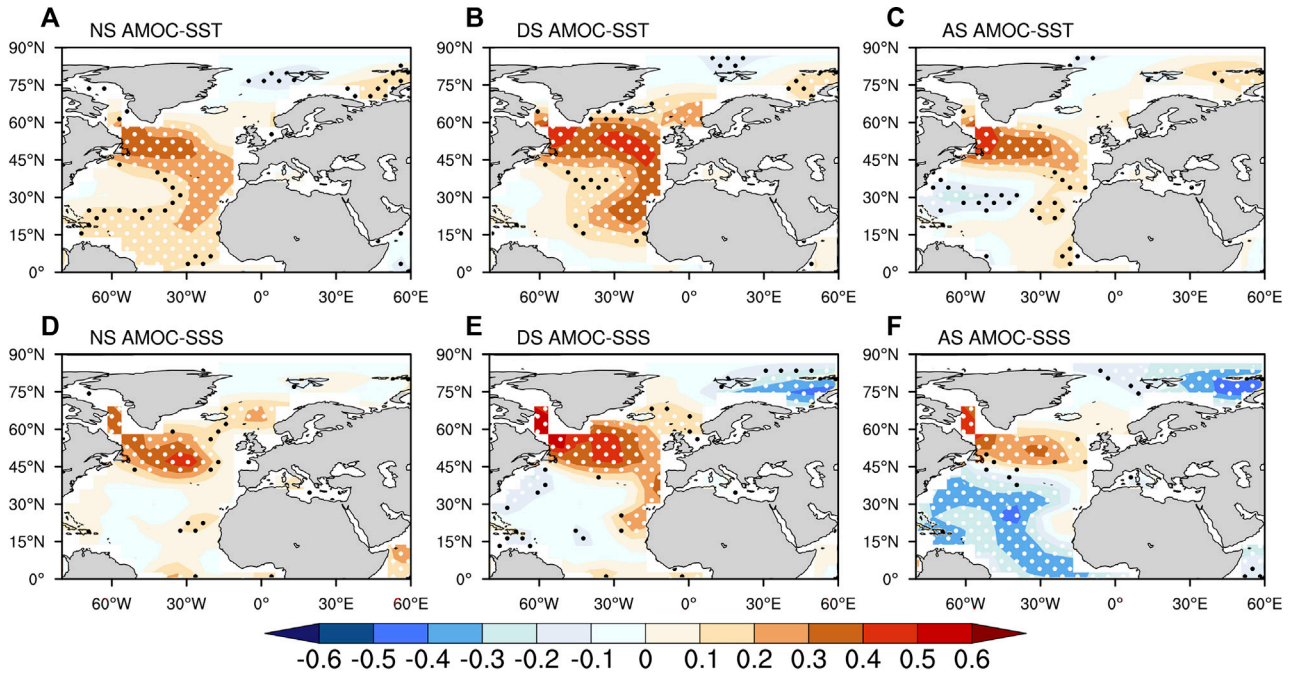

FIGURE 13
Correlation between annual AMOCI and SST (The top panels) and SSS (The bottom panels) in the NS test **(A,D)**, DS test **(B,E)**, and AS test **(C,F)** from 1800 to 2000. The black dots indicate the 95% significance level for the correlation, while the white indicates the 99% significance level. The contours represent the correlation coefficients.

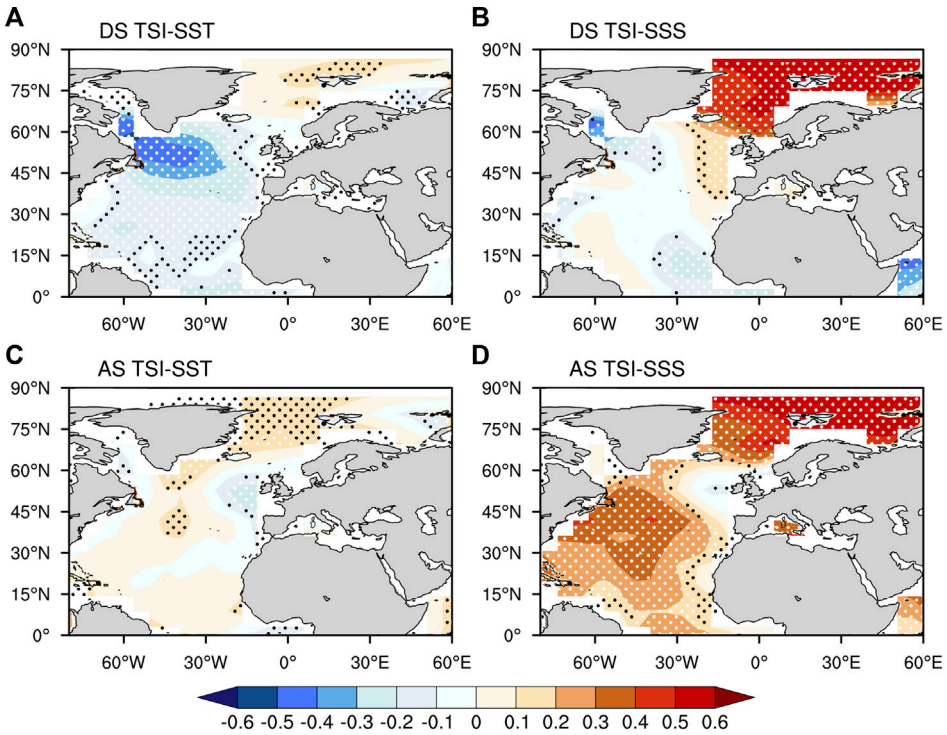

FIGURE 14
Oceanic fields correlated with the annual TSI forcing from 1800 to 2000. **(A)** SST in the DS test (in °C), **(B)** SSS in DS (in psu), **(C)** SST in the AS test, and **(D)** SSS in AS. The black dots in **(A–D)** indicate the 95% significance level, while the white dots indicate the 99% significance level. The contours represent correlation coefficients.

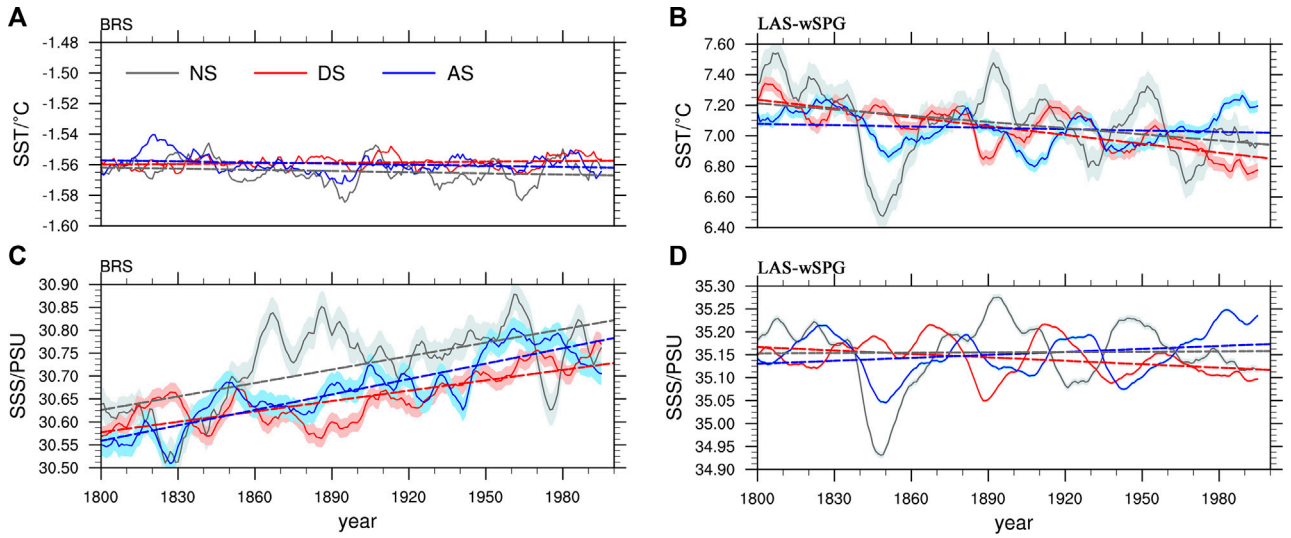

FIGURE 15
Mean values (11-year smoothed) of the sea surface temperature (SST) and sea surface salinity (SSS) in the BRS (75°N–90°N, 20°E–60°E) **(A,B)** and LAS-wSPG (50°N–70°N, 45°W–65°W) **(C,D)**. Gray line, NS test; red line, DS test; blue line, AS test; dashed lines, fitting curves of the results from 1800 to 2000.

TABLE 1 Solar forcing response of the AMOCI based on a regression analysis. The regression coefficients (R.C.) for the SST and SSS in the BRS and LAS-wSPG are shown. *95% statistical significance; **99% statistical significance.

AMOCI in the sensitivity test	Regression coefficients			
	SST in the BRS	SST in the LAS-wSPG	SSS in the BRS	SSS in the LAS-wSPG
NS test	−0.01	−0.05	0.05	0.35**
DS test	−0.02	−0.03	−0.12*	0.61**
AS test	0.06	0.13	−0.31**	0.32**

was attributed to the decadal variation in TSI through its negative effect on salinity in the LAS-wSPG and positive effect on salinity in the BRS. The decline in salinity due to increased freshwater flux from GrIS melting and transportation by strengthened EGC intensity and ice melting water from the LAS was the main contributor to the decline in the AMOC. In addition to TSI variability, which is 0.1%–0.2% of the TSI, solar activity also causes other changes that could directly affect the low atmosphere in the N.A., such as solar irradiance variation in the ultraviolet band (Haigh, 1994), the precipitation flux of energetic particles (Lu et al., 2008), solar wind, and the global electric circuit (Tinsley and Zhou, 2006). These factors could also be the source of the weakening AMOC. For example, solar wind-driven variability in relativistic electron flux could lead to a significant wind stress response in the N.A. region (Mironova et al., 2012; Zhou et al., 2014), and the response of the surface pressure and wind to the fluctuation in the interplanetary magnetic field has been reported (Lam et al., 2014; Zhou et al., 2018; Tinsley et al., 2021). The solar wind-driven global electric circuit has been suggested to lead to a significant atmospheric dynamic response in the N.A. region through electric-cloud microphysics (Tinsley, 2008), which could also contribute to AMOC variability.

This study assessed the effects of different TSI forcings on AMOC multidecadal variability since the Little Ice Age using an Earth System Model with intermediate complexity, PLASIM-GENIE, version 1.0. Although it is a coarse resolution model and the atmospheric part of the model is simplified, the main features of the ocean and atmosphere circulations can be successfully reproduced, including the two multidecadal variabilities in AMOC. According to the simulation results, the effect of GrIS melting through the Labrador Sea on the MLD in the wSPG was also detected.

Data availability statement

The raw data supporting the conclusion of this article will be made available by the authors, without undue reservation.

Author contributions

AY: conceptualization, methodology, software, simulation, data analysis, and writing—original draft; ZZ: data curation and writing—original draft; RZ: visualization; ZX: resources and investigation; LZ: conceptualization, funding acquisition, resources,

supervision, and writing—review and editing. All authors contributed to the article and approved the submitted version.

Funding

This work was funded in part by the Strategic Priority Research Program of CAS (Grant No. XBD 41000000) and the National Science Foundation of China (41971020 and 42271027).

Acknowledgments

The authors would like to thank Dr. Philip B. Holden for providing the code for PLASIM-GENIE v1.0.

Conflict of interest

The authors declare that the research was conducted in the absence of any commercial or financial relationships that could be construed as a potential conflict of interest.

Publisher's note

References

Aagaard, K., and Woodgate, R. A. (2001). Some thoughts on the freezing and melting of sea ice and their effects on the ocean. *Ocean. Model.* 3 (1-2), 127–135. doi:10.1016/S1463-5003(01)00005-1

Andrews, M. B., Knight, J. R., and Gray, L. J. (2015). A simulated lagged response of the North Atlantic Oscillation to the solar cycle over the period 1960-2009. *Environ. Res. Lett.* 10 (5), 054022. doi:10.1088/1748-9326/10/5/054022

Bagatinsky, V. A., and Diansky, N. A. (2021). Variability of the North Atlantic thermohaline circulation in different phases of the atlantic multidecadal oscillation from ocean objective analyses and reanalyses. *Izvestiya. Atmos. Ocean. Phys.* 57 (2), 208–219. doi:10.1134/S000143382102002X

Barton, B. I., Lenn, Y., and Lique, C. (2018). Observed atlantification of the Barents Sea causes the polar front to limit the expansion of winter sea ice. *J. Phys. Oceanogr.* 48 (8), 1849–1866. doi:10.1175/JPO-D-18-0003.1

Caesar, L., Mccarthy, G. D., Thornalley, D., Cahill, N., and Rahmstorf, S. (2021). Current atlantic meridional overturning circulation weakest in last millennium. *Nat. Geosci.* 14 (3), 118–120. doi:10.1038/s41561-021-00699-z

Caesar, L., Rahmstorf, S., Robinson, A., Feulner, G., and Saba, V. (2018). Observed fingerprint of a weakening Atlantic Ocean overturning circulation. *Nature* 556 (7700), 191–196. doi:10.1038/s41586-018-0006-5

Cheng, J., Liu, Z., Zhang, S., Liu, W., Dong, L., Liu, P., et al. (2016). Reduced interdecadal variability of atlantic meridional overturning circulation under global warming. *Proc. Natl. Acad. Sci.* 113 (12), 3175–3178. doi:10.1073/pnas.1519827113

Chylek, P., Folland, C., Frankcombe, L., Dijkstra, H., Lesins, G., and Dubey, M. (2012). Greenland ice core evidence for spatial and temporal variability of the Atlantic Multidecadal Oscillation. *Geophys. Res. Lett.* 39. doi:10.1029/2012GL051241

Collins, M. M. S. L. (2019). "IPCC special Report on the ocean and cryosphere in a changing climate," in *Chapter 6: Extremes, abrupt changes and managing risks*. Reprinted.

de Lavergne, C., Madec, G., Roquet, F., Holmes, R. M., and Mcdougall, T. J. (2017). Abyssal ocean overturning shaped by seafloor distribution. *Nature* 551 (7679), 181–186. doi:10.1038/nature24472

Delworth, M. L., Syukuro, M., and Ronald, S. (1993). Inter-decadal variations of the thermohaline circulation in a coupled ocean atmosphere model. *J. Clim.* 6. doi:10.1175/1520-0442(1993)006<1993:IVOTTC>2.0.CO;2

Eby, M., Weaver, A., Alexander, K., Zickfeld, K., Abe-Ouchi, A., Cimatoribus, A., et al. (2013). Historical and idealized climate model experiments: Anintercomparison of Earth system models of intermediate complexity. *Clim. Past* 9, 1111–1140. doi:10.5194/cp-9-1111-2013

Eddy, J. A. (1976). The maunder minimum. *Science* 192 (4245), 1189–1202. doi:10.1126/science.192.4245.1189

Escudier, R., Mignot, J., and Swingedouw, D. (2013). A 20-year coupled ocean-sea ice-atmosphere variability mode in the North Atlantic in an AOGCM. *Clim. Dyn.* 40, 619–636. doi:10.1007/s00382-012-1402-4

Foukal, P., Fröhlich, C., Spruit, H., and Wigley, T. M. L. (2006). Variations in solar luminosity and their effect on the Earth's climate. *Nature* 443, 161–166. doi:10.1038/nature05072

Goosse, H., and Renssen, H. (2006). Regional response of the climate system to solar forcing: The role of the ocean. *Space Sci. Rev.* 125 (1-4), 227–235. doi:10.1007/s11214-006-9059-0

Gray, L. J., Anstey, J. A., Kawatani, Y., Lu, H., Osprey, S., and Schenzinger, V. (2018). Surface impacts of the quasi biennial oscillation. *Atmos. Chem. Phys.* 18 (11), 8227–8247. doi:10.5194/acp-18-8227-2018

Gray, L. J., Beer, J., Geller, M., Haigh, J. D., Lockwood, M., Matthes, K., et al. (2010). Solar influences on climate. *Rev. Geophys.* 48. doi:10.1029/2009RG000282

Gray, L. J., Rumbold, S. T., and Shine, K. P. (2009). Stratospheric temperature and radiative forcing response to 11-year solar cycle changes in irradiance and ozone. *J. Atmos. Sci.* 66 (8), 2402–2417. doi:10.1175/2009JAS2866.1

Gray, L. J., Scaife, A. A., Mitchell, D. M., Osprey, S., Ineson, S., Hardiman, S., et al. (2013). A lagged response to the 11 year solar cycle in observed winter Atlantic/European weather patterns. *J. Geophys. Res. Atmos.* 118 (24), 13,405–13,420. doi:10.1002/2013JD020062

Gray, L. J., Woollings, T. J., Andrews, M., and Knight, J. (2016). Eleven-year solar cycle signal in the NAO and Atlantic/European blocking. *Q. J. R. Meteorological Soc.* 142 (698), 1890–1903. doi:10.1002/qj.2782

Gray, S. T., Graumlich, L. J., Betancourt, J. L., and Pederson, G. T. (2004). A tree-ring based reconstruction of the atlantic multidecadal oscillation since 1567 A.D. Reconstructed atlantic multidecadal oscillation. *Geophys. Res. Lett.* 31. doi:10.1029/2004GL019932

Gregory, J. M., Dixon, K. W., Stouffer, R. J., Weaver, A. J., Driesschaert, E., Eby, M., et al. (2005). A model intercomparison of changes in the Atlantic thermohaline circulation in response to increasing atmospheric CO_2 concentration. *Geophys. Res. Lett.* 32 (12), n/a. doi:10.1029/2005gl023209

Haigh, J. D. (1996). The impact of solar variability on climate. *Science* 272 (5264), 981–984. doi:10.1126/science.272.5264.981

Haigh, J. D. (1994). The role of stratospheric ozone in modulating the solar radiative forcing of climate. *Nature* 370, 544–546. doi:10.1038/370544a0

Harris, C. L., Plueddemann, A. J., and Gawarkiewicz, G. G. (1998). Water mass distribution and polar front structure in the Western Barents Sea. *J. Geophys. Research-Oceans* 103 (C2), 2905–2917. doi:10.1029/97JC02790

Holden, P. B., Edwards, N. R., Fraedrich, K., Kirk, E., Lunkeit, F., and Zhu, X. (2016). PLASIM–GENIE v1.0: A new intermediate complexity AOGCM. *Geosci. Model Dev.* 9 (9), 3347–3361. doi:10.5194/gmd-9-3347-2016

Holliday, N. P., Bersch, M., Berx, B., Chafik, L., Cunningham, S., Florindo-Lopez, C., et al. (2020). Ocean circulation causes the largest freshening event for 120 years in eastern subpolar North Atlantic. *Nat. Commun.* 11 (1), 585. doi:10.1038/s41467-020-14474-y

Huang, B., Zhu, J., and Yang, H. (2014). Mechanisms of atlantic meridional overturning circulation(AMOC)variability in a coupled ocean – atmosphere GCM. *Adv. Atmos. Sci.* 31, 241–251. doi:10.1007/s00376-013-3021-3

Huck, T., Vallis, G. K., and de Verdiere, A. C. (2001). On the robustness of the interdecadal modes of the thermohaline circulation. *J. Clim.* 14 (5), 940–963. doi:10.1175/1520-0442(2001)014<0940:OTROTI>2.0.CO;2

Ineson, S., Scaife, A. A., Knight, J. R., Manners, J. C., Dunstone, N. J., Gray, L. J., et al. (2011). Solar forcing of winter climate variability in the Northern Hemisphere. *Nat. Geosci.* 4 (11), 753–757. doi:10.1038/NGEO1282

Jackson, L. C., Roberts, M. J., Hewitt, H. T., Iovino, D., Koenigk, T., Meccia, V. L., et al. (2020). Impact of ocean resolution and mean state on the rate of AMOC weakening. *Clim. Dyn.* 55 (7-8), 1711–1732. doi:10.1007/s00382-020-05345-9

Jiang, Z., Liu, Z., Zhang, X., Eisenman, I., and Liu, W. (2014). Linear weakening of the AMOC in response to receding glacial ice sheets in CCSM3. *Geo. Res. Lett.* 41, 6252–6258. doi:10.1002/2014GL060891

Kanzow, T., Cunningham, S. A., Johns, W. E., Hirschi, J., Marotzke, J., Baringer, M. O., et al. (2010). Seasonal variability of the atlantic meridional overturning circulation at 26.5°N. *J. Clim.* 23 (21), 5678–5698. doi:10.1175/2010JCLI3389.1

Kuroda, Y., Kodera, K., Yoshida, K., Yukimoto, S., and Gray, L. (2022). Influence of the solar cycle on the North Atlantic oscillation. *J. Geophys. Research-Atmospheres* 127 (1). doi:10.1029/2021JD035519

Lam, M. M., Chisham, G., and Freeman, M. P. (2014). Solar wind-driven geopotential height anomalies originate in the Antarctic lower troposphere. *Geophys. Res. Lett.* 41, 6509–6514. doi:10.1002/2014GL061421

Latif, M., Sun, J., Visbeck, M., and Bordbar, H. (2022). Natural variability has dominated atlantic meridional overturning circulation since 1900. *Nat. Clim. Chang.* 12, 455–460. doi:10.1038/s41558-022-01342-4

Lean, J. L. (2010). Cycles and trends in solar irradiance and climate. *Wiley Interdiscip. Reviews-Climate Change* 1 (1), 111–122. doi:10.1002/wcc.18

Lee, S. K., and Wang, C. Z. (2010). Delayed advective oscillation of the atlantic thermohaline circulation. *J. Clim.* 23 (5), 1254–1261. doi:10.1175/2009JCLI3339.1

Lenton, T. M., Marsh, R., Price, A. R., Lunt, D. J., Aksenov, Y., Annan, J. D., et al. (2007). Effects of atmospheric dynamics and ocean resolution on bi-stability of the thermohaline circulation examined using the Grid ENabled Integrated Earth system modelling (GENIE) framework. *Clim. Dyn.* 29 (6), 591–613. doi:10.1007/s00382-007-0254-9

Li Dongling, S. L. L. Y. (2016). The influence of the meso-late Holocene cold water mass on disko bay, west Greenland. *Oceanol. Limnologia Sinica* 47 (06), 1126–1139. doi:10.11693/hyhz20160500101

Li, F., Lozier, M. S., Bacon, S., Bower, A. S., Cunningham, S. A., de Jong, M. F., et al. (2021). Subpolar North atlantic Western boundary density anomalies and the meridional overturning circulation. *Nat. Commun.* 12, 3002. doi:10.1038/s41467-021-23350-2

Lin, P., Yu, Z., Lü, J., Ding, M., Hu, A., and Liu, H. (2019). Two regimes of atlantic multidecadal oscillation: Cross-basin dependent or atlantic-intrinsic. *Sci. Bull.* 64 (3), 198–204. doi:10.1016/j.scib.2018.12.027

Liu Jing, S. L. L. Y. (2014). "Middle-late Holocene diatom assemblages and their paleoenvironmental evolution in West Greenland," in *Acta micropalaeontologica sinica*. CNKI:SUN:WSGT.0.2014-02-001.

Liu, J., Wang, B., Cane, M. A., Yim, S. Y., and Lee, J. Y. (2013). Divergent global precipitation changes induced by natural versus anthropogenic forcing. *Nature* 493 (7434), 656–659. doi:10.1038/nature11784

Long, Z., and Perrie, W. (2017). Changes in ocean temperature in the Barents Sea in the twenty-first century. *J. Clim.* 30 (15), 5901–5921. doi:10.1175/JCLI-D-16-0415.1

Lourantou, A., Chappellaz, J., Barnola, J., Masson-Delmotte, V., and Raynaud, D. (2010). Changes in atmospheric CO_2 and its carbon isotopic ratio during the penultimate deglaciation. *Quat. Sci. Rev.* 29, 1983–1992. doi:10.1016/j.quascirev.2010.05.002

Lozier, M. S., Li, F., Bacon, S., Bahr, F., Bower, A. S., Cunningham, S. A., et al. (2019). A sea change in our view of overturning in the subpolar North Atlantic. *Science* 363 (6426), 516–521. doi:10.1126/science.aau6592

Lu, H., Clilverd, M., Seppala, A., and Hood, L. (2008). Geomagnetic perturbations on stratospheric circulation in late winter and spring. *J. Geophys. Res.* 113, D16106. doi:10.1029/2007JD008915

Lynch-Stieglitz, J. (2017). The atlantic meridional overturning circulation and abrupt climate change. *Annu. Rev. Mar. Sci.* 9 (1), 83–104. doi:10.1146/annurev-marine-010816-060415

Mann, M. E., Steinman, B. A., Brouillette, D. J., and Miller, S. K. (2021). Multidecadal climate oscillations during the past millennium driven by volcanic forcing. *Science* 371 (6533), 1014–1019. doi:10.1126/science.abc5810

Mann, M. E., Zhang, Z. H., Rutherford, S., Bradley, R. S., Hughes, M. K., Shindell, D., et al. (2009). Global signatures and dynamical origins of the Little ice Age and medieval climate anomaly. *Science* 326 (5957), 1256–1260. doi:10.1126/science.1177303

Marsh, R., Yool, A., Lenton, T. M., Gulamati, M. Y., Edwards, N. R., Shepherd, J. G., et al. (2004). Bistability of the thermohaline circulation identified through comprehensive 2-parameter sweeps of an efficient climate model. *Clim. Dyn.* 23 (7-8), 761–777. doi:10.1007/s00382-004-0474-1

Maslowski, W., Marble, D., Walczowski, W., Schauer, U., Clement, J. L., and Semtner, A. J. (2004). On climatological mass, heat, and salt transports through the Barents Sea and Fram Strait from a pan-Arctic coupled ice-ocean model simulation. *J. Geophys. Research-Oceans* 109 (C3). doi:10.1029/2001JC001039

Masson-Delmotte, V. P. Z. A. (2021). *The physical science Basis.Contribution of working group I to the Sixth assessment Report of the intergovernmental panel on climate change: IPCC, climate change 2021*. Reprinted.

Menary, M. B., Roberts, C. D., Palmer, M. D., Halloran, P. R., Jackson, L., Wood, R. A., et al. (2013). Mechanisms of aerosol-forced AMOC variability in a state of the art climate model. *J. Geophys. Research-Oceans* 118 (4), 2087–2096. doi:10.1002/jgrc.20178

Menary, M. B., and Scaife, A. A. (2014). Naturally forced multidecadal variability of the Atlantic meridional overturning circulation. *Clim. Dyn.* 42 (5-6), 1347–1362. doi:10.1007/s00382-013-2028-x

Mironova, I., Tinsley, B. A., and Zhou, L. (2012). The links between atmospheric vorticity, radiation belt electrons, and the solar wind. *Adv. Space Res.* 50. doi:10.1016/j.asr.2011.03.043

Moat, B. I., Smeed, D. A., Frajka-Williams, E., Desbruyères, D. G., Beaulieu, C., Johns, W. E., et al. (2020). Pending recovery in the strength of the meridional overturning circulation at 26° N. *Ocean Sci.* 16, 863–874. doi:10.5194/os-16-863-2020

Muthers, S., Raible, C. C., Rozanov, E., and Stocker, T. F. (2016). Response of the AMOC to reduced solar radiation – The modulating role of atmospheric chemistry. *Earth Syst. Dyn.* 7 (4), 877–892. doi:10.5194/esd-7-877-2016

Negre, C., Zahn, R., Thomas, A. L., Masque, P., Henderson, G. M., Martinez-Mendez, G., et al. (2010). Reversed flow of atlantic deep water during the last glacial maximum. *Nature* 468 (7320), 84–88. doi:10.1038/nature09508

Ortega, P., Mignot, J., Swingedouw, D., Sevellec, F., and Guilyardi, E. (2015). Reconciling two alternative mechanisms behind bi-decadal variability in the North Atlantic. *Prog. Oceanogr.* 137, 237–249. doi:10.1016/j.pocean.2015.06.009

øystein Skagseth, T. E. M. Å., Eldevik, T., Årthun, M., Asbjørnsen, H., Lien, V. S., and Smedsrud, L. H. (2020). Reduced efficiency of the Barents Sea cooling machine. *Nat. Clim. Change* 10, 661–666. doi:10.1038/s41558-020-0772-6

Park, W., and Latif, M. (2012). Atlantic Meridional Overturning Circulation response to idealized external forcing. *Clim. Dyn.* 39 (7-8), 1709–1726. doi:10.1007/s00382-011-1212-0

Ran Lihua, J. H. K. K. (2008). Paleomarine environmental records since the middle Holocene in the northern North Atlantic. *Mar. Sci. Bull* (05), 39–46+7. doi:10.3969/j.issn.1001-6392.2008.05.007

Sando, A. B., Nilsen, J. E. O., Gao, Y., and Lohmann, K. (2010). Importance of heat transport and local air-sea heat fluxes for Barents Sea climate variability. *J. Geophys. Research-Oceans* 115, C07013. doi:10.1029/2009JC005884

Scaife, A. A., Ineson, S., Knight, J. R., Gray, L., Kodera, K., and Smith, D. M. (2013). A mechanism for lagged North Atlantic climate response to solar variability. *Geophys. Res. Lett.* 40 (2), 434–439. doi:10.1002/grl.50099

Schauer, U., Loeng, H., Rudels, B., Ozhigin, V. K., and Dieck, W. (2002). Atlantic water flow through the Barents and kara seas. *Deep-Sea Res. Part Oceanogr. Res. Pap.* 49 (12), 2281–2298. doi:10.1016/S0967-0637(02)00125-5

Schauer, U., Muench, R. D., Rudels, B., and Timokhov, L. (1997). Impact of eastern arctic shelf waters on the Nansen Basin intermediate layers. *J. Geophys. Research-Oceans* 102 (C2), 3371–3382. doi:10.1029/96JC03366

Sedlacek, J., and Mysak, L. A. (2009). A model study of the Little ice Age and beyond: Changes in ocean heat content, hydrography and circulation since 1500. *Clim. Dyn.* 33 (4), 461–475. doi:10.1007/s00382-008-0503-6

Shindell, D. T., Schmidt, G. A., Mann, M. E., Rind, D., and Waple, A. (2001). Solar forcing of regional climate change during the maunder minimum. *Science* 294 (5549), 2149–2152. doi:10.1126/science.1064363

Sjolte, J., Sturm, C., Adolphi, F., Vinther, B. M., Werner, M., Lohmann, G., et al. (2018). Solar and volcanic forcing of North Atlantic climate inferred from a process-based reconstruction. *Clim. Past* 14 (8), 1179–1194. doi:10.5194/cp-14-1179-2018

Sutton, R. T., and Hodson, D. (2005). Atlantic Ocean forcing of North American and European summer climate. *Science* 309 (5731), 115–118. doi:10.1126/science.1109496

Swingedouw, D., Houssais, M. N., Herbaut, C., Blaizot, A. C., Devilliers, M., and Deshayes, J. (2022). AMOC recent and future trends: A crucial role for oceanic resolution and Greenland melting? *Front. Clim.* 4, 838310–838318. doi:10.3389/fclim.2022.838310

Swingedouw, D., Terray, L., Cassou, C., Voldoire, A., Salas-Melia, D., and Servonnat, J. (2011). Natural forcing of climate during the last millennium: Fingerprint of solar variability. *Clim. Dyn.* 36 (7-8), 1349–1364. doi:10.1007/s00382-010-0803-5

Timmermann, A., Latif, M., Voss, R., and Grotzner, A. (1998). Northern hemispheric interdecadal variability: A coupled air-sea mode. *J. Clim.* 11 (8), 1906–1931. doi:10.1175/1520-0442-11.8.1906

Ting, M. F., Kushnir, Y., Seager, R., and Li, C. H. (2011). Robust features of Atlantic multi-decadal variability and its climate impacts. *Geophys. Res. Lett.* 38. doi:10.1029/2011GL048712

Tinsley, B. A. (2008). The global atmospheric electric circuit and its effects on cloud microphysics. *Rep. Prog. Phys.* 71, 066801. doi:10.1088/0034-4885/71/6/066801

Tinsley, B. A., and Zhou, L. (2006). Initial results of a global circuit model with variable stratospheric and tropospheric aerosols. *J. Geophys. Research-Atmospheres* 111 (D16), D16205. doi:10.1029/2005JD006988

Tinsley, B. A., Zhou, L., Wang, L., and Zhang, L. (2021). Seasonal and solar wind sector duration influences on the correlation of high latitude clouds with ionospheric potential. *J. Geophys. Res. Atmos.* 126. doi:10.1029/2020JD034201

Wang, Y. J., Cheng, H., Edwards, R. L., He, Y. Q., Kong, X. G., An, Z. S., et al. (2005). The Holocene asian monsoon: Links to solar changes and North Atlantic climate. *Science* 308 (5723), 854–857. doi:10.1126/science.1106296

Xu, H. Y., Miyahara, H., Horiuchi, K., Matsuzaki, H., Sun, H. L., Luo, W. J., et al. (2019). High-resolution records of Be-10 in endogenic travertine from baishuitai, China: A new proxy record of annual solar activity? *Quat. Sci. Rev.* 216, 34–46. doi:10.1016/j.quascirev.2019.05.012

Yu Lei, G. Y. W. H. (2009). Response and mechanism of Atlantic meridional overturning circulation under high latitude freshwater forcing enhancement. *Chin. J. Atmos. Sci* 33 (01), 179–196. CNKI:SUN:DQXK.0.2009-01-015.

Yu, L., Gao, Y., Wang, H., Guo, D., and Li, S. (2010). The responses of east Asian summer monsoon to the North Atlantic meridional overturning circulation in an enhanced freshwater input simulation. *Chin. Sci. Bull.* 54, 4724–4732. doi:10.1007/s11434-009-0720-3

Zhang, R. (2008). Coherent surface-subsurface fingerprint of the Atlantic meridional overturning circulation. *Geophys. Res. Lett.* 35 (20), L20705. doi:10.1029/2008GL035463

Zhang, R., and Delworth, T. L. (2006). Impact of Atlantic multidecadal oscillations on India/Sahel rainfall and Atlantic hurricanes. *Geophys. Res. Lett.* 33 (17), L17712. doi:10.1029/2006GL026267

Zhao Yun, S. L. L. Y. (2015). "Paleo-environmental records based on diatoms since the last deglaciation of the northern shelf of Iceland," in *Marine geology and quaternary geology*. CNKI:SUN:HYDZ.0.2015-03-014.

Zhou, L. M., Tinsley, B. A., and Huang, J. (2014). Effects on winter circulation of short and long term solar wind changes. *Adv. Space Res.* 54, 2478–2490. doi:10.1016/j.asr.2013.09.017

Zhou, L., Tinsley, B. A., Wang, L., and Burns, G. (2018). The zonal-mean and regional tropospheric pressure responses to changes in ionospheric potential. *J. Atmos. Solar-Terrestrial Phys.* 171, 111–118. doi:10.1016/j.jastp.2017.07.010

Zorita, E., Von Storch, H., Gonzalez-Rouco, F. J., Cubasch, U., Luterbacher, J., Legutke, S., et al. (2004). Climate evolution in the last five centuries simulated by an atmosphere-ocean model: Global temperatures, the North Atlantic oscillation and the late maunder minimum. *Meteorol. Z.* 13 (4), 271–289. doi:10.1127/0941-2948/2004/0013-0271

frontiers | Frontiers in Earth Science

TYPE Original Research
PUBLISHED 05 July 2023
DOI 10.3389/feart.2023.1204191

OPEN ACCESS

EDITED BY
Limin Zhou,
East China Normal University, China

REVIEWED BY
Anthony Lupo,
University of Missouri, United States
Ana G. Elias,
Universidad Nacional de Tucumán, Argentina

*CORRESPONDENCE
Robert J. Leamon,
robert.j.leamon@nasa.gov

RECEIVED 11 April 2023
ACCEPTED 13 June 2023
PUBLISHED 05 July 2023

CITATION
Leamon RJ (2023), The triple-dip La Niña of 2020–22: updates to the correlation of ENSO with the termination of solar cycles.
Front. Earth Sci. 11:1204191.
doi: 10.3389/feart.2023.1204191

The triple-dip La Niña of 2020–22: updates to the correlation of ENSO with the termination of solar cycles

Robert J. Leamon[1,2]*

[1]Goddard Planetary Heliophysics Institute, University of Maryland–Baltimore County, Baltimore, MD, United States, [2]NASA Goddard Space Flight Center, Greenbelt, MD, United States

The Sun provides the energy required to sustain life on Earth and drive our planet's atmosphere. However, establishing a solid physical connection between solar and tropospheric variability has posed a considerable challenge across the spectrum of Earth-system science. Over the past few years a new picture to describe solar variability has developed, based on observing, understanding and tracing the progression, interaction and intrinsic variability of the magnetized activity bands that belong to the Sun's 22-year magnetic activity cycle. A solar cycle's fiducial clock does not run from the canonical min or max, instead resetting when all old cycle polarity magnetic flux is cancelled at the equator, an event dubbed the "termination" of that solar cycle, or terminator. In a recent paper, we demonstrated with high statistical significance, a correlation between the occurrence of termination of the last five solar cycles and the transition from El Niño to La Niña in the Pacific Ocean, and predicted that there would be a transition to La Niña in mid 2020. La Niña did indeed begin in mid-2020, and endured into 2023 as a rare "triple dip" event, but some of the solar predictions made did not occur until late 2021. This work examines what went right, what went wrong, the correlations between El Niño, La Niña and geomagnetic activity indices, and what might be expected for the general trends of large-scale global climate in the next decade.

KEYWORDS

sun, solar activity cycle, solar effects, space weather, solar irradiance, El Niño Southern oscillation, global change, global climate models

1 Introduction

In Leamon et al. (2021), hereafter Paper I, we showed a strong correlation between the end of solar activity cycles and the warm-to-cold transitions of the El Niño Southern Oscillation, that held for the 5 cycles 19–23, or from 1966–7 to 2010–11.

The key breakthrough that led to this discovery was thinking not about sunspot number as the driving measure, the defining measure, of a solar cycle. Rather, a solar cycle's fiducial clock does not run from the canonical sunspot min, or max, but instead resets when all old cycle polarity magnetic flux is cancelled at the equator, an event dubbed the "termination" of that Hale cycle, or terminator. The terminators occur about 18–24 months after the canonical minima, and although originally defined through observation of solar EUV and magnetograph images, *i.e.*, 2-D images, the time when the monthly-averaged solar radio flux, F10.7 = 90 sfu is a good scalar proxy. For further details on Hale Cycle terminators, their predictability, and impacts on solar activity and (space weather) output, the interested

reader is directed to McIntosh et al. (2019), Dikpati et al. (2019), Leamon et al. (2020, 2022), and McIntosh et al. (2023).

Although published in April 2021, Paper I was originally submitted in November 2017, a testament, perhaps, of its introductory paragraph, including:

> It is fair, then, to say that searching for the connection between the variability of the solar atmosphere and that of our troposphere has become "third-rail science"—not to be touched at any cost.

Paper I made the prediction that the termination of solar cycle 24 would occur in mid-late 2020, and thus there would be a transition to La Niña at that time. That was a very bold prediction when submitted in 2017, less bold on final acceptance. La Niña did indeed begin in mid-2020, and endured into 2023 as a rare "triple dip" event. However, some of the solar predictions that Paper I made did not occur until late 2021. In what follows we present updated data through January 2023, and examine what went right for Leamon et al., what went wrong, and what might be expected for the general trends of large-scale global climate in the next decade.

2 New observations

Figure 1 continues, and extends, our presentation of solar activity markers and proxies back over the past 60 years, combining and updating figures 1, 4 of Paper I through January 2023. Progressing down the figure, we see the total and hemispheric sunspot numbers, with colored shading representing a dominance of the north (red) and south (blue) hemispheres. Panel (b) shows a data-motivated depiction of the latitudinal progression of the Sun's magnetic cycle bands. As initially developed by (McIntosh et al., 2014), these "band-o-grams" are set by three parameters (points in time): the times of hemispheric maxima (the time that the band starts moving equatorward from 55°) and the terminator time. We assume a linear progression between those times in each hemisphere. Above 55° latitude we prescribe a linear progression of 10° per year, in keeping with "Rush to the Poles" seen in coronal green line data (Altrock, 1997). Panel (c) shows the variation of the galactic cosmic ray flux (GCR) as measured at the University of Oulu, Finland, anti-correlated with solar activity as strong (and complicated) solar magnetic fields essentially block cosmic rays from entering the Solar System, and hence the Earth's atmosphere during periods of high solar activity. Panel (d) shows the Penticton 10.7 cm radio flux, F10.7, which can be viewed as a disk-integrated measure of magnetic field strength and complexity. Above the ~65 sfu floor, which is predominantly thermal in nature and produced all over the solar disk, F10.7 is generated primarily by bremsstrahlung and gyro resonance with sufficiently strong magnetic field—*i.e.* in the corona above sunspots. Note that the final data point (January 2023, F10.7 = 182 sfu) is higher than any single month in Cycle 24! Panel (e) shows the composite index of the Sun's chromospheric variability measured through the ultraviolet emission of singly ionized Magnesium. This serves two purposes: (1) it is a measure of magnetic field strength in the chromosphere, and (2) it is a close proxy for solar ultraviolet flux at wavelengths near ~200 nm that are important for molecular oxygen dissociation and ozone formation in the stratosphere Finally, panel (f) shows the NOAA Oceanic Niño index (ONI), our primary measure of El Niño and La Niña. ONI is defined as the 3-month running mean of ERSST. v5 SST anomalies in the Niño 3.4 region [5°N–5°S, 120°–170°W]. Through all panels the vertical dashed lines mark the Hale Cycle terminators, including now that of Cycle 24 in December 2021 (McIntosh et al., 2023).

2.1 Successes

Paper I predicted that there would be a transition to La Niña in mid-2020. La Niña did indeed begin in mid-2020. Success! Well, maybe.

The ~5% drop in GCRs at the terminator was one of their defining features in Paper I. The GCRs again drop 5.5% after *observed* terminator in December 2021. As of January 2023, the GCR level is below the average of the entire 59-year record, is approaching the peak (nadir) level of Cycle 24, and is ahead of the same phase of Cycle 24, a year after terminator. This is not surprising given that all measures of solar activity have been higher in Cycle 25 than the relatively weak last Cycle 24.

Not shown in Figure 1 are measures of Atlantic hurricane season activity. Paper I predicted "a particularly active season in 2021, and maybe even 2020, depending on exactly when the terminator and ENSO transition occurs," based on the historical record: all Atlantic hurricane seasons are relatively strong in the first year of La Niña after an El Niño, when waters are still warm but upper-level wind shears are favorable for cyclone genesis (Vecchi and Soden, 2007). This was indeed the case: 2020 was the most active Atlantic hurricane season on record, and the 2021 season was the third-most active. The 2022 season was near-normal. In terms of *economic* damage, the costliest season to date was 2017, which again had a (weak) La Niña after the extremely strong 2015–16 El Niño.

2.2 What went wrong

Paper I's prediction for a 2020 La Niña was derived from solar cycle predictions of Leamon et al. (2020). They forecast late 2020, which did mean that Cycle 24 would have been short at less than 10 years (compared to almost 13.0 years for Cycle 23).

In reality, the Hale Cycle terminator did not occur until December 2021 (although November 2020 was a tantalising failure to launch). This meant that the length of Cycle 24 was 10.75 years, still (slightly) faster than average. McIntosh et al. (2023) discuss the failure to launch in more detail, and present a revised outlook for the *solar* activity for the rest of Cycle 25.

In Paper I we consciously tried to avoid discussion of causation, which, due to its controversial nature could lead to dismissal of the empirical relationship, and we wanted to open a broader scientific discussion of solar coupling to the Earth and its environment. But Paper I did suggest that corpuscular radiation—specifically galactic cosmic rays modulated by the large-scale heliospheric magnetic field—appears to have greater influence on ENSO than photons, independent of the exact mechanism by which they couple to the atmosphere. As Figure 1 shows, the second of the triple dips *does*

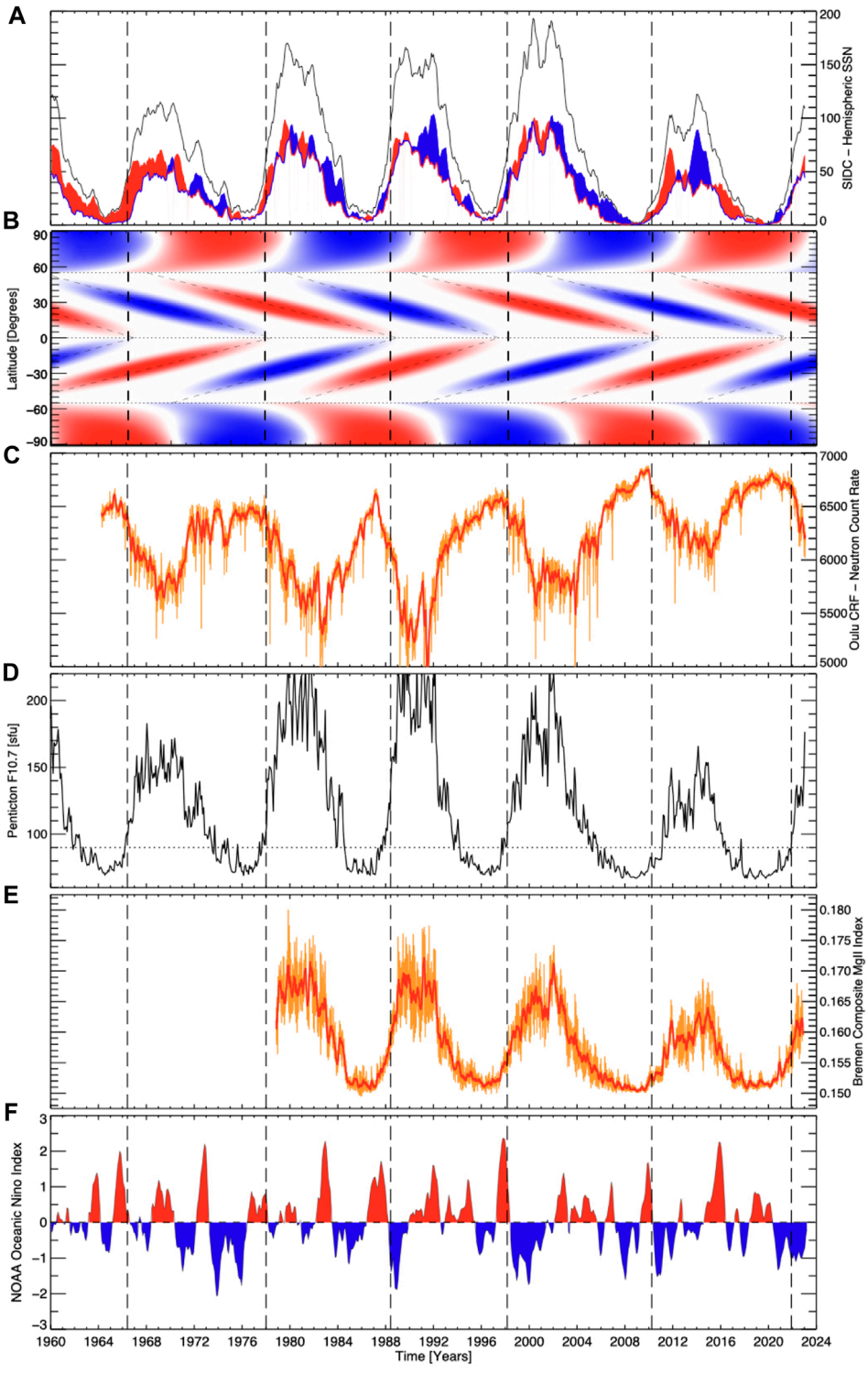

FIGURE 1
Comparing more than five decades of solar evolution and activity proxies, combining and updating Figures 1, 4 of Leamon et al. (2021). From top to bottom: **(A)** the total (black) and hemispheric sunspot numbers (north—red, and blue—south); **(B)** a data-motivated schematic depiction of the Sun's 22 years magnetic activity cycle; **(C)** the Oulu cosmic-ray flux; **(D)** the Penticton F10.7 cm radio flux; **(E)** the Mg II index of ultraviolet variability from the University of Bremen; and **(F)** the variability of the Oceanic Niño Index (ONI) over the same epoch. The black dashed lines mark the cycle terminators, including the December 2021 end of Cycle 24.

align with the big drop in cosmic rays. There is a small drop (from the peak) that aligns with the onset of La Niña in 2020, but this is only a ~1% drop in GCRs, compared to the ~5% drop at the terminator in 2021. So it is plausible, then, that the onset of La Niña in 2020 was just "random" internal fluctuations of the atmospheric system, and the second and third years were sustained by whatever mechanism drives the external coupling.

Nevertheless, independent of the exact coupling mechanisms, the question must be asked, why has the pattern occurred and reoccurred regularly for the past five solar cycles, or 60 years?

3 Discussion

3.1 Mechanisms

So if we cannot conclusively link the flux of incoming cosmic rays or other charged particles, how else might we explain a solar influence? We offer two potential solar-terrestrial mechanisms: (1) the effects of the Heliospheric Current Sheet, and (2) the effects of geomagnetic activity indices.

Figure 2 again shows the F10.7 radio flux, Oulu GCR count, and the ONI record, but adds the computed Heliospheric Current Sheet (HCS) tilt angle from the Wilcox Solar Observatory (Scherrer et al., 1977; Wilcox et al., 1980). Note that the Wilcox Solar Observatory has only been extant since 1976, so we only show the 4 + cycles since then (It did, conveniently perhaps, come online at the nadir of the Cycle 19 minimum.)

The first thing to observe in Figure 2 is that, like F10.7 = 90, when the HCS tilt exceeds the Earth's orbital obliquity, 23.4°, is also a good (scalar) proxy for the terminator. Similarly, on the downslope of the cycle, there seems to be a correlation between the decay of the post-maximum El Niño and when $H = 23.4°$.

The rapid rise in F10.7, and the increasing number and complexity of solar active regions that lead to the increasing tilt of the HCS, all occur at the terminators. When the slope of the change in solar activity is the steepest, that is, the period when the gradients in our atmosphere are the largest. It follows that there should be two such times, once during the ascending phase and again during the declining phase of the cycle. There is a difference in Figure 2 in the decay of tilt between two odd and the two even cycles, something that also visible in the production of X-flares (Leamon and McIntosh, 2022), and does seem to track in the timing of the El Niño to La Niña transition. The six terminators in Paper I, while highly statistically significant for $N = 6$, was a tough pill to swallow for some readers; a correlation for 4 (or even 2) is too much.

Figure 3 shows the relationship between the geomagnetic activity indices A_p (red) and K_p (green) and ONI record. The K_p and A_p record extends back further (1932) than ONI (1950), but we show the full record to see that the gross behaviour of A_p within a solar cycle remains similar independent of cycle strength. Two things are immediately apparent: 1) The El Niño near solar minimum (that precedes the El Niño to La Niña transition described in Paper I at the terminators—the dashed black lines) corresponds quite well to the local minimum of A_p. The transition to La Niña then occurs as the solar cycle and geomagnetic activity ramps up at the terminator. 2) We identify the strongest mid-cycle El Niño peaks (and mark them by pink dashed lines). These tend to be associated with the highest levels of geomagnetic activity. Note also the close—but not exact—correspondence of the dotted lines marking the 2/5 of the cycle phase and the El Niño peak pink lines, especially for the last 4 cycles (after 1978). Not every local maximum or minimum in A_p corresponds to an El Niño (and *vice versa*),

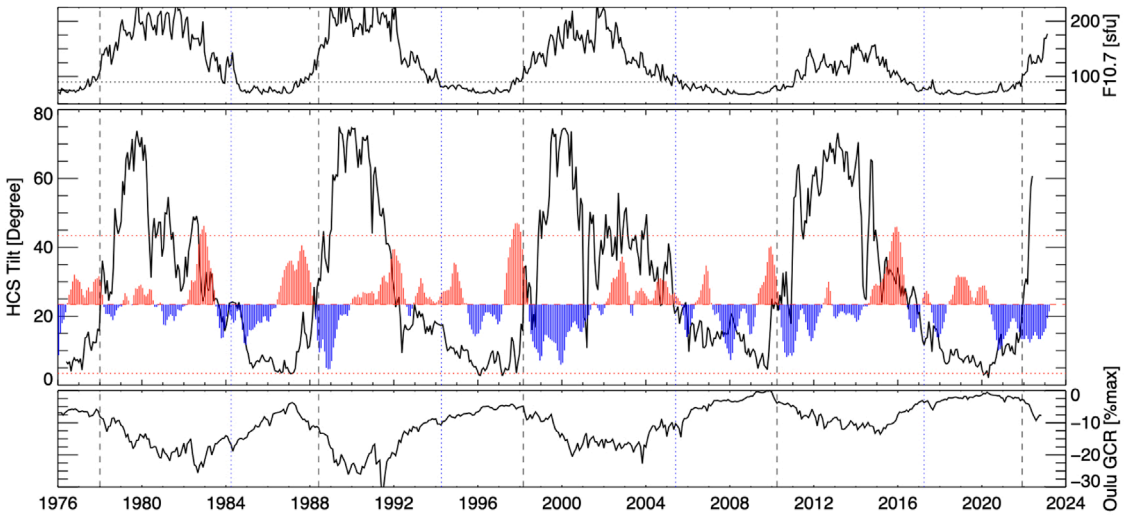

FIGURE 2
Showing the relationship between the tilt of the HCS current sheet (black) and ONI (red). The zero point for the ONI trace is offset to 23.4° (Earth's axial tilt), and the horizontal dotted lines correspond to ONI=±2. The top and bottom sub-panels show F10.7 and the Oulu GCR flux as context for the landmarks of the solar activity cycle. In all panels the dashed vertical lines correspond the Hale Cycle terminators, and the dotted vertical lines correspond to the 3/5 "pre-terminator" point as described in Chapman et al. (2020) and Leamon et al. (2022).

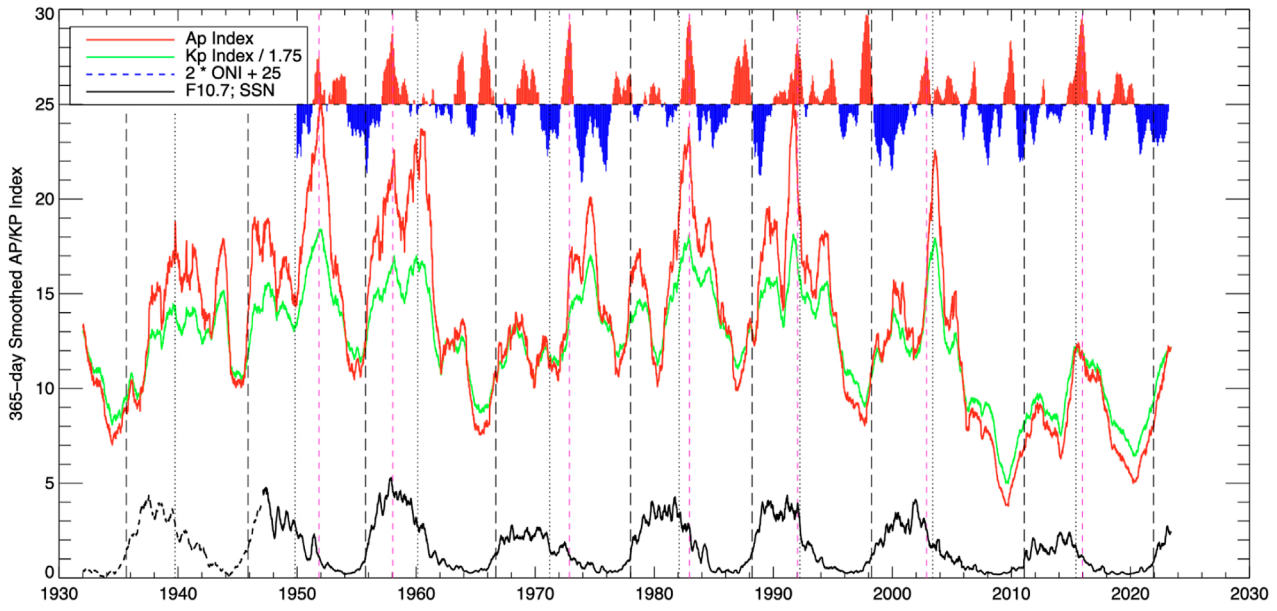

FIGURE 3
Showing the relationship between the geomagnetic activity indices A_p (red) and K_p (green) and ONI (red and blue, hot and cold). At the bottom the F10.7 radio flux (and SSN for 1932–1947) are shown, smoothed and scaled, as context for the landmarks of the solar activity cycle. As in Figure 2, the dashed vertical lines correspond the Hale Cycle terminators, but here the dotted vertical lines correspond to the 2/5 point—which closely corresponds to the sharp drop in F10.7 seen here, and the reformation of the sun's polar coronal holes Leamon et al. (2022). The magenta dashed lines mark the dates of the (strongest) mid-cycle El Niños. Note the close correspondence of the 2/5 dotted lines and El Niño peak dashed magenta lines, especially after 1978 (*i.e.*, the past 4 cycles).

but this simple correspondence can explain almost 90% (17/19) of El Niño events (ONI>0.5) since 1950. With 2 misses and 4 false alarms, the Heidke skill score for this forecast (or rather, hindcast) is $H = 0.71$.

Historically, scientists have looked at the extrema of the solar cycle, trying to correlate the timing of solar max and solar min with dynamic changes in terrestrial climatology and weather. Instead, we should be investigating the timing of the extrema of the first derivative of solar cycle activity and looking for correlations with global dynamic changes in our atmosphere during those periods. It is then no small wonder things appear more clearly when using the terminator as the fiducial time to anchor terrestrial climate epoch analyses. Summarizing, it would appear that an El Niño tends to develop starting at solar min and shortly after solar max, when the solar inputs to the atmosphere are relatively stable, and the ensuing transition to La Niña occurs when solar output is undergoing most change.

3.2 Other recent results

A common suggestion from previous studies is that a multi-year La Niña tends to occur after a strong El Niño. Iwakiri and Watanabe, 2021 argued that the duration of La Niña is strongly influenced by the amplitude of the preceding El Niño in both observations and a long climate model simulation, presumably due to a large initial discharge. The weird thing about 2020–23, however, is that this prolonged La Niña, unlike previous triple dips, has not come after a strong El Niño, which tends to build up a lot of ocean heat that takes a year or two to dissipate. Where's the dynamics for this? (Jones, 2022, quoting NOAA's M. L'Heureux). Paper I noted that the period of terminator-ENSO correlation corresponds to the close-to-monotonic rise in global sea surface temperatures over the same time period. As the world warms, and ice sheets melt, a slowdown of the Atlantic Meridional Overturning Circulation (AMOC) is expected from the influx of fresh water (Boers, 2021). Orihuela-Pinto et al. (2022) modelled a collapse of the AMOC, and showed that such a collapse would strengthen Pacific Trade Winds, push warm waters to the west, thus creating more La Niña-like conditions.

Generally, large-scale global climate models predict a shift to more El Niño-like states as the oceans warm, but this is not what has been observed for the past 50 years or so—as Figure 1 shows. Similarly, we may consider the shift from negative PDO to positive in 1976–77 (e.g., Mantua et al., 1997; Minobe, 1997, 2000), previously referred to as the Great Pacific Climate Shift (e.g., Trenberth, 1990; Miller et al., 1994), and the subsequent reversal to negative PDO in 2002–03, but neither phase shift is immediately apparent in Figure 1. The observed AMOC indices flipped from positive to negative in the early 1960s, but the statistical correlations of Paper I endured after the return flip in the late 1990s.

We have focused here (again) on ONI, a single scalar quantity of an area-averaged SST anomaly, rather than 2D maps of SST. McKenna and Karamperidou (2022) report a difference in the response of atmospheric blocking events, synoptic weather patterns that divert the jet stream from its typical path in the mid-to high-latitudes between "canonical" and "Modoki" (or Eastern and Central Pacific) flavors of El Niño. Put another way, there is more to *teleconnections* than just a scalar index can convey: the different

teleconnections and impacts on the mid-latitude circulation coming from Eastern and Central Pacific flavors of El Niño demonstrate different effects in blocking frequency and characteristics; significant disruption of weather patterns caused by blocking can have severe ecological and socio-economic impacts.

Similarly, the difference between flavors of El Niño (Trenberth and Stepaniak, 2001; Kao and Yu, 2009; Yeh et al., 2009) may be associated with the difference between those forced by "fixed" solar cycle landmarks and those responding to oceanic/atmospheric dynamics, although increasingly warming sea surface temperatures may just be the dominant Modoki El Niño driver (Yeh et al., 2009).

3.3 The "standard" cycle

As previously discussed, it is clear from the modified superposed epoch analysis of Leamon et al. (2021) that there is a coherent pattern to solar output and the terrestrial response from terminator to terminator. The logical next step, then, is to average the five solar cycles for which we have data into a "standard" unit cycle that we may use for skillful prediction of future cycles. As first discussed in Leamon et al. (2022), the monthly series data are interpolated into 100 points from terminator to terminator, and an average and standard deviation are computed at each interpolation point for each of 5 cycles. This is shown in Figure 4 for F10.7 and the ONI El Niño index. Given the almost 100% variation in peak F10.7 from cycle to cycle, the average rises more smoothly from solar minimum to solar maximum than any of the individual cycles of Figure 1; however, the changes in standard deviation (*i.e.*, the edges in the red shaded envelope) are clear at $x \sim 0$, 0.4 and 0.6, and are driven by changes below the solar surface as discussed in Leamon et al. (2022).

We may use this standard cycle as a prediction tool for future ENSO events. In the language of the state vector simple dynamic system formulation of ENSO of Penland and Sardeshmukh (1995), it is clear that the forcing term $f(t)$ must have a strong negative impulse at the terminator, a (strong) positive impulse through sunspot minimum to the terminator (and one—or two, for each hemisphere—weaker positive impulses associated with increased (E)UV insolation around solar maximum). As the **Appendix A** and Figure 6 show [and as Torrence and Compo (1998) and Wang and Wang (1996) showed], there is always power at shorter scales (3–7 years), between the terminators, corresponding to the intrinsic mode(s) of the system. Even if it is likely that the mid-cycle El Niño peak is related to increased solar output, we do not attempt to fit every bump and wiggle, or explain every (non-terminator) feature as solar-induced.

Nevertheless, it is an interesting exercise, if not an acid test, to predict Cycle 25: we *already* can estimate the date of the next terminator date as the brightpoints revealing the Cycle 25 activity band (*cf.* Figure 1B) have been present on disk long enough such that we may make a (well-constrained) linear extrapolation for when the Cycle 25 terminator will be and thus convert the unit cycle to real time out beyond 2030. This is shown in Figure 5: The lower panel updates Figure 1B, and shows the progression of the EUV brightpoint distribution for cycles 22–25. That the cycle 25 progression is well-established and, more importantly, linear, is clear. From extrapolating observations of the distribution of EUV brightpoints and their equatorward progression, we can already estimate that the Cycle 25 terminator will be late 2031—early 2032,

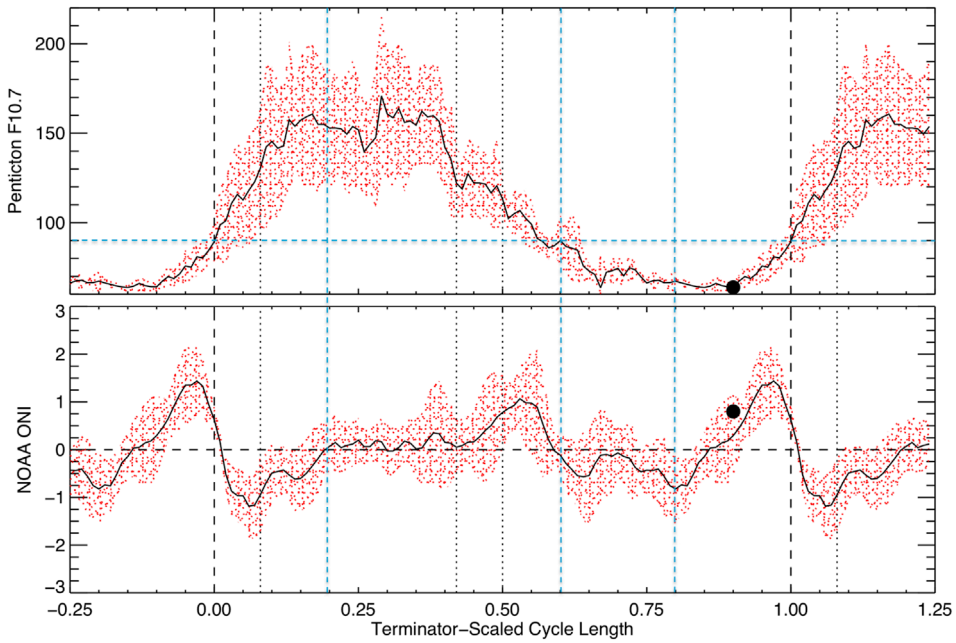

FIGURE 4
"Standard" cycle for F10.7 (top) and ONI (bottom). The black trace is the average of the past five cycles [*cf.* Figures 1D, F], and the red envelope is defined by one standard deviation. The dots correspond to 2019 May, the blue horizontal dashed line in the F10.7 panel corresponds to the terminator proxy threshold of 90 sfu, and the blue vertical dashed lines correspond to the "Circle of Fifths" outlined in Leamon et al. (2022).

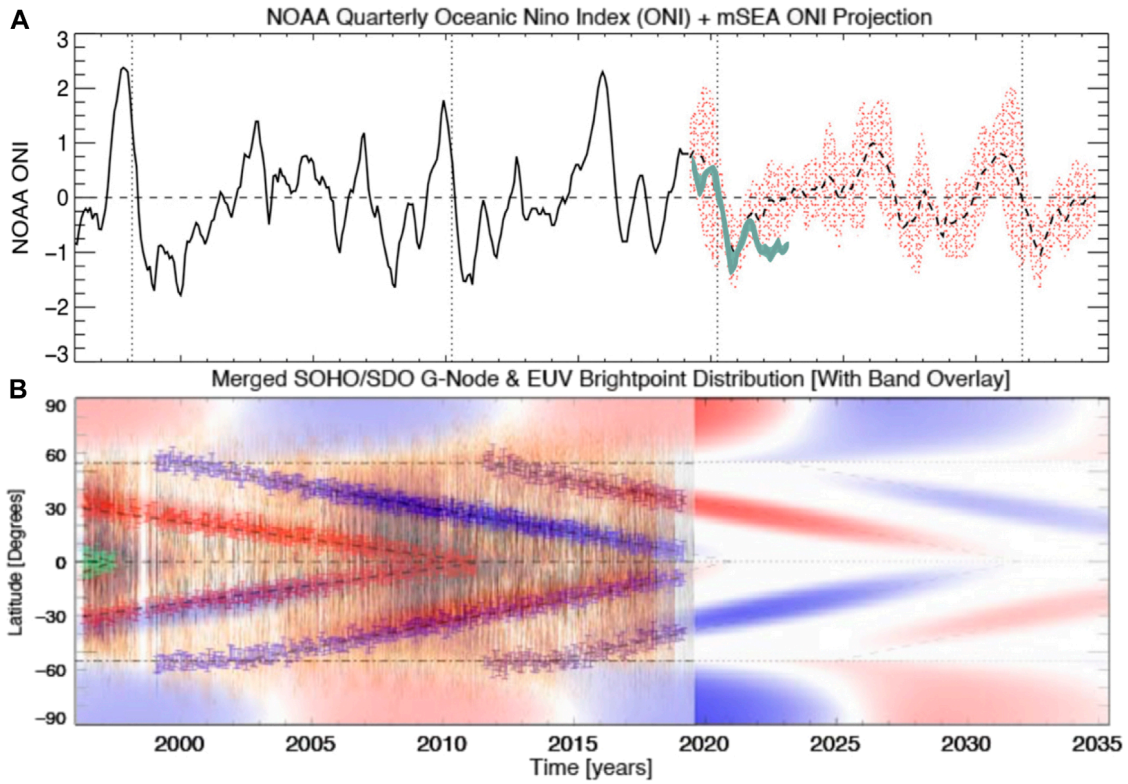

FIGURE 5
(A) "Standard" cycle from Figure 4 projected forward in (real) time from March 2019 to the Cycle 25 terminator, currently predicted (Leamon et al., 2022, from extrapolation of the band progression shown in Panel **(B)**) to be late 2031. EL Niños may be expected around 2026 and 2031, and La Niñas in 2020–21, 2027–28 and 2032–33. The green trace shows the *observed* ONI from March 2019 to December 2022.

with an uncertainty of about 9 months. Following the method outlined by Leamon et al. (2022), we can confirm, refine, or revise our estimate for the length of Cycle 25 as early as its polar field reversal, which we currently estimate to be early-mid 2024. While the timing of the 2020 La Niña turned out to be perhaps more serendipitous than a fantastic prediction 3 years in advance, the triple-dip that endured into 2023, and its previous analogue of 1998–2001, *one whole Hale Cycle ago*, we may be cautiously optimistic for the general trends of large-scale solar climate in the next decade.

The year 2023 does present an immediate acid test: Figure 5 suggests, statistically, that there will not a (strong) El Niño until around 2026, after the peak of the sunspot cycle, and ENSO-neutral conditions will endure from now until then. This is in contrast with the increasing drumbeats of a (strong) El Niño from various government agencies and NGOs worldwide. For instance, the European Center for Medium-Range Weather Forecasting (ECMWF) model, predicted on 1 Feb 2023 that the July measurement would be +0.91, a ~2° shift from January. That model might be the outlier in the ensemble, and we are the wrong side of the classic "spring Predictably Barrier," but such a +ENSO swing is a rare feat indeed, even after the triple dip La Niña. And, as Figure 3 shows, we have to go all the way back to 1957 to get a (strong) El Niño prior to solar maximum. Reiterating, the year 2023 presents an immediate acid test.

3.4 What have we learned?

It is all to easy to dismiss the solar cycle terminator–ENSO correlation of Leamon et al. (2021) as a quirk, a curiosity. Indeed, its citation record—4, plus one self-citation (Leamon et al., 2022) for the modified superposed epoch method—might concur with that sentiment.

Climate Science is messy; this is not a topic to wrap up neatly and put a bow on it. Interdisciplinary, transdisciplinary science is even harder. Not only does one have to wrap things up neatly and convince one's own discipline community, but then to convince the other community requires speaking their (specialized) language to communicate with them. The stacked time series plots of scalar quantities in all the Figures here rather than maps suggest I am still operating in an "above-the-atmosphere" mindset.

Paper I was written with an open mind as to what the coupling mechanism from the Sun to the ocean was and reported just the statistical correlations. We suspected that cosmic rays or precipitation of other charged particles might be modulating the teleconnections (e.g., Bjerknes, 1969; Domeisen et al., 2019) from equator to higher (terrestrial) latitudes, and the fact that these correlations turned on in the 1960s came from the warming planet. Rather than increased tropospheric temperatures, other long-time-scale trends, such as phase of the Atlantic Multi-decadal Oscillation (AMO; see, e.g., Omrani et al., 2022) could aid (or

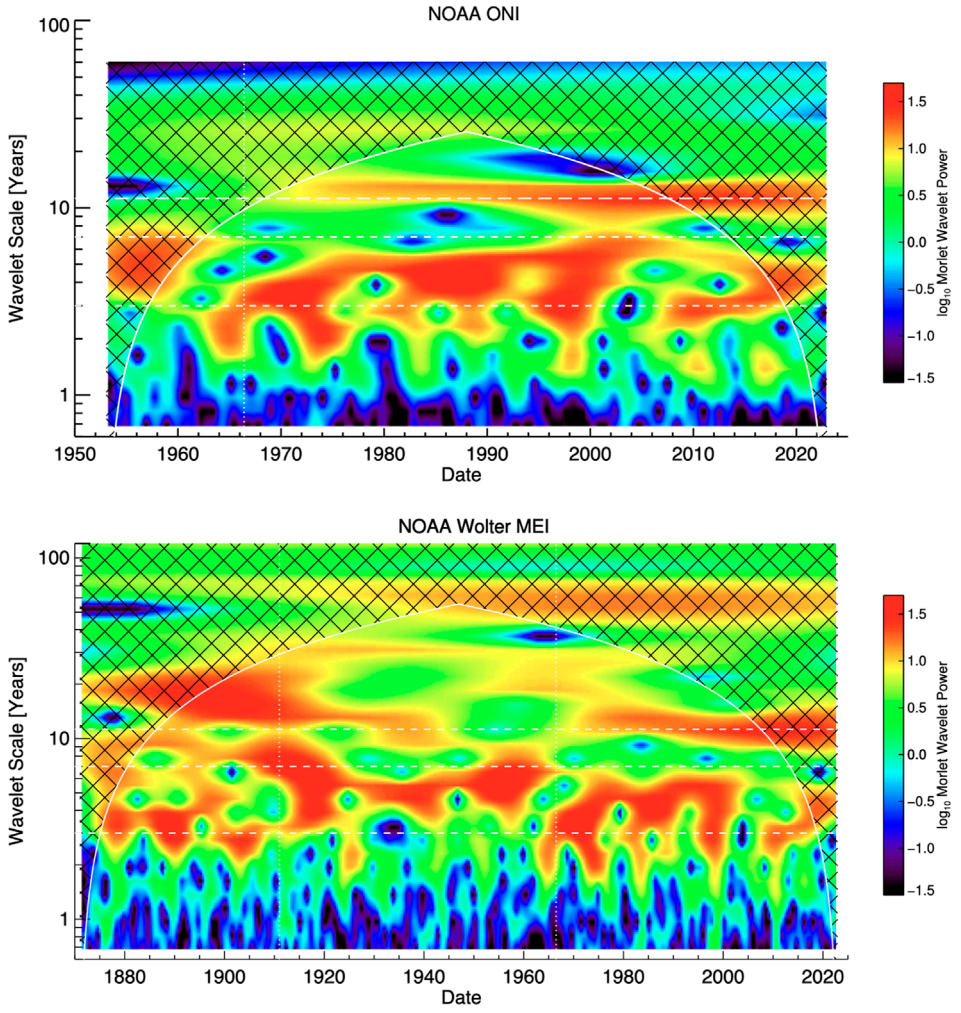

FIGURE 6
Wavelet power spectra for the NOAA indices ONI 1950–present (top) and the extended "Multivariate ENSO Index" (MEI) 1871–present (bottom; note change of abscissa scale). Cross-hatched regions on either end indicate the "cone of influence," where edge effects become important. Horizontal dashed and dotted white lines refer to periods of 3, 7, and 11 years; Vertical white lines indicate June 1966 (the Cycle 19 terminator), and, in the MEI panel, January 1911 (see text). Significant power is seen at solar cycle scales from the mid-1960s on, consistent with the results of Torrence and Compo (1998), and Wang and Wang (1996).

hinder) teleconnections, driving the observed ENSO variability. The AMO turned negative in the mid-60s, in time for the Cycle 19 terminator, but that negative phase ended around 2000, and there have been two more Hale Cycle terminators since then, with associated (multi-year) La Niña events.

The GCR flux did drop off slightly in mid-2020, corresponding to the onset of the current multi-year La Niña event, but the big (5.5%) drop corresponded to the late-2021 decrease in ONI, or return to values below −0.5. Tinsley et al. (1989) noted that while the GCR flux recorded by neutron monitors in Oulu (as used in this paper and elsewhere) lies in the range 1–10 GeV, it would be more appropriate to use as comparison with (storm intensity) the flux of particles with energies an order of magnitude lower, being "the main source of ionisation and a source of chemical species in the lower stratosphere and troposphere." This is consistent with the biggest change in Oxygen fluxes (ACE-SIS) from the mid-2020 peak came in the 7.3–10 MeV/nuc range (so 115–160 MeV total for an 8-proton, 8-neutron Oxygen nucleus) with a 30%–40% drop over the last half of 2020, and a further decrease aligned with the terminator (JS Rankin, personal communication; but see also Rankin et al., 2022).

The US$ billion socio-economic impacts of ENSO are such that it behooves us, as a community, to mitigate them by being able to predict ENSO on decadal timescales. We need an experiment, or series of experiments, field campaigns, models, both in the neutral atmosphere and plasma space above, to deduce the coupling pathway and mechanisms. Is charged particle precipitation properly accounted for in coupled circulation models, for instance? The method described here to describe the "unit cycle" of irradiance can then be forecast to a given/predicted solar cycle length and strength for use in higher-fidelity long-range future climate models. The various studies and authors quoted in Jones (2022) agree that the IPCC models are missing something—usually incorporation of ice sheets—but why not incorporation of upper atmosphere phenomena?

3.5 Where do we go now?

Any connection, or attempted connection between solar variability and oceanic variability is viewed with **deep scepticism.** Nevertheless, *any* prognostic skill at all, frankly, is mind-boggling. The correlations presented here and in Paper I are *not* happenstance. As previously mentioned, the year 2023 presents an immediate acid test of the predictions here (ENSO relatively neutral) and recent computer models calling for a strong El Niño, albeit while highly cognizant of the Spring Predictability Barrier.

To advance higher-fidelity long-range future climate models, we need a (large) team of open-minded individuals to explore what needs to be included. And, of course, not just funding, but interdisciplinary funding. Finally, there has in the last year or so, been a rapid increase in interest of Artificial Intelligence and Machine Learning for the scientific process—methods for predicting natural phenomena, and also discovering new physical insight based on hitherto unforeseen patterns in the data. Such a Neural Net technique was demonstrated for geomagnetic storm predictions by Cheung et al. (2017), and provides a clear pathway forward for our interests: What potential mechansisms can be found to explain the empirical sun-atmosphere correlation through correlated variations in the solar corona, EUV spectral irradiance, and solar wind down to the radiation belts, ITM structures and the stratosphere?

4 Conclusion

In Paper I (Leamon et al., 2021) we showed a strong correlation between the end of solar activity cycles and the warm-to-cold transitions of the El Niño Southern Oscillation, that held for the 5 cycles 19–23, or from 1966–7 to 2010–11. Paper I then predicted that the next such transition would be in 2020. La Niña did indeed begin in mid-2020, and endured into 2023. However, some of the solar predictions made in Paper I did not come to pass until late 2021.

It would appear, then, that the galactic cosmic ray-driven modulation suggested by Paper I to explain the El Niño to La Niña transitions is not correct. In lieu of GCRs, but still searching for a solar-modulated mechanism, we considered the we considered the tilt of the Heliospheric current sheet and the geomagnetic activity indices K_p and A_p. When the HCS tilt exceeds the Earth's orbital obliquity, 23.4°, is a good (scalar) proxy for the terminator, and thus an El Niño to La Niña transition.

The geomagnetic activity indices are a far more promising mechanism: 17 of the 19 significant El Niño events since 1950 are closely correlated in time with a local extremum in K_p and A_p. The El Niño to La Niña transition at the terminator comes as geomagnetic activity rises from its solar cycle minimum, and any mid-cycle El Niños are associated with local peaks in geomagnetic activity (especially that event that always seems to occur within a year of the 2/5 cycle landmark).

So, revising the conclusion from Paper I, maybe it is an El Niño that is driven by solar-terrestrial coupling, and a La Niña just follows as the coupled ocean-atmosphere system relaxes. However, these temporal correlations do not explain the magnitude of an El Niño event, or the La Niña event that follows, nor does it explain why post-terminator La Niña events tend to endure for two or more years, especially those at the end of even-numbered solar cycles, such as the 2020–23 event just ended.

Based on the solar cycle correlations shown in Figures 1, 3, we computed the average ENSO for a solar cycle, and predicted it forward for the next decade.

The rest of 2023 presents an immediate acid test for the statistical correlations presented here: we do not predict a strong El Niño, in opposition, perhaps, to dynamical forecasts. Statistical forecasts have no experience of the current unprecedentedly warm ocean waters worldwide; have dynamic forecasts properly included such sea surface temperatures? If any solar cycle-dependent model is to be believed, we have to go all the way back to 1957 to get a (strong) El Niño prior to solar maximum. We shall see.

To conclude, in light of the theme of this Frontiers Research Topic, "*Impact of Solar Activities on Weather and Climate*," we have shown that there are rapid changes in solar output, in terms of energetic photons, particulate ejecta and the large-scale heliospheric structure at specific, *predictable* times in the solar cycle, and that major swings in the various ENSO indices are correlated with at least one (The El Niño to La Niña transition at the terminator), if not two (the post-maximum El Niño peak), of these landmarks. As such, the results presented here suggest that solar (cycle-modulated) inputs are not properly captured in current models of ENSO, and thus we offer great utility for improving the fidelity of atmospheric and climate modelling in future.

Data availability statement

The original contributions presented in the study are included in the article/Supplementary Material, further inquiries can be directed to the corresponding author.

Author contributions

RL was solely responsible for the concept, intellectual content, writing and figure creation, and approved it for publication.

Funding

RL acknowledges support from NASA's Living With a Star Program and the grant of Indo-US Virtual Networked Center (IUSSTF-JC-011-2016) to support the joint research on Extended Solar Cycles.

Acknowledgments

I thank Dan Marsh and Scott McIntosh, coauthors of Paper I, for their continued discussion and insight. McIntosh is also due thanks for providing the model data shown in panel (b) of Figure 1. The Reviewers are greatly appreciated for the

encouragement to look at the geomagnetic indices discussed in Figure 3.

Conflict of interest

The authors declare that the research was conducted in the absence of any commercial or financial relationships that could be construed as a potential conflict of interest.

Publisher's note

References

Altrock, R. C. (1997). An 'extended solar cycle' as observed in Fe xiv. *Sol. Phys.* 170, 411–423. doi:10.1023/A:1004958900477

Bjerknes, J. (1969). Atmospheric teleconnections from the equatorial pacific. *Mon. Weather Rev.* 97, 163–172. doi:10.1175/1520-0493(1969)097⟨0163:ATFTEP⟩2.3.CO;2

Boers, N. (2021). Observation-based early-warning signals for a collapse of the atlantic meridional overturning circulation. *Nat. Clim. Change* 11, 680–688. doi:10.1038/s41558-021-01097-4

Chapman, S. C., McIntosh, S. W., Leamon, R. J., and Watkins, N. W. (2020). Quantifying the solar cycle modulation of extreme space weather. *Geophys. Res. Lett.* 47, e87795. doi:10.1029/2020GL087795

Cheung, C. M. M., Handmer, C., Kosar, B., Gerules, G., Poduval, B., Mackintosh, G., et al. (2017). "Modeling geomagnetic variations using a machine learning framework," in *AGU fall meeting abstracts*, 2017, SM23A–2591.

Dikpati, M., McIntosh, S. W., Chatterjee, S., Banerjee, D., Yellin-Bergovoy, R., and Srivastava, A. (2019). Triggering the birth of new cycle's sunspots by solar tsunami. *Sci. Rep.* 9, 2035. doi:10.1038/s41598-018-37939-z

Domeisen, D. I. V., Garfinkel, C. I., and Butler, A. H. (2019). The teleconnection of El Niño southern oscillation to the stratosphere. *Rev. Geophys.* 57, 5–47. doi:10.1029/2018RG000596

Fierstein, J., and Hildreth, W. (1992). The plinian eruptions of 1912 at Novarupta, Katmai national Park, Alaska. *Bull. Volcanol.* 54, 646–684. doi:10.1007/BF00430778

Iwakiri, T., and Watanabe, M. (2021). Mechanisms linking multi-year La Niña with preceding strong El Niño. *Sci. Rep.* 11, 17465. doi:10.1038/s41598-021-96056-6

Jones, N. (2022). Rare 'triple' La Niña climate event looks likely—What does the future hold? *Nature* 607, 21. doi:10.1038/d41586-022-01668-1

Kao, H.-Y., and Yu, J.-Y. (2009). Contrasting eastern-pacific and central-pacific types of ENSO. *J. Clim.* 22, 615–632. doi:10.1175/2008JCLI2309.1

Labitzke, K., and van Loon, H. (1988). Associations between the 11-year solar cycle, the QBO and the atmosphere. Part I: The troposphere and stratosphere in the Northern Hemisphere in winter. *J. Atmos. Terr. Phys.* 50, 197–206. doi:10.1016/0021-9169(88)90068-2

Leamon, R. J., McIntosh, S. W., Chapman, S. C., and Watkins, N. W. (2020). Timing terminators: Forecasting sunspot cycle 25 onset. *Sol. Phys.* 295, 36. doi:10.1007/s11207-020-1595-3

Leamon, R. J., McIntosh, S. W., and Marsh, D. R. (2021). Termination of solar cycles and correlated tropospheric variability. *Earth Space Sci.* 8, e2020EA001223. doi:10.1029/2020EA001223

Leamon, R. J., McIntosh, S. W., and Title, A. M. (2022). Deciphering solar magnetic activity: The solar cycle clock. *Front. Astronomy Space Sci.* 9, 886670. doi:10.3389/fspas.2022.886670

Leamon, R., and McIntosh, S. (2022). "How does the sun know which way is up? The difference between odd and even cycles and implications for sunspot cycle 25 max," in *AGU fall meeting abstracts*, 2022, SH52E–1507.

Mantua, N. J., Hare, S. R., Zhang, Y., Wallace, J. M., and Francis, R. C. (1997). A pacific interdecadal climate oscillation with impacts on salmon production. *Bull. Am. Meteorological Soc.* 78, 1069–1079. doi:10.1175/1520-0477(1997)078⟨1069:APICOW⟩2.0.CO;2

McIntosh, S. W., Leamon, R. J., and Egeland, R. (2023). Deciphering solar magnetic activity: The (solar) hale cycle terminator of 2021. *Front. Astronomy Space Sci.* 10, 1050523. doi:10.3389/fspas.2023.1050523

McIntosh, S. W., Leamon, R. J., Egeland, R., Dikpati, M., Fan, Y., and Rempel, M. (2019). What the sudden death of solar cycles can tell us about the nature of the solar interior. *Sol. Phys.* 294, 88. doi:10.1007/s11207-019-1474-y

McIntosh, S. W., Wang, X., Leamon, R. J., Davey, A. R., Howe, R., Krista, L. D., et al. (2014). Deciphering solar magnetic activity. I. On the relationship between the sunspot cycle and the evolution of small magnetic features. *Astrophys. J.* 792, 12. doi:10.1088/0004-637X/792/1/12

McKenna, M., and Karamperidou, C. (2022). "Impacts of El Niño flavors on northern hemisphere blocking," in *AGU fall meeting abstracts*, 2022, A55A–A0066. (Submitted to GRL).

Miller, A., Cayan, D., Barnett, T., Graham, N., and Oberhuber, J. (1994). The 1976–77 climate shift of the Pacific Ocean. *Oceanography* 7, 21–26. doi:10.5670/oceanog.1994.11

Minobe, S. (1997). A 50-70 year climatic oscillation over the North Pacific and North America. *Geophys. Res. Lett.* 24, 683–686. doi:10.1029/97GL00504

Minobe, S. (2000). Spatio-temporal structure of the pentadecadal variability over the North Pacific. *Prog. Oceanogr.* 47, 381–408. doi:10.1016/S0079-6611(00)00042-2

Omrani, N.-E., Keenlyside, N., Matthes, K., Boljka, L., Zanchettin, D., Jungclaus, J. H., et al. (2022). Coupled stratosphere-troposphere-Atlantic multidecadal oscillation and its importance for near-future climate projection. *npj Clim. Atmos. Sci.* 5, 59. doi:10.1038/s41612-022-00275-1

Orihuela-Pinto, B., England, M. H., and Taschetto, A. S. (2022). Interbasin and interhemispheric impacts of a collapsed atlantic overturning circulation. *Nat. Clim. Change* 12, 558–565. doi:10.1038/s41558-022-01380-y

Penland, C., and Sardeshmukh, P. D. (1995). The optimal growth of tropical sea surface temperature anomalies. *J. Clim.* 8, 1999–2024. doi:10.1175/1520-0442(1995)008⟨1999:TOGOTS⟩2.0.CO;2

Ramaswamy, V., Schwarzkopf, M. D., Randel, W. J., Santer, B. D., Soden, B. J., and Stenchikov, G. L. (2006). Anthropogenic and natural influences in the evolution of lower stratospheric cooling. *Science* 311, 1138–1141. doi:10.1126/science.1122587

Rankin, J. S., McComas, D. J., Leske, R. A., Christian, E. R., Cohen, C. M. S., Cummings, A. C., et al. (2022). Anomalous cosmic-ray oxygen observations into 0.1 AU. *Astrophys. J.* 925, 9. doi:10.3847/1538-4357/ac348f

Scherrer, P. H., Wilcox, J. M., Svalgaard, L., Duvall, T. L., Jr., Dittmer, P. H., and Gustafson, E. K. (1977). The mean magnetic field of the sun - observations at Stanford. *Sol. Phys.* 54, 353–361. doi:10.1007/BF00159925

Tinsley, B. A., Brown, G. M., and Scherrer, P. H. (1989). Solar variability influences on weather and climate: Possible connections through cosmic ray fluxes and storm intensification. *J. Geophys. Res.* 94, 14783–14792. doi:10.1029/JD094iD12p14783

Toohey, M., Krüger, K., Bittner, M., Timmreck, C., and Schmidt, H. (2014). The impact of volcanic aerosol on the northern hemisphere stratospheric polar vortex: Mechanisms and sensitivity to forcing structure. *Atmos. Chem. Phys.* 14, 13063–13079. doi:10.5194/acp-14-13063-2014

Torrence, C., and Compo, G. P. (1998). A practical guide to wavelet analysis. *Bull. Am. Meteorological Soc.* 79, 61–78. doi:10.1175/1520-0477(1998)079⟨0061:APGTWA⟩2.0.CO;2

Trenberth, K. E. (1990). Recent observed interdecadal climate changes in the Northern Hemisphere. *Bull. Am. Meteorological Soc.* 71, 988–993. doi:10.1175/1520-0477(1990)071<0988:roicci>2.0.co;2

Trenberth, K. E., and Stepaniak, D. P. (2001). Indices of El Niño evolution. *J. Clim.* 14, 1697–1701. doi:10.1175/1520-0442(2001)014⟨1697:LIOENO⟩2.0.CO;2

Vecchi, G. A., and Soden, B. J. (2007). Increased tropical Atlantic wind shear in model projections of global warming. *Geophys. Res. Lett.* 34. doi:10.1029/2006GL028905

Wang, B. (1995). Interdecadal changes in El Niño onset in the last four decades. *J. Clim.* 8, 267–285. doi:10.1175/1520-0442(1995)008⟨0267:ICIENO⟩2.0.CO;2

Wang, B., and Wang, Y. (1996). Temporal structure of the southern oscillation as revealed by waveform and wavelet analysis. *J. Clim.* 9, 1586–1598. doi:10.1175/1520-0442(1996)009⟨1586:TSOTSO⟩2.0.CO;2

Wilcox, J. M., Hoeksema, J. T., and Scherrer, P. H. (1980). Origin of the warped heliospheric current sheet. *Science* 209, 603–605. doi:10.1126/science.209.4456.603

Wolter, K., and Timlin, M. S. (2011). El Niño/Southern Oscillation behaviour since 1871 as diagnosed in an extended multivariate ENSO index (MEI.ext). *Int. J. Climatol.* 31, 1074–1087. doi:10.1002/joc.2336

Yeh, S.-W., Kug, J.-S., Dewitte, B., Kwon, M.-H., Kirtman, B. P., and Jin, F.-F. (2009). El Niño in a changing climate. *Nature* 461, 511–514. doi:10.1038/nature08316

Appendix A: Wavelet analysis

Given that the key result of the present paper is that ENSO variability is correlated with the terminators, which occur not at a fixed temporal frequency but at a fixed phase of the solar cycle, we are reticent to include a Fourier spectral analysis. Nevertheless, the question "Would you expect there to be significant power in a Fourier spectrum of the entire ENSO signal?" is a valid one, as there have been several previous spectral analyses of ENSO. Indeed, the seminal wavelet analysis paper (Torrence and Compo, 1998) uses ENSO data (the Niño3 timeseries) as its "practical example."

As such, Figure 6 shows wavelet power spectra for the ONI index as discussed above, and also for the longer term "Multivariate ENSO Index," MEI, (Wolter and Timlin, 2011) that combines air pressure, temperature and wind speed data along with sea surface temperatures, normalized such that the mean value for 1871–2005 is zero and the standard deviation is unity.

As a sanity check, the spectra of the two indices agree, and our analysis agrees with previous ENSO wavelet analyses (Wang and Wang, 1996; Torrence and Compo, 1998) that "the principal period of ENSO has experienced two rapid changes since 1872, one in the early 1910s and the other in the mid-1960s." Thus in both panels of Figure 6, vertical dot-dashed lines indicate June 1966 (the cycle 19 terminator), and in Figure 6B, somewhat arbitrarily, January 1911 marking the extent of the significance contour at 12–14 year scales and low power at scales shorter than about 4 years. An abrupt alteration anywhere between 1911 and 1914 would not be inconsistent with Figure 6B. However, given the likely role of tropospheric warming and stratospheric cooling in changing the properties of ENSO (Ramaswamy et al., 2006), and polar vortex—QBO teleconnections (Labitzke and van Loon, 1988; Toohey et al., 2014), it is believable that the June 1912 Novarupta volcano eruption in Katmai National Park, Alaska (Fierstein and Hildreth, 1992)—the largest eruption of the 20th century in terms of ash volume expelled, and which, unlike other major eruptions with stratospheric consequences, happened at high rather than equatorial latitudes—could be the trigger of the 1910s phase change seen in Figure 6. Another suggestion from Figure 6 is that another abrupt alteration of oscillation period occurred around 2003–5 to a dominant 3-year periodicity. Even though one could then argue that a 3-year intrinsic periodicity would also make a 2019–2020 prediction, the power at scales of a few years (almost always) exceeds that at solar cycle scales, and there is consistent, significant, power at 11-ish year scales over the past five solar cycles.

Not unrelated to the change in ENSO principal period and the onset of a significant signal at solar cycle scales in the mid-1960s, Wang (1995) noted that the onset of El Niño experienced an abrupt change in the late 1970s. He attributed the change to "a sudden variation in the background state, associated with "a conspicuous global warming" and deepening of the Aleutian Low in the North Pacific."

frontiers | Frontiers in Earth Science

TYPE Original Research
PUBLISHED 13 July 2023
DOI 10.3389/feart.2023.1203954

OPEN ACCESS

EDITED BY
Liang Zhao,
Chinese Academy of Sciences (CAS), China

REVIEWED BY
Chunhan Jin,
Xinjiang University, China
Hui Li,
Chinese Academy of Sciences (CAS), China

*CORRESPONDENCE
Ruili Wang,
wangrl_06@163.com

RECEIVED 11 April 2023
ACCEPTED 26 June 2023
PUBLISHED 13 July 2023

CITATION
Ma H, Wang R, Li X, Lai A and Li X (2023), 11-year solar cycle influences on the late-wintertime South Asian jet variability. *Front. Earth Sci.* 11:1203954. doi: 10.3389/feart.2023.1203954

11-year solar cycle influences on the late-wintertime South Asian jet variability

Hedi Ma[1,2], Ruili Wang[3]*, Xing Li[4], Anwei Lai[1] and Xiao Li[2,4]

[1]China Meteorological Administration Basin Heavy Rainfall Key Laboratory, Hubei Key Laboratory for Heavy Rain Monitoring and Warning Research, Institute of Heavy Rain, China Meteorological Administration, Wuhan, China, [2]Key Laboratory of Meteorological Disaster (KLME), Ministry of Education and Collaborative Innovation Center on Forecast and Evaluation of Meteorological Disasters(CIC-FEMD), Nanjing University of Information Science and Technology, Nanjing, China, [3]Wuhan Meteorological Observatory, Wuhan, China, [4]Plateau Atmosphere and Environment Key Laboratory of Sichuan Province, College of Atmospheric Science, Chengdu University of Information Technology, Chengdu, China

The South Asian jet leading wave train (SAJLWT) is a zonally elongated and equivalently barotropic stationary Rossby wave train along the wintertime South Asian subtropical jet, which stands out as the leading empirical orthogonal function mode of monthly meridional winds at the upper troposphere over southern Eurasia. The SAJLWT is closely related to weather and climate extremes over southern Eurasia, but up to now, the mechanisms of SAJLWT variability are still not fully understood. The present study reveals a significant 11-year solar cycle (SC) influence on the SAJLWT variability in late winter (January–March). The in-phase correlation between the SC and the SAJLWT is not only statistically significant but also consistent over time. Associated with the solar-induced SAJLWT anomalies, significant surface cooling exists over northeastern Africa and Middle East, while significant positive precipitation anomalies appear over southern China. Two routes of mechanisms are presented to clarify the SC–SAJLWT linkage. One is due to the solar-induced northwest–southeast tilted North Atlantic Oscillation (TNAO) pattern, which may reflect a "top–down" solar forcing and the ocean–atmosphere couplings in the North Atlantic Ocean. This TNAO pattern would trigger southeastward wave activity fluxes toward the SAJ, thus significantly impacting the upstream portions of the SAJLWT pattern. The other mechanism involves weakened convection over the Maritime Continent (MC) region, reflecting solar-induced weakening of Pacific Walker Circulation via "bottom–up" processes. The MC convection anomaly would also excite a SAJLWT-like circulation pattern. Our analysis highlights that the solar "top–down" and "bottom–up" mechanisms may act in concert to exert a significant impact on the SAJLWT and indicates that the SC forcing is an appreciable source of decadal predictability in southern Eurasia.

KEYWORDS

11-year solar cycle, South Asian jet, wave train, sea surface temperature, tropical convection

1 Introduction

In wintertime, the Asian subtropical westerly jet shifts southward to around 25°N, extending from Middle East to North Pacific, known as the South Asian jet (SAJ, Yang et al., 2004) stream. It acts as a waveguide for quasi-stationary waves that promote upstream disturbances to propagate efficiently to East Asia (Branstator, 2002; Watanabe, 2004).

Particularly, in the recent decade, growing interest had been focused on a zonally elongated and equivalently barotropic stationary Rossby wave train along the SAJ, which stands out as the leading empirical orthogonal function (EOF) mode of wintertime monthly meridional winds at the upper troposphere over southern Eurasia (Li et al., 2017; Li et al., 2020; Hu et al., 2018). It originates in the North Atlantic, propagates southeastward to the Arabian Sea, and then turns eastward along the SAJ toward East Asia (EA). This SAJ leading wave train (SAJLWT) features variabilities on a wide range of time scales and exerts substantial impacts on weather and climate over EA. Some extreme wintertime rainfalls, snowfalls, and temperature anomalies in EA are associated with this wave pattern (Wen et al., 2009; Ding and Li, 2017; Shen et al., 2019). Hence, it is important to discover the physical processes driving the variations of the SAJLWT.

A number of studies have investigated the triggering and maintaining mechanism of the SAJLWT. The results demonstrate it is an atmospheric internal mode, which can be triggered and sustained through wave–mean flow interactions (Wirth et al., 2018; Li, 2021). The causes of interannual and decadal variations of this wave pattern had also extracted much attention, and two types of drivers had been identified. One is the circulation patterns over the North Atlantic and European (NAE) region. Among them, the North Atlantic Oscillation (NAO) anomaly was found to be closely linked to this wave train (Song et al., 2014). In addition, the wave train can also be stimulated by quasi-zonally elongated cyclonic or anticyclonic anomalies over mid-high latitudes of the NAE region without the NAO. These NAE circulation disturbances would propagate eastward toward East Asia and North Pacific after being injected into the SAJ, due to the waveguide effect (Huang et al., 2020). On the other hand, tropical processes occurring along the wave path can also fuel this wave train. In general, the SAJLWT is associated with El Niño–Southern Oscillation (ENSO)-like patterns. Through the Gill–Matsuno mechanism, sea surface temperature (SST) and convection anomalies in the tropical eastern Pacific (EP), western Pacific (WP), and Indian Ocean (IO) were found to excite circulation anomalies along the SAJ (Leung et al., 2017; Hu et al., 2018; Wei et al., 2022). However, whether the SAJLWT can be driven by external forcing factors remains unclear. Thus, further analysis should be carried out to identify the external factors of this wave train as it is useful for predicting the EA climate anomalies.

As an important natural external forcing factor of the climate system, the 11-year solar cycle (SC) may exert non-negligible influences on regional climate (Gray et al., 2010). Recent studies identify several particularly strong SC influences on the troposphere at different regions. Particularly, increasing observational and modeling evidence supports the presence of SC impacts on NAE circulation anomalies (Ineson et al., 2011; Chen et al., 2015). Generally, enhanced solar activity tends to exert a positive NAO-like pattern in wintertime, but the SC signal exhibits substantial subseasonal variations (Gray et al., 2013; Gray et al., 2016; Ma et al., 2018). There are two crucial differences between the early and late winter SC signals. One is the issue of timing. In early winter, the positive NAO-like pattern emerges 2–4 years after SC maximum, while the late winter response tends to synchronize with the SC. The other is the difference in spatial patterns. The early winter response exhibits the north–south dipole that highly resembles the canonical NAO but with more statistical significance in the Azores region (i.e., the southern lobe). The late winter response exhibits a northwest–southeast tilted dipole structure, which contains an Icelandic low-pressure anomaly and a European high-pressure anomaly, a pattern that is somewhat distinct with the canonical NAO pattern (Brugnara et al., 2013). The lagged response in early winter is dominated by the ocean feedback in the Atlantic, and the synchronized late winter response may be jointly influenced by the "top-down" forcing from the stratosphere and the ocean–atmosphere coupling in the Atlantic (Scaife et al., 2013; Thiéblemont et al., 2015). The Indo-Pacific sector is also a hotspot of solar influence. Many previous studies identified cooling in the eastern/western Pacific and warming in the central Pacific in SC maximum years, resembling the CP type of El Niño (Roy and Haigh, 2010; Zhou and Tung, 2010; Hood et al., 2013; Kodera et al., 2016; Huo and Xiao, 2017). Correspondingly, the Pacific Walker Circulation is weakened (Misios et al., 2016). These SST and circulation anomalies may be attributed to a "bottom–up" mechanism, which involves changed hydrology or ocean dynamics in response to a warmer surface associated with the increase in the total solar irradiance (Misios et al., 2016; Misios et al., 2019; Huo et al., 2021).

As mentioned previously, both of these flavors of solar signals have the potential to impact the SAJLWT. Therefore, it comes naturally to ask whether there is an SC signal in the SAJLWT. In addition, what are the physical mechanisms lying behind? Particularly, interactive processes among the SAJ variability and the two types of solar signals deserve further discussion. Section 2 contains a description of the data and methods used. Section 3 presents a robust and significant connection between the SC and the SAJLWT. Section 4 provides the combined effects of solar-induced NAE circulation anomalies and solar-related tropical forcing on the SAJLWT. The discussion and summary are presented in Sections 5.

2 Data and methods

2.1 Datasets

In this study, we employ the European Centre for Medium-Range Weather Forecasts (ECMWF) 20th century reanalysis (ERA-20C) dataset with a horizontal resolution of 2.5° for the 1901–2010 period (Poli et al., 2016). We also employed the Hadley Centre Sea Ice and Sea Surface Temperature (HadISST) dataset (Rayner et al., 2003). The present study employed Climatic Research Unit (CRU) TS v4.01 temperature and precipitation data with a horizontal resolution of 0.5° (Harris et al., 2014). The monthly precipitation reconstruction released by the National Oceanic and Atmospheric Administration (NOAA) was also used (Chen et al., 2002), which has a horizontal resolution of 2.5°. To investigate the vertical structure of the solar signal and the stratospheric impact, the monthly mean European Centre for Medium-Range Weather Forecasts Interim reanalysis (ERA-Interim) data were employed (Dee et al., 2011). In this study, monthly sunspot numbers (SSNs) are used to quantify the solar activity, which can be downloaded at http://www.esrl.noaa.gov/psd/gcos_wgsp/Timeseries/SUNSPOT/. In order to characterize the impacts from the major volcanic eruptions, the Northern

Hemisphere-averaged stratospheric aerosol optical depth (AOD) is used, which can be downloaded from https://data.giss.nasa.gov/modelforce/strataer/.

2.2 Methods

It is challenging to isolate the SC signal from various sources of internal variability and external forcing. To address this issue, many previous studies of solar-climate linkage employ the multiple linear regression (MLR) method, which had been regarded as an effective way of separating SC influences (Lean and Rind, 2008; Frame and Gray, 2010; Roy and Haigh, 2010; Ma et al., 2018). Commonly, in these studies, four climate factors are considered, namely, solar forcing, volcanic forcing, ENSO, and anthropogenic forcing. Following these studies, we obtain the response of a climate variable T over location $\boldsymbol{x}$ (a vector) in year at l years leading/lagging the SC using the following MLR equation:

$$T(\boldsymbol{x},t) = C_{SSN}(\boldsymbol{x}) \cdot SSN(t-l) + C_{VOLC}(\boldsymbol{x}) \cdot VOLC(t) + C_{ENSO}(\boldsymbol{x}) \cdot ENSO(t) + C_{TREND}(\boldsymbol{x}) \cdot TREND(t) + \varepsilon(\boldsymbol{x},t). \quad (1)$$

The four indices employed in the MLR (Eq. 1) are as follows: 1) SSN: the January–February–March (JFM) mean SSN at l-year lag (Note that time variations greater than 15 years were subtracted from the SSN time series by applying a low-pass filter technique to ensure that we only extract the quasi-11-year SC signal); 2) VOLC: the JFM mean Northern Hemisphere-averaged stratospheric AOD that characterizes volcanic influences; 3) ENSO, characterized by the JFM mean SST anomalies over the region 5°N–5°S and 180–90°W; and 4) TREND, a linear trend term that approximately represents the anthropogenic forcing. ε represents the residual term of the MLR equation. We employed a prewhitening procedure to eliminate the potential autocorrelation in the residual term, following Chen et al. (2015). Subsequently, we used a 1000-trial bootstrap resampling test to determine the statistical significance level of the regression coefficients. The estimated SC signals are denoted by the SSN regression coefficients, which had been scaled (by multiplying the difference between the maximum and minimum values of the solar index) to obtain an estimate of the maximum likely atmospheric responses to the SC. Notably, sensitivity tests suggest increasing or decreasing of external or internal factors in the MLR analysis, for example, the Atlantic Multidecadal Oscillation, ENSO, volcanic forcing, or anthropogenic forcing does not substantially change the obtained SC signals (not shown).

To describe the upper tropospheric Rossby wave activity, the phase-independent wave activity flux (WAF; Takaya and Nakamura, 2001) was calculated. The WAF can be expressed as follows:

$$W = \frac{1}{2|U|}\begin{pmatrix} \bar{u}\left(\psi_x'^2 - \psi'\psi'_{xx}\right) + \bar{v}\left(\psi'_x\psi'_y - \psi'\psi'_{xy}\right) \\ \bar{u}\left(\psi'_x\psi'_y - \psi'\psi'_{xy}\right) + \bar{v}\left(\psi_y'^2 - \psi'\psi'_{yy}\right) \\ \frac{f^2}{R\sigma/P}\left\{\bar{u}\left(\psi'_x\psi'_p - \psi'\psi'_{xp}\right) + \bar{v}\left(\psi'_y\psi'_p - \psi'\psi'_{yp}\right)\right\} \end{pmatrix}.$$

Here, ψ denotes the stream function, f is the Coriolis parameter, R is the gas constant, $\mathbf{U}$ =(u, v) represents the horizontal wind velocity, and $\sigma = (R\bar{T}/C_p p) - d\bar{T}/dp$, with temperature T and the specific heat at constant pressure C_p. Overbars and primes represent the climatology and anomalies, respectively. The derived WAF is suitable for analyzing the propagation of the wave packet.

3 Robust and significant solar signatures in wintertime SAJ variability

To show solar signatures in the upper tropospheric circulation, Figure 1A displays the SC signal in the 250-hPa GPH and vector wind anomalies. It is seen that the solar signal exhibits a marked Rossby wave train extending from the North Atlantic to the North Pacific Ocean traveling along the subtropical jet. The wave-like structure consists of six geographically fixed lobes with centers being located over Iceland, southern Europe, Egypt, Arabian Sea, southern China, and the Japan Sea. Statistical significant GPH anomalies mainly exist in the upstream nodes of this wave train, i.e., Iceland, southern Europe, and the Middle East, whereas the downstream nodes of the GPH anomalies, i.e., the negative GPH anomalies around southwest China and the positive GPH anomalies over the Japan Sea, are with limited statistical significance. However, due to the enhanced pressure gradient between them, significant southerly anomalies can still be found over central-eastern China (Figure 1B).

This derived solar pattern bears high resemblance with the SAJLWT pattern revealed by previous studies (Hu et al., 2018, see their Figure 3A). To verify this, follow Hu et al. (2018); we first obtain the SAJLWT pattern by calculating the EOF leading mode based on monthly v anomalies at 250 hPa in the domain of 0–45°N and 0–140°E during JFM of 1901–2010 (Figure 2A), which represents the dominant mode of the quasi-stationary Rossby wave along the SAJ. It should be pointed out that the chosen domain is confined in mid-lower latitudes in order to distinguish the wave train propagating along the SAJ with the waves traveling along the polar jet. This does not mean the significant solar signal is solely located over the low latitude but because we focus on the relationship between solar activity and the SAJLWT.

Here, we use the PC1 of the EOF analysis on 250-hPa v anomalies in this domain (0–45°N,0–140°E) to characterize SAJLWT variability. Then, the regressed 250 hPa GPH and vector wind anomalies onto the JFM mean PC1 are shown in Figure 2B. Comparing Figure 1 and Figure 2, it is found the solar and the SAJLWT patterns are quite similar. In this study, we use the PC1 of the EOF1 mode to characterize the SAJLWT variability. As shown in Figure 3A, the time series of PC1 is significantly correlated with the SSN ($r = 0.362$, $p<0.01$), suggesting the significant influence of SC on the SAJLWT.

Next, we investigate the lead/lag nature of the solar–SAJLWT relationship. Figure 3B shows the lead/lag solar signal in PC1 estimated from the MLR analysis over the time period 1901–2010. Notably, the solar index here had been employed at different lead/lag times between 0 and 5 years. Considering the SC has quasi-11-year period, the lead/lag of zero years indicates the SC maximum (SCmax) and the lead/lag of 5 years represents SC minimum (SCmin). A maximum positive response at lag zero represents a signal whose maximum value coincides with the SCmax. As is seen, the maximum PC1 response appears at lag zero (corresponding to the SCmax phase), while the minimum

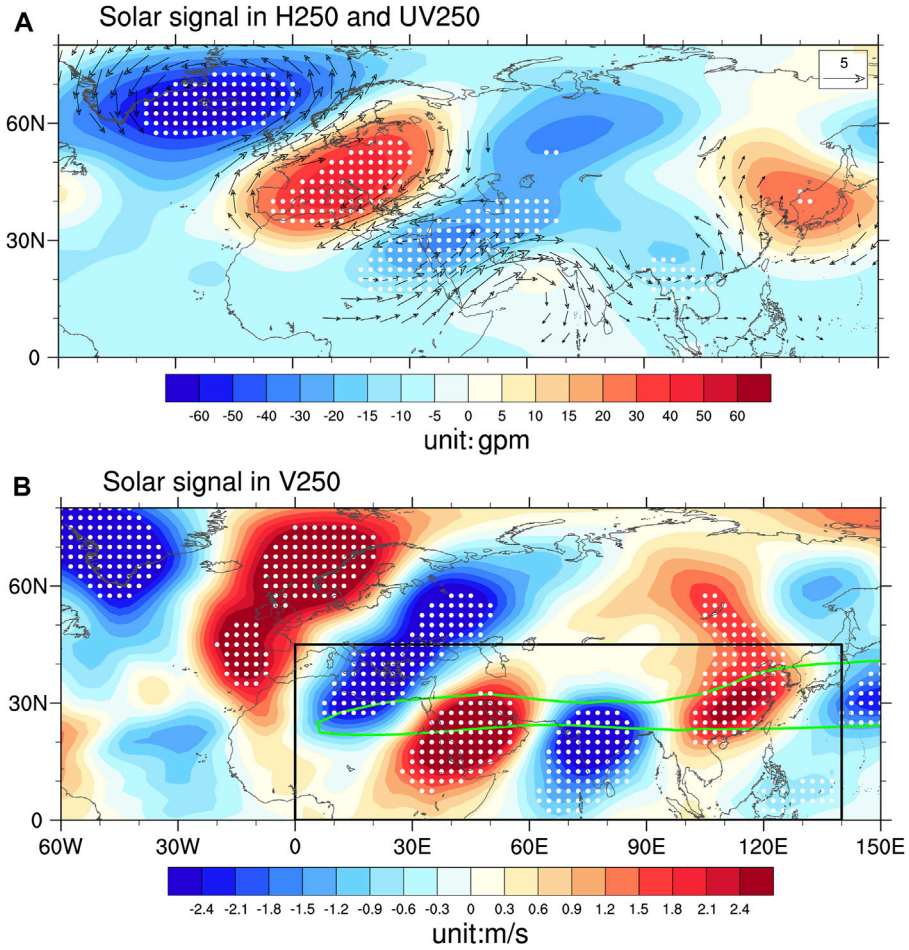

FIGURE 1
SC signals in upper tropospheric circulation anomalies. The SC signals are defined as the regression coefficients of SSN (derived from MLR Eq. 1) multiplied by the maximum peak-to-trough SSN, which can approximately represent the maximum likely atmospheric responses to the SC. **(A)** Spatial distributions of SC signals in GPH (shaded, unit: gpm) and wind anomalies (vector, unit: m/s) at 250 hPa for JFM. **(B)** SC signals in meridional wind (shaded, unit: m/s) at 250 hPa for January–March. Solid white dots denote regions where the SC signals are statistically significant at the 5% level (i.e., $p<0.05$) after prewhitening and a 1000-trial bootstrap resampling test. Only the wind vector that is significant at the 5% level is shown. In **(B)**, the green contour represents climatological jet stream (40 m/s of zonal wind), and the black rectangle is consistent with the area of EOF analysis in Figure 2A. The SC signals are obtained from MLR (Eq. 1).

PC1 response appears at lag 5 years and lead 5 years (corresponding to the SCmin phase). The significant ($p<0.05$) signals also appear around the SCmax and SCmin phases. These results suggest the wave train response is significant and generally synchronous to the SC. To further investigate the robustness of this solar signal, Figure 3C shows the 33-year sliding solar signal in PC1 over the time period 1901–2010. The year in the x-axis denotes the central year of the 33-year rolling window, while the year in the y-axis is labeled according to the lead/lag time employed. The results show positive PC1 response generally maximizing at zero lag for most of the time intervals, with significant ($p < 0.05$) signals mainly detected during 1940s–1990s, suggesting the wave train response is generally consistent over time. On the other hand, although the SC signal is relatively stable over time, a slight multidecadal drift still exists. Interestingly, we notice sometimes the strongest PC1 response occurs at 1 year, leading the Smax (e.g., 1940–1960). These slight drifts may be caused due to contamination from internal noises (Gray et al., 2016; Ma et al., 2018).

We note that SC affects not only the SAJLWT but also the SAJ itself. Figure 4 shows the solar signal in 250-hPa zonal wind. As is seen, significant strengthening of westerlies appear over the Arabian peninsula and Iranian plateau, while westerlies over the Mediterranean are significantly weakened, which is consistent with the negative GPH anomalies that exist from western Russia to the Middle East. Considering the western part of the SAJ (known as the Middle East jet stream, MEJ) is climatologically located over northern Egypt and Saudi Arabia (the green contour in Figure 4), the zonal wind pattern suggests enhanced solar activity tends to significantly shift the MEJ southeastward.

It is reasonable to anticipate that the significant solar-related circulation anomalies analyzed previously are accompanied by corresponding changes in the surface air temperature and

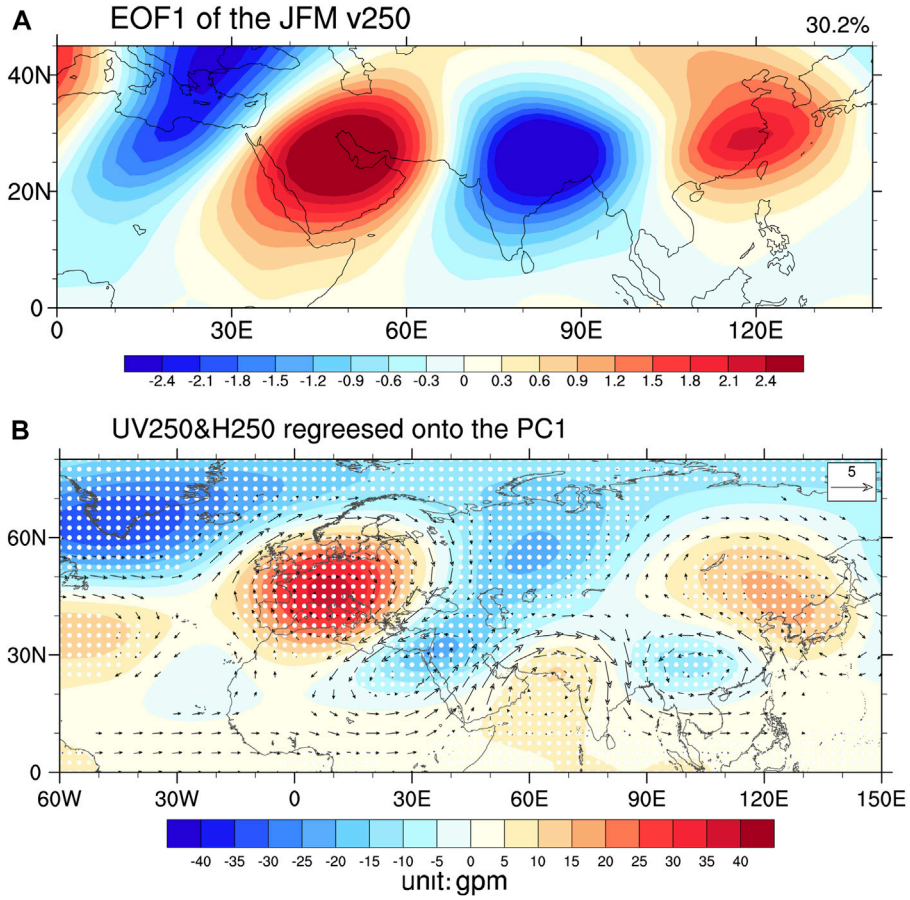

FIGURE 2
(A) First EOF mode of JFM mean meridional wind at 250 hPa for 1901–2010 over 0–45°N, 0–140°E. **(B)** Regressions of GPH (shaded, unit: gpm) and wind anomaly (vector, unit: m/s) at 250-hPa on the PC1. Solid white dots denote that the regression coefficients of GPH are statistically significant at the 5% level (i.e., $p<0.05$), and only the wind vector that is significant at the 5% level is shown.

precipitation field. Figures 5A, B show solar signals in JFM temperature and precipitation anomalies, respectively. Accompanied with southeastward movement of the MEJ, the positive GPH anomaly appears over Europe and the negative GPH anomaly appears over Middle East and northeastern Africa (Figure 1A). As is known, the positive (negative) GPH anomaly at the upper troposphere means active warm ridge (cold trough), which typically corresponds to surface warming (cooling). Therefore, significant warming is seen in Europe, while significant cooling is detected in Middle East and northeastern Africa (Figure 5A). On the other hand, significant positive precipitation anomalies appear over southern China, consistent with the finding of Ma et al. (2019). We may infer that SC influences southern China precipitation anomalies through modulating the SAJLWT since the correlation between PC1 and southern China precipitation anomalies (defined as CRU precipitation anomalies averaged over 22–32°N, 110–120°E) reaches 0.41 for 1901–2010 ($p < 0.01$). According to Hu et al. (2018), the rainfall could be affected by the wave train-induced upward motions and the low-tropospheric moisture vapor convergence induced by anomalous wind from tropical oceans as the India–Burma trough is intensified.

4 Possible mechanisms for the solar–SAJ linkage

As revealed previously, during late winter (JFM), there exists a robust and significant synchronized correlation between the SC and the SAJLWT. Over the southern Eurasian region, the solar signal also appears to significantly manifest in surface climate anomalies, including cooling in northeastern Africa and Middle East, and wet anomalies over southern China. In this section, we aimed to provide a possible explanation for these robust solar signals.

Previous studies have found that the SAJLWT pattern is closely associated with the upstream circulation patterns over the NAE region, as well as SST and convection anomalies over the tropical Indo-Pacific region (Wei et al., 2022). Coincidentally, significant solar signals exist in two regions, including a NAO-like pattern in the NAE region and a weakened Walker Circulation in the Indo-Pacific region. Therefore, both of these solar signals may impact the SAJ variability. In this section, the two routes of mechanisms are presented to clarify why the solar signal particularly manifests in the SAJLWT.

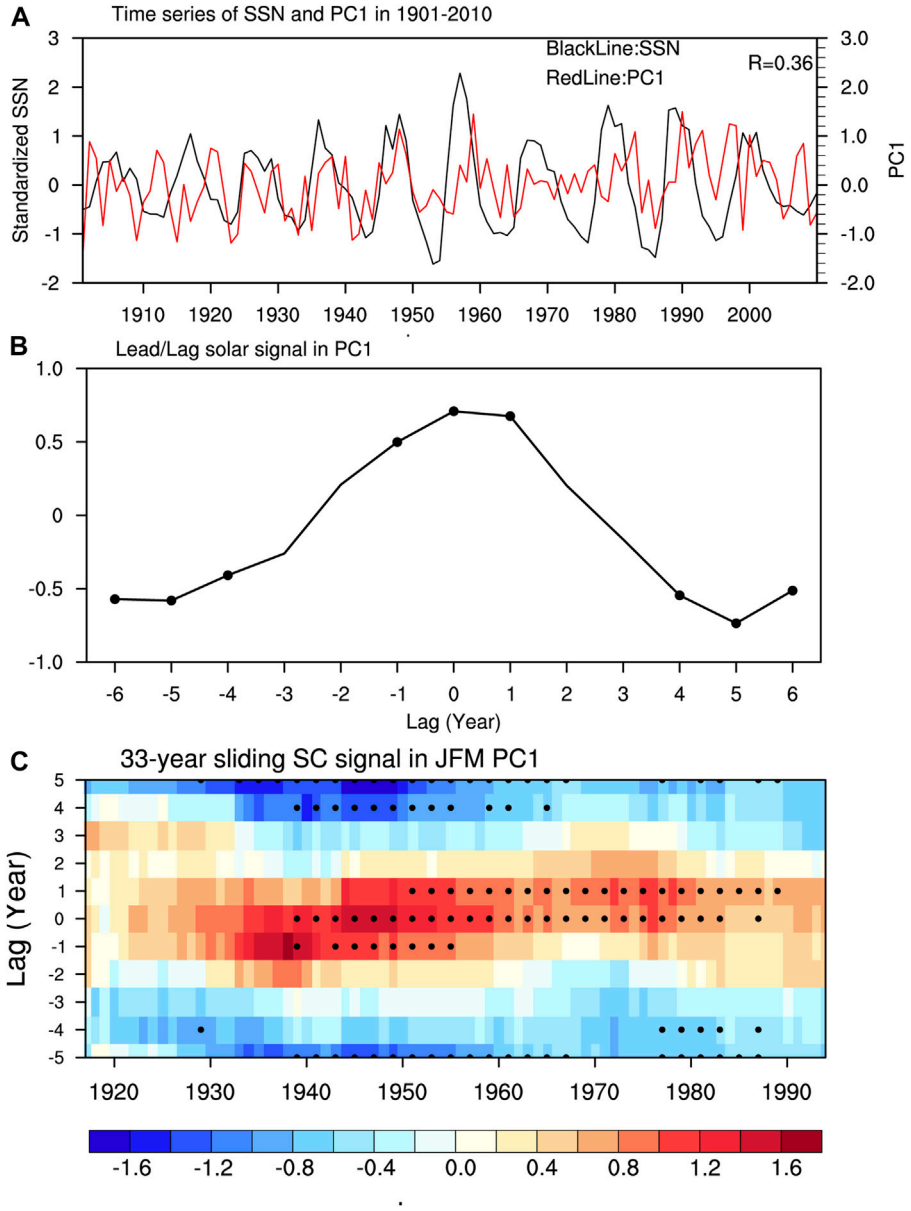

FIGURE 3
(A) Standardized time series of SSN and PC1. **(B)** SC signals in JFM PC1 at various lags (from −5 to +5 years) over the time period 1901–2010. **(C)** 33-year sliding SC signals in JFM PC1 at various lags (from −5 to +5 years). The x-axis, year, is labeled according to the central year of the 33-year window, which means that at a given year N, the MLR analysis is performed using datasets from year N-16 to year N+16. The y-axis shows the number of years that the PC1 lagging the SSN index in MLR (Eq. 1). The SC signals in **(B)** and **(C)** are obtained from MLR (Eq. 1). To determine the statistical significance, we first employed a prewhitening procedure to eliminate the potential autocorrelation in the residual term, following Chen et al. (2015). Subsequently, we used a 1000-trial bootstrap resampling test to determine the statistical significance level of the solar regression coefficients, following Ma et al. (2018). Solid black dots in **(B)** and **(C)** denote that the SC signals are statistically significant at the 5% level (i.e., $p<0.05$).

4.1 The NAE pathway of the solar modulation

In JFM, the solar pattern features a northwest–southeast dipole over the NAE region, including a significant negative (positive) GPH anomaly over the Iceland (Europe) region, consistent with the finding of Brugnara et al. (2013). To investigate the possible causes, Figure 6 shows the bi-month (November-December, December-January, January-February, and February-March, short for ND, DJ, JF, and FM, respectively) evolution of solar signals in zonal mean zonal wind averaged over the Atlantic sector (60–-0°W). As is seen, a significant positive zonal wind signal appears at around 60–80°N at 150–10 hPa in DJ, corresponding to an intensified stratospheric polar vortex. As had been suggested by many previous studies, this positive zonal wind anomaly is associated with the enlarged meridional temperature gradient in the stratosphere, which is related to variations in UV absorption and changes of ozone levels in the stratosphere. As season evolves, this

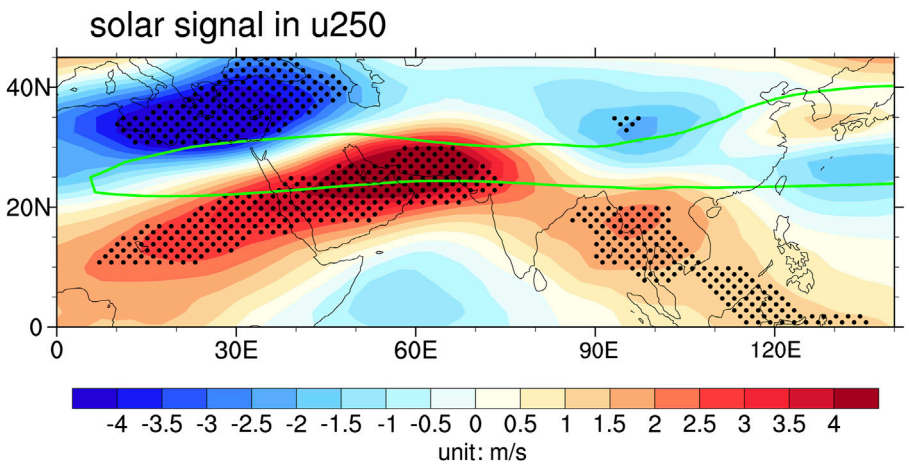

FIGURE 4
SC signals in 250-hPa zonal wind anomalies (shaded, unit: m/s); the definition of the SC signal here is same as Figure 1. Solid black dots denote that the SC signals are statistically significant at the 5% level (i.e., $p<0.05$) after prewhitening and a 1000-trial bootstrap resampling test. The green contour represents the climatological jet stream (40 m/s of zonal wind). The SC signals are obtained from MLR (Eq. 1).

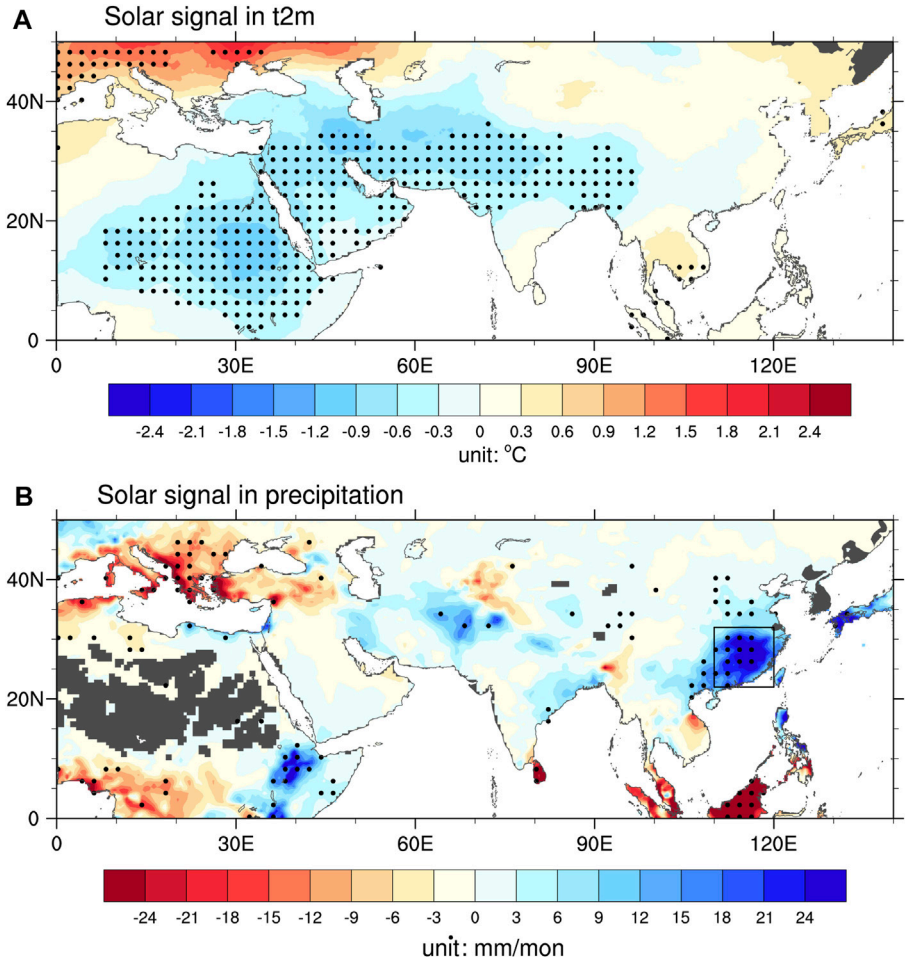

FIGURE 5
Same as Figure 4 but for SC signals in surface air temperature **(A)** and precipitation **(B)**.

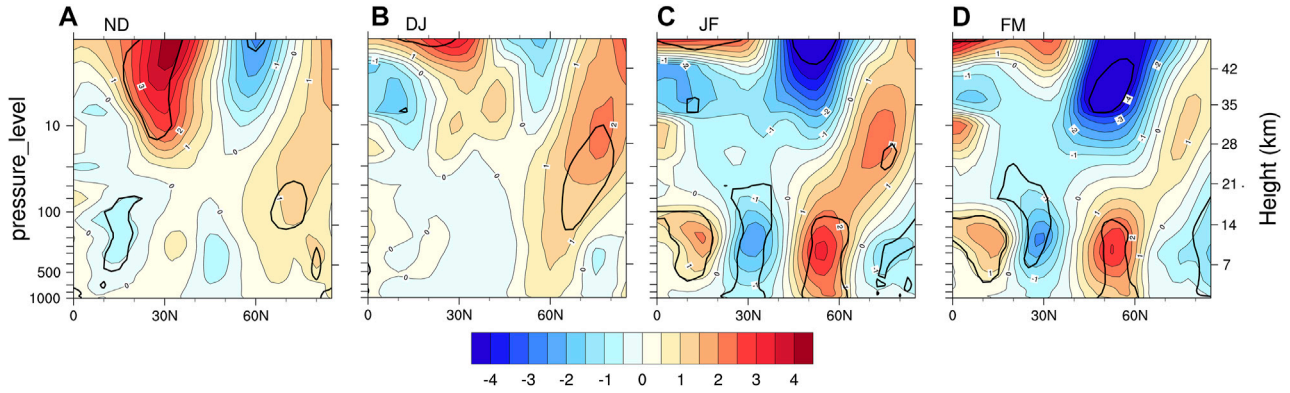

FIGURE 6
Latitude-height cross-sections of SC signals in zonal mean zonal wind (m/s) over the Atlantic sector (60-0°W) using the MLR Eq. 1 during **(A)** November-December (ND), **(B)** December-January (DJ), **(C)** January-February (JF) and **(D)** February-March (FM). Black contours denote regions statistical significant at the 10% level. This figure is based on ERA-Interim reanalysis covering winter 1979/1980-2009/2010.

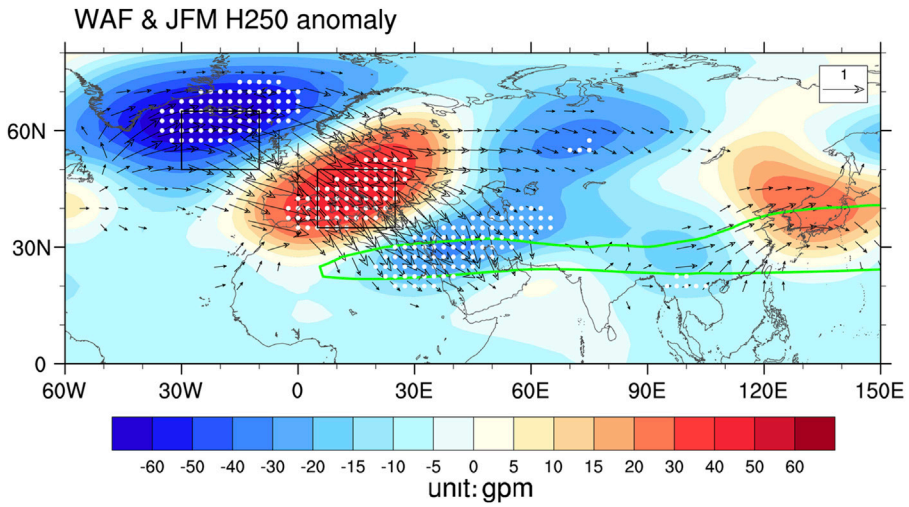

FIGURE 7
SC signals in the JFM 250-hPa GPH (unit: gpm); solid white dots denote statistical significance at the 5% level, and the vectors denote wave activity flux (Takaya & Nakamura, 2001) at 250 hPa (unit: $m^2 \cdot s^{-2}$).

stratospheric zonal wind anomaly exhibits clear downward propagation toward the troposphere. In JF and FM, the significant positive zonal wind reaches at around 60°N, physically consistent with the circulation pattern shown in Figure 1A. Therefore, our analysis suggests the observed circulation pattern over the NAE region may largely reflect a "top–down" solar forcing, consistent with the findings of previous studies (Ineson et al., 2011; Chen et al., 2015). Notably, several studies suggest the local ocean–atmosphere process also acts to shape the solar pattern over the NAE region (Gray et al., 2016).

Several recent studies had demonstrated this circulation pattern could excite the SAJLWT pattern through downstream propagation of the Rossby wave train (e.g., Huang et al., 2020). Thus, it is reasonable to speculate that the NAE solar pattern could trigger the SAJLWT through Rossby wave energy propagation. Figure 7 displays solar signals in 250-hPa GPH anomalies and the WAFs. The source of the solar wave train originates from the mid-high latitudes of the North Atlantic Ocean. The 250-hPa WAFs start from the Gulf stream region propagating eastward, and then intensify and turn southeastward over Europe. Afterward, the wave energy is injected into the entrance of the SAJ, which causes cyclonic anomalies over the Middle East and a southeastward shift of the MEJ (western part of the SAJ). Such clear and evident WAFs allow us to interpret these upstream lobes of the solar wave pattern, including circulation anomalies over the NAE region and the Middle East region, as stationary Rossby waves propagating southeastward from the North Atlantic Ocean. However, we note that the WAFs toward EA are less clear and evident than those in the NAE region.

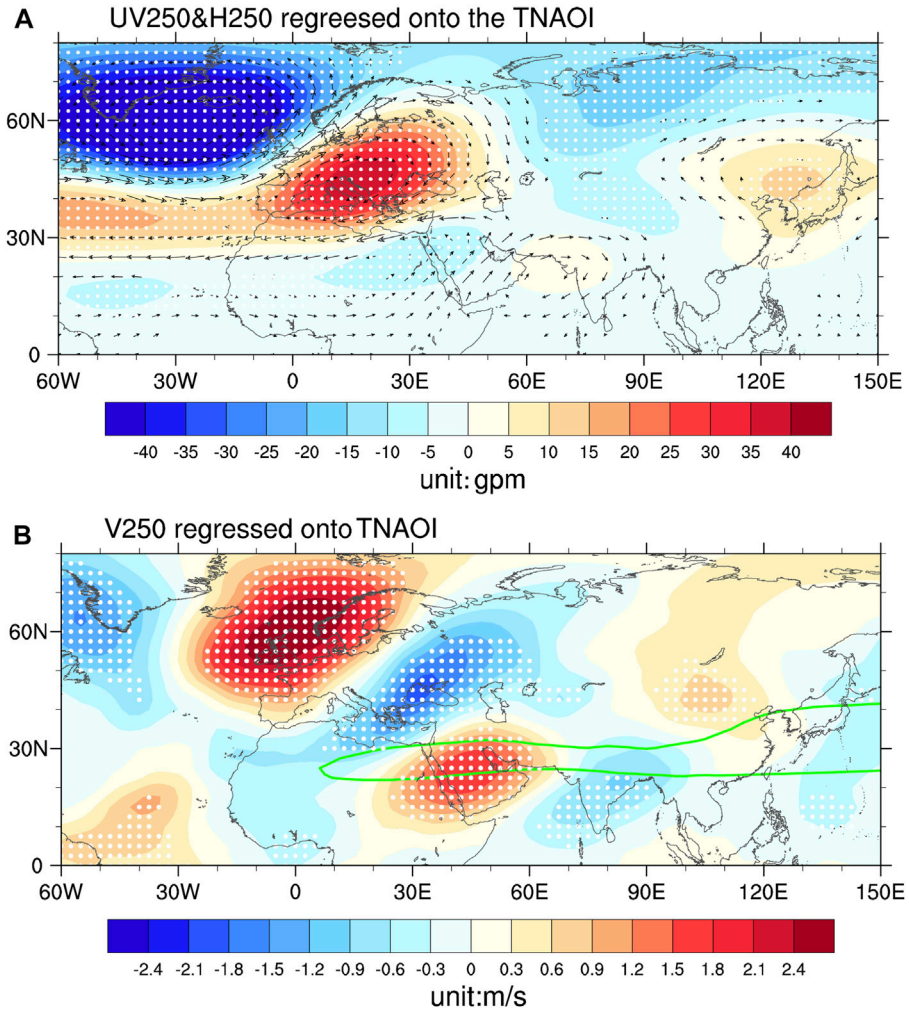

FIGURE 8
(A) Regressions of GPH (shaded, unit: gpm) and wind anomaly (vector, unit: m/s) at 250-hPa on TNAOI. **(B)** Regressions of meridional wind (shaded, unit: m/s) at 250 hPa on TNAOI. Solid black dots denote that the regression coefficients are statistically significant at the 5% level (i.e., $p<0.05$); only the wind vector that is statistically significant at the 5% level is shown. The green contour represents the climatological jet stream (40 m/s of zonal wind).

Considering the solar signal over the NAE region resembles a northwest–southeast tilted NAO (TNAO) pattern, here, we construct a TNAO index (TNAOI) to quantify the solar impact over the NAE region. The TNAOI is defined as the standardized difference of area averaged GPH anomalies over 35–50°N, 5–25°E and 50–65°N, 30–10°W regions, representing the strength of the northwest–southeast dipole anomaly over this region. The correlation between TNAOI and PC1 is 0.42 ($p < 0.01$), suggesting the TNAO pattern may bridge the SC–SAJLWT relationship. Figure 8 displays the TNAOI-associated circulation anomalies. By comparing Figure 8 and Figure 1, it is seen that the TNAO and solar patterns are generally consistent over the NAE region, the Middle East, and India, indicating the solar-associated TNAO pattern play an important role in the upstream portions of the SAJLWT. However, the TNAO impact is relatively weak over EA, thus suggesting the TNAO pattern may only partly explain the observed EA circulation anomalies. On the other hand, we also note that northeastward WAFs prevail between the South China Sea and Northeast Asia (Figure 7), hinting a remote influence of tropical convection to the EA circulation anomalies.

4.2 The Indo-Pacific pathway of solar modulation

Previous studies suggested that the SAJLWT pattern can be modulated by SST and convection anomalies over the Indo-Pacific sector (Hu et al., 2018; Wei et al., 2022). To demonstrate this, Figure 9 shows regressed SST, precipitation, and 850-hPa wind anomalies onto PC1. As is shown in Figure 9A, associated with the positive phase of the PC1, the SST anomaly resembles the El Niño pattern, with significant warming appearing over tropical EP and IO, while cooling exists over WP. Correspondingly, significant positive precipitation anomalies appear over tropical EP and IO, whereas significant negative precipitation anomalies are detected over the MC region

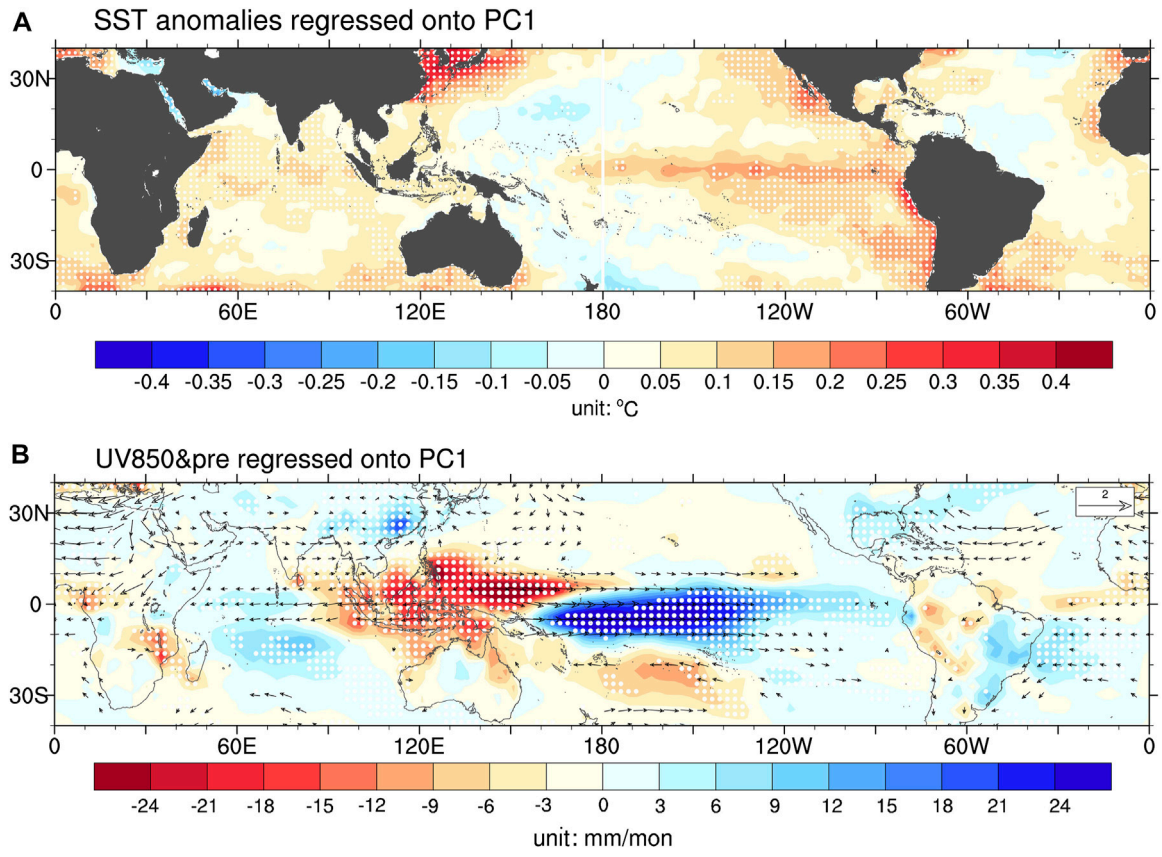

FIGURE 9
(A) Regression map of the SST anomaly (shading, unit: °C) against the PC1 in JFM for the period of 1901–2010. **(B)** Regressions of precipitation anomalies (shaded, unit: gpm) and wind anomaly (vector, unit: m/s) at 850-hPa on the PC1. Solid black dots denote that the regression coefficients of precipitation anomalies are statistically significant at the 5% level (i.e., $p<0.05$), and only the wind vector that is significant at the 5% level is shown.

(Figure 9B). The low-level easterly anomaly exists over MC and IO, and the westerly anomaly appears over CP and WP, indicative of a weakened Walker Circulation. These features are generally consistent with previous findings, which also demonstrate positive PC1 is associated with El Niño-like rainfall/convection anomalies in the tropics (Hu et al., 2018).

We then display the solar signal in tropical SST, precipitation, and 850-hPa wind anomalies, as shown in Figure 10. We note that the solar SST pattern (Figure 10A) across the tropics is distinct with the PC1-associated SST pattern. It dislikes the El Niño pattern, particularly over EP (Figure 10A). However, the SST distribution from CP to IO still bears some resemblance with El Niño. The CP and IO show warming, while WP shows cooling. Such an SST pattern would drive positive precipitation anomalies in tropical CP and IO, and negative significant precipitation anomalies over the MC region (Figure 10B). The correlation coefficient between the SSN and the MC precipitation index (MCPI), defined as the domain average of precipitation anomalies over the 10°S–10°N and 100–150°E region, is −0.32, exceeding the 0.01 significance level. In addition, the significant 850-hPa westerly anomaly appears at equatorial central-western Pacific Ocean. Therefore, enhanced solar activity is also associated with suppressed convection around over the MC and a weakened Walker Circulation, generally consistent with the previous finding of Misios et al. (2019).

As revealed previously, SC weakens the Walker Circulation and induces significant dry anomalies over the MC region. We, thus, hypothesized that the close relationship between the SC and the SAJLWT pattern could also be partly established via solar impact on the MC convection anomalies. To support this hypothesis, we compute regressed 250-hPa circulation anomalies onto MCPI, as shown in Figure 11. The GPH/wind field bears high resemblance for the downstream portions of the solar-associated wave pattern (Figure 1), suggesting MC convection anomalies may play a role in the solar–SAJLWT relationship.

Previous observational and modeling studies had pointed out that suppressed convection over the MC would reduce local latent heat release in the mid troposphere, which excites a Gill-type response with a cyclonic anomaly in the upper troposphere of the Indo-China Peninsula and southern China. Then, a northeastward anomalous Rossby wave train is triggered, resulting in a positive center of the GPH anomaly over the Japan Sea (Sakai and Kawamura, 2009; Leung et al., 2017). We note that Figure 11A shows a similar northeastward Rossby wave train over EA, physically consistent with these previous findings. The MC convection-induced GPH pattern would also determine v anomalies

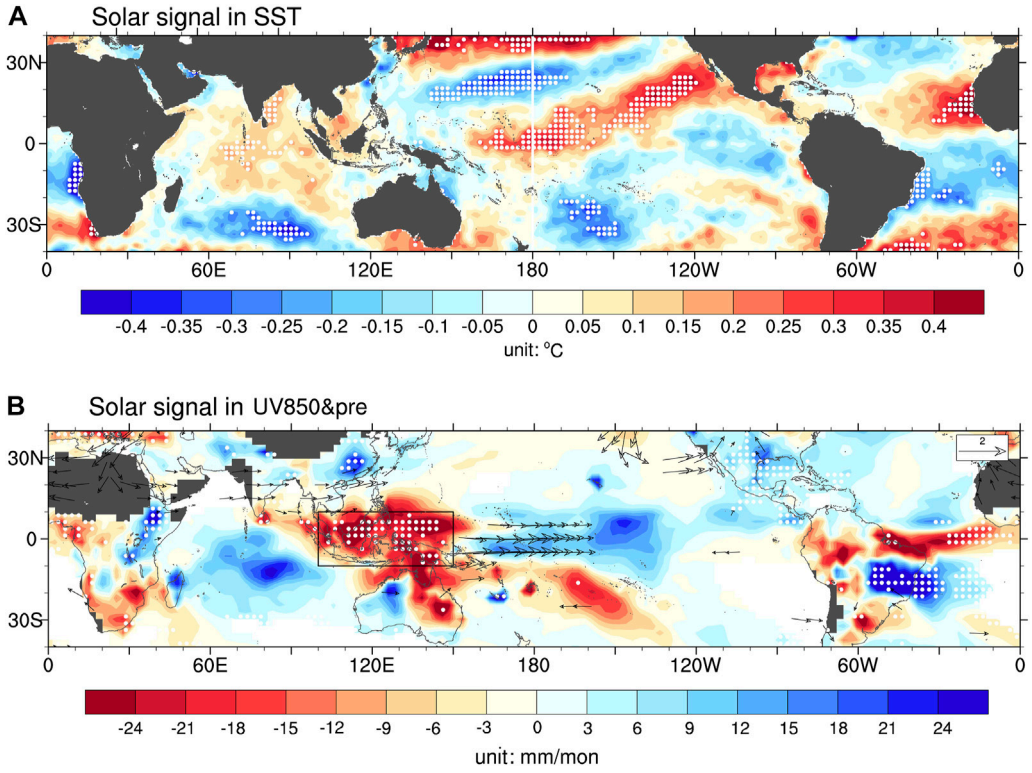

FIGURE 10
(A) SC signals in tropical SST (shading, unit: °C). **(B)** SC signals in precipitation anomalies (shaded, unit: gpm) and wind anomaly (vector, unit: m/s) at 850-hPa; the definition of the SC signal here is the same as Figure 1. Solid black dots denote regions where the SC signals are statistically significant at the 5% level (i.e., $p<0.05$) after prewhitening and a 1000-trial bootstrap resampling test. Only the wind vector that is statistically significant at the 5% level is shown. The black rectangle is consistent with the area of MCPI definition. The SC signals are obtained from MLR (Eq. 1).

over India and the East China Sea, coinciding with the downstream nodes of the SAJLWT. However, notably, Figures 11A, B also show wave-like circulation anomalies over Europe and Middle East, which is beyond the scope of MC convection-induced Rossby wave train. One possible explanation is the close correlation between MC convection and IO convection, and the latter had been demonstrated to be significantly linked to wave patterns over Europe and Middle East (Wei et al., 2022). Although the linear regression approach cannot well separate the effects of two closely dependent phenomena, therefore, we may infer that the MC convection mainly impacts the downstream parts of the SAJLWT over Asia.

It is necessary to further point out the TNAO pattern and the MC convection anomalies seem to be two independent solar signals. On one hand, according to a previous literature report, they have different driving mechanisms corresponding to "top–down" and "bottom–up" solar forcing (Kodera et al., 2016). On the other hand, the correlation between TNAOI and MCPI is weak (r = 0.07). Moreover, we had also examined the 250-hPa solar signal over the Pacific–North America sector (not shown) and ruled out the possibility that the NAE circulation pattern is induced by Rossby wave propagation from the Indo-Pacific domain. These aforementioned analyses demonstrate two independent solar signals in NAE and Indo-Pacific sectors that act in concert to exert significant impacts on the SAJLWT.

5 Summary and discussion

In wintertime, the SAJ plays a very important role in weather and climate variations over the southern part of the Eurasian continent. Particularly, in the recent decade, growing interest had been focused on the SAJLWT mode since some extreme wintertime rainfalls, snowfalls, and temperature anomalies are closely associated with this pattern (Wen et al., 2009). Thus, it is important to discover the physical processes that drive the SAJLWT. However, as an important source of regional decadal climate variability, the role of SC in SAJLWT variability remains unclear.

The present study reveals a robust and significant SC influence on the SAJLWT in late winter (January–March). Our analysis suggests that the in-phase correlation between SC and the SAJLWT is not only statistically significant but also consistent over time. Associated with the solar-induced SAJ anomalies, significant cooling exists over northeastern Africa and the Middle East, while significant positive precipitation anomalies appear over southern China. Two routes of mechanisms are presented to clarify why a solar signal particularly manifests in the SAJLWT pattern. One is due to the solar-induced TNAO pattern over the NAE region, which may reflect a "top–down" solar forcing and the ocean–atmosphere coupling in the North Atlantic Ocean. This TNAO pattern can trigger downstream WAFs along the SAJ,

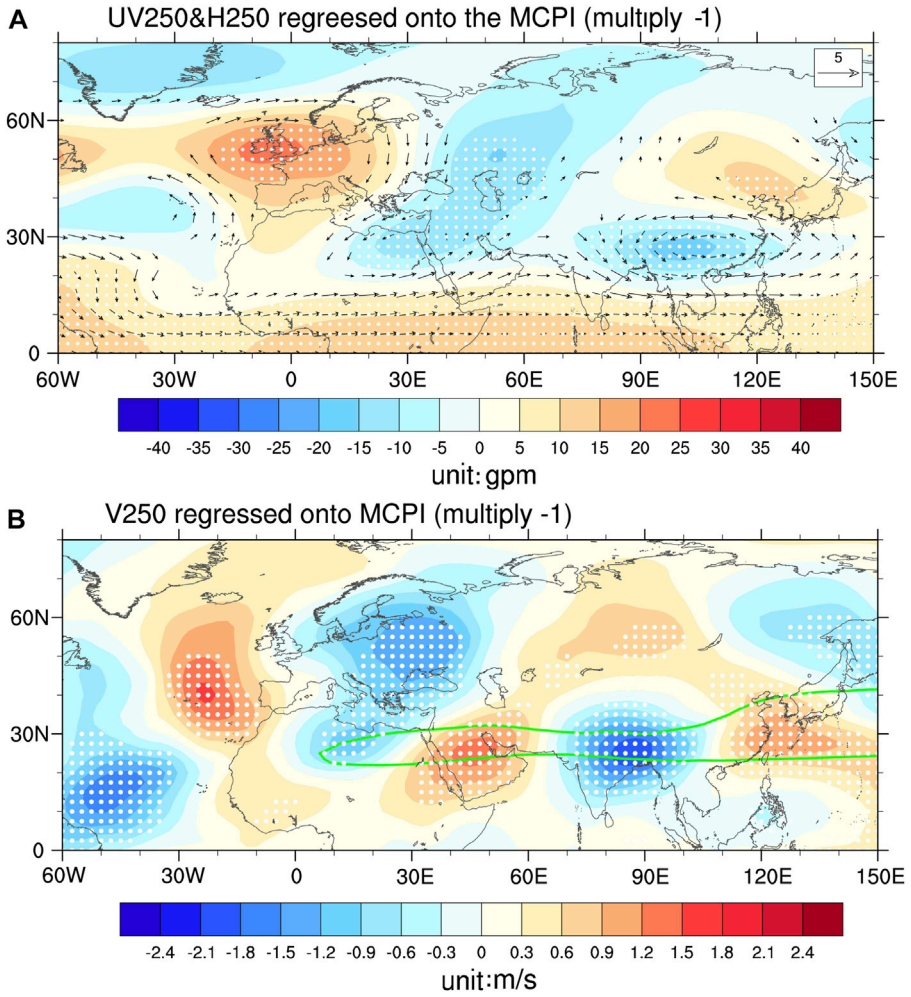

FIGURE 11
The same as Figure 8, but for regressions of **(A)** GPH (shaded, unit: gpm) and wind anomaly (vector, unit: m/s) at 250-hPa and **(B)** meridional wind (shaded, unit: m/s) at 250 hPa onto the MCPI.

thus forming the SAJLWT pattern. Notably, the TNAO-induced WAFs are more closely linked to the upstream portions of the SAJLWT while exerting relatively weaker impact on circulation anomalies over EA. The other mechanism involves weakened convection over the MC region, which reflects solar-induced weakened PWC via "bottom–up" processes. The MC convection anomaly associated with the weakened PWC would also excite a SAJLWT-like circulation pattern. Our analysis demonstrates two independent solar signals, namely, the TNAO pattern in the NAE region and the MC convection anomalies in the Indo-Pacific sectors, that act jointly to exert a significant impact on the SAJLWT.

In recent decades, much effort had been focused on two different groups of solar signals. One is the NAO-like pattern in the NH winter, which is dominated by the "top–down" solar forcing. The other is the CP ENSO-like pattern in the Indo-Pacific sector dominated by the "bottom–up" mechanism (Gray et al., 2010; Kodera et al., 2016). However, less attention had been paid on the potential combining effects of these two solar signals, particularly for the Eurasia continent, which receive remote forcing from both the NAE and the Indo-Pacific sector. The present study demonstrates these two different solar signals may work jointly to produce significant climate effects over southern Eurasia. Our results highlight that SC forcing is an appreciable source of SAJ decadal variability, which shows potential in improving decadal predictability in southern Eurasia. Although our analysis underlines the role of NAE circulation anomalies and the MC convection anomalies in controlling the SAJ responses, the current observational analysis does not allow us to determine their relative contributions quantitatively. Further modeling studies in future are required to achieve a comprehensive understanding on this issue.

Data availability statement

Publicly available datasets were analyzed in this study. These data can be found here: in this study, monthly sunspot numbers (SSNs) are used to quantify the solar activity, which can be

downloaded at http://www.esrl.noaa.gov/psd/gcos_wgsp/Timeseries/SUNSPOT/. In order to characterize the impacts from the major volcanic eruptions, the Northern Hemisphere-averaged stratospheric aerosol optical depth (AOD) is used, which can be downloaded from https://data.giss.nasa.gov/modelforce/strataer/.

Author contributions

HM and RW contributed to the conception and design of the study. XnL, XaL, and AL organized the database. XnL and XaL performed the statistical analysis. HM wrote the first draft of the manuscript. RW and XnL wrote sections of the manuscript. All authors contributed to the article and approved the submitted version.

Funding

This study was jointly supported by the Natural Science Foundation of Hubei Province (2022CFB983), Joint Open Project of KLME & CIC-FEMD, NUIST (KLME202101), Basic Research Fund of WHIHR (202311), Hubei Meteorological Administration Scientific Project (2023Q03), the Scientific Research Foundation of CUIT (KYTZ202124, KYTZ202123, and KYQN202201).

Conflict of interest

The authors declare that the research was conducted in the absence of any commercial or financial relationships that could be construed as a potential conflict of interest.

Publisher's note

All claims expressed in this article are solely those of the authors and do not necessarily represent those of their affiliated organizations, or those of the publisher, the editors, and the reviewers. Any product that may be evaluated in this article, or claim that may be made by its manufacturer, is not guaranteed or endorsed by the publisher.

References

Branstator, G. (2002). Circumglobal teleconnections, the jet stream waveguide, and the North Atlantic Oscillation. *J. Clim.* 15, 1893–1910. doi:10.1175/1520-0442(2002)015<1893:cttjsw>2.0.co;2

Brugnara, Y., Brönnimann, S., Luterbacher, J., and Rozanov, E. (2013). Influence of the sunspot cycle on the Northern Hemisphere wintertime circulation from long upper-air data sets. *Atmos. Chem. Phys.* 13, 6275–6288. doi:10.5194/acp-13-6275-2013

Chen, M., Xie, P., Janowiak, J., and Arkin, P. (2002). Global land precipitation: A 50-yr monthly analysis based on gauge observations. *J. Hydrometeorol.* 3, 249–266. doi:10.1175/1525-7541(2002)003<0249:glpaym>2.0.co;2

Chen, H., Ma, H., Li, X., and Sun, S. (2015). Solar influences on spatial patterns of Eurasian winter temperature and atmospheric general circulation anomalies. *J. Geophys. Res. Atmos.* 120, 8642–8657. doi:10.1002/2015jd023415

Dee, D., Uppala, S., Simmons, A., Berrisford, P., Poli, P., Kobayashi, S., et al. (2011). The ERA-interim reanalysis: Configuration and performance of the data assimilation system. *Q. J. R. Meteorol. Soc.* 137, 553–597. doi:10.1002/qj.828

Ding, F., and Li, C. (2017). Subtropical westerly jet waveguide and winter persistent heavy rainfall in South China. *J. Geophys. Res. Atmos.* 122, 7385–7400. doi:10.1002/2017jd026530

Frame, T., and Gray, L. (2010). The 11-yr solar cycle in ERA-40 data: An update to 2008. *J. Clim.* 23, 2213–2222. doi:10.1175/2009jcli3150.1

Gray, L. J., Beer, J., Geller, M., Haigh, J. D., Lockwood, M., Matthes, K., et al. (2010). Solar influences on climate. *Rev. Geophys.* 48, RG4001. doi:10.1029/2009RG000282

Gray, L., Scaife, A., Mitchell, D., Osprey, S., Ineson, S., Hardiman, S., et al. (2013). A lagged response to the 11 year solar cycle in observed winter Atlantic/European weather patterns. *J. Geophys. Res. Atmos.* 118, 13,405–13,420. doi:10.1002/2013jd020062

Gray, L., Woollings, T., Andrews, M., and Knight, J. (2016). Eleven-year solar cycle signal in the NAO and Atlantic/European blocking. *Q. J. R. Meteorol. Soc.* 142, 1890–1903. doi:10.1002/qj.2782

Harris, I., Jones, P., Osborn, T., and Lister, D. (2014). Updated high-resolution grids of monthly climatic observations–the CRU TS3. 10 Dataset *Int. J. Climatol.* 34 (3), 623–642. doi:10.1002/joc.3711

Hood, L., Schimanke, S., Spangehl, T., Bal, S., and Cubasch, U. (2013). The surface climate response to 11-yr solar forcing during northern winter: Observational analyses and comparisons with GCM simulations. *J. Clim.* 26, 7489–7506. doi:10.1175/JCLI-D-12-00843.1

Hu, K., Huang, G., Wu, R., and Wang, L. (2018). Structure and dynamics of a wave train along the wintertime Asian jet and its impact on East Asian climate. *Clim. Dyn.* 51, 4123–4137. doi:10.1007/s00382-017-3674-1

Huang, S., Li, X., and Wen, Z. (2020). Characteristics and possible sources of the intraseasonal South Asian jet wave train in boreal winter. *J. Clim.* 33, 10523–10537. doi:10.1175/JCLI-D-20-0125.1

Huo, W., and Xiao, Z. (2017). Modulations of solar activity on El niño modoki and possible mechanisms. *J. Atmos. Solar-Terrestrial Phys.* 160, 34–47. doi:10.1016/j.jastp.2017.05.008

Huo, W., Xiao, Z., Wang, X., and Zhao, L. (2021). Lagged responses of the tropical Pacific to the 11-yr solar cycle forcing and possible mechanisms. *J. Meteor. Res.* 35 (3), 444–459. doi:10.1007/s13351-021-0137-8

Ineson, S., Scaife, A., Knight, J., Manners, J., Dunstone, N., Gray, L., et al. (2011). Solar forcing of winter climate variability in the Northern Hemisphere. *Nat. Geosci.* 4, 753–757. doi:10.1038/ngeo1282

Kodera, K., Thieblemont, R., Yukimoto, S., and Matthes, K. (2016). How can we understand the solar cycle signal on the Earth's surface? *Atmos. Chem. Phys.* 138, 12925–12944. doi:10.5194/acp-16-12925-2016

Lean, J., and Rind, D. (2008). How natural and anthropogenic influences alter global and regional surface temperatures: 1889 to 2006. *Geophys. Res. Lett.* 35, L18701. doi:10.1029/2008gl034864

Leung, M., Cheung, H., and Zhou, W. (2017). Meridional displacement of the East Asian trough and its response to the ENSO forcing. *Clim. Dyn.* 48, 335–352. doi:10.1007/s00382-016-3077-8

Li, X., Chen, Y., and Zhou, W. (2017). Response of winter moisture circulation to the India-Burma trough and its modulation by the South Asian waveguide. *J. Clim.* 30, 1197–1210. doi:10.1175/JCLI-D-16-0111.1

Li, X., Wen, Z., and Huang, W. R. (2020). Modulation of South Asian jet wave train on the extreme winter precipitation over southeast China: Comparison between 2015/16 and 2018/19. *J. Clim.* 33, 4065–4081. doi:10.1175/JCLI-D-19-0678.1

Li, X. (2021). Maintenance of the South Asian jet wave train: eddy kinetic energy balance. *Clim. Dyn.* 57 (3-4), 687–700. doi:10.1007/s00382-021-05735-7

Ma, H., Chen, H., Gray, L., Zhou, L., Li, X., Wang, R., et al. (2018). Changing response of the North Atlantic/European winter climate to the 11 year solar cycle. *Environ. Res. Lett.* 13 (3), 034007. doi:10.1088/1748-9326/aa9e94

Ma, H., Chen, H., Lai, A., Li, X., Wang, R., and Gao, C. (2019). Robust solar signature in late winter precipitation over southern China. *Geophys. Res. Lett.* 46, 9940–9948. doi:10.1029/2019GL084083

Misios, S., Mitchell, D. M., Gray, L. J., Tourpali, K., Matthes, K., Hood, L., et al. (2016). Solar signals in CMIP-5 simulations: Effects of atmosphere-ocean coupling. *Q. J. R. Meteorol. Soc.* 142, 928–941. doi:10.1002/qj.2695

Misios, S., Gray, L. J., Knudsen, M. F., Karoff, C., Schmidt, H., and Haigh, J. D. (2019). Slowdown of the Walker circulation at solar cycle maximum. *Proc. Natl. Acad. Sci.* 116 (15), 7186–7191. doi:10.1073/pnas.1815060116

Poli, P., Hersbach, H., Dee, D., Berrisford, P., Simmons, A., Vitart, F., et al. (2016). ERA-20C: An atmospheric reanalysis of the twentieth century. *J. Clim.* 29 (11), 4083–4097. doi:10.1175/JCLI-D-15-0556.1

Rayner, N., Parker, D., Horton, E., Folland, C., Alexander, L., Rowell, D., et al. (2003). Global analyses of sea surface temperature, sea ice, and night marine air temperature since the late nineteenth century. *J. Geophys. Res. Atmos.* 108, 4407. doi:10.1029/2002JD002670

Roy, I., and Haigh, J. (2010). Solar cycle signals in sea level pressure and sea surface temperature. *Atmos. Chem. Phys.* 10, 3147–3153. doi:10.5194/acp-10-3147-2010

Sakai, K., and Kawamura, R. (2009). Remote response of the East Asian winter monsoon to tropical forcing related to El Niño–Southern Oscillation. *J. Geophys. Res.* 114, D06105. doi:10.1029/2008JD010824

Scaife, A., Ineson, S., Knight, J., Gray, L., Kodera, K., and Smith, D. (2013). A mechanism for lagged North Atlantic climate response to solar variability. *Geophys. Res. Lett.* 40 (2), 434–439. doi:10.1002/grl.50099

Shen, X., Zhou, N., Yang, S., and Miao, R. (2019). Analysis of two extreme precipitation events and circulation anomalies in Yunnan province in winter of 2015. *Torrential Rain Disasters* 38, 380–385. (in Chinese). doi:10.3969/j.issn.1004-9045.2019.04.011

Song, J., Li, C., and Zhou, W. (2014). High and low latitude types of the downstream influences of the North Atlantic Oscillation. *Clim. Dyn.* 42, 1097–1111. doi:10.1007/s00382-013-1844-3

Takaya, K., and Nakamura, H. (2001). A formulation of a phase-independent wave-activity flux for stationary and migratory quasigeostrophic eddies on a zonally varying basic flow. *J. Atmos. Sci.* 58, 608–627. doi:10.1175/1520-0469(2001)058<0608:AFOAPI>2.0.CO;2

Thiéblemont, R., Matthes, K., Omrani, N., Kodera, K., and Hansen, F. (2015). Solar forcing synchronizes decadal North Atlantic climate variability. *Nat. Commun.* 6, 8268. doi:10.1038/ncomms9268

Watanabe, M. (2004). Asian jet waveguide and a downstream extension of the North Atlantic oscillation. *J. Clim.* 17, 4674–4691. doi:10.1175/JCLI-3228.1

Wei, W., Ren, Q., Lu, M., and Yang, S. (2022). Zonal extension of the Middle East jet stream and its Influence on the Asian monsoon. *J. Clim.* 35 (14), 4741–4751. doi:10.1175/JCLI-D-21-0697.1

Wen, M., Yang, S., Kumar, A., and Zhang, P. (2009). An analysis of the large-scale climate anomalies associated with the snowstorms affecting China in January 2008. *Mon. Wea. Rev.* 137, 1111–1131. doi:10.1175/2008MWR2638.1

Wirth, V., Riemer, M., Chang, E., and Martius, O. (2018). Rossby wave packets on the mid-latitude waveguide: A review. *Mon. Wea. Rev.* 146, 1965–2001. doi:10.1175/MWR-D-16-0483.1

Yang, S., Lau, K., Yoo, S., Kinter, J., Miyakoda, K., and Ho, C. (2004). Upstream subtropical signals preceding the Asian summer monsoon circulation. *J. Clim.* 17 (21), 4213–4229. doi:10.1175/JCLI3192.1

Zhou, J., and Tung, K. (2010). Solar cycles in 150 years of global sea surface temperature data. *J. Clim.* 23, 3234–3248. doi:10.1175/2010JCLI3232.1

frontiers | Frontiers in Earth Science

TYPE Original Research
PUBLISHED 19 July 2023
DOI 10.3389/feart.2023.1157753

OPEN ACCESS

EDITED BY
Siming Liu,
Southwest Jiaotong University, China

REVIEWED BY
Sergey Alexander Pulinets,
Space Research Institute (RAS), Russia
Mirela Voiculescu,
Dunarea de Jos University, Romania

*CORRESPONDENCE
Hiroko Miyahara,
miyahara@musabi.ac.jp

RECEIVED 03 February 2023
ACCEPTED 06 July 2023
PUBLISHED 19 July 2023

CITATION
Miyahara H, Kusano K, Kataoka R, Shima S and Touber E (2023), Response of high-altitude clouds to the galactic cosmic ray cycles in tropical regions.
Front. Earth Sci. 11:1157753.
doi: 10.3389/feart.2023.1157753

Response of high-altitude clouds to the galactic cosmic ray cycles in tropical regions

Hiroko Miyahara[1,2]*, Kanya Kusano[3], Ryuho Kataoka[2,4,5], Shin-ichiro Shima[6] and Emile Touber[2,7]

[1]Humanities and Sciences/Museum Careers, Musashino Art University, Tokyo, Japan, [2]Okinawa Institute of Science and Technology, Okinawa, Japan, [3]Institute for Space-Earth Environmental Research, Nagoya University, Nagoya, Aichi, Japan, [4]National Institute of Polar Research, Tachikawa, Japan, [5]SOKENDAI, The Graduate University for Advanced Studies, Hayama, Kanagawa, Japan, [6]Graduate School of Information Science, University of Hyogo, Kobe, Japan, [7]Department of Mechanical Engineering, Imperial College London, London, United Kingdom

Galactic cosmic rays are one of the possible mediators of the solar influence on climate. However, the impacts of GCR on clouds and climate systems are not fully understood. In this paper, we show that the high-altitude clouds associated with deep convective activities are responding to the decadal-scale cycles of GCRs and that the susceptible areas are seasonally variable. Most notable responses were found in August over tropical land areas, suggesting that the susceptivity of clouds to GCRs depends on the depth of convective activities and the abundance of aerosol precursor materials. Furthermore, following the activation of high-altitude cloud formation, an increase in sea surface temperature (SST) gradient was observed over the Pacific. Although the response of sea surface temperature to solar activity has mostly been discussed as mediated by solar radiations, we propose that another mechanism is possible: through the impact of GCRs on clouds and the resultant changes in atmospheric circulations.

KEYWORDS

sun-climate connection, cosmic rays, clouds, atmospheric circulation, sea surface temperatures

1 Introduction

The possible responses of climate to solar activity variations have been reported for various time scales (Gray et al., 2010), and several mediators have been proposed, including solar radiations (Kodera & Kuroda, 2002; Matthes et al., 2006; Meehl et al., 2008; Misios et al., 2019), GCRs modulated by solar-wind magnetic field (Svensmark & Friis-Christensen, 1997; Carslaw et al., 2002), and the interplanetary magnetic field (Voiculescu et al., 2013; Scott et al., 2014). Notable responses of climate, such as temperatures and precipitation, to solar activity have been observed for millennial (Bond et al., 2001; Obrochta et al., 2012) and centennial time scales (Neff et al., 2001; Wang et al., 2005); however, identifying the relative importance of mediating solar-activity related parameters is difficult at such time scales, as the radiative and magnetic outputs of the Sun vary in a similar pattern. To identify the contribution of each of the parameters and trace the propagation of their impacts, it is needed to examine the shorter time scales, such as those associated with the solar decadal cycle, or even shorter, where the temporal variation of the solar radiative outputs and GCRs are slightly different (Miyahara et al., 2008; Yamaguchi et al., 2010).

Solar radiations vary based on the emergence and disappearance of sunspots and faculae on the solar surface (Domingo et al., 2009). Therefore, they change along with the decadal-scale variation of the activity level of sunspots. However, the flux of GCRs incident to the Earth's atmosphere is attenuated by the solar wind magnetic field in the heliosphere and is thus dependent on the evolution of the configuration and its direction (Jokipii & Thomas, 1981). As a result, the flux of GCRs is dependent on the solar magnetic polarity that reverses every solar cycle maximum (see Supplementary Figure S1). In addition, the transient intensification of the magnetic fields associated with solar coronal mass ejections contributes to the shielding of GCRs (Forbush, 1938). Due to the travel time of the solar magnetic field in the heliosphere and its influence on the trajectory of GCRs, the variation of GCRs at Earth occasionally delays up to ~1.4 years relative to the decadal variations in solar activity level (Usoskin et al., 2001; Koldobskiy et al., 2022). Such features might allow identifying the potential contribution of GCRs to the Sun–Climate connection.

The possible impact of the decadal-scale solar activity cycle on climate has been reported, e.g., in the North Atlantic region (Kodera, 2002; Gray et al., 2016; Kuroda et al., 2022), in the Pacific region (Dima & Voiculescu, 2016), and particularly in the tropical region (Gleisner and Thejll, 2003; van Loon et al., 2004; White, 2006; Misios et al., 2019). Recent studies have suggested that an increased solar activity results in a reduction in the east-west gradient of SST over the Pacific and in a weakening of the Pacific Walker Circulation (Misios et al., 2019). These decadal-scale Sun-Climate connections have been mostly attempted to be explained by the so-called "top-down" mechanism, through which solar UV (SUV) influences stratospheric temperature and subsequently alters tropospheric circulation (Kodera & Kuroda, 2002; Matthes et al., 2006) or by the "bottom-up" mechanism, through which the total solar irradiance (TSI) warms up the ocean to change atmospheric circulation (Meehl et al., 2008; Misios et al., 2019). However, significant positive feedback is needed for the latter mechanism to explain the observed temperature variations, as the variability of TSI over solar cycles is as small as 1 W/m^2.

It is, however, also possible that GCRs contribute to the decadal-scale Sun–Climate connection through the ionization and its impacts on cloud condensation nuclei (Dickinson, 1975; Carslaw et al., 2002; Kirkby et al., 2011; Svensmark et al., 2013), by enhancing the collision efficiency between aerosols and cloud droplets (Tinsley, 2000; Zhou et al., 2009; Tinsley, 2022), or by stabilizing the molecular cluster to grow to cloud condensation nuclei (Tinsley and Deen, 1991; Yu & Turco, 2001; Yu, 2002). However, it is not well understood where their effects may proceed in actual environments and how those impacts propagate in the climate system.

Originally, it was suggested that the cloud covers over oceans are enhanced with the increase in GCRs (Svensmark & Friis-Christensen, 1997). Later on, it was demonstrated that the low-altitude clouds over oceans are most significantly correlated to GCR variations (Marsh & Svensmark, 2003). Voiculescu et al. (2006) has suggested that the correlation to low-altitude clouds is significant over the mid latitudes of the Atlantic. However, both theoretical estimates and the laboratory chamber experiment have indicated that GCR-induced aerosol formations are rather efficient at low temperatures (Kazil et al., 2006; Yu et al., 2008; Kirkby et al., 2011; Dunne et al., 2016) (i.e., at high altitudes). The upper troposphere is also favorable in terms of the abundance of GCR-induced ions (Ney, 1959; Ermakov et al., 1997; Usoskin et al., 2004). Deep convection is a possible method for supplying aerosol precursors from the biogenic activities at the ground or ocean surfaces to the upper troposphere (Twohy et al., 2002; Kazil et al., 2006); therefore, the high-altitude clouds near highly convective areas are potentially most susceptive to GCRs, although the deep convection may also contribute to the transport of newly-formed cloud condensation nuclei to the lower troposphere to change the cloud properties (Williamson et al., 2019).

The impact of GCRs through the formation of aerosols may only be emphasized if there are few pre-existing aerosols in an ambient environment (Almeida et al., 2013), as newly formed aerosols tend to be adsorbed to pre-existing aerosols if they are abundant. Atmospheric aerosols, including the ones that have anthropogenic origins, are mostly confined within ~4 km from the surface, except over the mountains with high elevations (Koffi et al., 2016). This factor also suggests a possibility that only the middle to upper troposphere meets the criteria of significantly being impacted by GCRs.

In this paper, we examine the response of high-altitude clouds based on records over the past 43 years. Due to the possible long-term artifactual influence from satellite-based observations (Evan et al., 2007), it is crucial to examine the cloud behaviors based on multiple independent data sets, and, to concentrate on the short to mid-term fluctuations. Therefore, in this work, we base on two records (see methods) and focus on the response at the decadal scale. We used monthly-resolved high temporal-resolution data to constrain the possible conditions required for cloud activity to respond to GCR variations.

2 Methods

To examine the response of high-altitude clouds to GCR decadal cycles, we utilized a daily record of Outgoing Longwave Radiation (OLR) (Lee and NOAA CDR Program, 2001) with 1° × 1° resolution for Jan/1979–Dec/2021. OLR reflects the existence of high-altitude clouds, although only for low-latitude regions. For example, the existence of high clouds with low cloud-top temperatures leads to lower OLR value. In this study. We calculated the fraction of the days OLR is equal to or lower than a threshold value for each month. We produced four time series for each 1° × 1° grid with a threshold value: 170 W/m^2, 200 W/m^2, 230 W/m^2, and 260 W/m^2, respectively. In cases where the threshold used yielded a fraction of none or 100% for more than fifty percent of the time window used in the analysis, the threshold was considered too low or too high for that 1° × 1° tile and was discarded. The time series were then compared with the GCR variation to derive the Spearman's correlation coefficient. The maximum correlation coefficient among the four cases and the corresponding threshold were displayed on the maps. In the tropical regions, if the maximum correlation was obtained with the threshold of 200 W/m^2, it implies that tropospheric high-altitude clouds (cloud top pressure ≤ ~440 mb) are most sensitively responding to GCRs. On the other hand, if the maximum correlation was obtained with 230 W/m^2, it suggests that adding mid-altitude clouds (~440 mb < cloud top pressure ≤680 mb) improves the correlation.

The response of clouds to GCR may be accompanied by some time lags; therefore, correlations were examined for lags between 0 and 3 years. When estimating correlation coefficients with a time lag of 0 years, correlation coefficients with lags of −2 years (GCRs lag cloud variation with 2 years) to 0 years (no time lag) were calculated, and only the cases the correlation was maximized at 0 years were considered non-false correlation and displayed on the map. For the zero-year lag, the cloud data were compared with the monthly mean GCR flux and with the yearly mean for a lag of 1 year or longer. With the lag and threshold that yielded the maximum correlation coefficient, we estimated, based on the regression line, the maximum variability of high-altitude clouds over the GCR cycles, i.e., the variability for 1987–1990 when GCR variation was at its maximum. For the GCR variation, the neutron monitor data for Jan/1953–Nov/2006 obtained at the Climax station (http://cr0.izmiran.ru/clmx/main.htm) and those for Apr/1964–Dec/2021 obtained at the Oulu station (http://cr0.izmiran.ru/oulu/main.htm) were used. The daily data were normalized and averaged to obtain the monthly means. Prior to the analyses, the long-term trends were subtracted from the cloud and GCR data to concentrate on the decadal-scale variations.

We also analyzed the ISCCP-HGM series provided by the International Satellite Cloud Climatology Project (Rossow et al., 2016) to validate the response of OLR to GCRs. We used the monthly data of high (≤440 mb) and low (>680 mb) cloud fractions for July/1983–June/2017.

For the examination of the response of SST, we used the NOAA Optimum Interpolation SST V2 data provided by NOAA/OAR/ESRL PSL (Reynolds et al., 2002). We used the 1-degree grid data for Dec/1981–Dec/2021. We also used the Niño 4 index (Trenberth and Stepaniak, 2001) and the NCEI Pacific Decadal Oscillation index (Mantua, 1999). To analyze the response of surface pressure, zonal wind, and meridional wind, we used the JRA-55 (Japanese 55-year Reanalysis) data of monthly mean pressure reduced to mean sea level with 1.25° × 1.25° resolution (Kobayashi et al., 2015). We only used data from 1979 when the observational data was substantial and the reliability was high (Ebita et al., 2011). For the precipitation analysis, we used CMAP monthly mean precipitation data with 2.5° × 2.5° resolution (Huffman et al., 1997).

To examine the responses of SST and atmospheric data to TSI, the NOAA Climate Data Record of TSI (Coddington et al., 2015) was used. As an index of solar UV, NOAA adjusted the solar radio flux at 10.7 cm (https://lasp.colorado.edu/lisird/data/noaa_radio_flux/) were combined with the Penticton radio flux data for May/2018 to present (https://lasp.colorado.edu/lisird/data/penticton_radio_flux/).

Note that the data from Jun/1991 to May/1993 were excluded from the analyses so that the possible impacts from the eruption of Mt. Pinatubo in 1991 are eliminated.

3 Results

3.1 Relationship between high-altitude clouds and GCR cycles

The monthly data of high-altitude clouds, as monitored by OLR and those of International Satellite Cloud Climatology Project (ISCCP) H-series Gridded Monthly (HGM), were compared with GCR cycles (see Methods). Then, it was found that both series consistently indicate that there are regions in the tropics where high-altitude clouds show significant positive correlations to decadal-scale GCR cycles (Figures 1, 2, also see Supplementary Figures S2, S3), suggesting that GCRs may be contributing to the changes in cloud activity. However, these areas are localized and vary based on the seasons. Most significant correlations were found in August for the areas in which the formation of high-altitude clouds is active (see Figure 1), supporting the above-mentioned hypothesis; however, they were localized to the land areas and nearby oceans. There were also some regions in which high cloud formations were suppressed (see below). In boreal winter, the areas showing significant correlations migrated to the convective regions in the southern hemisphere (Figure 2, also see Supplementary Figure S3). The correlations were weaker compared with those of August; however, a prompt response was observed around the northern tip of Australia and the northwest coast of South America (Figure 2A). Figures 1F–I and Figures 2F–I indicate the OLR range that achieved the maximum correlation for each grid. While the threshold of 200 W/m^2 or lower suggests that the response is limited to the high-altitude clouds, the threshold of 230/m^2 or higher implies that the addition of mid- and possibly lower altitude clouds improves the correlation. For example, Figure 1F and Figure 2F suggest that the correlations off the northwest coast of South America involve the response of mid-altitude clouds.

In August, the correlations were maximized in 1 year (Figure 1B) and diminished afterward (Figures 1C, D). Such lagged responses of clouds imply that a positive feedback mechanism exists behind the GCR–cloud connection (see the fifth paragraph in the Discussion). The correlations around the Indonesian maritime continent were maximized with a further delay (Figures 1C, D), suggesting an impact through the mechanism involving atmospheric and ocean coupling. Similarly, the correlations around the northern tip of Australia and the northwest coast of South America in January diminished after 1 year, whereas the correlations around the Indonesian maritime continent were maximized in 2–3 years (Figures 2C, D).

The maximum variability of the ratio of existence days of high-altitude clouds over the GCR cycle is shown in Figure 1J and Figure 2J. The obtained maps indicate that there are regions where the variability is much larger than expected from the ion production rate in the tropics (see Supplementary Figure S12 of Dunne et al., 2016), also supporting the existence of a positive feedback mechanism. For example, while the variability of ion production rate in the upper troposphere is up to ~20% around 20–30°N and 20–30°S in the tropics and is smaller in the lower latitude regions, the variability of the fraction of days OLR is equal to or lower than 200 W/m^2 is larger than 20% in August around eastern India and Bangladesh (Figure 3), where the mean fraction is ~40% (Figure 1E), although the corresponding variability of cloud amount needs further investigations. Note that the enhancement in the fraction of days with the presence of high clouds as estimated based on the OLR thresholds may also be caused by the uplift of the convective cloud system in addition to the increase of cloud amount itself.

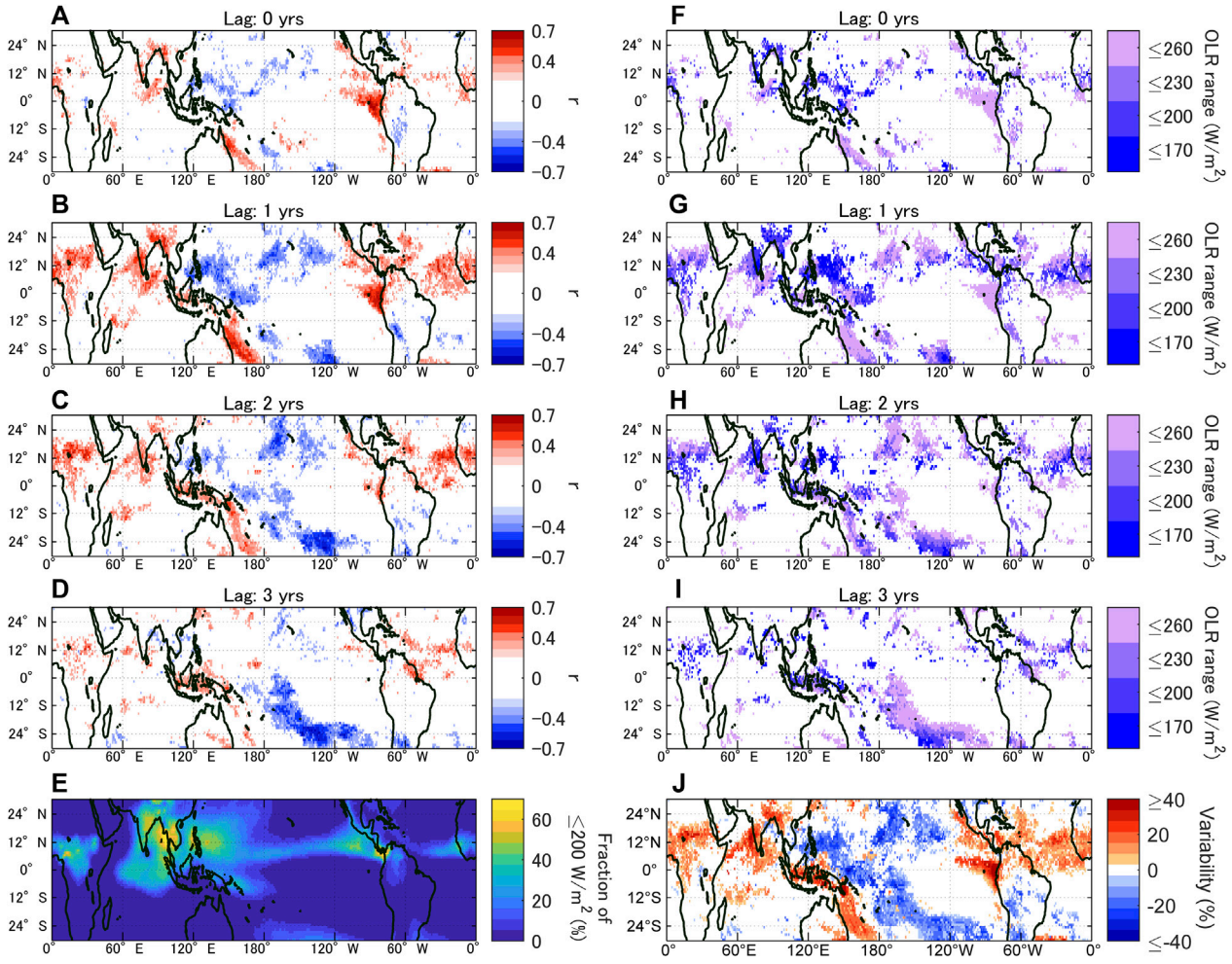

FIGURE 1
(A–D) Correlation coefficient r ($p \leq 0.05$) between the ratio of existence days of high-altitude clouds and GCRs in August for a time lag of 0 (no time lag) to 3 years (clouds lag GCRs). **(E)** Fraction of the days OLR is ≤200 W/m^2 in August. **(F–I)** OLR ranges that yielded the maximum correlation coefficients in **(A–D)**. **(J)** Maximum variability of the ratio of existence days of high-altitude clouds over the GCR cycles.

3.2 Relationship between SST and the GCR cycles

Figures 4A–E indicates the correlation coefficient between SST and GCRs in August when the most notable correlations were found for cloud activity. Figure 4F exhibits the spatial pattern of SST in August. The figures indicate that decadal-scale forcing results in a characteristic spatial pattern in the central and western Pacific. While the SST in the central Pacific tends to decrease as GCR is enhanced, especially in the winter hemisphere (Figure 4G), the SST in the southwestern Pacific tends to be increase, suggesting that the trade winds over the Pacific region are intensified at the GCR cycle maxima. This tendency is consistent with the previously suggested reduced east–west SST gradient and the weaker trade winds at the solar cycle minima (Misios et al., 2019). However, the response of SST to TSI, which was suggested as the forcing parameter in Misios et al. (2019), delays by 1 year compared to the response to GCR, and the correlations between SST and TSI were maximized with a lag of 3 years (see Figures 4H–N). The relationship between SST and SUV is more or less the same for TSI (see Supplementary Figure S4) and is peaked with a lag of ~3 years.

The areas showing significant correlations between SST and GCRs with no time lag were limited to the southern edge of the tropical zone around 20–30°S 100–130°W (Figure 4A); however, the impacts on SST were expanded and maximized with a lag of 2 years (Figure 4C). The maximum temperature change around the equatorial region over the GCR cycle was as large as 1.7 K and was observed in an area centered at about 180°W(E) (Figure 4G, also see Supplementary Figure S5 for the time profile). Regarding January, the east–west contrast was less well structured. However, the maximum change around the region reached 2.1 K (see Supplementary Figure S6). This region is often characterized by the El Niño modoki events (Ashok et al., 2007) and has been examined using the Niño 4 index, one of the indices of the El Niño–Southern Oscillation. Although the Niño 4 index is derived based on the SST over the region wider than those indicating correlations to GCRs, and thus the correlation coefficient between Niño 4 and GCRs is relatively lower, the lead-lag

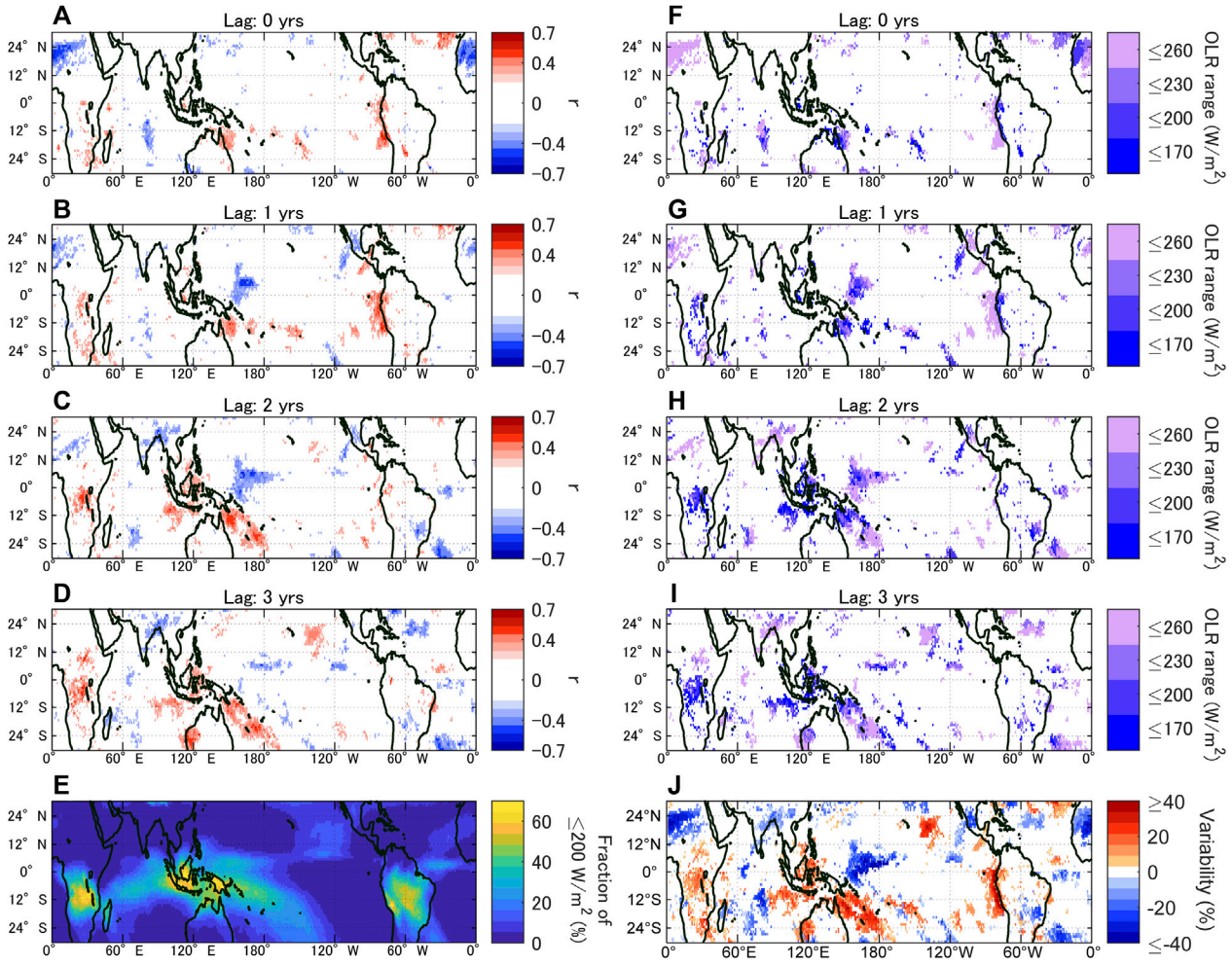

FIGURE 2
(A–J) Same as Figure 1 but for January.

analysis supports that the decadal component of SST in this region lags that of GCRs by about 2 years (see Supplementary Figures S7A, B).

Figures 4C, G indicates that the areas showing correlation with GCRs include the Bering Sea, which is within the region characterized by the Pacific Decadal Oscillation (Mantua et al., 1997), and that the correlations become maximum with a lag of 2 years. The lead-lag analysis between the Pacific Decadal Oscillation index and the GCRs shows that the correlation becomes maximum when the lag is about 2–3 years (see Supplementary Figures S7C, D), supporting that the decadal component of the Pacific Decadal Oscillation also lags that of GCRs.

In the cases the decadal components of the Niño 4 and the Pacific Decadal Oscillation indices were compared to the tropical high-altitude clouds, correlations were observed with a spatial pattern similar to those of Figures 1A, B; however, they were maximized when the lag was −2 to −1 years (see Supplementary Figures S8, S9), supporting that the decadal components in the Pacific Decadal Oscillation and the Niño 4 indices lag those of tropical cloud activities. Note that the direct comparison between the Niño 4 index and the Pacific Decadal Oscillation index shows that they are linked with an occasional lag of up to 1 year (see Supplementary Figures S7E, F).

3.3 Relationship between the surface pressure, zonal/meridional winds, and GCR cycles

The comparison between the surface pressure and GCRs (Figures 5A–F) indicates increased pressure around the southern edge of the tropical zone in the Pacific (Figure 5A), and the impacts are further intensified and expanded toward the northern hemisphere in 1–2 years (Figures 5B, C). On the contrary, the tropical regions between 120°W and 100°E indicate a tendency of decreasing pressure for the higher GCR, especially over the oceans. The zonal and meridional wind speed compared with GCRs suggests a possible intensification of trade winds or a westerly migration of the deep convection core around the western Pacific, especially in the northern hemisphere (see Supplementary Figure S10). When the

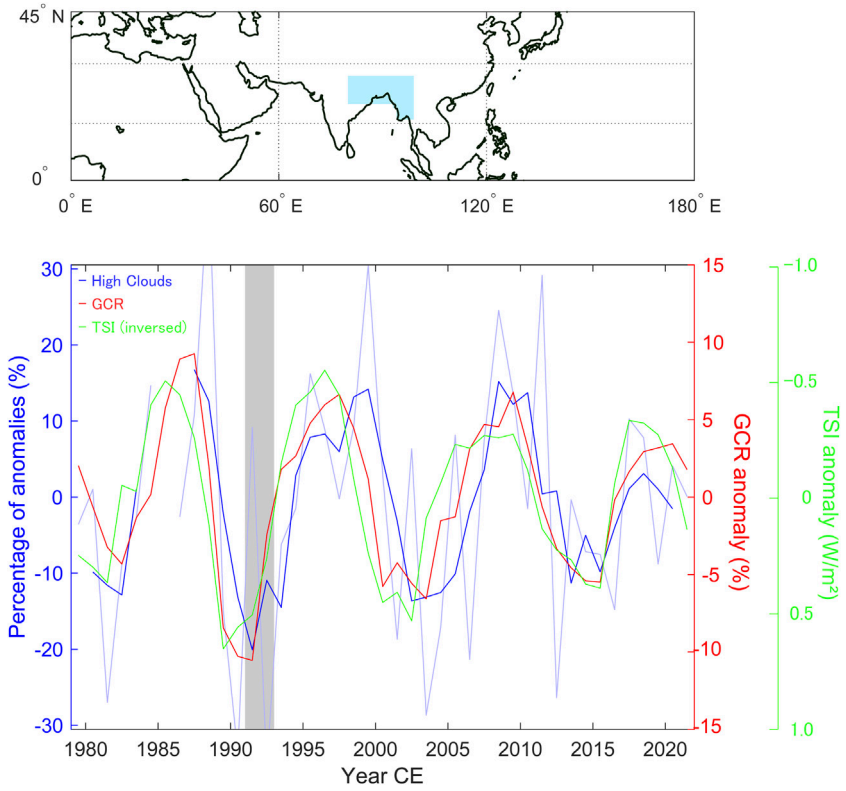

FIGURE 3
Variability of the ratio of existence days of high-altitude clouds as monitored by OLR with a threshold value of 200 W/m^2 (pale blue line) and the 3-point running averages (blue line) for the area shown in the map (highlighted by cyan), plotted together with the anomaly of GCR flux monitored by neutron monitors (red line) and TSI (green line). The variability of ion production rate in the upper troposphere over the solar cycles is about 20% around the region (Dunne et al., 2016). Note that all of the series are high-pass filtered for $p \leq 15$ yrs. Note also that the period of 2 years after the eruption of Mt. Pinatubo, indicated by the gray highlight, was excluded from the correlation analysis of this study.

pressure data were compared with TSI, slightly different behaviors were recognized (Figures 5G–L). One is the absence of immediate response of pressures (Figure 5G), and the other is the overall delay in the responses (Figures 5H–J) compared with the case for GCR (Figures 5A–C).

4 Discussion

Although the influence of solar cycles on climate has so far been mostly discussed under the framework of the "top-down" or "bottom-up" mechanisms described earlier, the present results suggest that another mechanism is possible: "deep-convective-clouds-mediated" mechanism through the influence of GCRs on the development of deep convective clouds, and their impact on atmospheric circulation and SST gradient.

The monthly-resolved high-resolution data allowed us to identify the areas where high-altitude clouds are responding to GCR variations and to understand the possible contributing factors determining their susceptivity, although high-resolution analyses might fail to capture the responses of the clouds that are not stationed and randomly advected after being formed or those whose locations are under the influence of other interannual variations such as the El Niño–Southern Oscillation. Significant positive GCR-cloud correlations were found in tropical regions; however, they are concentrated over land and nearby oceans, suggesting the importance of any of or all the following factors: 1) the presence of relatively deeper convections compared with oceans, 2) the abundance of continental aerosol precursors for ions to produce aerosols, and 3) a more pronounced diurnal cycle over lands (see below). Most notable correlations were found in August around West and Central Africa, India and Bangladesh, the northwest coast of South America, and the proximate oceans, with a lag of 0–1 years (Figures 1A, B). The correlations around eastern India and Bangladesh suggest that the sea breezes blowing toward elevated mountains may also contribute to creating an environment in which cloud formations become sensitive to GCRs. They uplift a substantial amount of water vapor and aerosol precursors to the upper troposphere, similar to deep convection. The correlations around the southern Brazil in February (see Supplementary Figure S11) may also be related to the same mechanism. Even though convective cloud formation is active over Brazil in austral summer, the correlations were not significant except for the areas facing oceans, thus suggesting the importance of marine aerosol precursors for the impact of ions.

The more pronounced impact in August, compared with January, can be associated with the relatively low pressure around the convective areas in August (Figure 5E, also see

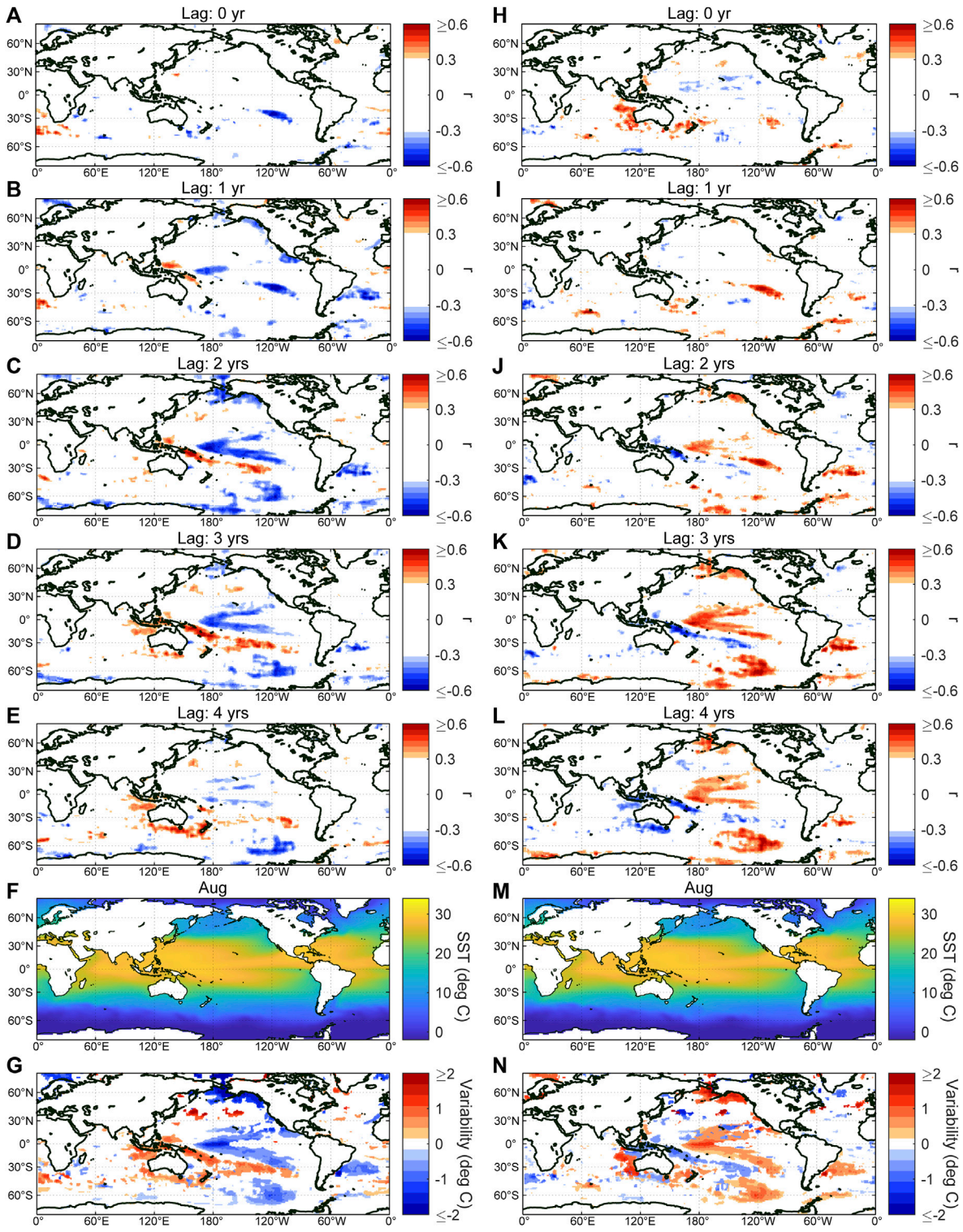

FIGURE 4
(A–E) Correlation coefficient r ($p \leq 0.05$) between GCRs and SST in August for a lag of 0–4 years. **(F)** Monthly mean SST for August. **(G)** Maximum variability of SST over the GCR cycles. **(H–N)** Same as **(A–G)** but for TSI.

Supplementary Figure S12), which provides improved conditions for supplying water vapor and aerosol precursors to the upper troposphere. In other words, the overlap of the Intertropical Convergence Zone (ITCZ) with the continental areas could be the key to strengthening the GCR-cloud connection. The significant northward excursion of ITCZ from the geomagnetic

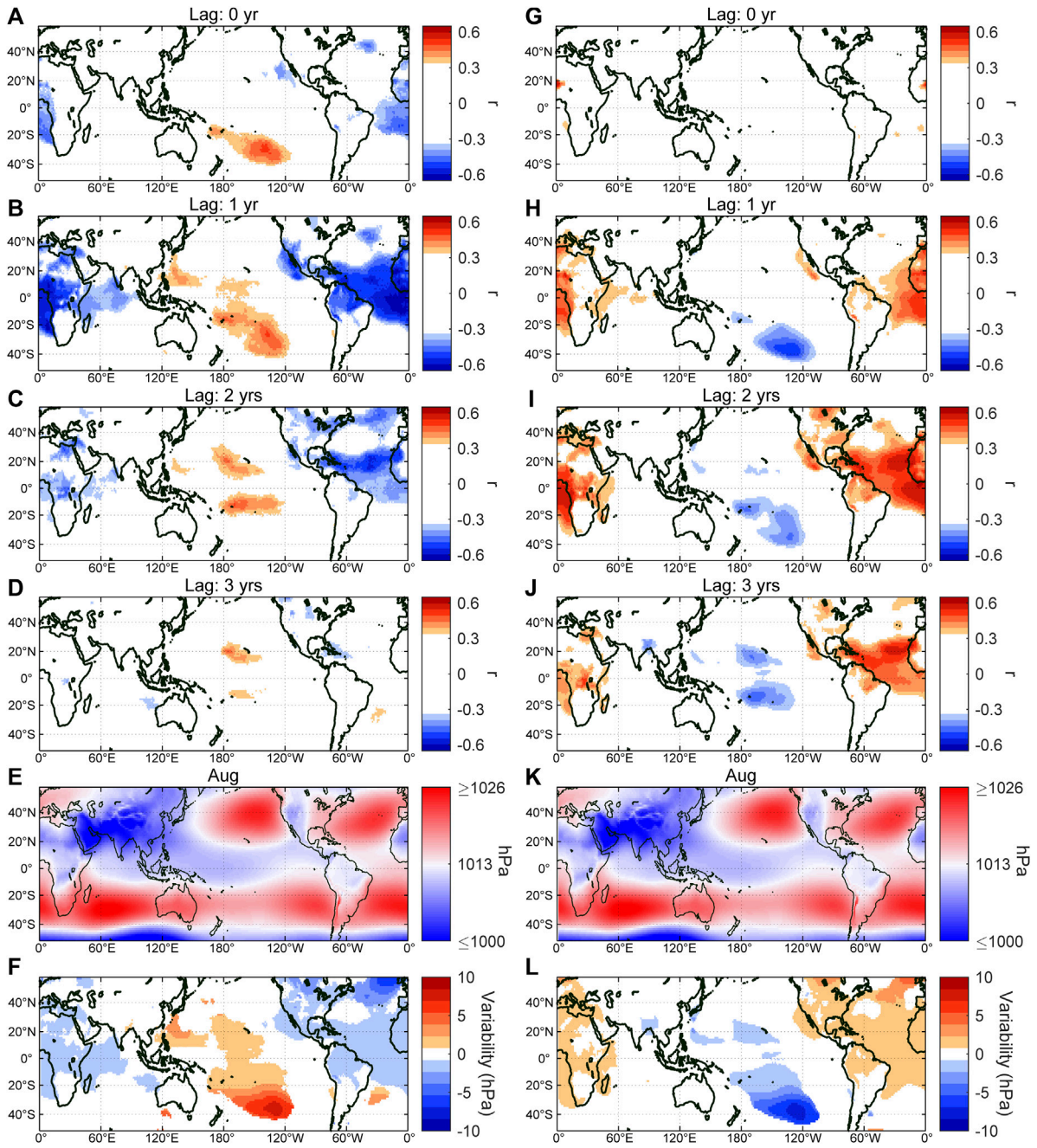

FIGURE 5
(A–D) Correlation coefficient r ($p \leq 0.05$) between surface pressure and GCRs in August for a lag of 0–3 years. **(E)** Monthly mean pressure reduced to the mean sea level for August. **(F)** Maximum variability of surface pressure over the GCR cycles. **(G–L)** Same as **(A–F)** but for TSI.

equator in August also contributes in terms of the magnitude of the variability in ion production rate. As also mentioned in the Results section, the variability of the abundance of GCR-induced ions is greater at higher latitudes, especially at high altitudes (see Supplementary Figure S12B of Dunne et al., 2016); thus, the excursion of ITCZ significantly increases the encounters between ions and aerosol precursors. The lower pressure in August also contributes to the higher GCR flux in the troposphere due to the reduced barometric effect (Myssowsky and Tuwim, 1926; De Mendonça et al., 2013), although the associated enhancement is only a few percent. The more significant impact in August may also be related to the seasonal variability in the emission of organic compounds from biogenic activities, the precursory materials for the aerosol formation (Kirkby, 2007; Almeida et al., 2013). For example, the flux of dimethyl sulfide is maximum in the northern hemisphere from July to September and is especially enhanced around the north part of the Indian Ocean, near the continental areas (Land et al., 2014).

Although the climatological condition is similar for July and August, the correlations between high clouds and GCRs are

significantly different. The impact in July is sparse and not notable for a lag of 0–1 years (see Supplementary Figures S13A, B), while correlations become pronounced around the Indonesian maritime continent for a lag of 2–3 years (see below). The possible explanation for the relatively weaker response in July may be related to the influence of the updrafted pre-existing aerosols masking the impact of GCRs. For example, the abundance of mineral dust in northern Africa is maximum in June and starts to decrease in July (Vandenbussche et al., 2020). It has also been reported that the aerosol optical depth in northern India is maximum in May and that it starts to decrease in July (Gautam et al., 2010). Further examinations are, however, needed to confirm the impact of pre-existing aerosols.

The tendency of the decreased pressure around tropical zones except for the Pacific region (Figures 5A–C) can be related to the activated formation of deep convective clouds, and it may be causing positive feedback to the promotion of cloud activity by the GCRs by enhancing the encounters between ions and aerosol precursory materials. It has been suggested that aerosol particles could prolong the lifetime of deep convective clouds by enhancing smaller ice crystals with smaller fall velocities (Grabowski & Morrison, 2020) and by increasing freezing water droplets to enhance the release of latent heat (Rosenfeld et al., 2008), resulting in the extension of associated anvils. Then, the extended thin anvil clouds over the proximate area would increase the net radiative forcing (warming) (Koren et al., 2010). It has been speculated that the enhancement of latent heat release may even strengthen deep convection (Rosenfeld et al., 2008), although this factor may only be significant for the altitudes below the freezing level (Grabowski & Morrison, 2020). The latent heat release is also expected to increase in the case the collisional processes in clouds are promoted by the electrification of aerosols and cloud drops by GCRs (Tinsley and Deen, 1991). Enhancement of latent heat then contributes to stronger and/or longer updrafts. The synchronized prolongation/activation of convections over land in tropical regions should result in a tendency of decreased pressure around the area. Note that while the correlations between clouds and GCRs were observed most significantly at the high altitudes, the process behind the intensification of deep convective cloud activities may also act at the middle layer of deep convective clouds. As mentioned in the Introduction, deep convection may transport the newly-formed cloud condensation nuclei to the lower altitudes.

The pressure decrease is more prominent over oceans and is significantly weaker over land (Figure 5B), and this might be related to the more pronounced diurnal cycle over land (Yang and Slingo, 2001), which may mask the signals of the transient pressure decreases in monthly averaged data. However, the diurnal cycle over land is probably playing an essential role in sustaining convective activity and supplying aerosol precursors to the upper troposphere, even under enhanced cloud formation. In fact, the precipitation pattern indicates increased precipitation around the areas where high-altitude clouds are increased (see Supplementary Figure S14), supporting this tendency. Increased precipitation might also contribute to removing pre-existing aerosols from the atmosphere.

The changed pressure gradient then affects atmospheric circulation (see Supplementary Figure S9), allowing the change in the SST gradient over the Pacific Ocean (Figures 4A–E). The reduced formation of high-altitude clouds over the western Pacific (Figures 1A, B) can be associated to the westward relocation of deep convections around the area. Low-altitude clouds, instead, are likely increased around the western Pacific (see Supplementary Figures S15G, H), consistent with the previously found correlation between GCRs and low-altitude clouds in this region (Marsh and Svensmark, 2003). It is worth noting that this is a region of typhoon generation (Bloemendaal et al., 2020). While less typhoon activity is suggested for the higher GCR flux at this region, more high-altitude clouds are expected for the higher GCR flux around the areas where hurricanes are generated, as suggested by the positive relationship over the low latitude regions of the North Atlantic (Figure 1B).

The westward extension of trade wind over the Pacific eventually warms the ocean around Indonesian maritime continent and off the northeast coast of Australia, and this warming is maximized with a lag of 2–3 years (Figures 4C, D). The enhancement of high-altitude clouds around the area with a lag of 2–3 years can be related to this increased SST. The correlation between the GCRs and the SST in the northern part of the Pacific Ocean with a lag of ~2 years suggests that the altered atmospheric circulation pattern may also eventually contribute to modulating the Pacific Decadal Oscillation, although the mechanism behind the connection to the Pacific Decadal Oscillation remains unknown and thus needs further examination.

The responses of atmospheric circulation and SST to the GCR cycles are similar to those suggested as a response to TSI cycles in previous studies; however, there are two notable differences. The first is the overall slower responses of atmospheric circulation and SST to TSI than when compared to GCR (Figures 4H–L; Figures 5G–J), consistent with the ~1-year delay of GCRs to TSI. The second is the warming of the eastern Indian Ocean as an immediate response to TSI (Figures 4H, N). This feature, however, contradicts the weakening of the easterly wind in the western Pacific and the cooling tendency around the region suggested for the TSI maxima, as seen for the lag of 2–4 years (Figures 4J–L). Instead, it is more likely that this warming is related to the positive response of this region to GCR with a lag of ~4 years (Figure 4E), which is a remnant of the impact around the Indonesian maritime continent (Figure 4D). Note that the areas responding positively to GCR with a lag of 4 years could indicate an apparent negative correlation to TSI with a lag of ~5.4 years because GCR lags ~1.4 years behind and correlates inversely with TSI. Five years are then nearly 180 degrees of a decadal solar cycle; thus, it could result in an apparent immediate positive response to TSI.

5 Concluding remarks

The possible solar influence pathway on climate systems through the variation of GCRs can be summarized as follows. First, GCRs impact the deep convective cloud activities in the tropics, primarily over the land areas, resulting in a decrease in pressure around the area, possibly giving positive feedback to cloud formation. Second, the reduced pressure intensifies atmospheric circulations and changes the SST pattern over the Pacific. Finally, the altered SST pattern activates the high-altitude cloud formation around the Indonesian maritime continent. Note that although the suggested characteristic response of clouds to GCRs seems to support the existence of GCR's impact through the formation of aerosols, it is possible that they also

affect clouds by the other paths, such as promoting the collisions between aerosols and cloud droplets (Tinsley, 2000; Zhou et al., 2009; Tinsley, 2022). Further investigations on the response of deep convective clouds to the GCR variations, especially over tropical land areas, should contribute to elucidate the contribution of ions, possibly through multiple mechanisms, and to realize the physics-based simulations to quantitatively evaluate the GCR's impacts on cloud activities and global climate.

It is noteworthy that no correlation was observed in SST around the eastern Pacific region, where the El Niño–Southern Oscillation is most prominent. It was, however, found that the areas showing response to GCRs include the regions where periodic behaviors are often observed in SST, such as El Niño Modoki, the Indian Ocean Dipole, and the Pacific Decadal Oscillation. It is, therefore, possible that the GCRs may enhance the variability of the decadal component in such periodic behaviors, but with one to a few years of time lag. Further investigations on the proposed impacts of GCRs on cloud activity and atmospheric circulation may shed light on the variability or the phase changes of the decadal-scale components in such unresolved oceanic variations.

Data availability statement

Publicly available datasets were analyzed in this study. This data can be found here: The OLR data are available at https://www.ncei.noaa.gov/products/climate-data-records/outgoing-longwave-radiation-daily. ISCCP-HGM series is available at https://www.ncei.noaa.gov/products/international-satellite-cloud-climatology. The Oulu and Climax neutron data are available at http://cr0.izmiran.ru/clmx/main.htm and http://cr0.izmiran.ru/oulu/main.htm, respectively. The NOAA OI SST V2 data are provided by NOAA/OAR/ESRL PSL on their website: https://psl.noaa.gov/data/gridded/data.noaa.oisst.v2.html. Japanese 55-year Reanalysis data are available at https://rda.ucar.edu/datasets/ds628.1/. The ESRL/NOAA Niño 4 index is available at https://psl.noaa.gov/data/correlation/nina4.data. The NCEI Pacific Decadal Oscillation index is available at https://www.ncei.noaa.gov/access/monitoring/pdo/. CMAP Precipitation data are provided by NOAA/OAR/ESRL PSL on their website: https://psl.noaa.gov/data/gridded/data.cmap.html. The NOAA Climate Data Record of TSI are available at https://www.ncei.noaa.gov/access/metadata/landing-page/bin/iso?id=gov.noaa.ncdc:C00828. The data of NOAA adjusted solar radio flux at 10.7 cm is available at https://lasp.colorado.edu/lisird/data/noaa_radio_flux/. The Penticton radio flux data are available at https://lasp.colorado.edu/lisird/data/penticton_radio_flux/.

Author contributions

HM designed the study with input from KK and HM performed data analyses and wrote the manuscript with input from all of the other authors. All authors contributed to the article and approved the submitted version.

Funding

This work was supported by JSPS KAKENHI grand number 15H05816 and the research scholarship provided to Musashino Art University by Mr. Haruo Suzuki.

Acknowledgments

We thank S. Masuda, H. Yamada, Y. Yamashiki, K. Munakata, for discussions. HM thanks Okinawa Institute of Science and Technology for hosting her sabbatical visit.

Conflict of interest

The authors declare that the research was conducted in the absence of any commercial or financial relationships that could be construed as a potential conflict of interest.

Publisher's note

Supplementary material

The Supplementary Material for this article can be found online at: https://www.frontiersin.org/articles/10.3389/feart.2023.1157753/full#supplementary-material

References

Almeida, J., Schobesberger, S., Kürten, A., Ortega, I. K., Kupiainen-Määttä, O., Praplan, A. P., et al. (2013). Molecular understanding of sulphuric acid–amine particle nucleation in the atmosphere. *Nature* 502, 359–363. doi:10.1038/nature12663

Ashok, K., Behera, S. K., Rao, S. A., Weng, H., and Yamagata, T. (2007). El Niño modoki and its possible teleconnection. *J. Geophys. Res.* 12, C11007. doi:10.1029/2006jc003798

Bloemendaal, N., Haigh, I. D., de Moel, H., Muis, S., Haarsma, R. J., and Aerts, J. C. J. H. (2020). Generation of a global synthetic tropical cyclone hazard dataset using STORM. *Sci. Data* 7, 40. doi:10.1038/s41597-020-0381-2

Bond, G. C., Kromer, B., Beer, J., Muscheler, R., Evans, M. N., Showers, W., et al. (2001). Persistent solar influence on North Atlantic climate during the holocene. *Science* 294, 2130–2136. doi:10.1126/science.1065680

Carslaw, K. S., Harrison, R. G., and Kirkby, J. (2002). Cosmic rays, clouds, and climate. *Science* 298, 1732–1737. doi:10.1126/science.1076964

Coddington, O., Lean, J. L., Lindholm, D., Pilewskie, P., and Snow, M. NOAA CDR Program (2015). NOAA climate data record (CDR) of total solar irradiance (TSI), NRLTSI version 2, N.O.A.A. *Natl. Centers Environ. Inf.* doi:10.7289/V55B00C1

De Mendonça, R. R. S., Raulin, J.-P., Echer, E., Makhmutov, V. S., and Fernandez, G. (2013). Analysis of atmospheric pressure and temperature effects on cosmic ray measurements. *J. Geophys. Res. Space Phys.* 118, 1403–1409. doi:10.1029/2012JA018026

Dickinson, R. E. (1975). Solar variability and the lower atmosphere. *Bull. Am. Meteorological Soc.* 56, 1240–1248. doi:10.1175/1520-0477(1975)056<1240:svatla>2.0.co;2

Dima, M., and Voiculescu, M. (2016). Global patterns of solar influence on high cloud cover. *Clim. Dyn.* 47, 667–678. doi:10.1007/s00382-015-2862-0

Domingo, V., Ermolli, I., Fox, P., Fröhlich, C., Haberreiter, M., Krivova, N., et al. (2009). Solar surface magnetism and irradiance on time scales from days to the 11-year cycle. *Space Sci. Rev.* 145, 337–380. doi:10.1007/s11214-009-9562-1

Dunne, E. M., Gordon, H., Kürten, A., Almeida, J., Duplissy, J., Williamson, C., et al. (2016). Global atmospheric particle formation from CERN CLOUD measurements. *Science* 354, 1119–1124. doi:10.1126/science.aaf2649

Ebita, A., Kobayashi, S., Ota, Y., Moriya, M., Kumabe, R., Onogi, K., et al. (2011). The Japanese 55-year Reanalysis "JRA-55": An interim report. *Sola* 7, 149–152. doi:10.2151/sola.2011-038

Ermakov, V. I., Bazilevskaya, G. A., Pokrevsky, P. E., and Stozhkov, Y. I. (1997). Ion balance equation in the atmosphere. *J. Geophys. Res. Atmos.* 102, 23413–23419. doi:10.1029/97jd01388

Evan, A. T., Heidinger, A. K., and Vimont, D. J. (2007). Arguments against a physical long-term trend in global ISCCP cloud amounts. *Geophys Res. Lett.* 34, L04701. doi:10.1029/2006gl028083

Forbush, S. E. (1938). On cosmic-ray effects associated with magnetic storms. *J. Geophys. Res.* 43, 203–218. doi:10.1029/TE043i003p00203

Gautam, R., Hsu, N. C., and Lau, K.-M. (2010). Premonsoon aerosol characterization and radiative effects over the Indo-Gangetic Plains: Implications for regional climate warming. *J. Geophys. Res.* 115, D17208. doi:10.1029/2010JD013819

Gleisner, H., and Thejll, P. (2003). Patterns of tropospheric response to solar variability. *Geophys. Res. Lett.* 30, 1711. doi:10.1029/2003GL017129

Grabowski, W. W., and Morrison, H. (2020). Do ultrafine cloud condensation nuclei invigorate deep convection? *J. Atmos. Sci.* 77, 2567–2583. doi:10.1175/jas-d-20-0012.1

Gray, L. J., Beer, J., Geller, M., Haigh, J. D., Lockwood, M., Matthes, K., et al. (2010). Solar influences on climate. *Rev. Geophys.* 48, RG4001. doi:10.1029/2009RG000282

Gray, L. J., Woollings, T. J., Andrews, M., and Knight, J. (2016). Eleven-year solar cycle signal in the NAO and Atlantic/European blocking. *Q. J. R. Meteorological Soc.* 142, 1890–1903. doi:10.1002/qj.2782

Huffman, G. J., Adler, R. F., Arkin, P., Chang, A., Ferraro, R., Gruber, A., et al. (1997). The global precipitation Climatology Project (GPCP) combined precipitation dataset. *Bull. Amer Meteor Soc.* 78, 5–20. doi:10.1175/1520-0477(1997)078<0005:tgpcpg>2.0.co;2

Jokipii, J. R., and Thomas, B. (1981). Effects of drift on the transport of cosmic rays. IV. Modulation by a wavy interplanetary current sheet. *Astrophysical J.* 243, 1115–1122. doi:10.1086/158675

Kazil, J., Lovejoy, E. R., Barth, M. C., and O'Brien, K. (2006). Aerosol nucleation over oceans and the role of galactic cosmic rays. *Atmos. Chem. Phys.* 6, 4905–4924. doi:10.5194/acp-6-4905-2006

Kirkby, J. (2007). Cosmic rays and climate. *Surv. Geophys.* 28, 333–375. doi:10.1007/s10712-008-9030-6

Kirkby, J., Curtius, J., Almeida, J., Dunne, E., Duplissy, J., Ehrhart, S., et al. (2011). Role of sulphuric acid, ammonia and galactic cosmic rays in atmospheric aerosol nucleation. *Nature* 476, 429–433. doi:10.1038/nature10343

Kobayashi, S., Ota, Y., Harada, Y., Ebita, A., Moriya, M., Onoda, H., et al. (2015). The JRA-55 Reanalysis: General specifications and basic characteristics. *J. Meteorological Sciety Jpn.* 93, 5–48. doi:10.2151/jmsj.2015-001

Kodera, K., and Kuroda, Y. (2002). Dynamical response to the solar cycle. *J. Geophys. Res.* 107, 4749. doi:10.1029/2002jd002224

Kodera, K. (2002). Solar cycle modulation of the North atlantic oscillation: Implication in the spatial structure of the NAO. *Geophys. Res. Lett.* 29, 59-1–59-4. doi:10.1029/2001GL014557

Koffi, B., Schulz, M., Bréon, F. M., Dentener, F., Steensen, B. M., Griesfeller, J., et al. (2016). Evaluation of the aerosol vertical distribution in global aerosol models through comparison against CALIOP measurements: AeroCom phase II results. *J. Geophys. Res. Atmos.* 121, 7254–7283. doi:10.1002/2015jd024639

Koldobskiy, S. A., Kähkönen, R., Hofer, B., Krivova, N. A., Kovaltsov, G. A., and Usoskin, I. G. (2022). Time lag between cosmic-ray and solar variability: Sunspot numbers and open solar magnetic flux. *Sol. Phys.* 297, 38. doi:10.1007/s11207-022-01970-1

Koren, I., Remer, L. A., Altaratz, O., Martins, J. V., and Davidi, A. (2010). Aerosol-induced changes of convective cloud anvils produce strong climate warming. *Atoms. Chem. Phys.* 10, 5001–5010. doi:10.5194/acp-10-5001-2010

Kuroda, Y., Kodera, K., Yoshida, K., Yukimoto, S., and Gray, L. (2022). Influence of the solar cycle on the North Atlantic oscillation. *J. Geophys. Res. Atmos.* 127, e2021. doi:10.1029/2021jd035519

Land, P. E., Shutler, J. D., Bell, T. G., and Yang, M. (2014). Exploiting satellite Earth observation to quantify current global oceanic DMS flux and its future climate sensitivity. *J. Geophys. Res. Oceans* 119, 7725–7740. doi:10.1002/2014JC010104

Lee, H. T. NOAA CDR Program (2001). *NOAA climate data record (CDR) of daily outgoing Longwave radiation (OLR), version 1.2*. NOAA National Climatic Data Center. (Date of access: 15/01/2022). doi:10.7289/V5SJ1HH2

Mantua, M. K., Hare, S. R., Zhang, Y., Wallace, J. M., and Francis, R. C. (1997). A Pacific interdecadal climate oscillation with impacts on salmon production. *Bull. Am. Meteorological Soc.* 78, 1069–1079. doi:10.1175/1520-0477(1997)078<1069:apicow>2.0.co;2

Mantua, N. J. (1999). "The pacific decadal oscillation and climate forecasting for north America," in *Climate risk solutions*. Editor M. Golnaraghi (Seattle: University of Washington), 10–13.

Marsh, N., and Svensmark, H. (2003). Galactic cosmic ray and el Niño–southern oscillation trends in international satellite cloud Climatology Project D2 low-cloud properties. *J. Geophys. Res. Atmos.* 108, 2001JD001264. doi:10.1029/2001JD001264

Matthes, K., Kuroda, Y., Kodera, K., and Langematz, U. (2006). Transfer of the solar signal from the stratosphere to the troposphere: Northern winter. *J. Geophys. Res.* 111, D06108. doi:10.1029/2005jd006283

Meehl, G. A., Arblaster, J. M., Branstator, G., and van Loon, H. (2008). A coupled air–sea response mechanism to solar forcing in the Pacific region. *J. Clim.* 21, 2883–2897. doi:10.1175/2007jcli1776.1

Misios, S., Gray, L. J., Knudsen, M. F., Karoff, C., Schmidt, H., and Haigh, J. D. (2019). Slowdown of the walker circulation at solar cycle maximum. *Proc. Natl. Acad. Sci. U. S. A.* 116, 7186–7191. doi:10.1073/pnas.1815060116

Miyahara, H., Yokoyama, Y., and Masuda, K. (2008). Possible link between multi-decadal climate cycles and periodic reversals of solar magnetic field polarity. *Earth Planet. Sci. Lett.* 272, 290–295. doi:10.1016/j.epsl.2008.04.050

Myssowsky, L., and Tuwim, L. (1926). Unregelmassige intensitätsschwankungen der Hohenstrahlung in geringer seehohe. *Zeitschrift für Physik A – Hadrons Nucl.* 39, 146–150. doi:10.1007/bf01321981

Neff, U., Burns, S. J., Mangini, A., Mudelsee, M., Fleitmann, D., and Matter, A. (2001). Strong coherence between solar variability and the monsoon in Oman between 9 and 6 kyr ago. *Nature* 411, 290–293. doi:10.1038/35077048

Ney, E. R. (1959). Cosmic radiation and the weather. *Nature* 183, 451–452. doi:10.1038/183451a0

Obrochta, S. P., Miyahara, H., Yokoyama, Y., and Crowley, T. J. (2012). A re-examination of evidence for the North Atlantic "1500-year cycle" at Site 609. *Quat. Sci. Rev.* 55, 23–33. doi:10.1016/j.quascirev.2012.08.008

Reynolds, R. W., Rayner, N. A., Smith, T. M., Stokes, D. C., and Wang, W. (2002). An improved *in situ* and satellite SST analysis for climate. *J. Clim.* 15, 1609–1625. doi:10.1175/1520-0442(2002)015<1609:aiisas>2.0.co;2

Rosenfeld, D., Lohmann, U., Raga, G. B., O'Dowd, C. D., Kulmala, M., Fuzzi, S., et al. (2008). Flood or drought: How do aerosols affect precipitation? *Science* 321, 1309–1313. doi:10.1126/science.1160606

Rossow, W. B., Walker, A., Golea, V., Knapp, K. R., and Young, A. (2016). NOAA's climate data record Program (2016). International satellite cloud Climatology Project climate data record. *H-Series HGM NOAA Natl. Centers Environ. Inf.* doi:10.7289/V5QZ281S

Scott, C. J., Harrison, R. G., Owens, M. J., Lockwood, M., and Barnard, L. (2014). Evidence for solar wind modulation of lightning. *Environ. Res. Lett.* 9, 055004. doi:10.1088/1748-9326/9/5/055004

Svensmark, H., Enghoff, M. B., and Pedersen, J. O. P. (2013). Response of cloud condensation nuclei (>50 nm) to changes in ion-nucleation. *Phys. Lett. A* 377, 2343–2347. doi:10.1016/j.physleta.2013.07.004

Svensmark, H., and Friis-Christensen, E. (1997). Variation of cosmic ray flux and global cloud coverage—a missing link in solar-climate relationships. *J. Atmos. Solar-Terrestrial Phys.* 59, 1225–1232. doi:10.1016/S1364-6826(97)00001-1

Tinsley, B. A., and Deen, G. W. (1991). Apparent tropospheric response to MeV-GeV particle flux variations: A connection via electrofreezing of supercooled water in high-level clouds? *J. Geophys. Res.* 96, 22283–22296. doi:10.1029/91JD02473

Tinsley, B. A. (2000). Influence of solar wind on the global electric circuit, and inferred effects on cloud microphysics, temperature, and dynamics in the troposphere. *Space Sci. Rev.* 94, 231–258. doi:10.1023/a:1026775408875

Tinsley, B. A. (2022). Uncertainties in evaluating global electric circuit interactions with atmospheric clouds and aerosols, and consequences for radiation and dynamics. *J. Geophys. Res. Atmos.* 127, e2021JD035954. doi:10.1029/2021jd035954

Trenberth, K. E., and Stepaniak, D. P. (2001). Indices of el Niño evolution. *J. Clim.* 14, 1697–1701. doi:10.1175/1520-0442(2001)014<1697:lioeno>2.0.co;2

Twohy, C. H., Clement, C. F., Gandrud, B. W., Weinheimer, A. J., Campos, T. L., Baumgardner, D., et al. (2002). Deep convection as a source of new particles in the midlatitude upper troposphere. *J. Geophys. Res. Atmos.* 107, AAC 6-1–AAC 6-10. AAC 6–AAC 1. doi:10.1029/2001JD000323

Usoskin, I. G., Gladysheva, O. G., and Kovaltsov, G. A. (2004). Cosmic ray-induced ionization in the atmosphere: Spatial and temporal changes. *J. Atmos. Solar-Terrestrial Phys.* 66, 1791–1796. doi:10.1016/j.jastp.2004.07.037

Usoskin, I. G., Mursula, K., Kananen, H., and Kovaltsov, G. A. (2001). Dependence of cosmic rays on solar activity for odd and even solar cycles. *Adv. Space Res.* 27, 571–576. doi:10.1016/s0273-1177(01)00084-9

van Loon, H., Meehl, G. A., and Arblaster, J. M. (2004). A decadal solar effect in the tropics in July–August. *J. Atmos. Solar-Terrestrial Phys.* 66, 1767–1778. doi:10.1016/j.jastp.2004.06.003

Vandenbussche, S., Callewaert, S., Schepanski, K., and De Mazière, M. (2020). North African mineral dust sources: New insights from a combined analysis based on 3D dust aerosol distributions, surface winds and ancillary soil parameters. *Atmos. Chem. Phys.* 20, 15127–15146. doi:10.5194/acp-20-15127-2020

Voiculescu, M., Usoskin, I., and Condurache-Bota, S. (2013). Clouds blown by the solar wind. *Environ. Res. Lett.* 8, 045032. doi:10.1088/1748-9326/8/4/045032

Voiculescu, M., Usoskin, I. G., and Mursula, K. (2006). Different response of clouds to solar input. *Geophys. Res. Lett.* 33, L21802. doi:10.1029/2006gl027820

Wang, Y., Cheng, H., Edwards, R. L., He, Y., Kong, X., An, Z., et al. (2005). The holocene asian monsoon: Links to solar changes and North Atlantic climate. *Science* 308, 854–857. doi:10.1126/science.1106296

White, W. B. (2006). Response of tropical global ocean temperature to the Sun's quasi-decadal UV radiative forcing of the stratosphere. *J. Geophys. Res.* 111, C09020. doi:10.1029/2004jc002552

Williamson, C. J., Kupc, A., Axisa, D., Bilsback, K. R., Bui, T. P., et al. (2019). A large source of cloud condensation nuclei from new particle formation in the tropics. *Nature* 574, 399–403. doi:10.1038/s41586-019-1638-9

Yamaguchi, Y. T., Yokoyama, Y., Miyahara, H., Sho, K., and Nakatsuka, T. (2010). Synchronized Northern Hemisphere climate change and solar magnetic cycles during the Maunder Minimum. *Proc. Natl. Acad. Sci. U. S. A.* 107, 20697–20702. doi:10.1073/pnas.1000113107

Yang, G.-Y., and Slingo, J. (2001). The diurnal cycle in the tropics. *Mon. Weather Rev.* 129, 784–801. doi:10.1175/1520-0493(2001)129<0784:tdcitt>2.0.co;2

Yu, F. (2002). Altitude variations of cosmic ray induced production of aerosols: Implications for global cloudiness and climate. *J. Geophys. Res.* 107, 1118. doi:10.1029/2001ja000248

Yu, F., and Turco, R. P. (2001). From molecular clusters to nanoparticles: Role of ambient ionization in tropospheric aerosol formation. *J. Geophys. Res. Atmos.* 106, 4797–4814. doi:10.1029/2000jd900539

Yu, F., Wang, Z., Luo, G., and Turco, R. (2008). Ion-mediated nucleation as an important global source of tropospheric aerosols. *Atmos. Chem. Phys.* 8, 2537–2554. doi:10.5194/acp-8-2537-2008

Zhou, L., Tinsley, B. A., and Plemmons, A. (2009). Scavenging in weakly electrified saturated and subsaturated clouds, treating aerosol particles and droplets as conducting spheres. *J. Geophys. Res.* 114, D18201. doi:10.1029/2008JD011527

frontiers | Frontiers in Earth Science

TYPE Mini Review
PUBLISHED 23 August 2023
DOI 10.3389/feart.2023.1164636

OPEN ACCESS

EDITED BY
Yan Liu,
Xi'an University of Architecture and Technology, China

REVIEWED BY
Maxim Ogurtsov,
Ioffe Institute (RAS), Russia

*CORRESPONDENCE
Jingsong Wang,
wangjs@cma.gov.cn

RECEIVED 13 February 2023
ACCEPTED 28 July 2023
PUBLISHED 23 August 2023

CITATION
Wang J, Zhao L, Xiao Z, Zhang P, Ren Z, Zong W, Qi J, Huang C, Xu Y and Lu Y (2023), Energy transmission processes in the effectuation chain of solar forcing to the terrestrial atmosphere—a review. *Front. Earth Sci.* 11:1164636. doi: 10.3389/feart.2023.1164636

Energy transmission processes in the effectuation chain of solar forcing to the terrestrial atmosphere—a review

Jingsong Wang[1,2]*, Liang Zhao[3], Ziniu Xiao[3], Peng Zhang[2,4], Zhipeng Ren[5,6,7], Weiguo Zong[1,2], Jin Qi[2,4], Cong Huang[1,2], Ying Xu[8] and Yixiong Lu[9]

[1]Key Laboratory of Space Weather, National Satellite Meteorological Center, China Meteorological Administration, Beijing, China, [2]Innovation Center for FengYun Meteorological Satellite (FYSIC), National Satellite Meteorological Center, China Meteorological Administration, Beijing, China, [3]State Key Laboratory of Numerical Modeling for Atmosphere Sciences and Geophysical Fluid Dynamics (LASG), Institute of Atmospheric Physics, Chinese Academy of Sciences, Beijing, China, [4]Key Laboratory of Radiometric Calibration and Validation for Environmental Satellites, National Satellite Meteorological Center, China Meteorological Administration, Beijing, China, [5]Key Laboratory of Earth and Planetary Physics, Institute of Geology and Geophysics, Chinese Academy of Sciences, Beijing, China, [6]Beijing National Observatory of Space Environment, Institute of Geology and Geophysics, Chinese Academy of Sciences, Beijing, China, [7]College of Earth and Planetary Sciences, University of the Chinese Academy of Sciences, Beijing, China, [8]National Climate Center, China Meteorological Administration, Beijing, China, [9]CMA Earth System Modeling and Prediction Centre, China Meteorological Administration, Beijing, China

The Sun has an obvious quasi-11-year cycle and numerous short-term eruptive activities. There are four processes of energy transmission in the effectuation chain of solar forcing to the climate system: solar energy input into the atmosphere, atmospheric absorption of the input energy, transformation of the absorbed energy into dynamic and thermodynamic responses in the atmosphere, and coupling among all the layers affected by solar forcings. However, the four processes have not been discussed in their entirety. This present paper reviews studies over the last decade on how solar radiation varies during the solar cycle and solar eruptions, and, correspondingly, how the terrestrial atmosphere absorbs the input solar energy.

KEYWORDS

solar activity, climate, energy transmission, solar radiation, high-and low-level atmosphere coupling

Introduction

The Sun is a typical middle-aged dwarf star on the main sequence (Tayler, 1997). It emits an electromagnetic spectrum approximating to radiation from a black body at a temperature of 5770K and provides the principal source of energy driving the Earth's atmospheric circulation (Kopp, 2018; Ding, 2019). The Sun has an obvious quasi-11-year cycle and numerous short-term eruptive activities. Whether and how these solar activities affect the Earth's climate has been studied and debated for hundreds of years. The most recent and realistic problem is whether there is a connection between the stagnation period of global warming in the Northern Hemisphere since the beginning of the 21st century and a decrease in solar activity (Lockwood et al., 2010a; Sirocko et al., 2012), recalling the possible recurrence of scenarios like the Maunder minimum. Although there has been much research on this, it has lacked significance and consistency. Over the past 10 years, due

to improvements in solar/terrestrial observation technology and the reconstruction and improvement in quality of long series data, our understanding of the impact of the Sun on climate has made some important progress.

Four processes of energy transmission in the effectuation chain of solar forcing to the climate system are relevant to this discussion: solar energy input into the atmosphere, atmospheric absorption of this input energy, transformation of the absorbed energy into dynamic and thermodynamic responses in the atmosphere, and coupling of all the layers affected by solar forcing. This present paper reviews how solar radiation varies during the solar cycle and eruptions, and, correspondingly, how the terrestrial atmosphere absorbs the input solar energy.

Solar irradiance variations during the solar cycle

The continued observation of total solar irradiance (TSI) from space is recorded by different mission instruments, starting in 1978 (Figure 1). The absolute value of TSI has been newly defined at a low value of approximately 1,361 W/m^2, which was first observed by TIM aboard the SORCE mission (Kopp and Lean, 2011) and again by PICARD/PREMOS, NORSAT-1/CLARA, and TSIS-1/TIM. A new laboratory calibration technique with the TSI radiometer facility (TRF) can support end-to-end calibration for irradiance, which explained the difference between VIRGO, ACRIM3, and TIM and corrected the dataset to the same reference level (Kopp et al., 2012). The newest TSI product from FY-3E/SIM-II also shows a value of 1,361.82W/m^2 (Zhang, et al., 2022). The TSI climate composite data have been built up with different combined methods showing the same 11-year solar cycle patterns, leading to a TSI variation of approximately 0.1% (Dewitte and Nevens, 2016; Dudok de Wit et al., 2017; Montillet et al., 2022). The long-term TSI trend is still under discussion and is partially limited by the accuracy of historical TSI observations. The precision of instrument on-orbit degradation monitoring has become another key point in solving this problem, especially when the instrument has more than a 10-year lifetime.

The accurate measurement of solar spectral irradiance (SSI) is much more difficult than TSI, especially for absolute calibration and degradation monitoring. The SSI data from different missions usually differ in spectral range and spectral resolution, and also in some gaps in time series. The SORCE mission has given a long time series of approximately 17 years of continued solar spectral irradiance data, which has improved our understanding of the long-term trend of specific wavelength (Woods, et al., 2021). In addition to observations from the upper atmosphere, predictions by theoretical and semi-empirical modeling also give a reference dataset for climate and solar physics application. A time-series comparison between observation and models at a selected wavelength showed that the long-term trend differs much more when it is above 300 nm. Seven spectra which presented the solar minimum state showed differences greater than the instrument pronounced accuracy (Thuillier, et al., 2022). For further improvements, high-accuracy detectors and more robust observation data are needed.

A new solar reference spectrum, TSIS-1 hybrid solar reference spectrum (HSRS), at 0.025 nm resolution from 200 nm to 2,730 nm (Coddington, et al., 2021) was recommended by the committee on Earth observation satellite (CEOS) as the new solar irradiance reference spectrum in March 2022. However, the most violent changes in solar radiation occur at much lower wavelengths and are believed to be major influences on terrestrial climate. The

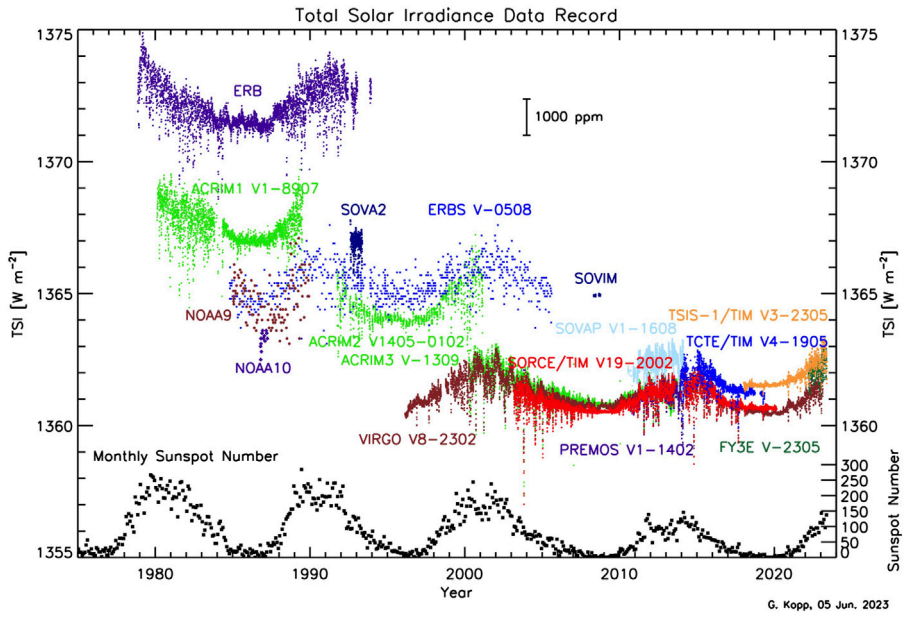

FIGURE 1
Time series of the total solar irradiance dataset and sunspot number (from Greg Kopp's TSSI Page: https://spot.colorado.edu/~koppg/TSI/index.html).

ultra-violet (UV) proportion varies from 6% to 8% over the solar cycle and leads to more ozone and warming during solar maxima in the upper stratosphere (Haigh, 1994; Crooks and Gray, 2005). The magnitudes of UV irradiance variability are wavelength-dependent; emissions differ according to their origins in different layers of the solar atmosphere. Over a solar cycle, chromospheric emissions vary by factors of 1.5–1.7, the transition region and upper chromospheric emissions vary by factors of 1.8–2.4, and coronal emissions vary by a factor of 8 (Woods et al., 2008). Although empirical models have emerged for investigating chromospheric and coronal emissions (Lean et al., 2011), they are contested in the literature (Huang et al., 2016). Due to the data gap and uncertainties surrounding the spectral irradiance observations, UV irradiance variability is still unclear and needs further study.

Solar irradiation variations related to solar activities

The agreement between the variability of TSI and solar activity originated in the evolution of the solar surface magnetic field. Kilogauss-strength magnetic concentrations in the photosphere cyclically emerge in association with dark sunspots and bright faculae on the solar disk (Solanki et al., 2006). Sunspots and pores are dark due to magnetic suppression of the overturning convection around the magnetic concentrations (Rempel and Schlichenmaier, 2011). Lateral heating around the magnetic concentrations overcomes the magnetic suppression to produce increasing brightness (Vögler et al., 2005), and the side walls between the magnetic concentrations and the surrounding heating have a greater view away from the solar disk center (Steiner, 2005). Thus, TSI shows an increasing trend when the active region rotates to the solar limb. Using sunspot and faculae datasets, the observed TSI variability can be reproduced with high accuracy (Lean et al., 2020).

Meanwhile, the effect of flares on TSI is not negligible: large flares make a major contribution to the visible domain (Kretzschmar et al., 2010). During the extraordinary solar storms between 18 October 2003 and 5 November 2003, TSI dropped by an unprecedented 0.34% during this period due to dark sunspots. When an X17 (4B optical) flare erupted on 28 October, TSI increased by 270 ppm in a synthetic result (Woods et al., 2004). However, a possible climate response to the synoptic change of TSI still lacks evidence.

Eruption is another critical form of solar energy export. Burst energy could be carried by radiation, energetic particles, and plasma. Changes during a solar burst at wavelengths shorter than UV are dramatically larger than at longer wavelengths. The initial release of energy during an eruption accelerates charged particles, which precipitate into the denser plasma. This heating of the plasma in the lower solar atmosphere drives an increase of hard X-ray flux via bremsstrahlung. Thereafter, the heated particles confined within the magnetic loops thermally radiate in soft X-rays (SXRs) and in some portions of UV (Neupert, 1968). During large solar flares, the variability of SXR 0.1–14 nm can reach a factor of 150, the EUV region shorter than 115 nm can increase to a factor of 40, the enhancement of FUV 115–200 nm radiation declines toward the longer wavelength, and the total variation is approximately 10% (Woods, 2006). Solar flare irradiance models have been developed to derive the variability of solar irradiance during flares, but much work is required to reconcile the deviation from the observations (Chamberlin et al., 2008; Reep et al., 2022). Radio burst is another violent manifestation of solar eruption. However, it has no direct interaction with our atmosphere.

The physics of the solar atmosphere dominates TSI and SSI variations, as well as the occurrence of solar eruptions. It is the reason why TSI and SSI have the same quasi-11-year variations as solar activity. Although they are highly correlated, TSI and SSI mainly display a decadal variation, while the solar eruptions display as events on timescales of days or shorter. Thus, there is more attention on the solar cycle variation of TSI or SSI when solar forcing on climate is investigated than on eruptive energy changes.

The absorption of the terrestrial atmosphere to solar irradiation at short wavelengths

The absorption of solar visible and infrared radiation is mainly the focus of climatologists. Comparatively, atmospheric absorption of solar radiation at shorter wavelengths is mainly discussed in the domain of space weather. Supplementary Figure S1 shows the altitude of maximum solar radiation absorption by the Earth's atmosphere for different spectral bands at short wavelengths. These have sometimes been neglected by climate researchers since these absorptions occur in the middle and upper atmosphere. Solar X-ray radiation and extreme UV radiation (wavelengths shorter than 100 nm) are mainly absorbed by the thermosphere; far UV radiation (wavelengths between 100 nm and 200 nm) is absorbed primarily by the thermo- and mesosphere; mid UV radiation (wavelengths between 200 nm and 300 nm) is mostly absorbed by the meso- and stratosphere; near-UV radiation (wavelengths between 300 nm and 400 nm) is primarily absorbed by the strato- and mesosphere; and visible and infrared spectral radiation (wavelengths greater than 400 nm) can reach the troposphere and down to the earth's surface (including the ocean) (see also Schoeberl and Strobel, 1978; Torr et al., 1980a; Torr et al., 1980b; London, 1980; Brasseur and Solomon, 2005).

The absorption mechanism of solar radiation in the earth's atmosphere is highly complex. In addition to direct radiation absorption and heating, atmospheric photoionization and photodecomposition directly convert partial radiation energy into atmospheric chemical energy and the kinetic energy of photoelectrons, therefore modulating the absorption efficiency of solar radiation (Roble et al., 1987). The precipitation of high-energy particles (Ree et al., 1983) and Joule heating (Roble and Emery, 1983) related to solar activity can also change the temperature and density in the polar region of the upper atmosphere. Atmospheric chemical, dynamic, thermodynamic, and radiation cooling processes further redistribute absorbed solar radiation energy among different atmospheric layers, thus affecting the temperature structure of the whole atmospheric region (Roble, 1995). To systematically study the solar radiation absorption efficiency of the different Earth atmospheric layers for different spectral bands, a comprehensive study with numerical simulation at its core is necessary (Roble et al., 1987; Roble, 1995; Ren et al., 2009), and three key scientific issues are often the focus. First, the

absorption of solar radiation by the earth's atmosphere usually depends on the atmosphere's specific chemical composition (Schoeberl and Strobel, 1978; Mertens et al., 1999). Atmospheric chemical composition actually dominates the absorption efficiency of solar radiation, while solar radiation can adjust the atmospheric composition through photochemical processes, affecting the absorption efficiency (Tor and Torr, 1979; Zellner, 1999). Second, atmospheric dynamic processes and heat conduction can directly affect the distribution of atmospheric temperature and can also affect atmospheric chemical processes by transporting the atmosphere's specific chemical compositions, such as oxygen (Garcia and Solomon, 1994), carbon, hydrogen (Qian et al., 2018), and nitrogen compounds. These processes result in the redistribution of absorbed solar radiation energy between different atmospheric regions and even between different atmospheric layers. Third, the solar radiation energy absorbed by different atmospheric layers of the Earth is often dissipated in the form of long-wave radiation cooling (see López-Puertas and Taylor, 2001 and its references). CO_2 (Fomichev et al., 1998), O_3 (Fomichev and Shved, 1985), H_2O, NO (Kockarts, 1980), and O (Kockarts and Peetermans, 1970) play important roles in long-wave radiation cooling. The coupling between solar radiation absorption, atmospheric radiation cooling, and other mechanisms codetermines the temperature structure of the earth's atmosphere (Roble, 1995). Changes in the atmospheric radiation cooling process can adjust the effective absorption of solar radiation energy by affecting the temperature and then changing the atmospheric composition (Roble and Dickinson, 1989).

Another factor which may influence the physical processes in the Earth's atmosphere and change its radiative balance is the flux of cosmic rays. Galactic cosmic rays (GCRs) are influenced by heliospheric magnetic changes, with their intensity peaking during the solar minimum due to quiet solar activity (Fu et al., 2021). SEPs originate in solar eruptions, but their energy is lower than GCR. Large-scale solar wind flow and turbulent interplanetary magnetic fields dominate the transport of cosmic rays and their links to solar activity need more study.

The impact of solar irradiation variation on terrestrial climate

Although the variation range of the total solar radiation is generally considered as one thousandth, the variation ranges of several other influence mechanisms, such as UV radiation and energy particles, are much larger than those of total solar radiation (Gray et al., 2010; Lilensten et al., 2015). Two recent assessment reports from the intergovernmental panel on climate change (IPCC) indicate that, although the total solar radiation mechanism had little impact on modern climate, it could not be ruled out that the Sun might affect the interdecadal change of climate through several indirect radiation amplification mechanisms (IPCC, 2013, 2021). Although there is little consensus on the understanding of the relationship between the Sun and climate on an interdecadal scale (Chiodo, 2019), the observed hiatus in surface warming from 1998 to 2012 may be due to a reduced radiative forcing and a cooling contribution from natural internal variability (medium confidence). The reduced trend in radiative forcing is primarily due to volcanic eruptions and the weakening of solar activity. However, there is low confidence in evaluating the effect of solar forcing on the climate warming hiatus (IPCC, 2013).

In addition, cooling in the tropical upper stratosphere under solar minimum years, which weakens the equator-to-pole temperature gradient, can propagate a solar signal downward to slow tropospheric westerlies, thus causing a negative phase of the arctic oscillation (AO) or NAO and cold winters in Eurasia (Ineson et al., 2011; Kuroda et al., 2022). However, this point needs careful confirmation because, according to reports, there is no significant AO or NAO response to solar irradiance variations on average in the CMIP5 models (Gillett and Fyfe, 2013).

The solar ultraviolet radiation variability recommended by CMIP6 can reach several percent (such as the 200 nm band) in a solar cycle, which is far greater than the TSI variability. Its contribution to the TSI variability has been predicted to increase from 35% of CMIP5 to 50% of CMIP6, and the spectral resolution is high enough. Ozone and atmospheric heating rate changes caused by the solar spectrum are also greatly affected in CMIP6 compared with CMIP5—closer to the latest observations (Matthes et al., 2017). These will help uncover and confirm the response of the middle and lower atmospheres to solar radiation as well as its mechanism. The climate simulation forced by the new SSI input found that the wind field response of the real atmosphere and the resulting climate response are likely to be significantly greater than the model simulation (Ermolli, et al., 2013; Chiodo et al., 2016). In addition, CMIP6 provides a solar-driven energy particle forcing dataset for the first time, which enables it to have a certain ability to simulate high-energy particle forcing (Matthes et al., 2017).

The 11-year cycle is the most stable feature of solar activity variations that can be used to improve interdecadal prediction techniques (Smith et al., 2012; Thieblemont et al., 2015). Previous studies have shown that the 11-year solar cycle change is a source of skills for near-term climate prediction (Dunstone et al., 2016; Kushnir et al., 2019), which has been verified in some regions. The possibility that the stratospheric polar vortex serves as a link between lower atmosphere circulation and solar activity has been noted by Veretenenko and Ogurtsov (2013) and Veretenenko (2022). Dunstone et al. (2016) confirmed that the improvement of the interannual NAO forecasting skills in the North Atlantic region is due to the climate variability of the tropical Pacific and the intensity of the stratospheric polar vortex, which is mainly driven by predictable solar forcing. In the tropical Pacific, verification of the interdecadal modulation of the Sun on Walker circulation has enhanced the confidence of the model in predicting Walker circulation and tropical precipitation (Misios et al., 2019). These results indicate that the prediction method of "Sun+a factor" shows potential to help recent climate prediction, which is consistent with the "drivers of teleconnectivity" framework for interdecadal prediction (Cassou et al., 2018).

One possible way to transform "teleconnectivity" to an understandable causation is to pay more attention to possible climate effects caused by solar eruptions. As discussed previously,

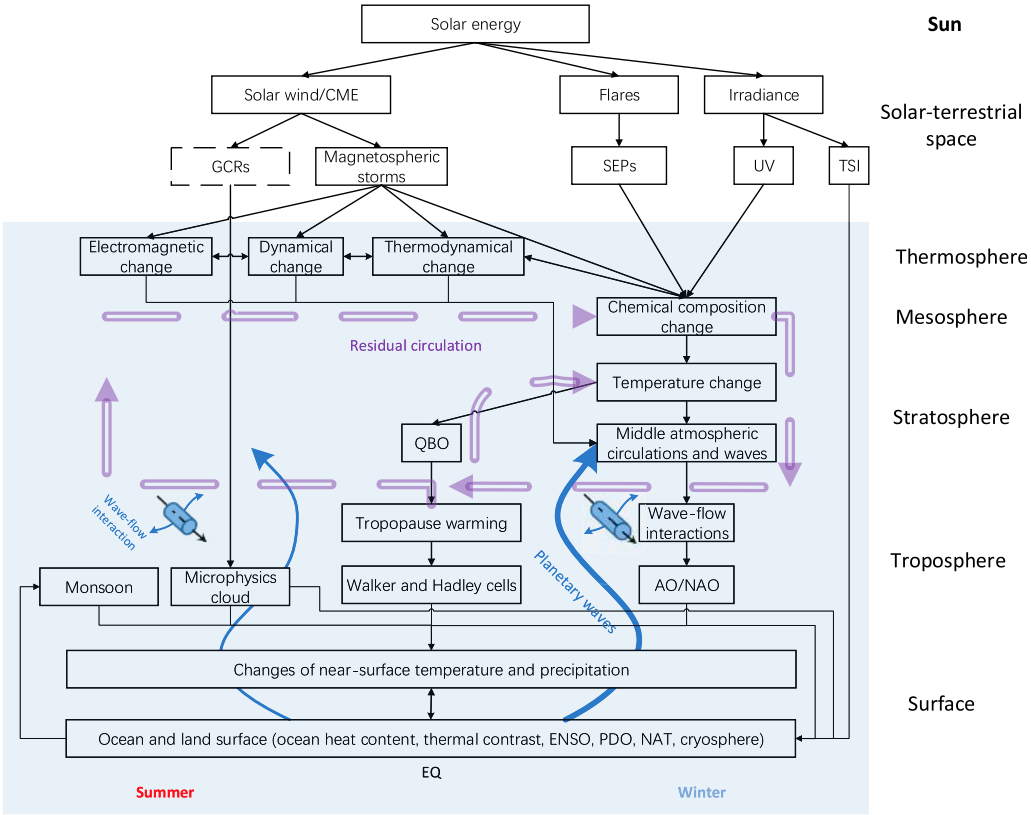

FIGURE 2
Sketch of possible routes of solar forcing to the Earth's climate.

the upper and middle atmosphere could vary dramatically and systematically due to solar bursts. A short-term solar eruption can cause dramatic changes in radiation (almost at all bands), CME, flares, and solar wind, which cause strong responses in the Earth's upper atmosphere (partly bridged by the magnetosphere) (Zhou et al., 2014). The Earth's upper and middle atmospheric responses include direct radiation absorption and heating, composition change, dynamical change, and electromagnetic change. Such changes can further affect variations in the meridional temperature gradient, vertical propagation of planetary wave, ozone cycle, and upper westerly jets, which can couple with the lower atmosphere (Kodera et al., 2016). However, how this coupling occurs is still poorly understood. For instance, Wang and Zhao (2012) found that the solar cycle modulation on the monsoon rain belt could be attributed to the coupling between the circulations in the upper and lower atmospheres. Nevertheless, how this coupling process occurs and by what mechanism it is amplified and transmitted downward is not very clear (Zhao et al., 2014; Zhao et al., 2017). Furthermore, the fact that most evidence for solar burst impacts on the climate system are around the decadal scale, while the events themselves are of time scales around days or even shorter (or of synoptic scale) means that synoptic-scale factors are often equated to or inundated by irradiation variations since they both vary in synchrony with the solar cycle. Decisive progress could be made in two directions: finding evidence of solar bursts impacts on the climate system at the synoptic scale, and clarifying the coupling processes between/among the dynamical, thermodynamical, chemical, and other processes in the upper, middle, and lower atmospheres.

Conclusion

Both solar irradiation and solar activity have a quasi-11-year period, and these two variations have essential physics connections. Forcing caused by TSI/SSI on the Earth's climate mainly presents on a decadal scale. Energy surges from the Sun during solar bursts can only slightly change TSI, but these can export energy to the Earth via radiation at bands of EUV and shorter, energetic particles, plasmas, and electro-magnetic fields which dramatically impact the Earth's upper atmosphere and induce storms there. Whether such storms can couple with the middle and even the lower atmosphere effectively enough to modify the climate system still needs more investigation. However, we can still try to draft a frame diagram for possible routes of solar forcing to climate (Figure 2). As an increment to previous descriptions, this diagram emphasizes more energy transmission through the "space weather" routines from the Sun to the lower terrestrial atmosphere.

At present, solar activity is experiencing a significant decrease after eight strong solar cycles, and some studies suggest that solar activity may even decline to the level of the Maunder minimum by the middle of the 21st century (Lockwood, 2010b; Wang et al., 2010); this may add new uncertainties to future climate change projections.

Will this extremely low solar activity period continue to develop after the 24th solar cycle, and will the 11a period change lead to a new cold period (like the Maunder minimum)? These challenging scientific questions are one of the core issues of climate change, and an in-depth study of them will help assess and project future climate risks.

Author contributions

JW: conceptualization, methodology, and writing—reviewing; LZ: drawing, and writing—original draft preparation and editing; ZX, PZ, ZR, WZ, JQ, CH, YX, and YL: Writing—original draft preparation. All authors contributed to the article and approved the submitted version.

Funding

This work is supported by the National Natural Science Foundation of China (42274217 and 42075040).

Conflict of interest

The authors declare that the research was conducted in the absence of any commercial or financial relationships that could be construed as a potential conflict of interest.

Publisher's note

All claims expressed in this article are solely those of the authors and do not necessarily represent those of their affiliated organizations, or those of the publisher, the editors, and the reviewers. Any product that may be evaluated in this article, or claim that may be made by its manufacturer, is not guaranteed or endorsed by the publisher.

Supplementary material

The Supplementary Material for this article can be found online at: https://www.frontiersin.org/articles/10.3389/feart.2023.1164636/full#supplementary-material

References

Brasseur, G., and Solomon, S. (2005). *Aeronomy of the middle atmosphere: Chemistry and physics of the stratosphere and mesosphere, atmospheric and oceanographic sciences library*. Berlin, Germany: Springer, 32. doi:10.1007/1-4020-3824-0

Cassou, C., Kushnir, Y., Hawkins, E., Pirani, A., Kucharski, F., Kang, I., et al. (2018). Decadal climate variability and predictability: Challenges and opportunities. *Bull. Am. Meteorol. Soc.* 99, 479–490. doi:10.1175/BAMS-D-16-0286.1

Chamberlin, P. C., Woods, T. N., and Eparview, F. G. (2008). Flare irradiance spectral model (FISM): Flare component algorithms and results. *Space weather.* 6 (5), S05001. doi:10.1029/2007SW000372

Chiodo, G., Garcíaherrera, R., Calvo, N., Vaquero, J. M., Añel, J. A., Barriopedro, D., et al. (2016). The impact of a future solar minimum on climate change projections in the Northern Hemisphere. *Environ. Res. Lett.* 11 (3), 034015. doi:10.1088/1748-9326/11/3/034015

Chiodo, G., Oehrlein, J., Polvani, L. M., Fyfe, J. C., and Smith, A. K. (2019). Insignificant influence of the 11-year solar cycle on the North Atlantic oscillation. *Nat. Geosci.* 12, 94–99. doi:10.1038/s41561-018-0293-3

Coddington, O. M., Richard, E. C., Harber, D., Pilewskie, P., Woods, T. N., Chance, K., et al. (2021). The TSIS-1 hybrid solar reference spectrum. *Geophys. Res. Lett.* 48, e2020GL091709. doi:10.1029/2020GL091709

Crooks, S., and Gray, L. (2005). Characterization of the 11-year solar signal using a multiple regression analysis of the ERA-40 dataset. *J. Clim.* 18, 996–1015. doi:10.1175/JCLI-3308.1

Dewitte, S., and Nevens, S. (2016). The total solar irradiance climate data record. *Astrophysical J.* 830 (1), 25. doi:10.3847/0004-637x/830/1/25

Ding, Y. H. (2019). Effect of solar activity on Earth's climate and weather. *Meteor. Mon.* 45 (3), 297–304. doi:10.7519/j.issn.1000-0526.2019.03.001

Dudok de Wit, T., Kopp, G., Fröhlich, C., and Schöll, M. (2017). Methodology to create a new total solar irradiance record: Making a composite out of multiple data records. *Geophys. Res. Lett.* 44 (3), 1196–1203. doi:10.1002/2016GL071866

Dunstone, N., Smith, D., Scaife, A., Hermansonet, L., Eade, R., Robinson, N., et al. (2016). Skilful predictions of the winter North Atlantic Oscillation one year ahead. *Nat. Geosci.* 9, 809–814. doi:10.1038/ngeo2824

Ermolli, I., Matthes, K., de Wit, D., Krivova, N. A., Tourpali, K., Weber, M., et al. (2013). Recent variability of the solar spectral irradiance and its impact on climate modelling. *Atmos. Chem. Phys.* 13, 3945–3977. doi:10.5194/acp-13-3945-2013

J. Lilensten (2015). *Earth's climate response to a changing Sun* (Paris: EDP Sciences).

IPCC (2013). "Climate change 2013:the physical science basis," in *Contribution of working group I to the fifth assessment report of the intergovernmental Panel on climate change*. T. F. Stocker, D. Qin, and G.-K. Plattner Editors (Cambridge, United Kingdom: Cambridge University Press), 1535.

Fomichev, V. I., Blanchet, J.-P., and Turner, D. S. (1998). Matrix parameterization of the 15 μm CO 2 band cooling in the middle and upper atmosphere for variable CO2 concentration. *J. Geophys. Res.* 103 (D10), 11505–11528. doi:10.1029/98JD00799

Fomichev, V. I., and Shved, G. M. (1985). Parameterization of the radiative flux divergence in the 9.6-μm O3 band. *J. Atmos. Terr. Phys.* 47 (11), 1037–1049. doi:10.1016/0021-9169(85)90021-2

Fu, S., Zhang, X., Zhao, L., and Li, Y. (2021). Variations of the galactic cosmic rays in the recent solar cycles. *Astrophysical J. Suppl. Ser.* 254 (2), 37. doi:10.3847/1538-4365/abf936

Garcia, R. R., and Solomon, S. (1994). A new numerical model of the middle atmosphere: 2, ozone and related species. *J. Geophys Res.* 99 (12), 12937. doi:10.1029/94JD00725

Gillett, N. A., and Fyfe, J. C. (2013). Annular mode changes in the CMIP5 simulations: Annular mode changes in CMIP5. *Geophys. Res. Lett.* 40, 1189–1193. doi:10.1002/grl.50249

Gray, L. J., Beer, J., Geller, M., Haigh, J. D., Lockwood, M., Matthes, K., et al. (2010). Solar influences on climate. *Rev. Geophys.* 48, RG4001. doi:10.1029/2009rg000282

Haigh, J. D. (1994). The role of stratospheric ozone in modulating the solar radiative forcing of climate. *Nature* 370, 544–546. doi:10.1038/370544a0

Huang, J. P., Hao, Y. Q., Zhang, D. H., and Xiao, Z. (2016). Changes of solar extreme ultraviolet spectrum in solar cycle 24. *J. Geophys. Res. Space Phys.* 121, 6844–6854. doi:10.1002/2015JA022231

Ineson, S., Scaife, A. A., Knight, J. R., Manners, J. C., Dunstone, N. J., Gray, L. J., et al. (2011). Solar forcing of winter climate variability in the Northern Hemisphere. *Nat. Geosic* 4 (11), 753–757. doi:10.1038/ngeo1282

Kockarts, G. (1980). Nitric oxide cooling in the terrestrial thermosphere. *Geophys. Res. Lett.* 7 (2), 137–140. doi:10.1029/GL007i002p00137

Kockarts, G., and Peetermans, W. (1970). Atomic oxygen infrared emission in the earth's upper atmosphere. *Space Sci.* 18 (2), 271–285. doi:10.1016/0032-0633(70)90163-7

Kodera, K., Thiéblemont, R., Yukimoto, S., and Matthes, K. (2016). How can we understand the global distribution of the solar cycle signal on the earth's surface? *Atmos. Chem. Phys.* 16 (20), 12925–12944. doi:10.5194/acp-16-12925-2016

Kopp, G. (2018). "Earth's incoming energy: The total solar irradiance," in *Reference module in earth systems and environmental Sciences. Comprehensive remote sensing* (Amsterdam, Netherlands: Elsevier), 32–66. doi:10.1016/B978-0-12-409548-9.10366-5

Kopp, G., Fehlmann, A., Finsterle, W., Harber, D., Heuerman, K., and Willson, R. (2012). Total solar irradiance data record accuracy and consistency improvements. *Metrologia* 49 (2), S29–S33. doi:10.1088/0026-1394/49/2/S29

Kopp, G., and Lean, J. L. (2011). A new, lower value of total solar irradiance: Evidence and climate significance. *Geophys. Res. Lett.* 38, L01706. doi:10.1029/2010GL045777

Kuroda, Y., Kodera, K., Yoshida, K., Yukimoto, S., and Gray, L. (2022). Influence of the solar cycle on the North Atlantic oscillation. *J. Geophys. Res. Atmos.* 127, e2021JD035519. doi:10.1029/2021JD035519

Kushnir, Y., Scaife, A. A., Arritt, R., Balsamo, G., Boer, G., Doblas-Reyes, F., et al. (2019). Towards operational predictions of the near-term climate. *Nat. Clim. Change* 9, 94–101. doi:10.1038/s41558-018-0359-7

Lean, J. L., Coddington, O., Marchenko, S. V., Machol, J., DeL and, M. T., and Kopp, G. (2020). Solar irradiance variability: Modeling the measurements. *Earth Space Sci.* 7, 00645. doi:10.1029/2019EA000645

Lean, J. L., Woods, T. N., Eparvier, F. G., Meier, R. R., Strickland, D. J., Correira, J. T., et al. (2011). Solar extreme ultraviolet irradiance: Present, past, and future. *J. Geophys. Res. Space Phys.* 116, 1102. doi:10.1029/2010JA015901

Lockwood, M., Harrison, R. G., Woollings, T., and Solanki, S. K. (2010a). Are cold winters in Europe associated with low solar activity? *Environ. Res. Lett.* 5 (2), 024001. doi:10.1088/1748-9326/5/2/024001

Lockwood, M. (2010b). Solar change and climate: An update in the light of the current exceptional solar minimum, *Proc. R. Soc. A* 466 (2114), 303–329. doi:10.1098/rspa.2009.0519

London, J. L. (1980). "Radiative energy sources and sinks in the stratosphere and mesosphere," in *Atmospheric ozone and its variation and human influences. Proc NATO advanced study* (Springfield, Va: NTIS).

López-Puertas, M., and Taylor, F. W. (2001). *Non-LTE radiative transfer in the Atmosphere volume 3*. Singapore: World Scientific. Available at: https://www.worldscientific.com/doi/abs/10.1142/4650.

Matthes, K., Kruschke, T., Shangguan, M., Barnard, L., Beer, J., Charbonneau, P., et al. (2017). Solar forcing for CMIP6 (v3.2). *Geosci. Model. Dev.* 10 (6), 2247–2302. doi:10.5194/gmd-10-2247-2017

Matthieu, K., Thierry, D. W., Werner, S., Sabri, M., Jean-François, H., and Dewitte, S. (2010). The effect of flares on total solar irradiance, *Nat. Phys.* 10, 690–692. doi:10.1038/nphys1741

Mertens, C. J., Mlynczak, M. G., Garcia, R. R., and Portmann, R. W. (1999). A detailed evaluation of the stratospheric heat budget, 1. Radiation transfer. *J. Geophys Res.* 104, 6021–6038. doi:10.1029/1998JD200100

Misios, S., Gray, L. J., Knudsen, M. F., Haigh, J. D., and Schmidt, H. (2019). Slowdown of the Walker circulation at solar cycle maximum. *Proc. Natl. Acad. Sci.* 116 (15), 7186–7191. doi:10.1073/pnas.1815060116

Montillet, J.-P., Finsterle, W., Kermarrec, G., Sikonja, R., Haberreiter, M., Schmutz, W., et al. (2022). Data fusion of total solar irradiance composite time series using 41 years of satellite measurements. *J. Geophys. Res. Atmos.* 127, e2021JD036146. doi:10.1029/2021JD036146

Neupert, W. N. (1968). Comparison of solar X-ray line emission with microwave emission during flares. *Astrophys. J.* 153, L59. doi:10.1086/180220

Qian, L., Burns, A. G., Solomon, S. S., Smith, A. K., McInerney, J. M., Hunt, L. A., et al. (2018). Temporal variability of atomic hydrogen from the mesopause to the upper thermosphere. *J. Geophys. Res. Space Phys.* 123, 1006–1017. doi:10.1002/2017JA024998

Reep, J., David, E., and Warren, H. (2022). Solar flare irradiance: observations and physical modeling. *The Astrophysi. J.* 97, 103. doi:10.3847/1538-4357/ac4784

Rees, M. H., Emery, B. A., Robie, R. G., and Stamnes, K. (1983). Neutral and ion gas heating by auroral electron precipitation. *J. Geophys. Res.* 88, 6289. doi:10.1029/JA088iA08p06289

Rempel, M., and Schlichenmaier, R. (2011). Sunspot modeling: From simplified models to radiative MHD simulations. *Living Rev. Sol. Phys.* 8, 3. doi:10.12942/lrsp-2011-3

Ren, Z., Wan, W., and Liu, L. (2009). GCITEM-IGGCAS: A new global coupled ionosphere-thermosphere-electrodynamics model. *J. Atmos. Sol. Terr. Phys.* 71 (17&18), 2064–2076. doi:10.1016/j.jastp.2009.09.015

Roble, R. G., and Dickinson, R. E. (1989). How will changes in carbon dioxide and methane modify the mean structure of the mesosphere and thermosphere? *Geophys. Res. Lett.* 16, 1441–1444. doi:10.1029/GL016i012p01441

Roble, R. G., and Emery, B. A. (1983). On the global mean temperature of the thermosphere. *Planet Space Sci.* 31, 597–614. doi:10.1016/0032-0633(83)90002-8

Roble, R. G. (1995). "Energetics of the mesosphere and thermosphere," in *The upper mesosphere and lower thermosphere: A review of experiment and theory, geophys. Monogr. Ser*. Editors R. M. Johnson and T. L. Killeen (Washington, D.C: Am. Geophys. Union), 1. doi:10.1029/GM087

Roble, R. G., Ridley, E. C., and Dickinson, R. E. (1987). On the global mean structure of the thermosphere. *J. Geophys. Res.* 92 (A8), 8745–8758. doi:10.1029/JA092iA08p08745

Schoeberl, M. R., and Strobel, D. F. (1978). The zonally averaged circulation of the middle atmosphere. *J. Atmos. Sci.* 35, 577–591. doi:10.1175/1520-0469(1978)035<0577:tzacot>2.0.co;2

Sirocko, F., Brunck, H., and Pfahl, S. (2012). Solar influence on winter severity in central europe: Rhine freezing. *Geophys. Res. Lett.* 39 (16), 16704. doi:10.1029/2012GL052412

Smith, D. M., Scaife, A. A., and Kirtman, B. P. (2012). What is the current state of scientific knowledge with regard to seasonal and decadal forecasting. *Environ. Res. Lett.* 7, 015602. doi:10.1088/1748-9326/7/1/015602

Solanki, S. K., Inhester, B., and Schüssler, M. (2006). The solar magnetic field. *Rep. Prog. Phys.* 69, 563–668. doi:10.1088/0034-4885/69/3/r02

Steiner, O. (2005). Radiative properties of magnetic elements. II. Center to limb variation of the appearance of photospheric faculae. *Astron. Astrophys.* 430, 691–700. doi:10.1051/0004-6361:20041286

Tayler, R. J. (1997). *The Sun as a star*. Cambridge: Cambridge University Press.

Thieblemont, R., Matthes, K., Omrani, N. E., Kodera, K., and Hansen, F. (2015). Solar forcing synchronizes decadal North Atlantic climate variability. *Nat. Commun.* 6, 8268. doi:10.1038/ncomms9268

Thuillier, G., Zhu, P., Snow, M., Zhang, P., and Ye, X. (2022). Characteristics of solar-irradiance spectra from measurements, modeling, and theoretical approach. *Light Sci. Appl.* 11, 79. doi:10.1038/s41377-022-00750-7

Torr, D. G., and Torr, M. R. (1979). Chemistry of the thermosphere and ionosphere. *J. Atmos. Terr. Phys.* 41, 797–839. doi:10.1016/0021-9169(79)90126-0

Torr, M. R., Torr, D. G., and Hinteregger, H. E. (1980a). Solar flux variability in the Schumann-Runge continuum as a function of solar cycle 21. *J. Geophys. Res.* 85, 6063. doi:10.1029/JA085iA11p06063

Torr, M. R., Torr, D. G., and Richards, P. G. (1980b). The solar ultraviolet heating efficiency of the midlatitude thermosphere. *Geophys. Res. Lett.* 7, 373–376. doi:10.1029/GL007i005p00373

Veretenenko, S., and Ogurtsov, M. (2013). The stratospheric polar vortex as a cause for the temporal variability of solar activity and galactic cosmic ray effects on the lower atmosphere circulation. *J. Phys. Conf. Ser.* 409, 012238. doi:10.1088/1742-6596/409/1/012238

Veretenenko, S. (2022). Stratospheric polar vortex as an important link between the lower atmosphere circulation and solar activity. *Atmosphere* 13(7):1132. doi:10.3390/atmos13071132

Vögler, A., Shelyag, S., Schüssler, M., Cattaneo, F., Emonet, T., and Linde, T. (2005). Simulations of magneto-convection in the solar photosphere. Equations, methods, and results of the MURaM code. *Astron. Astrophys.* 429, 335–351. doi:10.1051/0004-6361:20041507

Wang, J. S., and Zhao, L. (2012). Statistical tests for a correlation between decadal variation in June precipitation in China and sunspot number. *J. Geophys. Res.* 117 (D23), D23117. doi:10.1029/2012JD018074

Wang, S. W., Wen, X. Y., and Huang, J. B. (2010). Global cooling in the immediate future? *Chin. Sci. Bull.* 55, 3847–3852. doi:10.1007/s11434-010-4177-1

Woods, Thomas N., Kopp, Greg, and Chamberlin, Phillip C. (2006). Contributions of the solar ultraviolet irradiance to the total solar irradiance during large flares. *J. Geophys. Res.* 111, A10S14. doi:10.1029/2005JA011507

Woods, T. N., Eparvier, F. G., Fontenla, J., Harder, J., Kopp, G., McClintock, W. E., et al. (2004). Solar irradiance variability during the October 2003 solar storm period. *Geophys. Res. Lett.* 31, L108021–L108024. doi:10.1029/2004GL019571

Woods, T. N., Harder, J. W., Kopp, G., McCabe, D., Rottman, G., Ryan, S., et al. (2021). Overview of the solar radiation and climate experiment (SORCE) seventeen-year mission. *Sol. Phys.* 296 (127), 127. doi:10.1007/s11207-021-01869-3

Woods, T. N. (2008). Recent advances in observations and modeling of the solar ultraviolet and X-ray spectral irradiance. *Adv. Space Res.* 42, 895–902. doi:10.1016/j.asr.2007.09.026

Zellner, R. (1999). "Chemistry of the stratosphere," in *Global aspects of atmospheric chemistry* (Berlin, Germany: Springer Verlag).

IPCC (2021). "Summary for policymakers," in *Climate change 2021: The physical science basis. Contribution of working group I to the sixth assessment report of the intergovernmental Panel on climate change* Editors P. Zhai, A. Pirani, S. L. Connors, C. Péan, S. Berger, N. Caud, et al. (Cambridge, United Kingdom: Cambridge University Press), 3–32. doi:10.1017/9781009157896.001

Zhang, P., Hu, X. Q., Lu, Q. F., Zhu, A. J., Lin, M. Y., Sun, L., et al. (2022). FY-3E: The first operational meteorological satellite mission in an early morning orbit. *Adv. Atmos. Sci.* 39, 1–8. doi:10.1007/s00376-021-1304-7

Zhao, L., Wang, J., Liu, H., and Xiao, Z. (2017). Amplification of the solar signal in the summer monsoon rainband in China by synergistic actions of different dynamical responses. *J. Meteor. Res.* 31 (1), 61–72. doi:10.1007/s13351-016-6046-6

Zhao, L., and Wang, J. (2014). Robust response of the East Asian monsoon rainband to solar variability. *J. Clim.* 27 (8), 3043–3051. doi:10.1175/JCLI-D-13-00482.1

Zhou, L. M., Tinsley, B., and Huang, J. (2014). Effects on winter circulation of short and long term solar wind changes. *Adv. Space Res.* 54, 2478–2490. doi:10.1016/j.asr.2013.09.017

frontiers | Frontiers in Earth Science

TYPE Original Research
PUBLISHED 08 September 2023
DOI 10.3389/feart.2023.1169685

OPEN ACCESS

EDITED BY
Teng Wu,
University at Buffalo, United States

REVIEWED BY
Marni Pazos,
National Autonomous University of Mexico, Mexico
Diana Francis,
Khalifa University, United Arab Emirates

*CORRESPONDENCE
Ziniu Xiao,
xiaozn@lasg.iap.ac.cn

RECEIVED 19 February 2023
ACCEPTED 23 August 2023
PUBLISHED 08 September 2023

CITATION
Li D, Xiao Z, Xu J and Zhao L (2023), Asymmetric modulation of solar activity on tropical cyclone frequency over the western North Pacific and the possible mechanism.
Front. Earth Sci. 11:1169685.
doi: 10.3389/feart.2023.1169685

Asymmetric modulation of solar activity on tropical cyclone frequency over the western North Pacific and the possible mechanism

Delin Li[1,2,3,4], Ziniu Xiao[2]*, Jianjun Xu[1,3,4] and Liang Zhao[2]

[1]South China Sea Institute of Marine Meteorology, Guangdong Ocean University, Zhanjiang, China, [2]State Key Laboratory of Numerical Modeling for Atmospheric Sciences and Geophysical Fluid Dynamics, Institute of Atmospheric Physics, Chinese Academy of Sciences, Beijing, China, [3]Shenzhen Research Institute of Guangdong Ocean University, Shenzhen, China, [4]Joint Laboratory for Marine Meteorology, China Meteorological Administration-Guangdong Ocean University, Zhanjiang, China

The impacts of solar activity on the tropical Pacific climate have been widely reported. However, few studies focus on the effects of solar activity on the tropical cyclone (TC). Based on the observational and reanalysis data for 1979–2020, this study investigated the solar modulation of TC frequency over the western North Pacific in different solar cycle phases. Results suggest that the regressions of TC frequency to solar activity are asymmetric in the high- and low-solar activity years (HS and LS). Specifically, the intensified solar activity could markedly induce more TCs in HS; however, no significant modulation can be found in LS. Further exploration reveals a possible air–sea coupled mechanism for this interesting phenomenon. The relatively cloud-free area in the western North Pacific could receive more incoming solar radiation at the surface in HS than in LS. This increased regional surface net solar radiation in HS could produce a stronger surface upward latent heat flux and, thus, greater evaporation. Along with that, the local upward motion is dramatically enhanced over the TC source. Then, for compensation, the regional sea level pressure is reduced, and the low-level winds become cyclonic over the TC origin. All of these solar-caused regional atmospheric anomalies in HS contribute to more TC generations. The key to this possible mechanism is the increased regional solar forcing at the ocean surface that is amplified by regionally enhanced upward latent heat flux and evaporation.

KEYWORDS

solar activity, tropical cyclone, asymmetric modulation, western North Pacific, air–sea coupled amplification mechanism

1 Introduction

A tropical cyclone (TC) is an intense warm-cored cyclonic vortex that generates over tropical oceans. The rainstorm, strong breeze, storm surge, and other disastrous weather conditions induced by TCs often bring serious economic losses and casualties to the affected areas. TCs generally form on the ocean surface with a high sea surface temperature (SST) exceeding 26.5°C and suitable dynamic conditions such as low-level pressure disturbance and weak tropospheric vertical wind shear (Gray, 1968). The western North Pacific,

including the South China Sea, is the most important source region of TCs. Due to the influence and restriction of large-scale air–sea backgrounds, the TC frequency over the western North Pacific is characterized by seasonal, interannual, and interdecadal variations (Chan, 2005; Li and Zhou, 2018; Zhan et al., 2019). The generation of TCs could be influenced by some large-scale air–sea coupled systems over the tropical Pacific inside the climate system, such as the ENSO, Intertropical Convergence Zone, and western Pacific subtropical high. Meanwhile, previous studies have reported that, as the external forcing of the earth system, solar activity can significantly affect these systems that are closely tied to TC formation. For instance, the peak of the 11-year solar cycle in the tropical Pacific showed a La Nina-like event, and the Intertropical Convergence Zone and local Hadley cell were strengthened (van Loon et al., 2004; 2007; van Loon and Meehl, 2008; Meehl et al., 2008; Bal et al., 2011). While Roy and Haigh (2010) reported that the El Nino-like pattern appeared in the tropical Pacific with increased solar forcing at an interannual timescale, Huo et al. (2021) and Wang et al. (2019) found a lagged El Nino Modoki in response to decadal solar peaks. Duan (2008) pointed out that, in solar cycle peaks, the East Asian summer monsoon intensified, and the western Pacific subtropical high strengthened and shifted westward. Based on these aforementioned factors, it suggests that solar activity might modulate TC generation by affecting the regional air–sea conditions over the tropical Pacific.

It is believed that the contribution of solar activity to weather and climate change cannot be ignored (Haigh, 1996; Gray et al., 2010; Xiao et al., 2017). Based on satellite observations, the solar radiation output in a quasi-11-year solar cycle varies by approximately 1% (Kopp and Lean, 2011). Previous studies have revealed the marked responses of tropical Pacific air–sea systems to the initially small solar forcing; thus, there must exist the amplification mechanisms of solar forcing on the tropical Pacific, namely, the "top–down" solar ultraviolet radiation mechanism and the "bottom–up" total solar irradiance mechanism (Meehl et al., 2009; Gray et al., 2010). In the "top–down" mechanism, stratospheric ozone can dramatically respond to the solar ultraviolet variability, changing the thermal and dynamic conditions in the stratosphere, and then, the solar signal can be amplified and transferred downward to the troposphere by the wave mean flow interactions (Kodera and Kuroda, 2002; Haigh et al., 2005; Haigh and Blackburn, 2006; Matthes et al., 2006; Kodera et al., 2016; Li et al., 2019). In the "bottom–up" mechanism, due to the greater solar energy input at the ocean surface in the cloud-free areas, the small solar irradiance variability can be manifested by the dynamic air–sea coupling over the tropical-to-subtropical Pacific (van Loon et al., 2004; van Loon et al., 2007; Meehl et al., 2008). The combined effects of the "top–down" and "bottom–up" mechanisms can amplify the initially small solar variability and cause significant changes in the tropical Pacific air–sea systems.

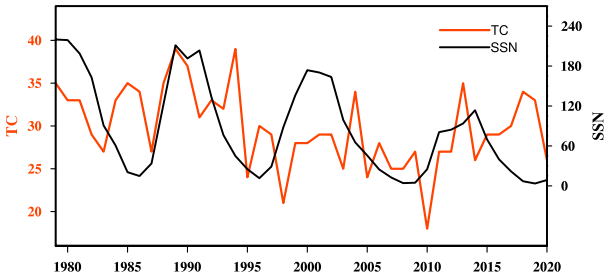

FIGURE 1
Time series of the annual mean SSN (black) and yearly TC frequency (red) for the period 1979–2020.

The generation of TCs over the western North Pacific depends on the thermal and dynamic conditions over the tropical Pacific. The impacts of solar activity on the tropical Pacific climate have been widely investigated in many previous studies. Understanding the modulation of solar activity on a severe air–sea coupled system such as TC is important. However, little attention has been paid to the solar effect on TCs over the western North Pacific. Tian (2005) pointed out that in low (high)-solar activity years, more TCs were generated in the western North Pacific when the quasi-biennial oscillation was in the westerly (easterly) phase. Based on the observations from 1977 to 2016, Kim et al. (2017) found that in the solar maximum period, compared with the solar minimum period, TCs over the western North Pacific tended to form southward and eastward and lasted longer with lower central pressure. The recent work of Li et al. (2023) indicated that in El Niño (La Niña) years during declining (ascending) phases of the solar cycle, strong positive (negative) TC genesis frequency anomalies occurred in the southeastern part of the western North Pacific. We, thus, notice that there are no specialized studies on solar effects on TC generations over the western North Pacific.

Despite previous efforts, there may still be a lack of information revealing the specific influence of solar activity on TCs over the western North Pacific. Therefore, the present study focuses on the solar modulation of the TC frequency over the western North Pacific and the possible mechanism. Section 2 describes the data and method used in this analysis. In Section 3, we examine the asymmetric relationship between solar activity and TC frequency in different solar phases and try to further explain the mechanism. We end with a brief conclusion and discussion in Section 4.

2 Data and methods

2.1 Data

On the one hand, TC activity over the western North Pacific may enter a new period after the abrupt climate change that occurred in the mid-late 1970s. On the other hand, considering the higher credibility and accuracy of satellite observations since 1979, we selected the period 1979–2020 for analysis. The best-track data of TCs over the western North Pacific, including the South China Sea, for the period 1979–2020 were obtained from the China Meteorological Administration (CMA) Tropical Cyclone Data Center (http://tcdata.typhoon.org.cn) (Ying et al., 2014; Lu et al., 2021). Similar to most previous studies, we used the sunspot number (SSN) as solar activity proxy data. Monthly SSNs could be downloaded from the World Data Center Sunspot Index and Long-term Solar Observations (SILSO) of the Royal Observatory of Belgium (http://sidc.oma.be/silso/). The gridded monthly data of sea level pressure (SLP), wind, Ω, total cloud cover, surface upward

TABLE 1 HS and LS for the period 1979–2020. The number in bracket represents the total of HS (LS).

HS (18)	1979, 1980, 1981, 1982, 1983, 1988, 1989, 1990, 1991, 1992, 1998, 1999, 2000, 2001, 2002, 2003, 2013, 2014
LS (24)	1984, 1985, 1986, 1987, 1993, 1994, 1995, 1996, 1997, 2004, 2005, 2006, 2007, 2008, 2009, 2010, 2011, 2012, 2015, 2016, 2017, 2018, 2019, 2020

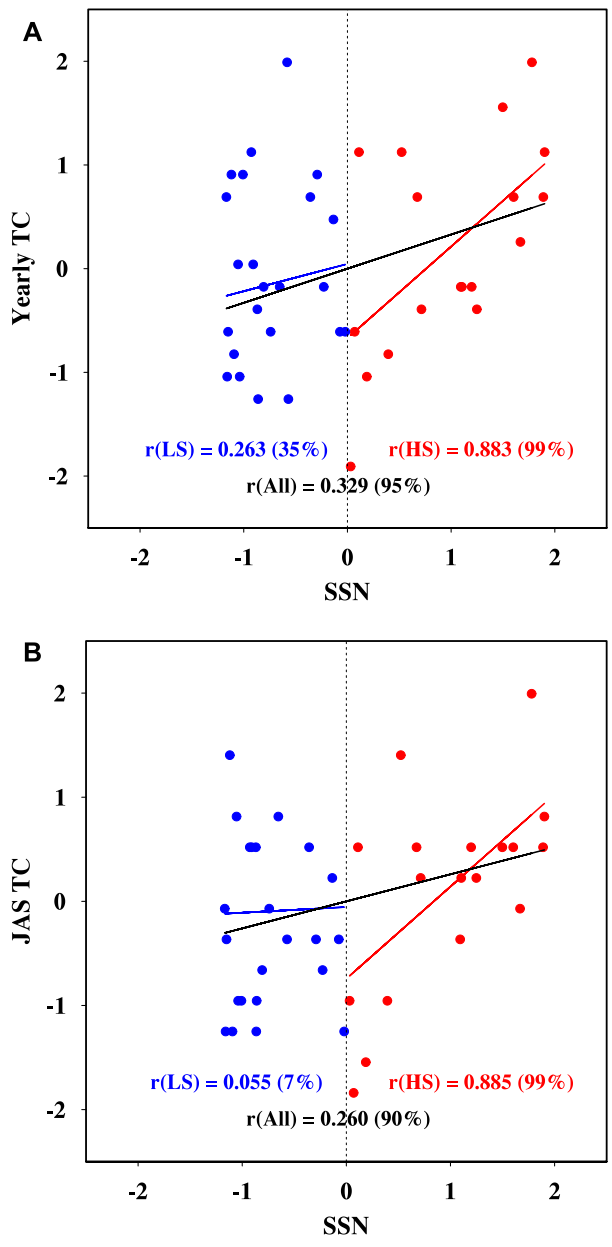

FIGURE 2
(A) Scatterplot of standardized yearly SSN and yearly TC frequency in HS (red) and LS (blue). The three lines indicate the regression lines of TC frequency on the SSN in the whole period (black), HS (red), and LS (blue), respectively. Here, "r" represents the slope of the regression line. **(B)** Same as **(A)** but for the JAS TC frequency.

latent heat flux, and precipitable water of the entire atmosphere for 1979–2020 with 2.5° × 2.5° horizontal resolution were taken from the National Centers for Environmental Prediction/Department of Energy (NCEP/DOE) Reanalysis II dataset (Kanamitsu et al., 2002). The monthly gridded SST analysis was based on the Met Office Hadley Centre Sea Ice and Sea Surface Temperature (HadISST) dataset (Rayner et al., 2003) with 1° × 1° horizontal resolution for the same period. The Nino 3.4 index (mean SSTs over 5°S–5°N latitudes and 170°–120°W longitudes) calculated by the HadISST dataset was used to represent ENSO variability.

TABLE 2 Average TC frequency over the western North Pacific and the average SSN in HS and LS.

	HS	LS
TC frequency	30.72	29.12
SSN	155.09	33.94

2.2 Methods

The high-solar activity years and low-solar activity years are defined depending on whether the SSN is higher or lower than the mean value. The correlation and regression analyses were adopted to examine the asymmetric relationship between solar activity and TC frequency over the western North Pacific. The linear trends of these gridded meteorological data were removed before analysis. When investigating the solar asymmetric impacts on the air–sea backgrounds for TC generation, the ENSO signal was removed from the meteorological variables to avoid its interference in the tropics. First, the linear regression of the original variable field against the standardized Nino 3.4 index is performed to get the ENSO-related field. Second, the ENSO-related field is subtracted from the original variable field to get the meteorological variable without the ENSO signal.

3 Results

3.1 Asymmetric relationship between solar activity and tropical cyclone frequency over the western North Pacific

The time series of yearly SSN and yearly TC frequency for the period 1979–2020 are shown in Figure 1. The SSN varies with a quasi-11-year cycle, spanning from the solar cycle 21 to 24. The TC frequency is characteristic of interannual and interdecadal variations. There are some similarities between the variations of SSN and TC frequency in Figure 1, especially on the interdecadal timescale. Notably, the correlation coefficient between yearly SSN and TC frequency is 0.329 at a 95% confidence level, suggesting that stronger solar activity might induce more TCs over the western North Pacific.

Divided by the mean value of the SSN, the whole 42 years from 1979 to 2020 are stratified into HS (18 years) and LS (24 years). HS and LS are listed in Table 1. Table 2 shows the average TC number over the

10.3389/feart.2023.1169685

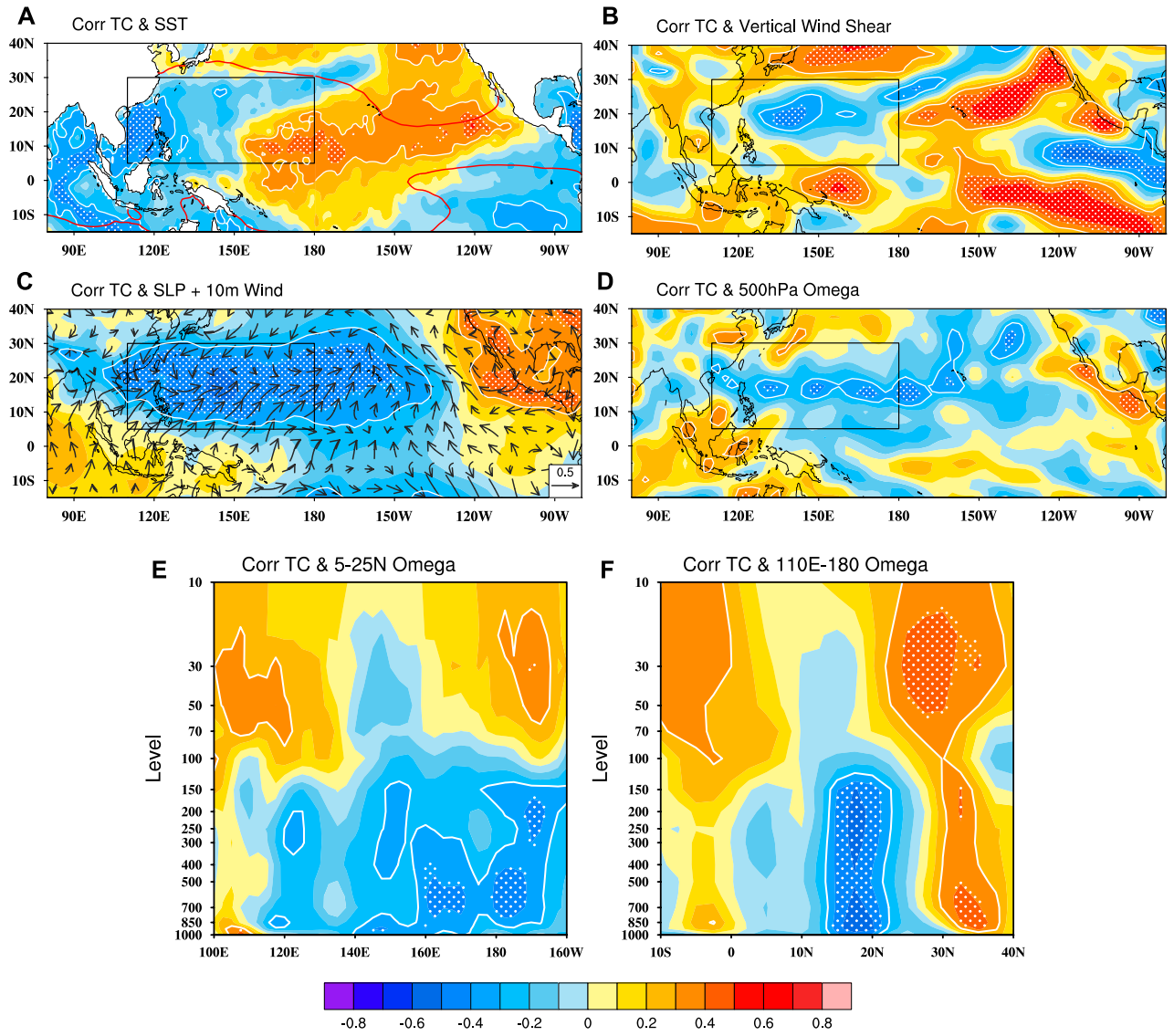

FIGURE 3
Correlations between JAS TC frequency and JAS **(A)** SST, **(B)** vertical wind shear, **(C)** SLP and 10 m wind (arrows), **(D)** 500 hPa Ω, **(E)** 5°–25°N meridional-mean Ω, and **(F)** 110°E–180° zonal-mean Ω for 1979–2020. Correlation coefficients above the 99% (95%) confidence level are indicated by white dots (white contours). The black box represents the TC origin (5°–30°N, 110°E–180°). Red contours in **(A)** denote the climatological SST exceeding 26.5°C.

western North Pacific and the average SSN in HS and LS. Although the average TC frequency in HS (30.72) is higher than that in LS (29.12), their difference (1.6) is not very significant. To compare the relationships between solar activity and TC frequency in different solar cycle phases, the standardized yearly TC frequency is linearly regressed on the standardized yearly SSN in HS and LS, respectively (Figure 2A). As shown in Figure 2A, the regression coefficient between yearly SSN and TC frequency in HS is 0.883 with a 99% confidence level, while the regression coefficient in LS is merely 0.263 without reaching a high level of significance. Considering over 60% of TCs generated in July–August–September (JAS), we employ the same analyses in JAS (Figure 2B). Similar asymmetric results can be noticed in Figure 2B. The regression coefficient of JAS TC frequency against SSN in the whole period is 0.260 at a 90% confidence level, and the regression in HS is 0.885 with a 99% confidence level, whereas the regression in LS is insignificant (r = 0.055). This investigation reveals that the responses of TC frequency over the western North Pacific to solar activity are asymmetric. Specifically, the increased solar activity could markedly induce more TCs over the western North Pacific in HS, while no significant modulation can be found in LS.

3.2 Asymmetric modulation of solar activity on tropical cyclone generation over the western North Pacific

Since the asymmetric responses of JAS TC frequency to solar activity are also very striking, we focus on JAS in this section for convenience. In order to compare solar asymmetric modulation on TC generation in HS and LS, we first need to clarify the basic air–sea

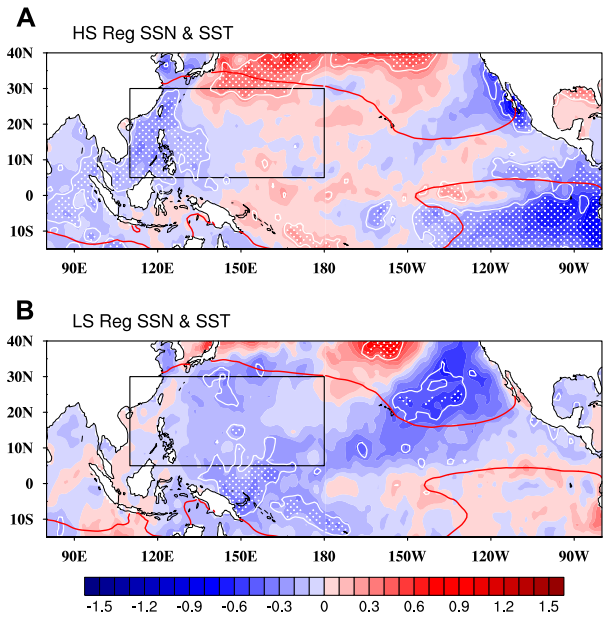

FIGURE 4
Regressions for JAS SST (unit: ˚C) (with the ENSO signal removed) against standardized SSN in **(A)** HS and **(B)** LS. Regression coefficients above the 95% (90%) confidence level are highlighted by white dots (white contours). The black box indicates the source region of TC. Red contours in **(A)** and **(B),** respectively, denote the climatological SST exceeding 26.5˚C in HS and LS.

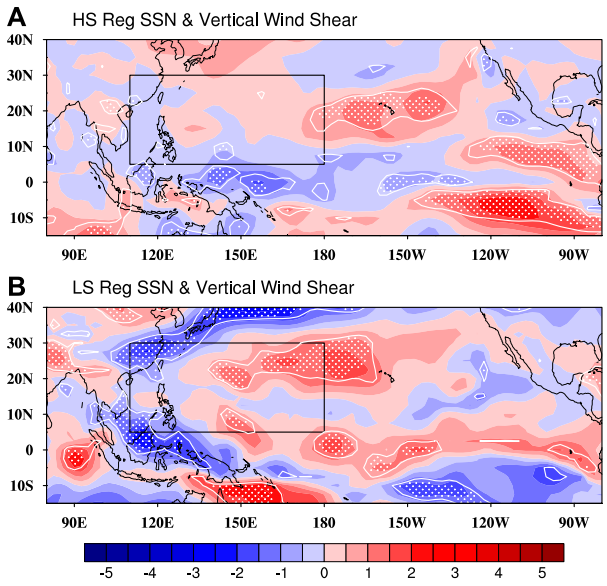

FIGURE 5
Same as Figure 4 but for the regressions of vertical wind shear (unit: m/s) against standardized SSN in **(A)** HS and **(B)** LS.

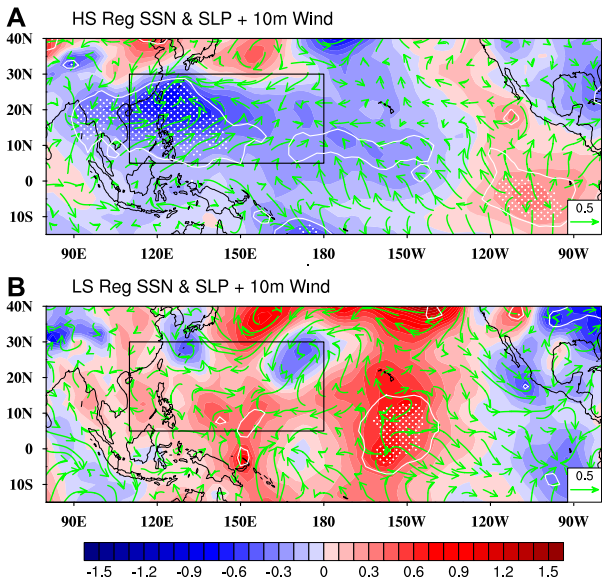

FIGURE 6
Same as Figure 4 but for the regressions of SLP (color shading, unit: hPa) and 10 m wind (green arrows, unit: m/s) against standardized SSN in **(A)** HS and **(B)** LS.

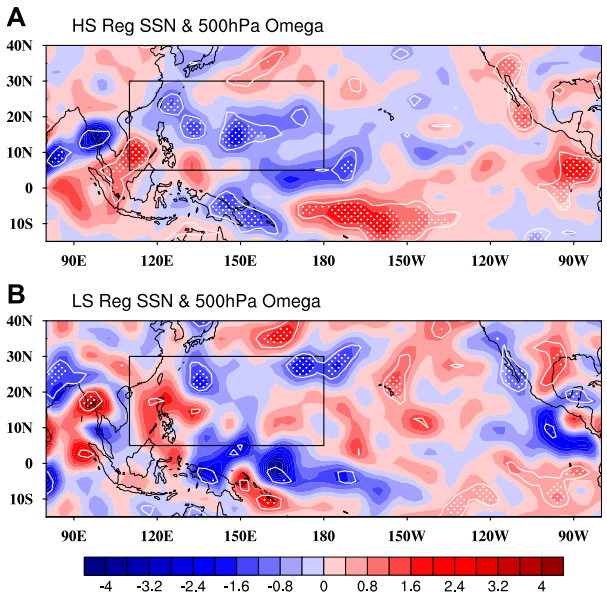

FIGURE 7
Same as Figure 4 but for the regressions of 500 hPa Ω (unit: 10^{-2} Pa/s) against standardized SSN in **(A)** HS and **(B)** LS.

conditions that are closely connected to TC frequency for 1979–2020. The linear trends of these gridded meteorological variables were removed before analysis. Several important large-scale air–sea backgrounds related to JAS TC generation are exhibited in Figure 3.

The SST is an indispensable thermal condition for TC formation, and the correlations of JAS SST with TC frequency are shown in Figure 3A. Within the TC origin (black box in Figure 3A), the significant positive correlations appear in the central tropical Pacific and the significant negative correlations appear in the South China Sea. Meanwhile, the SSTs in the TC source sector exceed the threshold value of 26.5˚C (red contours in

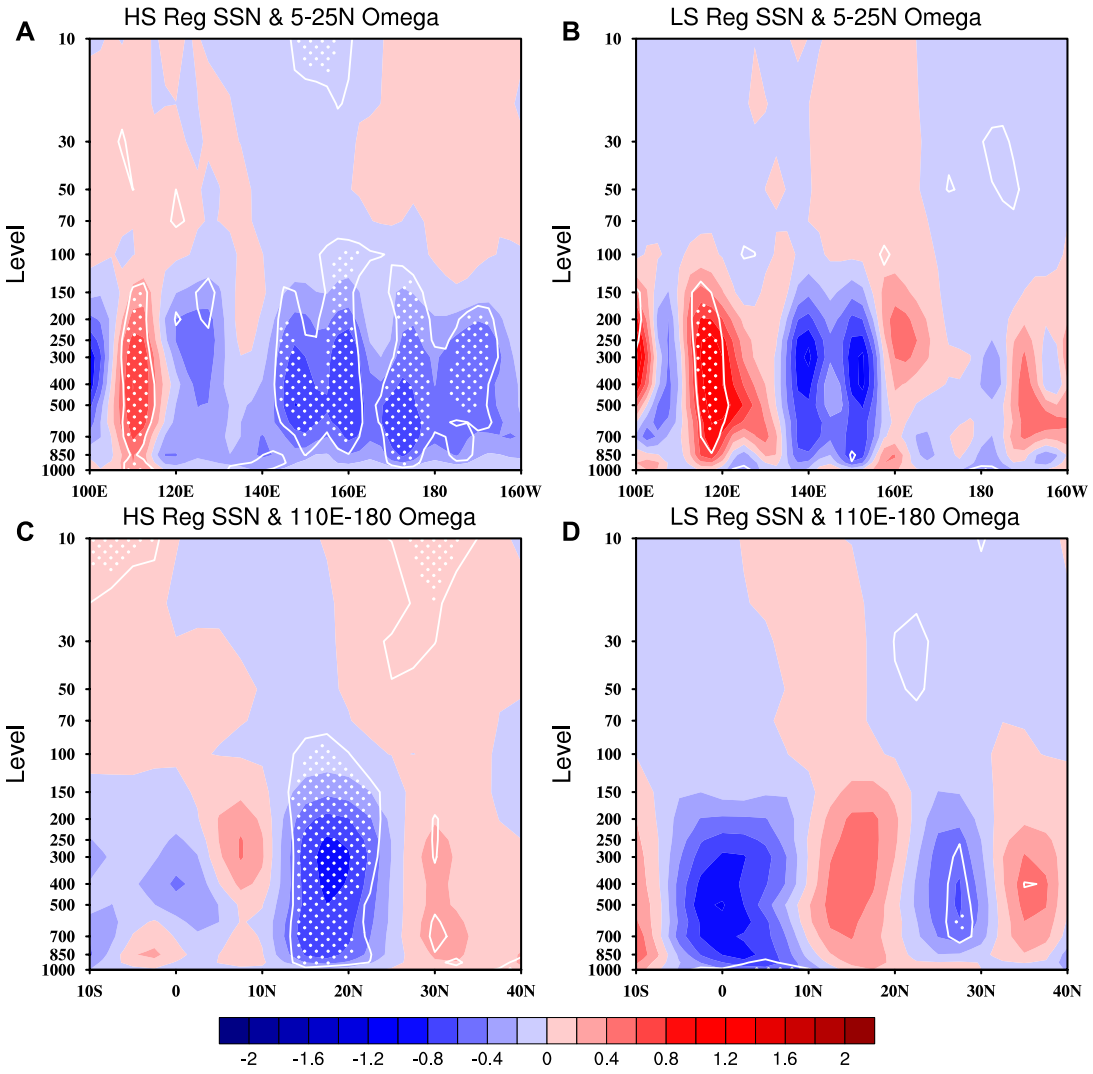

FIGURE 8
Same as Figure 4 but for the regressions of 5°–25°N meridional-mean Ω against standardized SSN in **(A)** HS and **(B)** LS; the regressions of 110°E–180° zonal-mean Ω against standardized SSN in **(C)** HS and **(D)** LS. Unit: 10^{-2} Pa/s.

Figure 3A). It indicates that, as long as the basic SST condition (≥26.5°C) is satisfied, the local SST anomalies might have little impact on TC frequency over the western North Pacific.

The tropospheric vertical wind shear, also known as convection ventilation, is an important influence factor for TC generation. The weak vertical wind shear can facilitate the concentration of potential heat in a limited space and, thus, prompt the formation of a TC warm core. Following the work of Chen and Ding (1979), the vertical wind shear is represented by the absolute value of the weighted average zonal wind of the upper part of the troposphere (600–200 hPa) minus that of the lower part (1000–600 hPa). As displayed in Figure 3B, the remarkable weaker vertical wind shear appears over the main TC source region, suggesting the weaker vertical wind shear contributes to TC formation.

The atmospheric circulation anomalies are crucial to the formation and development of TC. Figure 3C exhibits the correlations of JAS SLP and 10 m wind with TC frequency. The TC-related lower SLP markedly occupies the whole TC origin, and anomalous cyclonic circulation at 10 m lies over the western North Pacific. It is without doubt that the lower SLP and anomalous low-level wind convergence are conducive to the formation of an initial low-pressure disturbance for TC. Furthermore, the correlations between JAS TC frequency and 500 hPa Ω are shown in Figure 3D. The marked negative correlations are present over the main TC origin. Moreover, the cross sections of correlations of JAS 5°–25°N meridional-mean and 110°E–180° zonal-mean Ω with TC frequency are displayed in Figures 3E,F. We can see the pronounced negative Ω appearing over the main TC source region in the whole troposphere. It indicates that the stronger ascending motion could facilitate TC generation.

Therefore, among these air–sea backgrounds, the weaker tropospheric vertical wind shear, the lower SLP, the anomalous low-level wind convergence, and the stronger upward motion can actually contribute to more TC generations over the western North Pacific. In addition, the regional SST anomalies do not affect TC

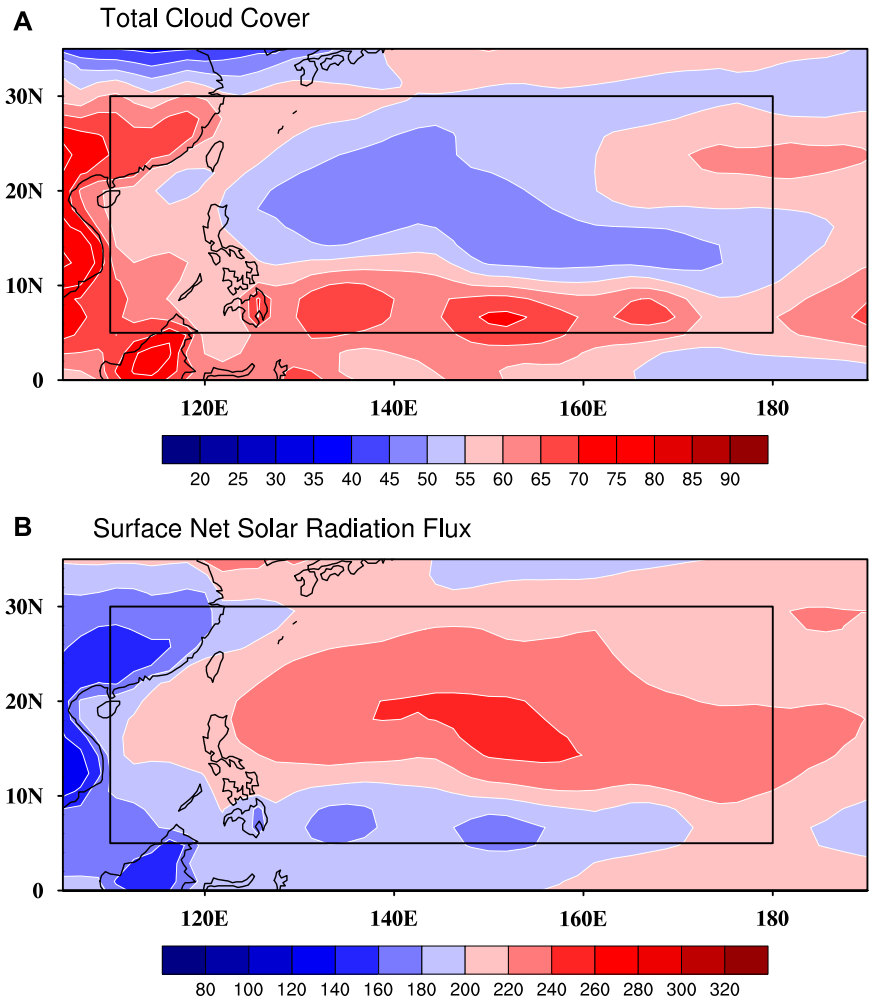

FIGURE 9
Climatological JJASO **(A)** total cloud cover (unit: %) and **(B)** surface net solar radiation flux (unit: W/m^2, downward is positive) for 1979–2020. The black box represents the TC origin (5°–30°N, 110°E–180°).

formation when reaching the threshold value (≥26.5°C) of the thermal condition.

In Section 3.1, we find that solar modulation on TC frequency over the western North Pacific is asymmetric, but the reason for this interesting phenomenon remains to be explained. We will detect the asymmetric influences of solar activity on the air–sea backgrounds of TC generation and further illustrate why the regression of TC frequency to solar activity is much more significant in HS than in LS. Ruzmaikin (1999) pointed out that, as a stochastic driver, the ENSO can make the solar forcing on climate feasible. Hence, before analysis, the ENSO signal was removed from the meteorological variables to avoid its interference in the tropics.

Figure 4 provides the regressions for JAS SST against standardized SSN in HS and LS, respectively. In HS, the significant colder SST responses appear in the west of the TC origin, and the pronounced warmer SST responses lie in the north of the TC origin (Figure 4A). In LS, the whole TC source region is occupied by negative regressions, and few significant areas are present in the TC origin (Figure 4B). Both the climatological SSTs in HS and LS exceed the threshold value (≥26.5°C). The roles of these local SST anomalies in HS and LS in TC formation might be unnecessary. Combined with Figure 3A, it suggests that the solar influence on regional SST cannot explain the solar asymmetric modulation on TC frequency over the western North Pacific.

The responses of JAS tropospheric vertical wind shear to standardized SSN in HS and LS are shown in Figure 5. In LS, the significant enhanced vertical wind shear lies over the central-east part of the TC source, and the markedly weakened vertical wind shear appears over the northwest and southwest of the TC origin (Figure 5B). In HS, few pronounced responses can be observed within the TC source (Figure 5A). It indicates that the solar impacts on tropospheric vertical wind shear cannot be the reason for solar asymmetric modulation on TC frequency over the western North Pacific.

To examine the solar asymmetric impacts on near-surface atmospheric circulation, the regressions for JAS SLP and 10 m wind against standardized SSN in HS and LS are presented in Figure 6. In HS, the remarkable negative SLP anomalies with a maximum reduction of 1 hPa, together with the anomalous cyclonic wind at 10 m, occupy the central-west part of the TC origin

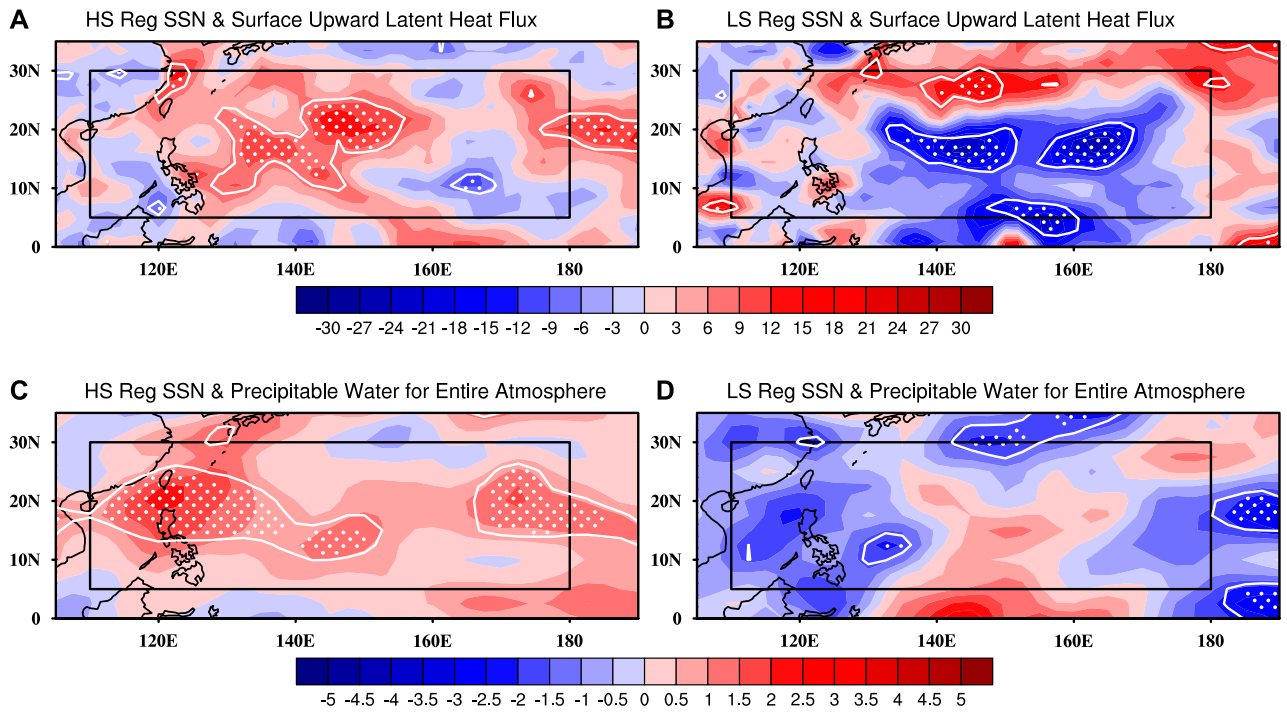

FIGURE 10
Regressions of JAS surface upward latent heat flux (unit: W/m^2, upward is positive) against standardized SSN in **(A)** HS and **(B)** LS; Regressions of JAS precipitable water for the entire atmosphere (unit: kg/m^2) against standardized SSN in **(C)** HS and **(D)** LS. The ENSO signal was removed from these meteorological variables before analyzing. Regression coefficients above the 95% (90%) confidence level are highlighted by white dots (white contours). The black box indicates the TC origin.

(Figure 6A). However, neither a significant response of SLP nor abnormal near-surface wind convergence can be noticed in the TC source in LS (Figure 6B). As displayed in Figure 6A, the SSN-induced lower SLP and near-surface cyclonic wind anomaly in HS are conducive to TC generation, which could be one of the reasons for the distinct solar modulation on TC frequency in HS.

In order to reveal the solar asymmetric modulation on the tropospheric vertical wind over the western North Pacific, Figure 7 and Figure 8 exhibit the responses of JAS 500 hPa Ω, 5°–25°N meridional-mean, and 110°E–180° zonal-mean Ω to standardized SSN in HS and LS. In HS, the significant negative 500 hPa Ω anomalies with a maximum reduction of 2 x 10^{-2} Pa/s dominate the main TC origin sector (Figure 7A), and this anomalous local upward motion can avail the TC formation. In LS, the significant areas are small and scattered in the TC source (Figure 7B). In addition, as shown in the cross sections in Figure 8, the prominent enhanced upward motions appear over (13°–23°N, 140°E–175°W) in the whole troposphere in HS, whereas no significant features can be observed over the TC origin in LS. Results indicate that the noteworthy solar asymmetric effects on the regional vertical motion over the TC source could be one of the main reasons for solar asymmetric modulation on the TC frequency.

To sum up, in HS, the increased solar activity could significantly produce lower SLP, low-level cyclonic wind anomalies, and anomalous upward motion over the TC origin, all of which are conducive to TC generation. However, no obvious features can be found in LS. In other words, the remarkable and sensitive responses of regional atmospheric circulation to solar activity in HS are crucial to explaining solar asymmetric modulation on TC frequency over the western North Pacific. Based on that, we will focus on why this marked solar signal in local circulation only shows up in HS to further clarify the possible mechanism.

3.3 Possible air–sea coupled mechanism

In Section 3.2, we find an interesting phenomenon that the western North Pacific might be a sensitive area for solar effects on atmospheric circulation in HS. To detect the particularity of this area, we first give the climatological June–October (JJASO) total cloud cover for 1979–2020 in Figure 9A. It is worth noting that relatively less total cloud cover (<55%) than surrounding subtropics and tropics appears over (10°–30°N, 120°E–180°) within the TC source region. It is a cloud-free area. Then, Figure 9B shows the climatological JJASO surface net solar radiation flux for 1979–2020. The relatively higher net solar radiation flux at the surface (>220 W/m^2) can be observed over the region (10°–30°N, 120°E–180°) that finely lies in the TC origin. The region of increased surface net solar radiation corresponds perfectly with this cloud-free area (Figure 9). Hence, we hypothesize that this relatively cloud-free area could facilitate more incoming solar radiation at the surface over the TC source in HS than that in LS, subsequently causing regional changes in air–sea backgrounds over the western North Pacific.

Furthermore, the responses of JAS surface upward latent heat flux and precipitable water for the entire atmosphere (with the ENSO signal removed) against standardized SSN in HS and LS are displayed in Figure 10. The significant intensified surface upward latent heat flux on

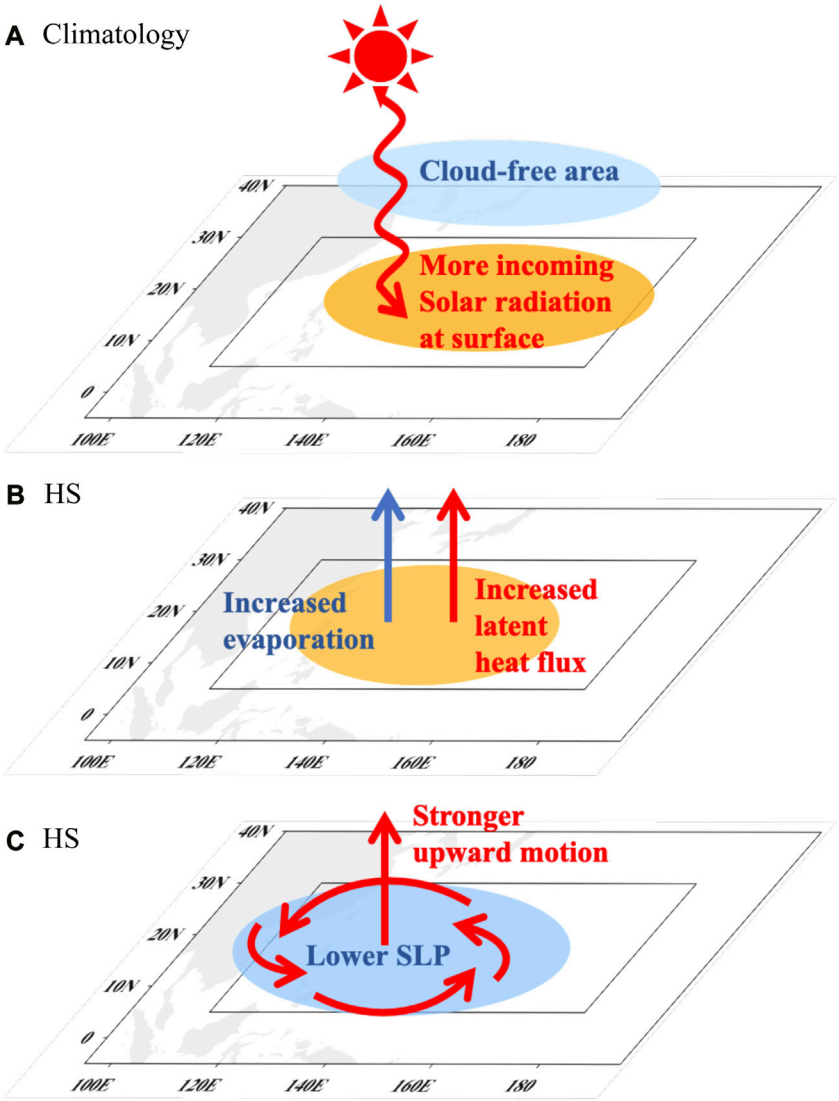

FIGURE 11
Schematic illustration for the possible air–sea coupled mechanism of the significant solar modulation on TC frequency over the western North Pacific in HS. **(A)** Climatological total cloud cover and downward solar radiation at the surface. **(B)** Solar-induced regional increased surface upward latent heat flux and evaporation in HS. **(C)** Solar-caused anomalous local atmospheric circulation (low-level cyclonic wind convergence, lower SLP, and stronger upward motion) in HS. The black box represents the TC source region.

the order of 9–15 W/m^2 is located in the central region of the TC source in HS (Figure 10A). While in LS, most of the TC origin shows weakened upward latent heat flux (Figure 10B). The precipitable water in the entire atmosphere can represent the amount of water vapor contained in the air column. In HS, the precipitable water for the entire atmosphere increases markedly in the TC origin, with the maximum anomaly exceeding 2.5 kg/m^2 (Figure 10C). However, no marked features can be found in LS (Figure 10D). It indicates the evaporation is dramatically intensified in HS compared to LS. Along with the solar-induced stronger upward latent heat flux and greater evaporation at the ocean surface in the TC source in HS (Figures 10A,C), the local upward motion is visibly enhanced (Figure 7A; Figure 8A,C). Then, for compensation, the regional SLP is reduced and the low-level winds become cyclonic (Figure 6A), resulting in more TCs over the western North Pacific in HS.

Based on these analyses, we finally provide a schematic illustration for the possible air–sea coupled mechanism of this significant solar modulation on TC frequency over the western North Pacific in HS (Figure 11). The relatively cloud-free area over the western North Pacific could absorb more incoming solar radiation at the surface in HS than in LS (Figure 11A). This increased surface net solar radiation in HS could produce a stronger surface upward latent heat flux and, thus, greater evaporation over the TC source (Figure 11B). Along with that, the local upward motion is visibly strengthened (Figure 11C). Then, the regional SLP is reduced, and the low-level winds become cyclonic over the TC origin (Figure 11C). All of these solar-caused anomalies in atmospheric circulation in HS are in favor of TC generation over the western North Pacific.

This possible mechanism involves the increased surface solar forcing in the cloud-free area that is manifested by regionally enhanced upward

latent heat flux and evaporation. Therefore, it seems like an air–sea coupled amplification mechanism in HS. In climatology, the combined actions of the North Pacific subtropical gyre in the ocean and the Northwest Pacific subtropical high in the atmosphere could maintain the cloud-free region. As for ocean circulation, although the local ocean surface receives more solar radiation in HS, the effect of regional solar shortwave radiation on large-scale ocean circulation is very limited. Thus, the influence of ocean circulation has not been explored in this study. As for the atmosphere, we find the weakened Northwest Pacific subtropical high in HS (Figures 6–8), which is not conducive to the maintenance of cloud-free areas. So, there might be a restraining factor that makes the mechanism more complex.

4 Conclusion and discussion

The impacts of solar activity on the tropical Pacific and the possible underlying mechanisms have been widely reported in prior studies. However, few studies focus on the effects of solar activity on the TC over the western North Pacific. Based on the observations from the CMA and SILSO and the reanalysis data from the NCEP/DOE and Hadley Centre for the period of 1979–2020, we examine the solar asymmetric modulation on TC frequency over the western North Pacific in different solar phases and further illustrate the possible mechanism.

We first find a significant positive correlation with the 95% confidence level between yearly SSN and TC frequency for 1979–2020. It suggests that stronger solar activity might induce more TCs over the western North Pacific. It is worth noting that the responses of TC frequency to solar activity are obviously asymmetric when dividing the whole period into HS and LS. Specifically, the increased solar activity could markedly produce more TCs in HS (with a 99% confidence level); however, no significant modulation can be found in LS.

Then, we detect the asymmetric effects of solar activity on the air–sea backgrounds of TC generation. In HS, the stronger solar activity significantly causes lower SLP, near-surface cyclonic wind anomalies, and anomalous upward motion over the TC origin, all of which are conducive to more TC generation. However, no obvious features can be found in LS. It seems that the remarkable and sensitive responses of regional atmospheric circulation to increased solar activity in HS are crucial to explaining solar asymmetric modulation on TC frequency over the western North Pacific.

Further investigation reveals a possible air–sea coupled mechanism for this significant solar modulation on TC frequency over the western North Pacific in HS. The relatively cloud-free area in the western North Pacific could absorb more incoming solar radiation at the surface in HS than in LS. This increased regional surface net solar radiation in HS could produce a stronger surface upward latent heat flux and, thus, greater evaporation in the TC source. Along with that, the local upward motion is dramatically strengthened over the TC origin. Then, for compensation, the regional SLP is reduced and the near-surface winds become cyclonic. All of these solar-caused regional anomalies in atmospheric circulation in HS contribute to more TCs over the western North Pacific.

The key to this feasible mechanism is that the increased regional solar forcing at the ocean surface in the cloud-free area could be manifested by the regionally strengthened upward latent heat flux and evaporation. This air–sea coupled mechanism has some similarities with the "bottom–up" mechanism (Meehl et al., 2008; Meehl et al., 2009). The "bottom–up" mechanism is used to explain the La Nina-like response of the tropical Pacific to the 11-year solar cycle peaks (van Loon et al., 2004; van Loon et al., 2007; Meehl et al., 2008). However, we neither selected the solar decadal peaks nor separated solar activity into different timescales, so the results were different from these previous studies. Moreover, some unknown restraining factors in the atmosphere and ocean might be underestimated. Furthermore, the "top–down" mechanism of solar modulation on TC has not been explored in this work. We think the phases of quasi-biennial oscillation should be considered when investigating the "top–down" transfer of the solar signal into the TC in further studies.

Data availability statement

Publicly available datasets were analyzed in this study. These data can be found at the China Meteorological Administration Tropical Cyclone Data Center for the best-track data of tropical cyclones over the western North Pacific (http://tcdata.typhoon.org.cn); the World Data Center Sunspot Index and Long-term Solar Observations of Royal Observatory of Belgium for the sunspot number data (http://sidc.oma.be/silso/); the National Centers for Environmental Prediction/Department of Energy Reanalysis II for the gridded meteorological data (https://psl.noaa.gov/data/gridded/data.ncep.reanalysis2.html); and the Met Office Hadley Centre Sea Ice and Sea Surface Temperature Dataset for the gridded sea surface temperature data (https://www.metoffice.gov.uk/hadobs/hadisst/).

Author contributions

DL contributed to data analysis. ZX and JX designed the research idea and process. DL and LZ contributed to drafting this manuscript. All authors contributed to the article and approved the submitted version.

Funding

This work is jointly supported by the National Natural Science Foundation of China (42205025, 42075040, 42130605), the program for scientific research start-up funds of Guangdong Ocean University (060302032102), and the Guangdong Basic and Applied Basic Research Foundation (2019A1515111009).

Acknowledgments

We thank the reviewers for the helpful suggestions and the editor for the supervision of this article.

Conflict of interest

The authors declare that the research was conducted in the absence of any commercial or financial relationships that could be construed as a potential conflict of interest.

Publisher's note

References

Bal, S., Schimanke, S., Spangehl, T., and Cubasch, U. (2011). On the robustness of the solar cycle signal in the Pacific region. *Geophys. Res. Lett.* 38, L14809. doi:10.1029/2011GL047964

Chan, J. C. L. (2005). Interannual and interdecadal variations of tropical cyclone activity over the Western North Pacific. *Meteorology Atmos. Phys.* 89, 143–152. doi:10.1007/s00703-005-0126-y

Chen, L., and Ding, Y. (1979). *Introduction to the western pacific typhoon*. Beijing, China: Science Pres.

Duan, C. C. (2008). Impacts of solar activities on abnormality of general circulation and Yunnan rainfall in summer. *Plateau Mt. Meteorology Res.*, 28(3): 37–43. doi:10.3969/j.issn.1674-2184.2008.03.006

Gray, L. J., Beer, J., Geller, M., Haigh, J. D., Lockwood, M., Matthes, K., et al. (2010). Solar influences on climate. *Rev. Geophy.* 48, RG4001. doi:10.1029/2009RG000282

Gray, W. M. (1968). Global view of the origin of tropical disturbances and storms. *Mon. Weather Rev.* 96, 669–700. doi:10.1175/1520-0493(1968)096<0669:GVOTOO>2.0.CO;2

Haigh, J. D., Blackburn, M., and Day, R. (2005). The response of tropospheric circulation to perturbations in lower stratospheric temperature. *J. Clim.* 18, 3672–3685. doi:10.1175/JCLI3472.1

Haigh, J. D., and Blackburn, M. (2006). Solar influences on dynamical coupling between the stratosphere and troposphere. *Space Sci. Rev.* 125, 331–344. doi:10.1007/s11214-006-9067-0

Haigh, J. D. (1996). The impact of solar variability on climate. *Science* 272, 981–984. doi:10.1126/science.272.5264.981

Huo, W., Xiao, Z., Wang, X., and Zhao, L. (2021). Lagged responses of the tropical Pacific to the 11-yr solar cycle forcing and possible mechanisms. *J. Meteorol. Res.* 35, 444–459. doi:10.1007/s13351-021-0137-8

Kanamitsu, M., Ebisuzaki, W., Woollen, J., Yang, S.-K., Hnilo, J. J., Fiorino, M., et al. (2002). NCEP-DOE AMIP-II reanalysis (R-2). *B. Am. Meteorol. Soc.* 83, 1631–1643. doi:10.1175/BAMS-83-11-1631

Kim, J. H., Kim, K. B., Chang, H. Y., Cho, M. H., Ahn, Y. H., Choi, H. J., et al. (2017). Long-term repeated rituximab treatment for childhood steroid-dependent nephrotic syndrome. *J. Astronomy Space Sci.* 34, 257–263. doi:10.23876/j.krcp.2017.36.3.257

Kodera, K., and Kuroda, Y. (2002). Dynamical response to the solar cycle. *J. Geophys. Res.* 107, 4749. doi:10.1029/2002JD002224

Kodera, K., Thiéblemont, R., Yukimoto, S., and Matthes, K. (2016). How can we understand the global distribution of the solar cycle signal on the Earth's surface? *Atmos. Chem. Phys.* 16, 12925–12944. doi:10.5194/acp-16-12925-2016

Kopp, G., and Lean, J. L. (2011). A new, lower value of total solar irradiance: evidence and climate significance. *Geophys. Res. Lett.* 38, L01706. doi:10.1029/2010GL045777

Li, D., Xiao, Z., and Zhao, L. (2019). Preferred solar signal and its transfer in the Asian–Pacific subtropical jet region. *Clim. Dyn.* 52, 5173–5187. doi:10.1007/s00382-018-4443-5

Li, R. C., and Zhou, W. (2018). Revisiting the intraseasonal, interannual and interdecadal variability of tropical cyclones in the western North Pacific. *Atmos. Ocean. Sci. Lett.* 11 (2), 198–208. doi:10.1080/16742834.2018.1459460

Li, S., Li, Z., and Ling, S. (2023). Combined effect of the solar activity and ENSO on the tropical cyclone genesis frequency in the southeastern part of the western North Pacific. *Front. Earth Sci.* 11, 1139699. doi:10.3389/feart.2023.1139699

Lu, X. Q., Yu, H., Ying, M., Zhao, B. K., Zhang, S., Lin, L. M., et al. (2021). Western North pacific tropical cyclone database created by the China meteorological administration. *Adv. Atmos. Sci.* 38 (4), 690–699. doi:10.1007/s00376-020-0211-7

Matthes, K., Kuroda, Y., Kodera, K., and Langematz, U. (2006). Transfer of the solar signal from the stratosphere to the troposphere: northern winter. *J. Geophys. Res.* 111, D06108. doi:10.1029/2005JD006283

Meehl, G. A., Arblaster, J. M., Branstator, G., and van Loon, H. (2008). A coupled air-sea response mechanism to solar forcing in the Pacific region. *J. Clim.* 21 (12), 2883–2897. doi:10.1175/2007JCLI1776.1

Meehl, G. A., Arblaster, J. M., Matthes, K., Sassi, F., and van Loon, H. (2009). Amplifying the Pacific climate system response to a small 11-year solar cycle forcing. *Science* 325, 1114–1118. doi:10.1126/science.1172872

Rayner, N. A., Parker, D. E., Horton, E. B., Folland, C. K., Alexander, L. V., Rowell, D. P., et al. (2003). Global analyses of sea surface temperature, sea ice, and night marine air temperature since the late nineteenth century. *J. Geophys. Res.* 108 (D14), 4407. doi:10.1029/2002jd002670

Ruzmaikin, A. (1999). Can El Niño amplify the solar forcing of climate? *Geophys. Res. Lett.* 26, 2255–2258. doi:10.1029/1999GL900535

Tian, R. X. (2005). Solar effect on the relationship between tropical cyclone activity over the west of North Pacific and the stratospheric quasi-biennial oscillation. *J. Zhejiang Univ. Sci. Ed.* 32 (3), 350–354. doi:10.3321/j.issn:1008-9497.2005.03.024

van Loon, H., Meehl, G. A., and Arblaster, J. M. (2004). A decadal solar effect in the tropics in July–August. *J. Atmos. Solar-Terr. Phys.* 66, 1767–1778. doi:10.1016/j.jastp.2004.06.003

van Loon, H., Meehl, G. A., and Shea, D. J. (2007). Coupled air-sea response to solar forcing in the Pacific region during northern winter. *J. Geophys. Res.* 112, D02108. doi:10.1029/2006JD007378

van Loon, H., and Meehl, G. A. (2008). The response in the Pacific to the sun's decadal peaks and contrasts to cold events in the Southern Oscillation. *J. Atmos. Solar-Terr. Phys.* 70, 1046–1055. doi:10.1016/j.jastp.2008.01.009

Wang, W., Matthes, K., Tian, W., Park, W., Shangguan, M., and Ding, A. (2019). Solar impacts on decadal variability of tropopause temperature and lower stratospheric (LS) water vapour: A mechanism through ocean–atmosphere coupling. *Clim. Dynam.* 52, 5585–5604. doi:10.1007/s00382-018-4464-0

Xiao, Z., Li, D., Zhou, L., Zhao, L., and Huo, W. (2017). Interdisciplinary studies of solar activity and climate change. *Atmos. Ocean. Sci. Lett.* 10, 325–328. doi:10.1080/16742834.2017.1321951

Ying, M., Zhang, W., Yu, H., Lu, X., Feng, J., Fan, Y., et al. (2014). An overview of the China Meteorological Administration tropical cyclone database. *J. Atmos. Ocean. Technol.* 31, 287–301. doi:10.1175/JTECH-D-12-00119.1

Zhan, R., Wang, Y., and Zhao, J. (2019). Contributions of SST anomalies in the indo-pacific ocean to the interannual variability of tropical cyclone genesis frequency over the Western North pacific. *J. Clim.* 32, 3357–3372. doi:10.1175/JCLI-D-18-0439.1

Frontiers in Earth Science

Investigates the processes operating within the major spheres of our planet

Advances our understanding across the earth sciences, providing a theoretical background for better use of our planet's resources and equipping us to face major environmental challenges.

Discover the latest Research Topics

See more →

Frontiers

Avenue du Tribunal-Fédéral 34
1005 Lausanne, Switzerland
frontiersin.org

Contact us

+41 (0)21 510 17 00
frontiersin.org/about/contact